CVR JOURNAL OF SCIENCE AND TECHNOLOGY

Vol.No. 26, June 2024
P-ISSN 2277 - 3916
DOI 10.32377/CVRJST26
E-ISSN 2581 - 7957

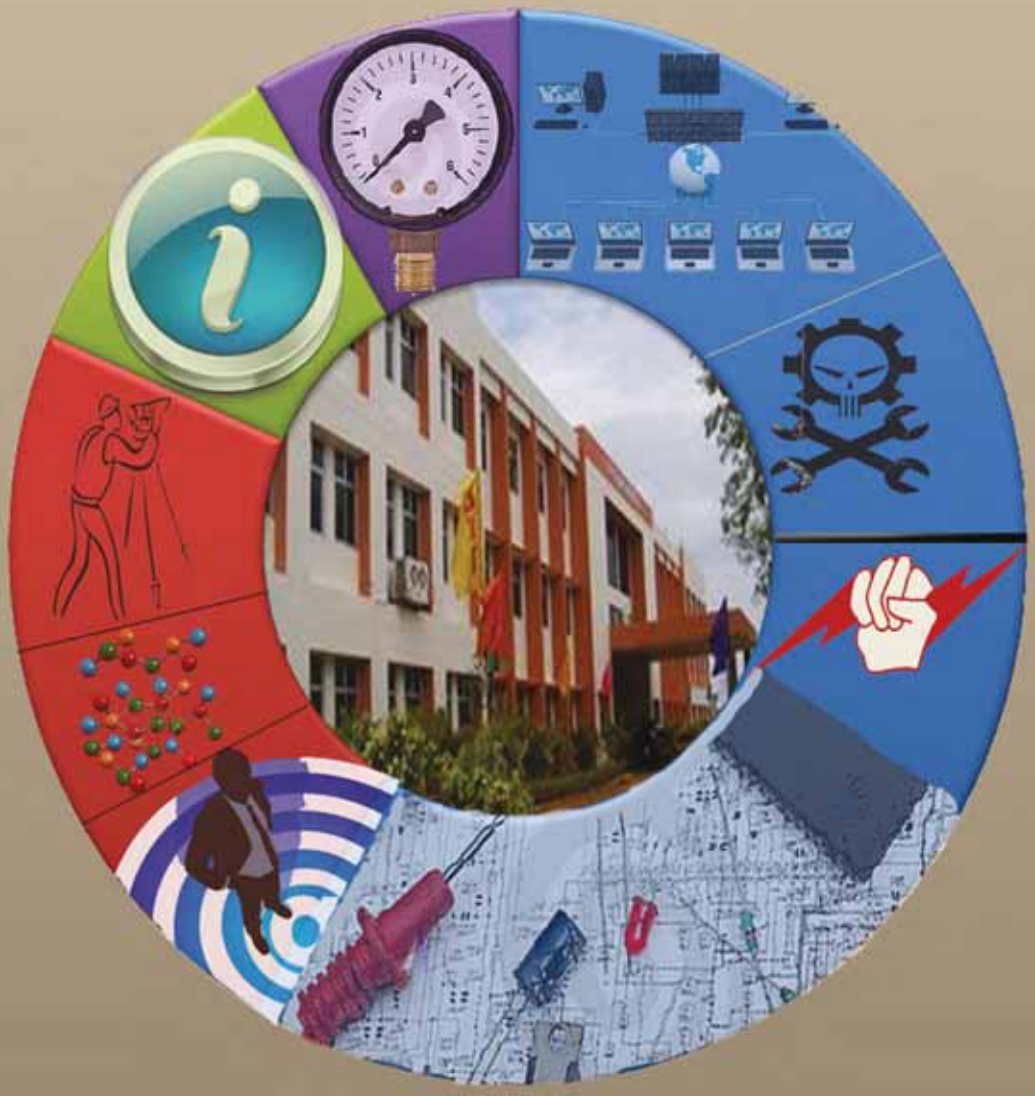

CVR COLLEGE OF ENGINEERING

In Pursuit of Excellence

CVR JOURNAL OF SCIENCE AND TECHNOLOGY

Indexed by

- Google Scholar
- Directory of Research Journals Indexing (DRJI)
- Scientific Indexing Services (SIS)
- International Institute of Organised Research (I2OR)
- Scholar Impact - Journal Index
- Citefactor
- Member Crossref / DOI

Accredited by NAAC with 'A' GRADE

CVR COLLEGE OF ENGINEERING

(UGC Autonomous - Affiliated to JNTU Hyderabad)
Mangalpalli (V), Ibrahimpatnam (M),
R.R. District, Telangana. – 501510
http://cvr.ac.in

EDITORIAL

This issue is the 26th Volume of the Biannual CVR Journal of Science and Technology. The editorial team is very happy to bring out this Volume very much in time. The journal is being published since 2011, regularly without any break, even during corona pandemic time, overcoming many hurdles. For the last 6 months, the editorial team is working tirelessly, to complete the task on time. Thanks are due to the authors, reviewers and all others involved in this work.

We are taking care to see that standard practices are followed in the publication of the Journal. Blind review is done, and a number of iterations are done till the reviewers are fully satisfied with the standard of the research paper. Senior faculty of English language Department, take care of the language issues. Template verification and typographical errors are checked before the articles go for publishing. Hope the researchers appreciate this effort. Many research articles published in the journal are being referred by other researchers across the globe, as indicated by DOI, Crossref data.

This Volume covers research articles in the following disciplines:

CIVIL–3, ECE– 5, EEE–4, EIE-1, IT-1, CSE-2, ET–2, MECH–3

In this issue, one paper on Implementation of 5G New Radio (NR) Secondary Synchronization on FPGAs is presented. The proposed design, for funding physical cell Identity is verified and executed on Xylinx ZYNQFPGA board. The authors mentioned that logic utilization is reduced, and low power dissipation is observed. Another paper on Area-Delay-Power Efficient VLSI Architecture 2D FIR Filter using Modified Multipliers and Adders is also published. According to authors, by this design, power consumption is reduced by 44% and delay by 20%. Authors used Modified Carry Look Ahead (MCLA) address and pipelining methods, to achieve such impressive results.

In another paper, a protype Artificial Mechanical Ventilator device based on IoT, at low cost for patients, is proposed by authors. During the covid pandemic time, there was worldwide shortage of ventilators. This device is designed such that it is easily accepted by patients. The focus in this model is to minimize components and increase efficiency of the ventilator and the patients feel comfortable while using. For detection and classification of Brain Tumors in MRI images, a paper is presented in which, tumors are segmented using EPFCM and classified using ML-ELM. The authors conclude that EPCMA+ML+ELM yields better results in contrast to DL Classifiers and ELM. The identified quantitative measures of exact tumor regions help physicians and radiologists in effective treatment. Another paper on IR Sensor based Smart Parking System is also published. Some articles published have potential to be taken up by incubation units and start-ups to bring them into commercial production.

Students are being encouraged to publish research papers based on the project work done by them. P.G. students spend almost one year on the project work. So, this should result in significant work suitable for publication in a journal. Project supervisors guiding the students must give research orientation for the work of the students. Selected research papers of U.G. students are also published in this volume. It is heartening to see that U.G. students are also showing enthusiasm for publishing papers. Hope this trend will continue.

Thanks are due to **HOD, H & S,** and the staff of English Department for reviewing the papers. I am also thankful to **Dr. S. Venkateshwarlu, Dr. P. Uma Maheshwera Reddy Assoc. Editors and Mr. Ch. Gangadhar, DTP Operator** in the Office of Dean Research, for the preparation of research papers in Camera - Ready form.

For further clarity on waveforms, graphs, circuit diagrams and figures, readers are requested to browse the soft copy of the journal, available on the college website, www.cvr.ac.in wherein a link is provided. Authors can also submit their papers through our online open journal system (OJS) www.ojs.cvr.ac.in or www.cvr.ac.in/ojs

Prof. K. Lal Kishore
Editor

CONTENTS Page No.

E-ISSN 2581 – 7957
P-ISSN 2277 – 3916

CVR Journal of Science and Technology, Volume 26, June 2024
DOI: 10.32377/cvrjst2601

Enhancing Lightweight Concrete with Overburnt Broken Brickbats: Investigating Optimal Replacement Levels

N. Ramanjaneyulu
Sr.Asst. Professor, CVR College of Engineering/Civil Engg. Department, Hyderabad, India
Email: rams.613@gmail.com

Abstract: **The abstract summarizes the research findings on lightweight self-compacting concrete (LWSCC) incorporating unburnt broken brick bats as partial replacements for natural gravel aggregates. Mechanical properties, including compressive, split tensile, and flexural strengths, were evaluated for LWSCC samples with replacement levels of 0%, 10%, 20%, and 30% by volume of natural gravel. The compressive strengths ranged from 28.133 to 33.85 N/mm², split tensile strengths ranged from 8.3 to 10.6 N/mm², and flexural strengths ranged from 3.24 to 5.73 N/mm² across the replacement levels. Additionally, fresh properties of the LWSCC have been assessed using L box, V funnel, and J ring tests to evaluate workability according to EFNARC guidelines. The results have indicated satisfactory workability properties for all replacement levels, confirming the feasibility of using unburnt broken brick bats in LWSCC mixtures. This research contributes to the understanding of incorporating alternative lightweight aggregates in concrete production, potentially reducing environmental impact and resource consumption associated with traditional aggregates. Furthermore, the mechanical properties demonstrate the potential of unburnt broken brick bats as a viable lightweight aggregate option in LWSCC formulations. These findings offer valuable insights for engineers and researchers seeking sustainable solutions in concrete technology and construction practices.**

Index Terms: **Broken Brick Bats, Environmental Impact, Lightweight Concrete, Mechanical Properties, Sustainable Aggregates, Workability Assessment**

I. Introduction

The research focuses on using structural lightweight concrete in multi-storied buildings to reduce the dead load, which is crucial for high-rise structures. The study specifically investigates the use of 'over-burnt brickbats' as a partial replacement for coarse aggregate in the concrete mix.[1]. The aim is to observe the cost and physical properties of concrete. The construction industry increasingly seeks sustainable solutions to address environmental concerns and optimize resource utilization. [2] Concrete, one of the most widely used construction materials globally, plays a significant role in this quest for sustainability. Traditional concrete production relies heavily on natural aggregates, such as gravel and crushed stone, which can deplete finite resources and contribute to environmental degradation through extraction and transportation processes. The use of 'pumice' as a lightweight aggregate also reduces the density of the concrete, resulting in a decrease in the dead weight of the structure. Additionally, pumice has been found to exhibit pozzolanic properties, making it suitable as a cement replacement material [3-5]. To mitigate these challenges, researchers and engineers have been exploring alternative materials and techniques to enhance the sustainability of concrete. One promising approach is the utilization of industrial by-products and waste materials as aggregates in concrete mixtures. These materials offer a sustainable alternative to natural aggregates and opportunities for waste valorization and resource efficiency. Among such materials, Over Burnt Brick Bats (OBB) stand out as a potential coarse aggregate replacement due to their abundance in certain regions and their properties conducive to concrete production [6,7].

The use of OBB in concrete offers several potential benefits, including reduced environmental impact, cost-cutting, and improved material performance. By diverting OBB from landfills and incorporating them into concrete mixtures, the construction industry can contribute to waste reduction efforts and promote circular economy principles. Moreover, OBB possesses intrinsic properties that can enhance concrete's mechanical and durability characteristics, thereby expanding its application in various construction projects. However, the successful integration of OBB into concrete requires a thorough understanding of their effects on concrete properties and performance. Several factors, including the size, shape, and composition of OBB and the replacement ratio, can influence the resulting concrete mixture's workability, strength, and durability. Therefore, comprehensive experimental investigations are necessary to assess the feasibility and efficacy of using OBB to replace traditional coarse aggregates [8-11].

In this context, this study aims to evaluate the potential of OBB as a coarse aggregate replacement in lightweight self-compacting concrete (LWSCC) mixtures. LWSCC offers distinct advantages over conventional concrete, including improved flowability and reduced labor requirements during placement. [12-15] By incorporating OBB into LWSCC mixtures, this study seeks to harness the benefits of lightweight aggregates and waste materials in concrete production. This research focuses on assessing the mechanical properties, including compressive, split tensile, and flexural strengths, of LWSCC samples with varying percentages of OBB replacement. Additionally, the study investigates the fresh properties of concrete mixtures, such as workability, through standardized tests to ensure compliance with industry guidelines and specifications [16-18].

Received on 12-03-2024, Revised on 11-04-2024, Accepted on 11-05-2024.

CVR Journal of Science and Technology, Volume 26, June 2024
DOI: 10.32377/cvrjst2601

Figure 1. Overburnt brickbats

Overburnt brickbats: Overburnt brickbats refer to bricks that have been fired at an excessively high temperature, resulting in a darkened, distorted appearance and reduced strength.

Figure 2. Difference between Normal Brick Bats and Over Burnt Brick Bats

This study aims to provide insights into the feasibility and effectiveness of using OBB as a sustainable alternative in LWSCC production through systematic experimentation and analysis. The findings of this research can be advantageous to concrete producers, engineers, and policymakers about the potential benefits and challenges associated with incorporating OBB into concrete mixtures, contributing to the advancement of sustainable construction practices.

II. Literature Review

Husain M (1995) examined the application of untreated or treated bricks with different viscosity cement syrups as coarse aggregate. They discovered that, at? 28 days, the compressive strengths of crushed brick concrete were 75–80% of those of regular concrete, while the splitting tensile strength and modulus of elasticity were higher and lower, respectively than those of regular concrete.

Khalaf, F .M, and Devenny, A. S. (2005) conducted a study to assess the mechanical and physical characteristics of freshly burned and crushed bricks for aggregate in Portland cement concrete. According to the author, when the parent brick's compressive strength declines, the brick aggregate's impact value rises. The outcomes demonstrated the potential of using over-burned crushed brick aggregates to produce concrete for low-level civil engineering applications.

Farid Debib and Said Kenai (2017) investigated the impact by substituting coarse and fine concrete with crushed bricks from an overburn. Concrete was tested for split tensile, flexure, and compressive strength at 25, 50, 75, and 100% replacement levels.

According to the authors, broken brick concrete has a lower density than regular concrete. The test results gave substitution levels of 25% for coarse aggregate and 50% for fine aggregate.

Vikash Kumar Gautam (2019) This study investigates the use of crushed burn bricks as a coarse aggregate in concrete. Two types of concrete mixtures are prepared, one with a 1:2:4 ratio and the other with varying weights of crushed over-burn bricks. Thirty concrete specimens are tested under compression and split tension according to British standards. Results show that mistreatment of crushed bricks reduces concrete strength and increases the water-to-cement ratio. The study also investigates lightweight foamed concretes made with partial waste substitution over burn brick as coarse aggregate. Four different percentages of concrete mixtures are prepared, with the most optimal proportion being 25th. Foam is injected into the mixture to provide lightweight concrete with the correct proportions. The results show that waste burn bricks are suitable for creating concrete with acceptable strength characteristics. The study concludes that waste burn bricks are lightweight and helpful for creating lightweight concrete structures. However, using crushed bricks as a coarse combination decreases concrete compressive strength by 11-87% at 28 days. The recycled brick combination concrete created with this OBBA is suitable for use in unstable concrete.

Haque (2022) investigates using Khama brick chips as a partial replacement for coarse aggregate in lightweight structural concrete. The study tested the concrete's compressive strength and unit weight at different percentages of jhama brick chip replacements. Results showed up to 25% of the replacements met ASTM C 330 compressive strength requirements. The study also examines the properties of jhama brick chips, including sieve analysis.

III. Experimental Programme

This experimental program aims to determine the behavior of self-compacting concrete produced using overburnt brickbats replacing 10%, 10%, 20%, and 30% of normal coarse aggregate. Mechanical and Fresh properties of lightweight self-compacting concrete at 28 days are investigated for M20 grade.

Objectives

➤ To design the M20 mix by partially replacing the coarse aggregate with overburnt brickbat aggregate.

➤ To find out the fresh properties of LWOBBAC (lightweight overburnt brickbat aggregate concrete).

CVR Journal of Science and Technology, Volume 26, June 2024
DOI: 10.32377/cvrjst2601

➤To study the mechanical properties of LWOBBAC (lightweight overburnt brickbat aggregate concrete).

➤ To reduce the self-weight and density of the LWOBBAC

IV. Materials And Methods

A. Cement

A pozzolanic material is essentially a siliceous or aluminous material that, despite not having cementitious properties, will react with calcium hydroxide, which is released during the hydroxide process at room temperature when it is in a finely divided state and in the presence of water to form a compound with cementitious properties. The physical properties of cement values are shown in Table 1.

TABLE I.
FRESH PROPERTIES OF CEMENT

S. No.	Property	Test Results
1.	Normal consistency	31%
2	Initial setting time	50 minutes
3	Final setting time	550 minutes
4	Soundness test	3 mm
5.	Specific gravity	3.15

B. Fine Aggregates

River sand that had been sieved up to 4.750 mm and was readily available in the area was used as the "fine aggregate". The IS: 2386-1963 was used to analyze the properties of sand.

C. Coarse Aggregates

Typically, fractured stone serves as the coarse aggregate in concrete mixtures, comprising a significant portion of its volume. Locally sourced coarse aggregates, with a nominal size of 20 mm, were utilized in this study. Before incorporation, the aggregates underwent a thorough washing process to remove any dirt or dust contaminants. The selection of coarse aggregate size depends on the intended application, with maximum sizes dictated by specific project requirements and standards. In accordance with Indian Standard Specifications IS: 383-1970, stringent tests are conducted to assess the quality and suitability of coarse aggregates for concrete production.

C. Over Burnt Brickbats:

Overburnt brickbats are fragments of bricks subjected to excessive firing temperatures, rendering them dark and brittle. They are commonly used as coarse aggregates in concrete production, offering reduced cost and environmental sustainability benefits. However, their high absorption rate and irregular shape can impact concrete properties. OBB Properties values are shown in Table No. 2.

D. Soaking Burnt Brickbats *in water:* Due to the composition of clay and earth materials, overburnt brick bats possess numerous voids, leading to significant absorption capacity. Direct incorporation into concrete without pre-treatment results in water absorption, potentially compromising the mix. Thus, soaking the bats in water followed by drying is imperative to achieve Saturated Surface Dry conditions before utilization.

Figure 3. Soaking Burnt Brickbats in water.

TABLE II.
Physical Properties of Over Burnt Brickbats

S. No.	Properties	Results
1	Size	20mm passing and 16mm retaining
2	Shape	Angular
3	Specific Gravity	2.17
4	Loose Bulk Density	602.3kg/m^3
5	Compacted Bulk Density	698.49kg/m^3
6	Fineness modulus	7.20

D. Water

Water plays a key role in concrete, facilitating the binding of cement and particles and forming a cohesive mixture. Therefore, only clean, and potable water is used to prepare concrete mixes to ensure optimal hydration and strength development.

TABLE III.
Physical Properties of Over Burnt Brickbats

Percentage Replacements	Cement (kg)	Coarse Aggregate (kg)	OBB (kg)	Fine Aggregate (kg)	Water (lit)
0%	358.18	1181.77	0	707.335	197
10%	358.18	1063.57	71.4	707.335	197
20%	358.18	945.39	142.	707.335	197
30%	358.18	827.224	214.	707.335	197

D. Casting of Specimens: Specimens have been cast using overburnt brickbat concrete to determine compressive, flexural, and split tensile strength. For compressive strength, cube specimens with dimensions of 150mm were molded.

CVR Journal of Science and Technology, Volume 26, June 2024
DOI: 10.32377/cvrjst2601

Rectangular prisms of 100mm x 100mm x 500mm were prepared for flexural strength testing. In addition, cylindrical specimens with 150mm diameter and 300mm height were utilized for split tensile strength evaluation. All specimens were vibrated during casting to ensure uniformity and cured under standard conditions before testing.

Figure 4. Casting of Specimens

V. Results And Discussions

Compressive Strength: Place cylindrical specimens in a compression testing machine. Apply load gradually until failure occurs. The compressive strength values at the 7 and 28 days are shown in Table No.7. Calculate compressive strength using the formula:

Figure 5. Compression Test Machine

Split Tensile Strength:
Set cylindrical specimens horizontally between the loading platens of a testing machine. Apply the load perpendicular to the cylinder's axis until it fails. Table 7 shows the split tensile strength values at 7 and 28 days.

Figure 6. Split Tensile test machine.

Flexural Strength:
Position rectangular prisms on a flexural testing machine. Apply load at the midpoint of the specimen until failure. Table 7 shows the flexural strength values at 7 and 28 days.

Figure 7. Flexural Strength Test Machine.

CVR Journal of Science and Technology, Volume 26, June 2024
DOI: 10.32377/cvrjst2601

TABLE IV.
MECHANICAL PROPERTIES OF LWOBBA CONCRETE

Designation	Cube Compressive Strength Mpa		Prism flexural strength Mpa		Cylinder split tensile. strength Mpa	
	7Days	28 Days	7 Days	28 Days	7 Days	28 Days
NC	19.5	29.92	1.1	5.5	2.4	9.4
10%	19.6	31.1	1.2	5.6	2.4	9.6
20%	19.7	33.85	1.4	5.73	2.6	10.6
30%	16.2	28.133	1.8	3.24	2.2	8.3

Mechanical properties like compressive strengths got 29.92, 31.106, 33.85 and 28.133 N/mm2, split tensile strengths got 9.4, 9.6, 10.6 and 8.3 N/mm2, and flexural strengths got 5.5,5.6, 5.73 and 3.24 for the lightweight self-compacting concrete partially replaced with over burnt brickbats with 0%, 10%, 20% and 30% respectively by volume of natural gravel and its fresh properties using L box, V funnel, and J ring test performed to verify its workability properties and got satisfied as per EFNARC guidelines,

Density: The density of Overburnt brickbat concrete for 0%, 10%, 20%, and 30% replacements was determined by weighing each specimen. Using the formula below, densities were calculated for comparison. Density of concrete values shown in table 5.

$$\text{density} = \frac{\text{Average Weight Of Samples (kg)}}{\text{volume of sample } (m^3)}$$

TABLE V.
DENSITIES OF LWOBBA CONCRETE

Percentage of replacement	Density in (in Kg/m²)
LWOBBAC-0%	2359
LWOBBAC -10%	2364
LWOBBAC -20%	2370
LWOBBAC -30%	2079

Slump Test: The workability of Over Burnt Brickbat concrete at 0%, 10%, 20%, and 30% replacements was assessed using the slump test. A slump cone was filled in three layers, each compacted with 25 blows. After removal, the decrease in height from the cone's top to the displaced concrete surface was measured. The reduction in slump with increasing replacement percentage is due to the presence of coarse aggregates like brickbats, which can result in decreased workability as they may hinder the flow of the concrete mix. The workability of concrete by slump test values is shown in Table 7.

Figure 8. Workability by Slump Test

TABLE VI.
WORKABILITY OF LWOBBA CONCRETE

Percentage of replacement	Workability in mm
LWOBBAC-0%	75
LWOBBAC -10%	72
LWOBBAC -20%	65
LWOBBAC -30%	50

Firstly, regarding compressive strength, it is observed that as the percentage of OBB replacement increases from 0% to 20%, there is a progressive enhancement in compressive strength, with values ranging from 29.92 to 33.85 N/mm². This indicates that the potential for OBB to influence the structural integrity of LWSCC mixes positively. However, beyond 20% replacement, a slight decrease in compressive strength is noted, suggesting a threshold beyond which excessive OBB content may compromise overall strength. Similarly, the split tensile strength exhibits a similar trend, with incremental improvements observed up to 20% OBB replacement, ranging from 9.4 to 10.6 N/mm². Beyond this point, a reduction in tensile strength is observed, indicating a diminishing returns scenario.

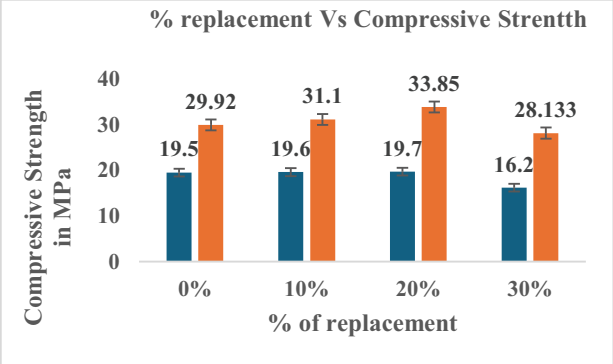

Figure 9. Compressive Strength of 7 and 28 days cured M20 grade concrete.

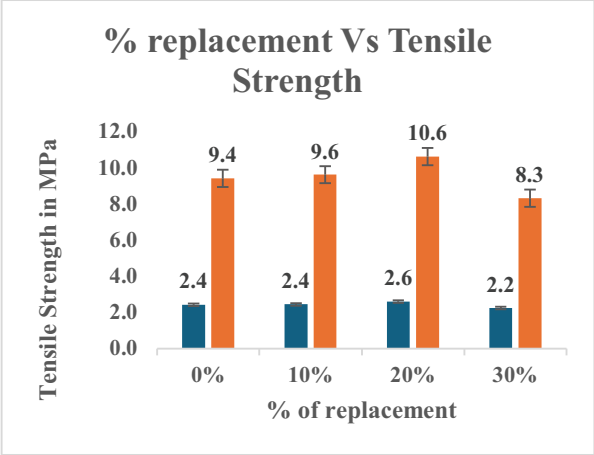

Figure 10. Split tensile strength of 7 and 28 days cured M20 grade concrete.

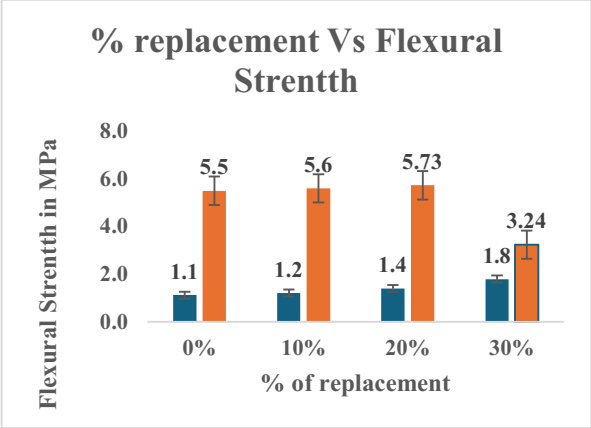

Figure 11. Flexural strength of 7 and 28 days cured M20 grade concrete.

On the contrary, the flexural strength findings exhibit a nuanced trend in response to OBB replacement. Initially, there is a rise in flexural strength with up to 20% replacement, reflected in values ranging from 5.5 to 5.73 N/mm². However, a notable decrease is evident at 30% replacement, indicating a potential structural constraint at higher replacement rates. Additionally, the satisfactory workability performance of NWC, validated through Abram's cone test, evaluates the workability of concrete by measuring the time it takes to flow through a standard cone. Codal provisions ensure concrete consistency for construction quality. This suggests that incorporating OBB maintains the concrete's ability to flow and fill molds effectively. These findings imply that OBB can be successfully employed as a partial substitute for natural gravel in NWC mixes, enhancing mechanical properties up to a certain replacement threshold. Nonetheless, carefully considering the optimal replacement level is imperative to ensure balanced performance and structural soundness.

VI. Conclusion

The following significant conclusions are derived from the experimental investigations that have been conducted. The investigation focused on determining optimal replacement levels for enhancing lightweight concrete with overburnt broken brick bats.

1. Slump values decreased with increasing over burnt brickbat aggregate replacement: 75 mm (0%), 72 mm (10%), 65 mm (20%), and 50 mm (30%).
2. Compressive strengths varied: 29.92 MPa (0%), 31.1 MPa (10%), 33.85 MPa (20%), and 28.133 MPa (30%), Flexural strengths exhibited fluctuations: 5.5 MPa (0%), 5.6 MPa (10%), 5.73 MPa (20%), and 3.24 MPa (30%) and Split tensile strengths displayed changes: 9.4 MPa (0%), 9.6 MPa (10%), 10.6 MPa (20%), and 8.3 MPa (30%).
3. The density of lightweight aggregate concrete was altered to 2359 kg/m³ (0%), 2364 kg/m³ (10%), 2370 kg/m³ (20%), and 2079 kg/m³ (30%).
4. The study identified 20% of over burnt brickbat aggregate replacement as optimal, balancing workability, mechanical properties, and density.
5. These findings offer practical insights for engineers and practitioners to enhance lightweight concrete while utilizing overburnt broken brick bats.
6. Utilizing recycled materials in concrete production contributes to sustainability and resource conservation in the construction industry.
7. Future research could investigate lightweight concrete's long-term performance and durability with overburnt brickbat aggregates.
8. Further exploration of the economic feasibility and environmental impacts of integrating overburnt brickbats into concrete production processes is warranted.
9. This study contributes valuable data and insights into optimizing lightweight concrete with overburnt brickbat aggregate, advancing sustainable construction practices and resource utilization in the industry.

References

[1] Haque, M. R. (2022, September 2). Performance Evaluation of Structural Lightweight Concrete Using Jhama Brick as a Partial Replacement of Coarse Aggregate. *Journal of Cement Based Composites*, *3*(2), 1–4. https://doi.org/10.36937/cebacom.2022.5676

[2] Kuldeepak Dwivedi, “Study On properties of concrete using overburnt brick chips and demolished concrete waste as partial replacement of coarse aggregate”, November 2017.

[3] Ramanjaneyulu, N., Seshagiri Rao, M V & Bhaskar Desai.,V Behavior of Self-Compacting Concrete Partial Replacement of Coarse Aggregate with Pumice Lightweight Aggregate in the journal International Journal of Recent Technology and Engineering (IJRTE) ISSN: 2277-3878, Volume-7, Issue-6C2, April 2019

[4] Yashwanth Pamu & Prasanna SVSNDL (2023) An experimental analysis for clay bricks manufacturing with partial replacement of glass wool, Australian Journal of Structural Engineering, DOI: 10.1080/13287982.2023.2197320

[5] Apebo N. S., Agunwamba. J. C, “The suitability of crushed over burnt brick as coarse aggregate,” in International Journal of Engineering Science and Innovative Technology, Vol. 3, 2014.

[6] Bidve Ganesh Shivkanth, G.N. Shete, Experimental study on the effect of partial replacement of coarse aggregate by overburn brick Bats, April 2019.
[7] Mr. Akshay N.Kadu, "Use of partial replacement of over burnt brick and demolished brickbats as a coarse aggregate in fresh concrete", August 2020.
[8] Rashid. M. A, Hossain. T and Islam M. A, "Properties of Higher Strength Concrete made with crushed brick as aggregate," in Journal of Civil Engineering, Vol. 37(1), pp. 43 -52, 2009.
[9] Mr. G.S.Patil, "Effect of partial replacement of coarse aggregate by Jhama class brick in concrete", August 2015.
[10] Kuldeepak Dwivedi, "Study On properties of concrete using overburnt brick chips and demolished concrete waste as partial replacement of coarse aggregate", November 2017.
[11] Apebo N. S., Agunwamba. J. C, "The suitability of crushed over burnt brick as coarse aggregate," in International Journal of Engineering Science and Innovative Technology, Vol. 3, 2014.
[12] Bidve Ganesh Shivkanth, G.N. Shete, Experimental study on effect of partial replacement of coarse aggregate by overburn brick Bats, April 2019.
[13] Mr. Akshay N. Kadu, "Use of partial replacement of overburnt brick and demolished brick bats as a coarse aggregate in fresh concrete," August 2020.
[14] Rashid. M. A, Hossain. T and Islam M. A, "Properties of Higher Strength Concrete made with crushed brick as aggregate," in Journal of civil Engineering, Vol. 37(1), pp. 43 - 52, 2009.
[15] Mr. G.S.Patil, "Effect of partial replacement of coarse aggregate by Jhama class brick in concrete", August 2015.
[16] Yashwanth Pamu, V.S.S. Kumar, Mohammad Abdul Shakir, Hemanjali Ubbana, Life Cycle Assessment of a building using Open-LCA software, Materials Today: Proceedings, Volume 52, Part 3, 2022, Pages 1968-1978, ISSN 2214-7853.
[17] Yashwanth Pamu, Sanjana Alugubelli, A comparative study of environmental impacts due to conventional and sustainable concrete, Materials Today: Proceedings, 2023, ISSN 2214-7853.
[18] Ramanjaneyulu, N., Seshagiri Rao, M V & Bhaskar Desai., Comprehensive Study on Fresh and Hardened Behaviour of Sintered Fly Ash Aggregate based Lightweight Self-Consolidating Concrete in the IJSRD (International Journal of Scientific Research and Development) | Vol. 9, Issue 8, 2021 | ISSN (online): 2321-0613
[19] Kuldeepak Dwivedi, "Study On properties of concrete using overburnt brick chips and demolished concrete waste as partial replacement of coarse aggregate", November 2017.
[20] Apebo N. S., Agunwamba. J. C, "The suitability of crushed over burnt brick as coarse aggregate," in International Journal of Engineering Science and Innovative Technology, Vol. 3, 2014.
[21] Bidve Ganesh Shivkanth, G.N.Shete, Experimental study on effect of partial replacement of coarse aggregate by over Burn brick Bats, April 2019.
[22] Mr. Akshay N.Kadu, "Use of partial replacement of over burnt brick and demolished brickbats as a coarse aggregate in fresh concrete," August 2020.
[23] Rashid. M. A, Hossain. T and Islam M. A, "Properties of Higher Strength Concrete made with crushed brick as aggregate," in Journal of civil Engineering, Vol. 37(1), pp. 43 - 52, 2009.
[24] Mr. G.S.Patil, "Effect of partial replacement of coarse aggregate by Jhama class brick in concrete", August 2015.

E-ISSN 2581 – 7957
P-ISSN 2277 – 3916

CVR Journal of Science and Technology, Volume 26, June 2024
DOI: 10.32377/cvrjst2602

Evaluating the Performance of Concrete Containing Reclaimed Asphalt Pavement as Coarse Aggregate

Matsyapuri Bhagya Lakshmi[1], Kunamineni Vijay[2] and M. Ashok Kumar[3]
[1]UG Student, Vishnu Institute of Technology/ Civil Engg. Department, Bhimavaram, India
Email: 22PA5AO111@vishnu.edu.in
[2]Assistant Professor, CVR College of Engineering/ Civil Engg. Department, Hyderabad, India
Email: vijay.k@vishnu.edu.in
[3]Assistant Professor, CVR College of Engineering/ Civil Engg. Department, Hyderabad, India
Email: m.ashokkumar@cvr.ac.in

Abstract: **Reclaimed asphalt pavement is a recycled pavement material consisting of asphalt and aggregate that has been treated. The majority of RAP is recycled back into pavements; hence there is a general dearth of data on the properties of RAP in other prospective uses such as Portland cement concrete. In this work, the characteristics of Portland cement concrete with coarse RAP were examined in the laboratory. Further, basalt fibers have been employed in the concrete mix to enhance the properties of concrete. The different proportions of RAP have been added into the concrete as a replacement to coarse aggregate for finding the optimum dosage for enhancing strength and durability. All samples were tested for workability, compressive strength, flexural strength, and acid attack tests to investigate the impact of RAP as coarse aggregate on concrete performance. The test results indicate that the inclusion of RAP makes concrete more workable while decreasing its strength. The reason for this is the inadequate adhesion between the cement matrix and RAP aggregate. Additionally, the durability and strength of RAP concrete are improved by the incorporation of basalt fibers. In addition to RAP as a partial substitute for coarse aggregate, the investigation suggests employing basalt fibers.**

Index Terms: **Reclaimed asphalt pavement, workability, Strength, Durability, Replacement, Fly ash, Sustainability**

I. Introduction

The utilization of concrete has been increasing day-by-day due to its strength, durability, and easy availability of raw materials [1]. Building with a wide variety of structures is made up of concrete, requires the use of a substantial quantity of aggregates. The earth is the source of these aggregates, and the extraction of such large quantities is detrimental to the ecology. As a result of the advantages that rigid pavements have over flexible pavements, the building of rigid pavements has seen a significant increase in recent years. Furthermore, rigid pavements have a far lower life cycle maintenance cost than flexible pavements. The India Ministry of Road Transport and roads predicts that the conventional building technique for national roads will progressively shift to rigid pavement. Bitumen roads degrade more rapidly, therefore concrete roads eventually replace them [2]. The removal of the road produces a significant quantity of waste materials. Worldwide, road and highway maintenance produces millions of tonnes of reclaimed asphalt pavement (RAP) in this scenario. In the United States alone, the expected annual quantities for milled asphalt exceed 100 million tonnes [3]. Previous studies have demonstrated that improper RAP disposal is one factor that has led to environmental deterioration, particularly when RAP comes into contact with water [4]. A significant amount of hazardous contaminants, including heavy metals, polycyclic aromatic hydrocarbons, and volatile organic compounds, cause damage to the environment after they have been washed off of RAP material and are subjected to temperature [5], [6]. Therefore researchers are utilizing RAP as a replacement for natural aggregates to minimize the problem of availability of natural aggregates [7]–[9]. It decreases aggregate consumption and diminishes greenhouse gas emissions, therefore preserving valuable land and generating sustainable concrete [10], [11]. The performance of concrete may be adversely affected by the use of RAP aggregates [12]–[14]. To understand the causes behind the decrease in the overall strength of RAP concrete, it was found that the presence of an asphalt layer and agglomerated particles caused the decline [10], [14], [15]. Several studies have proposed diverse methodologies to eliminate the bitumen layer surrounding the aggregates to enhance the properties of RAP aggregates and fortify the bond between cement mortar and RAP aggregates [16], [17]. The efficient bonding of RAP aggregates and cement mortar is enhanced by the Abrasion and Attrition (AB&AT) procedure [18]. There is a need to further improve the bond between the cement and mortar. In this investigation, an attempt has been made to enhance the properties of RAP concrete by incorporating basalt fibers in it.

II. Materials

Ordinary Portland cement of grade 43, which possesses a specific gravity of 3.15, was obtained from a nearby supplier to employ it as a binder. As fine aggregate, sand that was readily accessible in the area and confirmed zone II with a specific gravity of 2.6 was employed. In this investigation, coarse aggregate with a specific gravity of 2.7 has been used. The National Highway 16 route is where the RAP aggregates are collected and utilized in this study.

Received on 04-03-2024, Revised on 03-04-2024, Accepted on 03-05-2024.

CVR Journal of Science and Technology, Volume 26, June 2024
DOI: 10.32377/cvrjst2602

III. Methodology

A. Concrete Mix Details

The mix details of M20 grade concrete are prepared by IS:10262-2019 standards and depicted in Table 1. The work involves casting and testing concrete using RAP as a partial substitute for coarse aggregate and basalt fibers. The mix designations of various mixes are depicted in Table I. In Table II, the control mix is denoted as CM. Further R20, R40, and R60 denote the mixes containing 10%, 20%, and 30% of RAP as a substitute for coarse aggregate. Also, the mixes FCM, FR20, FR40, and FR60 denote the mixes with 1% of basalt fibers along with 0%, 10%, 20%, and 30% of RAP as coarse aggregate replacement.

TABLE I.
MIX PROPORTIONS (kg/m^3)

Cement	Fine Aggregate	Coarse Aggregate	Water
315	749	1300	197

TABLE II.
MIX DESIGNATIONS

Mix Details	RAP (%)	Fibers (%)
CM	0	0
R10	20	0
R20	40	0
R30	60	0
FCM	0	1
FR10	20	1
FR20	40	1
FR30	60	1

B. Test Procedure

In the current study, the workability of concrete was examined utilizing a slump cone test according to IS 1199-2018 [19]. The compressive and flexural strength tests are employed to assess the strength characteristics of concrete following IS:516-2021 [20]. The durability of concrete was examined by executing a water absorption test and an acid attack test on the surface of hardened concrete using cubes measuring 150 x 150 x 150 mm. The acid attack test on concrete was done using the ASTM C267 standards [21]. The water absorption test was performed on all mixes, to determine the increase in resistance towards water penetration in concrete.

IV. Results And Analysis

A. Workability of Concrete

The test results are depicted in Figure 1. From Figure 1, it is seen that the inclusion of RAP aggregate enhances the workability. The workability is directly related to the dosage of RAP. The inclusion of 20% RAP as a replacement for aggregate shows a 5.5% enhancement in the workability in contraction with the control mix. Similarly, the addition of 40% and 60% of RAP aggregate shows 11% and 18.8% enhancement in the workability in contraction with the control mix. The improvement is because of the presence of asphalt in the pores of the aggregate it decreases the water absorption of concrete and increases the workability [22], [23].

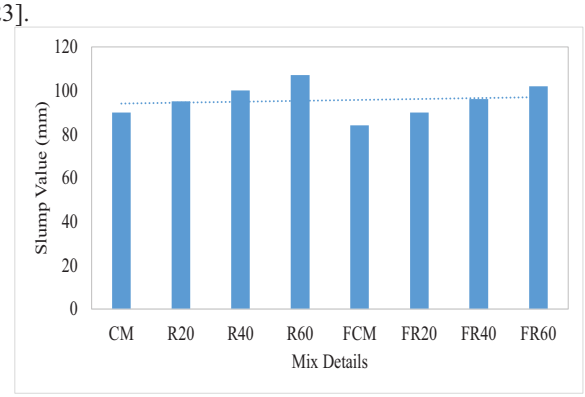

Figure 1. Slump test results of different mixes

Further, the inclusion of basalt fibers reduces workability. It reduces the workability of concrete containing RAP aggregate also. This is mostly due to the development of a fiber network inside the concrete mixture, which obstructs the movement of large particles and enhances resistance to flow [24].

B. Compressive Strength

All concrete mixes were tested in triplicate for a 7- and 28-day curing time. The test results are depicted in Figure 2. The inclusion of 20% RAP as a replacement for coarse aggregate reduces the compressive strength by 5.4% and 6.9%, respectively, in contraction with the control mix after 7 and 28 days of curing. The inclusion of 40% RAP as a replacement for coarse aggregate reduces the compressive strength by 10.4% and 13.1%, respectively, in contraction with the control mix after 7 and 28 days of curing. Similarly, adding 60% RAP reduces the compressive strength by 18.6% and 20.7% in contraction with the control mix after 7 and 28 days of curing, respectively. The loss in strength is due to improper bonding [23]. The strength of concrete decreases as asphalt builds up over aggregate, creating a smooth surface and a weak bond with mortar and cement paste.

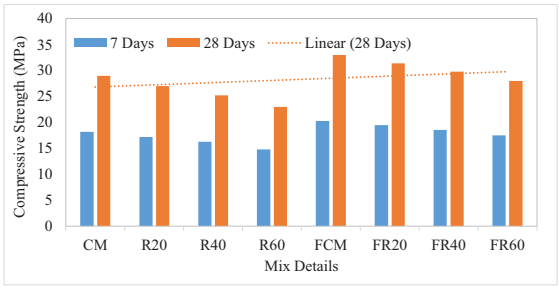

Figure 2. Compressive strength test results

Furthermore, to increase the strength characteristics of RAP concrete, basalt fibers are used to strengthen the bonding between the aggregate, mortar, and cement paste. The inclusion of fibers in the control mix increases the strength by 11.5% and 13.8% for curing periods of 7 and 28

days, respectively. The addition of fibers in the concrete with 10% RAP increases the strength by 7.1% and 8.3%, respectively, from the control mix. The inclusion of fibers in the RAP concrete mix increases the strength of the concrete by improving bonding between particles and acting as bridges between cracks, allowing the concrete to carry further loading before failing.

C. Flexural Strength

Figure 3 shows the test results for each concrete mix. It is evident from Figure. 3 that the flexural strength test results and the compression strength test results for the concrete were similar. The flexural strength is adversely affected when RAP is added in place of coarse aggregate. Concrete's flexural strength is reduced when the RAP dose is increased in place of coarse aggregate. This demonstrates that, in contraction with the control mix, the bonding between the aggregate and mortar is poor. It was also confirmed by the visual observation of the failure pattern of the concrete.

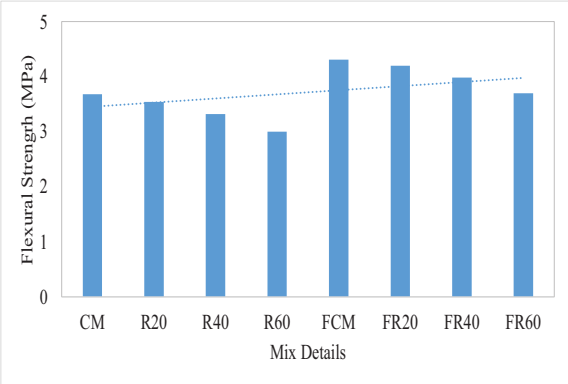

Figure 3. Flexural strength test results

The inclusion of basalt fibers in the concrete mix increases flexural strength when compared to the control mix. The fibers improve the connection between the aggregate and mortar by bridging action [25], [26]. The RAP concrete flexural strength is also enhanced by the addition of basalt fibers in it.

C. Acid Attack Test

This test was employed using 28-day water-cured concrete cubes measuring 100 x 100 x 100 mm. These cubes were removed from the curing chamber and soaked in water containing 5% H2SO4 solution for 28 days in plastic tubs. The percentage of weight loss was recorded to determine the effect of acid on the surface of the concrete. The test results are displayed in Figure. 4. Figure. 4 shows that using RAP as a substitute for coarse material improves the weight loss % of concrete. This is due to a poor connection between the aggregate and mortar. Because of this, H_2SO_4 can enter the concrete mix and increase the weight loss percentage.

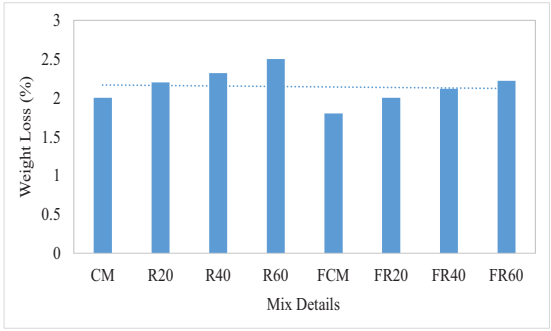

Figure 4. Acid attack test results

The addition of basalt fibers to the control mixture lowers the weight loss of concrete. Furthermore, the inclusion of basalt fibers in RAP concrete has comparable outcomes in terms of reducing concrete weight loss. Basalt fibers offer a higher resilience to acid harm [27]. The inclusion of basalt fibers in RAP concrete strengthens the material's resistance against acid degradation.

C. Water Absorption of Concrete

The test has been performed on all concrete mixes using cubes cured at 28 days. The test results are shown in Figure. 5. From Figure 5 it was observed that the inclusion of RAP in concrete shows increased water absorption values. It is confirmed that the increase in dosage of RAP as aggregate increases the water absorption of concrete.

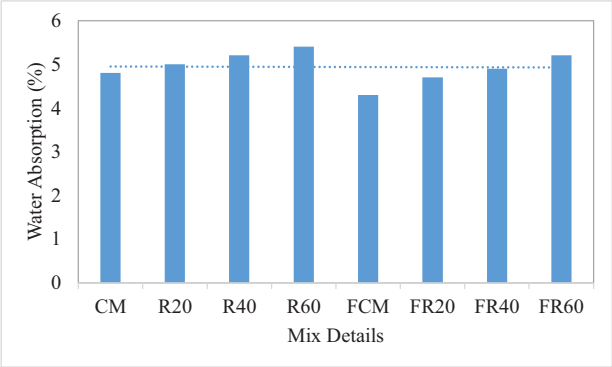

Figure 5. Water absorption test results

The inclusion of 20% of RAP as aggregate exhibits a 4% increase in water absorption in contraction with the control mix. The inclusion of 40% of RAP as aggregate exhibits an 8% increase in water absorption in contraction with the control mix. Similarly, the inclusion of 60% of RAP as aggregate exhibits a 13% increase in water absorption in contraction with the control mix. This is because of the poor bonding between the aggregates and mortar. It allows water to enter into the concrete. Further, the inclusion of basalt fibers minimizes the water absorption of concrete. The inclusion of fibers exhibits a 10% reduction in the water absorption in contraction with the control mix. The inclusion fibers in 20% of RAP aggregate concrete exhibit a 3% reduction in the water absorption in contraction with the control mix. The inclusion of fibers in 40% of RAP aggregate concrete exhibits a 2% increase in water

absorption in contraction with the control mix. The inclusion of fibers enhances the bonding between the aggregates and mortar by bridging action. Thus water absorption capacity diminishes.

V. Conclusions

In this work, the influence of RAP combined with basalt fibers on concrete performance was examined.

1. The use of RAP as a substitute for coarse aggregate has significantly improved the workability. This is due to decreased particle friction and less water absorption.
2. The presence of RAP in concrete reduces its mechanical characteristics. As the RAP dose increases, the concrete's strength declines.
3. The acid attack test findings showed a similar pattern of results. This is due to the development of a weak connection between coarse aggregate and mortar.
4. Furthermore, adding basalt fibers to the concrete matrix improves the overall performance of the concrete.
5. The utilization of basalt fibers reduces the workability of concrete. The addition of basalt fibers to concrete significantly increases its strength and durability.
6. The study suggests employing RAP as a partial replacement for coarse aggregate, combined with basalt fibers.

References

[1] V. V. S. Sarma, S. Subhan Alisha, K. Vijay, P. Gireesh Kumar, and K. S. Sai Kumar, "Mechanical performance enhancement of recycled aggregate concrete using GGBS and fly ash for sustainable construction," Multiscale and Multidisciplinary Modeling, Experiments and Design, 2023, doi: 10.1007/s41939-023-00271-9.

[2] F. Sri Handayani, F. Pungky Pramesti, M. Agung Wibowo, and A. Setyawan, "Estimating and Reducing the Release of Greenhouse Gases in Local Road Pavement Constructions," vol. 9, no. 5, 2019.

[3] A. O. Al-Shujairi, A. J. Al-Taie, and H. M. Al-Mosawe, "Review on applications of RAP in civil engineering," IOP Conf Ser Mater Sci Eng, vol. 1105, no. 1, p. 012092, Jun. 2021, doi: 10.1088/1757-899x/1105/1/012092.

[4] C. J. Spreadbury, K. A. Clavier, A. M. Lin, and T. G. Townsend, "A critical analysis of leaching and environmental risk assessment for reclaimed asphalt pavement management," Science of the Total Environment, vol. 775. Elsevier B.V., Jun. 25, 2021. doi: 10.1016/j.scitotenv.2021.145741.

[5] K. von Gunten, K. O. Konhauser, and D. S. Alessi, "Potential of asphalt concrete as a source of trace metals," Environ Geochem Health, vol. 42, no. 2, pp. 397–405, Feb. 2020, doi: 10.1007/s10653-019-00370-y.

[6] B. J. Mahler, P. C. Van Metre, and W. T. Foreman, "Concentrations of polycyclic aromatic hydrocarbons (PAHs) and azaarenes in runoff from coal-tar- and asphalt-sealcoated pavement," Environmental Pollution, vol. 188, pp. 81–87, May 2014, doi: 10.1016/j.envpol.2014.01.008.

[7] S. Singh, G. D. Ransinchung R. N., and P. Kumar, "Performance Evaluation of RAP Concrete in Aggressive Environment," Journal of Materials in Civil Engineering, vol. 30, no. 10, Oct. 2018, doi: 10.1061/(asce)mt.1943-5533.0002316.

[8] N. Hossiney, M. Tia, and M. J. Bergin, "Concrete Containing RAP for Use in Concrete Pavement," 2010.

[9] S. Singh, G. D. Ransinchung R.N., and P. Kumar, "Laboratory Investigation of Concrete Pavements Containing Fine RAP Aggregates," Journal of Materials in Civil Engineering, vol. 30, no. 2, Feb. 2018, doi: 10.1061/(asce)mt.1943-5533.0002124.

[10] S. Singh, G. D. Ransinchung, and P. Kumar, "An economical processing technique to improve RAP inclusive concrete properties," Constr Build Mater, vol. 148, pp. 734–747, Sep. 2017, doi: 10.1016/j.conbuildmat.2017.05.030.

[11] M. K. Diptikanta Rout, S. Biswas, and A. K. Sinha, "Evaluation of Mechanical Properties of Rigid Pavement with High RAP Content," pp. 285–298, 2023, doi: 10.1007/978-981-19-2273-2_20.

[12] S. El Euch Ben Said, S. El Euch Khay, and A. Loulizi, "Experimental Investigation of PCC Incorporating RAP," Int J Concr Struct Mater, vol. 12, no. 1, pp. 1–11, Dec. 2018, doi: 10.1186/S40069-018-0227-X/FIGUREURES/16.

[13] S. Singh, G. D. R. N. Ransinchung, K. Monu, and P. Kumar, "Laboratory investigation of RAP aggregates for dry lean concrete mixes," Constr Build Mater, vol. 166, pp. 808–816, Mar. 2018, doi: 10.1016/j.conbuildmat.2018.01.131.

[14] P. Solanki and B. Dash, "Mechanical Properties of Concrete Containing Recycled Asphalt Pavement and Class C Fly Ash." [Online]. Available: http://www.flyash.info/

[15] S. Singh, G. D. Ransinchung, and P. Kumar, "Effect of mineral admixtures on fresh, mechanical and durability properties of RAP inclusive concrete," Constr Build Mater, vol. 156, pp. 19–27, Dec. 2017, doi: 10.1016/j.conbuildmat.2017.08.144.

[16] S. M. Abraham and G. D. R. N. Ransinchung, "Influence of RAP aggregates on strength, durability and porosity of cement mortar," Constr Build Mater, vol. 189, pp. 1105–1112, Nov. 2018, doi: 10.1016/J.CONBUILDMAT.2018.09.069.

[17] H. Al Dughaishi et al., "Encouraging Sustainable Use of RAP Materials for Pavement Construction in Oman: A Review," Recycling 2022, Vol. 7, Page 35, vol. 7, no. 3, p. 35, Jun. 2022, doi: 10.3390/RECYCLING7030035.

[18] R. L. Al-Mufti and A. N. Fried, "Improving the strength properties of recycled asphalt aggregate concrete," Constr Build Mater, vol. 149, pp. 45–52, Sep. 2017, doi: 10.1016/j.conbuildmat.2017.05.056.

[19] IS 1199 (Part 2) : 2018, "Fresh Concrete - Methods of Sampling, Testing and Analysis, Part 2 Determination of Consistency of Fresh Concrete (First Revision)." Bureau of Indian Standards New Delhi, India, 2018.

[20] IS 516 (Part 1/Sec 1) : 2021, "Hardened Concrete - Methods of Test - Part 1 Testing of Strength of Hardened Concrete - Section 1 Compressive, Flexural and Split Tensile Strength." Bureau of Indian Standards New Delhi, India, 2021.

[21] "C267 Standard Test Methods for Chemical Resistance of Mortars, Grouts, and Monolithic Surfacings and Polymer Concretes." Accessed: Dec. 25, 2023. [Online]. Available: https://www.astm.org/c0267-20.html

[22] S. Singh, G. D. Ransinchung, S. Debbarma, and P. Kumar, "Utilization of reclaimed asphalt pavement aggregates containing waste from Sugarcane Mill for production of concrete mixes," J Clean Prod, vol. 174, pp. 42–52, Jan. 2018, doi: 10.1016/j.jclepro.2017.10.179.

[23] S. Singh, G. D. R. N. Ransinchung, and P. Kumar, "Feasibility study of RAP aggregates in cement concrete pavements," Road Materials and Pavement Design, vol. 20, no. 1, pp. 151–170, Jan. 2019, doi: 10.1080/14680629.2017.1380071.

[24] E. T. Al-Rousan, H. R. Khalid, and M. K. Rahman, "Fresh, mechanical, and durability properties of basalt fiber-reinforced concrete (BFRC): A review," Developments in the Built Environment, vol. 14, Apr. 2023, doi: 10.1016/j.dibe.2023.100155.
[25] V. Fiore, T. Scalici, G. Di Bella, and A. Valenza, "A review on basalt fibre and its composites," Compos B Eng, vol. 74, pp. 74–94, 2015, doi: 10.1016/j.compositesb.2014.12.034.
[26] K. Vijay and M. Murmu, "A review on basalt fibre reinforced concrete," International Journal of Structural Engineering, vol. 12, no. 4, p. 388, 2022, doi: 10.1504/IJSTRUCTE.2022.126195.
[27] S. Elshafie and G. Whittleston, "Evaluating the Efficiency of Basalt and Glass Fibres on Resisting the Alkaline, Acid, and Thermal Environments," American Journal of Materials Science, vol. 6, no. 1, pp. 19–34, 2016, doi: 10.5923/j.materials.20160601.02.

E-ISSN 2581 – 7957
P-ISSN 2277 – 3916

CVR Journal of Science and Technology, Volume 26, June 2024
DOI: 10.32377/cvrjst2603

Base Isolation and Energy Dissipating System in Earthquake Resistant Building Design

Ramavath Rambabu[1] and Batchu Ramanjaneyulu[2] and Kona Mahesh[3]
[1] PG Scholar, CVR College of Engineering/Civil Engg. Department, Telangana, India
Email: rambabu.r@cvr.ac.in
[2,3]Asst. Professor, CVR College of Engineering/ Civil Engg. Department, Hyderabad, India
Email: b.ramanjaneyulu@cvr.ac.in, k.mahesh@cvr.ac.in

Abstract: The utilization of base isolation is a crucial strategy for enhancing seismic resilience in structures. The method involves installing isolators and energy-absorbing devices beneath a building's superstructure to mitigate the destructive effects of earthquakes. When base isolation is implemented in a building, it not only makes the structure stronger and more stable, but also helps to safeguard lives and properties. This technique is particularly valuable for seismic retrofitting of historical buildings. In the present study, software called simulation of seismic isolation systems in structural analysis is employed, considering isolator characteristics, whether they exhibit nonlinear or equivalent linear behavior. Adhering to the IS 1893:2016 Code, the analysis utilized the SAP 2000 software package. A study was carried out to compare the effectiveness of base isolation systems versus fixed-base buildings in dealing with seismic activity. The study focused on analyzing various seismic indicators such as joint displacement, shear force, bending moment, building torsion, and the period of natural frequency. Results showed that models utilizing base isolation systems had significantly higher base shear values than those with a fixed-base building configuration. However, there was a significant 35% reduction in story shear values for the rubber isolation system and a 40% decrease for the friction pendulum model. Additionally, there was a 25% reduction in story drift for the rubber base model and a 30% decrease for the friction pendulum model. The friction pendulum model demonstrated the most effective control of these parameters across various seismic zone conditions.

Key words: The topic of discussion pertains to Seismic Isolation with Rubber Bearing System and the Friction Pendulum Technique. Additionally, it includes SAP2000 Analysis, Story Drift Measurement, and Shear Force Evaluation in relation to these techniques.

I. Introduction

Seismic isolation is a method employed to minimize the consequences of shocks during earthquakes on structures and their components, thus ensuring their protection from damage. This technique employs specific mechanisms, which will be detailed later, to reduce the lateral movement (drift) of structures.

Seismic isolation is a fundamental concept in earthquake engineering, involving the separation or decoupling of a structure from its foundation. [1-7] Put simply, it is a method designed to prevent or minimize structural damage during seismic events. This essay aims to elucidate the notion of base isolation by drawing parallels with examples from other engineering and sports disciplines. Such examples include automotive suspension systems and defensive strategies in boxing. Furthermore, the essay will present experimental data and analytical graphs to enhance comprehension of the base isolation concept. [8-10]

This study simulates seismic isolation systems using structural analysis software and considers isolator characteristics such as non-linear or equivalent linear behavior. The analysis adheres to the IS 1893:2016 Code and is conducted using the SAP 2000 software package. The effectiveness of base isolation systems is compared to fixed-base structures by analyzing various seismic indicators, including joint displacement, shear force, bending moment, building torsion, and natural frequency period. [11-12]

In the realm of structural design aimed at withstanding the destructive forces of earthquakes, two pivotal systems come to the forefront: base isolation and energy dissipating systems. These engineering methods serve as integral components in contemporary earthquake-resistant building design, working in concert to bolster safety, reduce structural harm, and safeguard human lives in seismic scenarios. [13-15] In the following exploration, we will delve into the fundamental principles and practical applications of these systems, shedding light on their vital roles in fortifying buildings against earthquake-induced challenges.

The primary objective of this research is to contribute to the understanding of base isolation and energy dissipating systems, providing insights into their practical applications and effectiveness in designing earthquake-resistant buildings. [16-17] through a comprehensive analysis and comparison, this study aims to identify the most effective seismic mitigation strategies for enhancing structural resilience and minimizing earthquake-related damage.

1.1Friction pendulum bearings

Friction pendulum systems are widely employed as kinematic systems, particularly in the field of base isolation. These systems are characterized by the presence of a steel pendulum, which is positioned between two steel concave curved surfaces or within a cylindrical component with

Received on 12-12-2023, Revised on 11-01-2024, Accepted on 10-02-2024.

CVR Journal of Science and Technology, Volume 26, June 2024
DOI: 10.32377/cvrjst2603

spherical contact surfaces. Special metals are utilized in crafting these components.

Friction pendulum bearings, commonly known as FPs or friction pendulum isolators, stand as a pivotal advancement in the realm of structural engineering and seismic isolation technology. These mechanical components are strategically engineered to bolster the earthquake resistance of buildings and bridges through the facilitation of controlled movement and the dissipation of energy when seismic forces come into play. In the following exploration, we will delve into the underlying principles, design considerations, and practical applications of friction pendulum bearings, underscoring their vital role in fortifying structures against the destructive impacts of earthquakes.

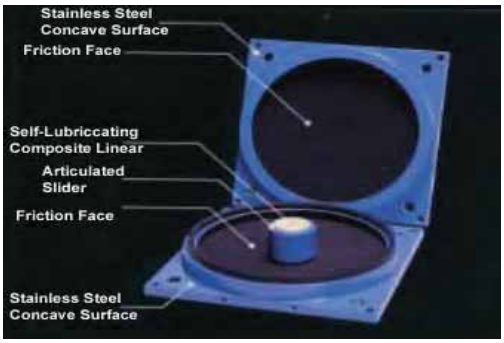

Figure 1. Friction pendulum bearing system

1.2 Rubber Bearings isolation

Rubber bearing isolation, commonly known as base isolators, represents a significant breakthrough in the realm of structural engineering, specifically in the context of earthquake-resistant design. [18] These specialized elements serve a crucial purpose in safeguarding buildings and infrastructure against the destructive effects of seismic forces. In the ensuing discourse, we shall delve into the fundamental principles, design factors, and real-world implementations of rubber bearing isolation, underscoring its substantial role in enhancing structural resilience and minimizing earthquake-related harm.

Apart from the bridge bearings, these systems come in various types, including steel laminated rubber bearings, steel laminated rubber bearings with a lead core, and those made from a combination of rubber and neoprene materials. The rubber elements, originally used in bridge bearings, underwent enhancements, and were later reintroduced as elastomeric bearings. These elastomeric bearings that used as seismic isolators have gained widespread adoption. Rubber laminated isolators are created by vulcanizing thin steel plates to rubber plates. Among these, the most advanced are the laminated rubber bearings with a lead core. The Lead Laminated Rubber Bearing systems are a sophisticated seismic isolation technology that comprises of layers of steel and rubber laminated with a central core of lead.

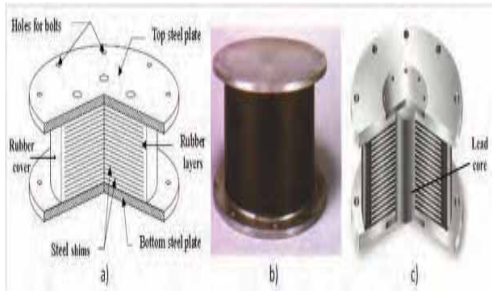

Figure: 2. Lead rubber bearing isolation

The main objectives of this ongoing research project are to examine the seismic behavior of a G+9 building according to the IS 1893:2002 code, using the response spectrum method in the SAP2000 software. The research aims to assess the performance of the G+9 building in Seismic Zone V using different base isolation systems, namely Rubber Bearing Isolation and Friction Pendulum Bearing Isolation systems. A comparative analysis will be conducted to evaluate the seismic performance of structures employing different base isolation systems compared to a fixed-base building in various seismic zone scenarios. The aim is to determine the most effective earthquake-resistant system based on the analysis outcomes, which encompass parameters like joint displacements, shear forces, bending moments, torsion, base shear, and the building's time period.

II. Literature Review

Gyawali et al. (2020): An investigation was conducted on GF+4 storied buildings with regular, plain irregular, and vertical irregular designs using SAP software for both fixed-base and base-isolated models. The analysis utilized the response spectrum method by IS1893:2002 and cross-validated the findings with ETABS software. As per the results, implementing Lead Rubber Bearings (LRB) was found to decrease the base shear by 45 to 50% as compared to buildings with a fixed base. However, it was also observed that the displacement at the top story of the buildings increased by 81 to 99% when LRB systems were used.

Dr. R. S. Tali Koti et al. (2014): In a separate study by a comprehensive examination was conducted on the design, functionality, testing, and compliance with Indian Standards of base isolation. The study focused on a (G+15) RCC building, which was modeled in SAP2000 software. The building was analyzed under various conditions, including fixed base, bracing, and isolator systems. Theoretical analyses were performed using SAP2000 software to compare fixed base structures with base-isolated structures. Various parameters were considered in these comparisons, which included base shear, modal period, story displacement, story drift, and story acceleration.

CVR Journal of Science and Technology, Volume 26, June 2024
DOI: 10.32377/cvrjst2603

III. Methodology

Several factors were considered in these analyses, such as the base shear, modal period, story displacement, story drift, and story acceleration. In this specific study, IS 1893:2016 (Part 1) was used as the governing code. Key data such as seismic zone factors and soil types were obtained from the relevant tables within the IS 1893:2016 (Part 1) code.

In this analysis, a standard damping ratio of 5% was applied. The response spectrum curve, designed for medium soil conditions, is presented in the figure below. This graphical representation illustrates the correlation between time period and spectral acceleration coefficient (Sa/g).

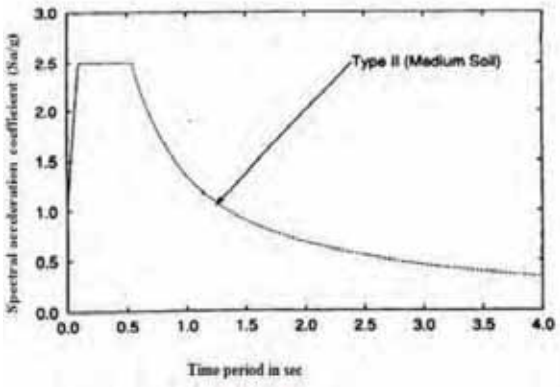

Figure 3. Response spectrums for medium soil type with 5% damping.

Our objective for this study is to determine the strength of the forces, specifically X, Y, and Z, and evaluate their effects on the structure. To achieve this, we're utilizing various combination techniques, which include absolute summation, square root of the sum of squares (SRSS), and complete quadratic combination (CQC) - an adaptation of SRSS that's suitable for modes that are closely spaced.

It is important to keep in mind that the results obtained through Response Spectrum Analysis can differ significantly from those produced by linear dynamic analysis using ground motions. The accuracy of response analysis may be compromised in situations involving irregular or high-rise structures. In such cases, alternative methods such as non-linear static or dynamic analysis are required. The main objective of our study was to assess the behavior of a medium rise building with a conventional structure when subjected to seismic loads.

IV. Specifications And Building Models

Within this research, we examined a multi-story G+9 building and constructed a three-dimensional model of the structure using SAP 2000 software.

Here are the key parameters considered for the analysis:

1. Building Occupancy: Residential
2. Number of Stories: Ground + 9 (10 stories)
3. Building Height: 30 meters
4. Building's Shape: Rectangular
5. Geometric Specifications:

a. Ground Floor Elevation: 3 meters
b. Inter-Floor Height: 3 meters

6. Material Specifications:
   -Concrete grade specified for columns and beams: M30.
   - Type of Steel: HYSD 415
   - Soil Bearing Capacity: 200 kN/m^2
7. Type of Construction: Reinforced Concrete (RCC)
8. Column Dimensions: 0.35 meters × 0.35 meters
9. Beam Dimensions: 0.25 meters × 0.35 meters
10. Slab Thickness: 0.125 meters
11. Live Load: 2.5 kN/m^2 (as per IS: 875:1987)
12. Site Type: II
13. Significance Factor: 1.0
14. Seismic Response Reduction Factor specified: 3.
15. Damping Coefficient: 5%
16. Structural Category: C
17. Wind design code referenced: IS 875: 1987 (Part 3)
18. Reinforced Concrete Design Code: IS 456:2000
19. Steel design code referred to: IS 800: 2007
20. Earthquake design code specified: IS 1893: 2016

Building models in SAP 2022.

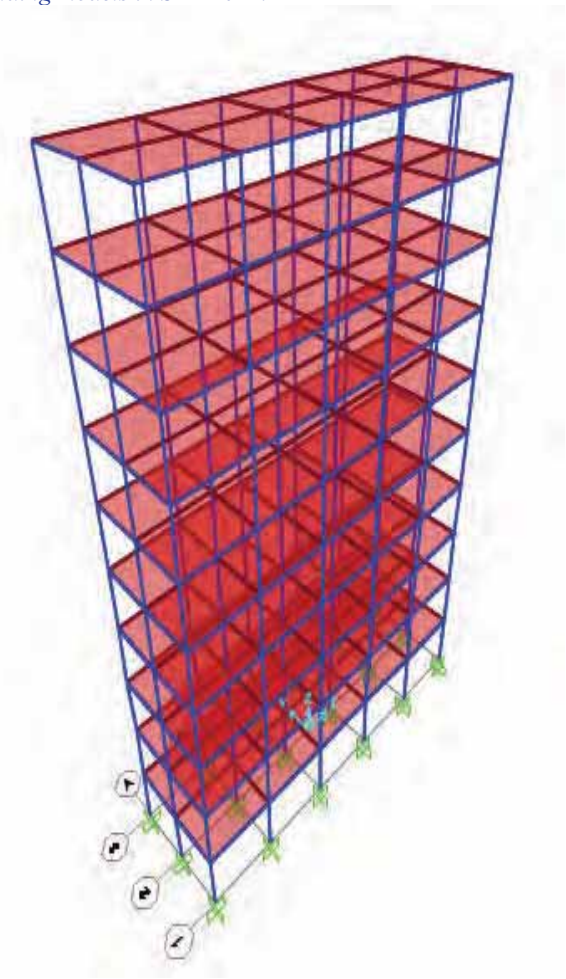

Figure 4. Building fixed Model with supports

E-ISSN 2581 – 7957
P-ISSN 2277 – 3916

CVR Journal of Science and Technology, Volume 26, June 2024
DOI: 10.32377/cvrjst2603

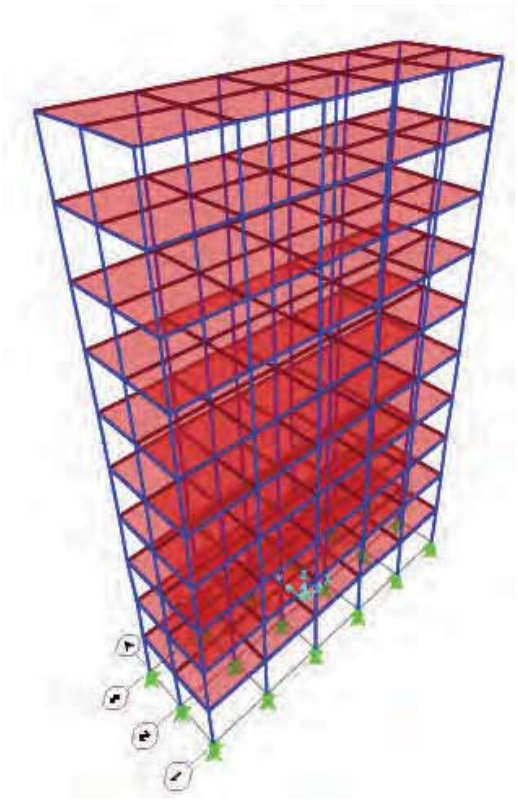

Figure 5. Building Model with rubber isolator at supports

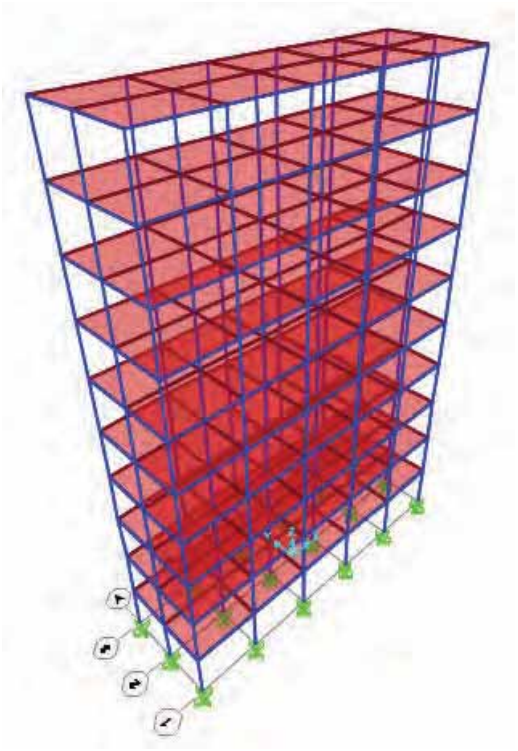

Figure 6. Building Model with friction isolator at supports

V. Results and Discrection

1.Comparison of joint displacement

TABLE I.
JOINT DISPLACEMENT VALUES FOR DIFFERENT STORIES

S.no	Load Case	Joint displacement in mm for fixed base	Joint displacement in mm for rubber base	Joint displacement in mm for friction base
1	RSA	0	0	0
2	RSA	4.23	7.08	2.909
3	RSA	1.48	2.109	1.039
4	RSA	1.72	1.609	1.2009
5	RSA	1.71	1.309	1.2009
6	RSA	1.75	1.309	1.209
7	RSA	1.6	1.279	1.159
8	RSA	1.69	1.309	1.109
9	RSA	0	0	0
10	RSA	1.97	1.057	1.3811
11	RSA	2.42	6.813	1.611
12	RSA	1.05	1.162	7.352
13	RSA	7.16	2.412	5.012
14	RSA	1.64	2.412	1.111
15	RSA	1.26	1.412	8.812

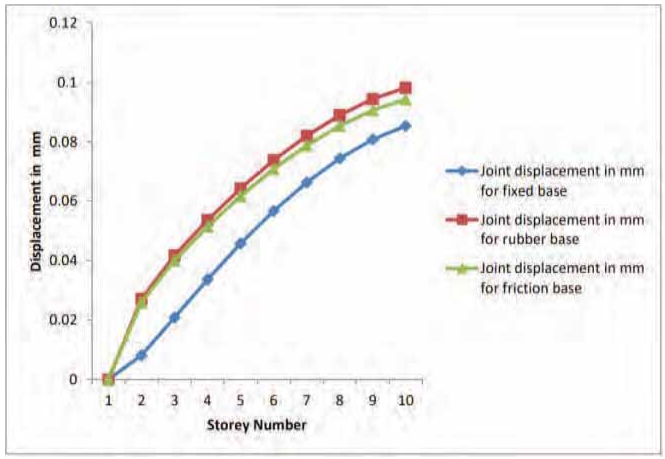

Figure 7. Comparison of joint displacement for different base conditions in Zone V

Based on the test results mentioned above, a comparison was made between the joint displacements under seismic conditions. Based on the observations, it was found that the joint displacement values were higher in the rubber fixed base, rubber base, and friction pendulum systems present in the zone base as compared to the fixed base and friction pendulum models. This can be attributed to the intense seismic loading, which specifically causes increase in displacement values for the rubber base model when compared to other isolation systems.

2. Comparison of Lateral load P

TABLE II.
COMPARISON OF LATERAL LOAD P FOR DIFFERENT STORIES

Storey Number	Lateral P for fixed base in kN	Lateral P for rubber base in kN	Lateral P for friction base in kN
Storey 1	0.026	0.043	0.018
Storey 2	0.0008	0.019	0.00060
Storey 3	0.0016	0.003	0.00116
Storey 4	0.0010	0.00047	0.00073
Storey 5	0.0010	0.00070	0.0007
Storey 6	0.0007	0.00050	0.00051
Storey 7	0.0008	0.00054	0.00060
Storey 8	0.0006	0.0002	0.00047
Storey 9	0.0041	0.003	0.002
Storey 10	0.0085	0.007	0.005

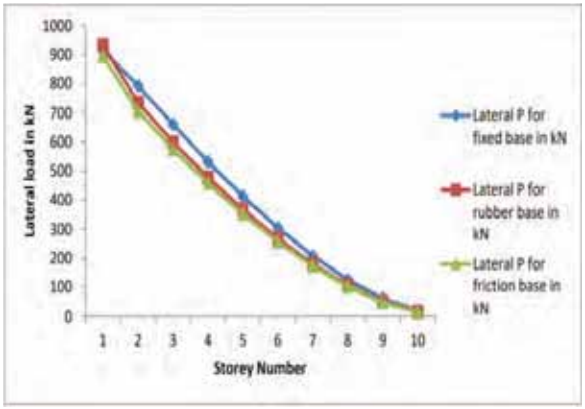

Figure 8. Comparison of Lateral load for different base conditions in Zone V

The G+10 building model encounters more significant effects from lateral load conditions in zone II seismic conditions when employing a rubber base isolation system as opposed to other isolation methods. This discrepancy arises from the comparatively lower resistance rate exhibited by the rubber base model.

3. Comparison of Story Shear

TABLE III.
COMPARISON OF STORY SHEAR FOR DIFFERENT STORIES

Storey Number	Shear Vx for fixed base in kN	Shear Vx for rubber base in kN	Shear Vx for friction base in kN
Storey 1	0.367	0.543	0.257
Storey 2	0.37	0.341	0.259
Storey 3	0.343	0.301	0.24
Storey 4	0.31	0.269	0.217
Storey 5	0.276	0.238	0.193
Storey 6	0.239	0.204	0.167
Storey 7	0.197	0.165	0.138
Storey 8	0.148	0.12	0.103
Storey 9	0.087	0.067	0.061
Storey 10	0.03	0.021	0.021

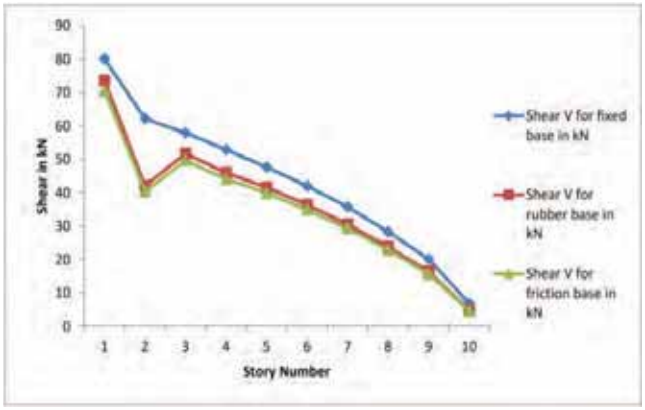

Figure 9. Comparison of stores shear V for different base conditions in Zone V

The Y direction shear values are compared in the graph depicted above. From the results, it can be deduced that the utilization of isolation systems can effectively resist seismic loading, leading to a reduction in shear values.

4. Comparison of Torsion T

TABLE IV.
COMPARISON OF TORSION T FOR DIFFERENT STORIES

Storey Number	Torsion T for fixed base in kN-m	Torsion T for rubber base in kN-m	Torsion T for friction base in kN-m
Storey 1	6.62E-06	6.58E-06	4.64E-06
Storey 2	1.27E-05	1.03E-05	8.91E-06
Storey 3	1.76E-05	1.30E-05	1.23E-05
Storey 4	2.31E-05	1.72E-05	1.62E-05
Storey 5	2.84E-05	2.08E-05	1.99E-05
Storey 6	3.30E-05	2.40E-05	2.31E-05
Storey 7	3.68E-05	2.66E-05	2.57E-05
Storey 8	3.95E-05	2.86E-05	2.76E-05
Storey 9	4.09E-05	2.96E-05	2.86E-05
Storey 10	6.04E-05	4.34E-05	4.23E-05

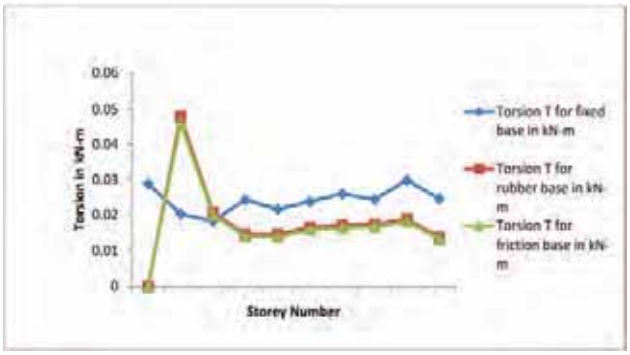

Figure 10. Comparison of Torsion T for different base conditions in Zone V

CVR Journal of Science and Technology, Volume 26, June 2024
DOI: 10.32377/cvrjst2603

The comparison of torsion is shown in the above graph due to the unequal forces in both directions. The torsion is created in multi storey building, the effect of seismic isolation will be decreased, which is demonstrated from above graph.

5. Comparison of Storey moment

TABLE V.
COMPARISON OF STORY MOMENT DIFFERENT STORIES

Storey Number	Bending My in fixed base in kN-m	Bending My in rubber base in kN-m	Bending My in friction base in kN-m
Storey 1	1.0842	1.5879	0.759
Storey 2	1.1049	1.0255	0.7734
Storey 3	1.02	0.8926	0.714
Storey 4	0.9206	0.7978	0.6444
Storey 5	0.8156	0.7028	0.5709
Storey 6	0.7045	0.6008	0.4931
Storey 7	0.579	0.4851	0.4053
Storey 8	0.4311	0.35	0.3017
Storey 9	0.2516	0.1925	0.1761
Storey 10	0.0757	0.0498	0.053

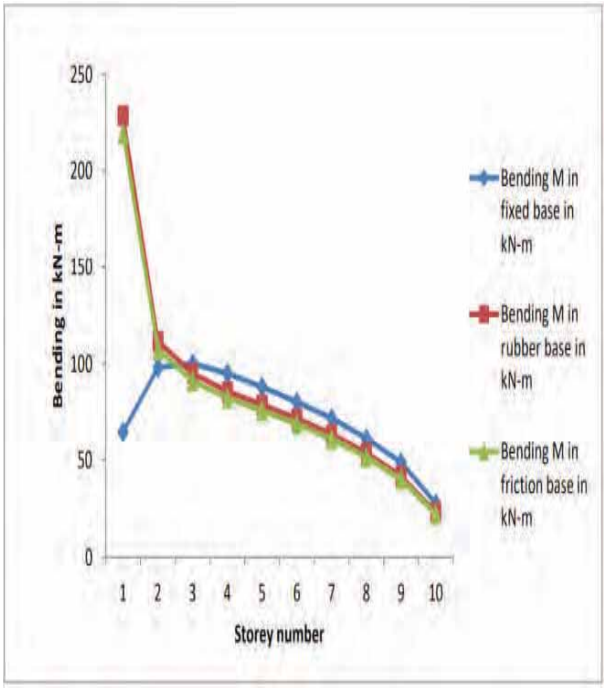

Figure 11. Comparison of moment M for different base conditions in Zone V

The above graph illustrates a reduction in the intensity of seismic loading action in zone II condition, which can be attributed to the presence of base isolation systems. Furthermore, the values of bending consistently rise from storey 1 to storey 10 across all the isolation models.

6. Comparison of Base shear

TABLE VI.
COMPARISON OF BASE SHEAR DIFFERENT STORIES

S. No	Building Type	Base shear in kN
1	Fixed base	11.928
2	Rubber base	10.879
3	Friction pendulum	8.35

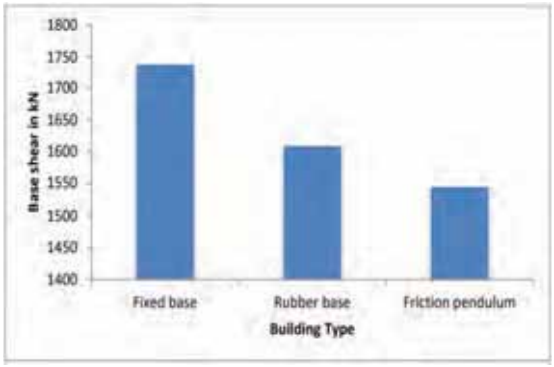

Figure 12. Comparison of base shear for different base conditions in Zone V

Based on the graph provided, it can be observed that both friction pendulum and rubber base isolation models show a decrease in base shear values when compared to the fixed base isolation system. This suggests that seismic loading conditions have less impact on the former two models, resulting in a reduction in the overall impact of seismic activity.

7. Comparison of Time period

TABLE VII.
COMPARISON OF TIME PERIOD FOR VARIOUS TYPES OF BASES

Mode Number	Time period for fixed base	Time period for rubber base	Time period for friction base
1	1.58	1.897	1.588
2	1.348	1.627	1.348
3	1.254	1.492	1.254
4	0.522	0.6180	0.522
5	0.44	0.524	0.446
6	0.41	0.48	0.413
7	0.3012	0.337	0.301
8	0.2619	0.293	0.2619
9	0.2420	0.270	0.245
10	0.214	0.232	0.214
11	0.184	0.202	0.186
12	0.16	0.184	0.1697

CVR Journal of Science and Technology, Volume 26, June 2024
DOI: 10.32377/cvrjst2603

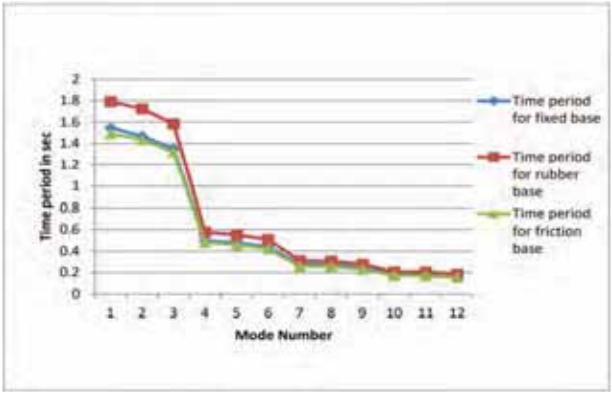

Figure 13. Comparison of time -period for different base conditions in Zone V

It is evident from the table and graph that the time-period values of the rubber base isolation system model in all modes are higher than those of the fixed base isolation system building model, because of seismic loading conditions. The time-period values decrease for both models as the mode number increases from 1 to 12.

8. *Comparison of frequency*

TABLE: VIII
COMPARISON OF FREQUENCY FOR VARIOUS TYPES OF BASES.

Mode Number	Frequency for fixed base	Frequency for rubber base	Frequency for friction base
1	0.62932	0.52708	0.629327
2	0.74179	0.6142	0.74179
3	0.7970	0.6698	0.79701
4	1.91257	1.6180	1.91257
5	2.23993	1.9058	2.2399
6	2.41607	2.080	2.4160
7	3.31934	2.959	3.3193
8	3.81780	3.4054	3.81780
9	4.13060	3.692	4.130
10	4.6715	4.306	4.67152
11	5.36986	4.9494	5.3698
12	5.8898	5.4120	5.88985

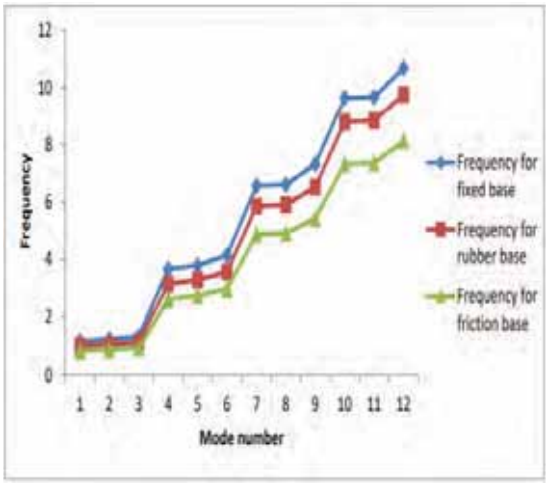

Figure 14. Comparison of frequency for different base conditions in Zone V

The comparison of frequency values is shown in the graph and Table, from these observations it clearly states that the frequency values are increasing from mode 1 to mode 12 for both the cases it has higher values for fixed base isolation building and friction pendulum than the rubber base isolation systems.

VI. CONCLUSIONS

It is evident from the results of simulation that the implementation of base isolation techniques plays a crucial role in reducing the seismic response of a building when compared to a fixed base structure. The changes in various result parameters concerning the building's stories in comparison to the fixed base model are discussed below:

1. Across all seismic zones, the implementation of Lead Rubber Isolation and Friction Pendulum Isolation systems consistently leads to a decrease in the stories shear values. By incorporating rubber base isolation and friction pendulum systems at the base, the story shear values decrease by 28.57% and 34.427%, respectively.
2. The story moment values decrease by 16.88% and 23.20% for the rubber base isolation and friction pendulum isolation, respectively.
3. A reduction in story torsion of 44.12% for the Rubber Base Isolation model and 48.52% for the Friction Pendulum Base Isolation model was observed.
4. The utilization of base isolation systems leads to increased joint displacements in all seismic zones by 15.08% for the rubber base model and 5.63% for the friction pendulum model.
5. Base isolation results in a significant decrease in story lateral loads in all seismic zones, with reductions of 17.95% and 24.69% for the rubber base model and friction pendulum model, respectively.
6. Employing isolation systems has the potential to reduce steel consumption, resulting in substantial savings of 8.7% for rubber base isolation and 30%

for friction pendulum systems. This reduction significantly influences building design.

7. The parameters under consideration are best controlled when the building is equipped with Friction Bearing Isolation systems.
8. Base isolation leads to a substantial decrease in base shear in all seismic zones, with reductions of 7.36% and 14.97% for the rubber base model and friction pendulum model, respectively.

To sum up, the results of this study indicate that both the Rubber Base Isolation system and the Friction Pendulum system serve as valuable supplementary damping systems for managing seismic loads. Nevertheless, when comparing the two, it becomes evident that the Friction Pendulum Bearing Isolation system stands out as the superior and optimal choice for the building type under consideration in this project.

REFERENCES

[1] A.N.L in, Member1 and H. W. Shenton III 2," Seismic performance of fixed base and base isolated steel frames, ASCE, Journal of Engineering mechanics, VOl.118, No-5(1992).

[2] Farhan MA, Bommisetty J (2019) Seismic analysis of multistoried RCC buildings regular and irregular in plan. Int J Eng Res Tech 08(11):115–121

[3] J. C. Ramallo1, et al (2008), Seismic Analysis of Fixed Based and Base Isolated Building Structures, International Journal of Multidisciplinary and Current Research,Vol 3.

[4] Sonali Anilduke et al (2015), Comparison of Building for Sesmic Response by using Base Isolation, International Journal of Research in Engineering and Technology, Volume: 04 Issue: 06.

[5] S.D.Darshale and N.L.Shelke," seismic Response Control of R.C.C. Structure using Base Isolation", International Journal of research in Engineering science and Technology, vol.2, No.1, (2016).

[6] N Murali Krishna et al (2016), nonlinear time History Analysis of Building with Seismic Control Systems, International Journal of Science Technology and Engineering.

[7] N Murali Krishna et al (2016), nonlinear time History Analysis of Building with Seismic Control Systems, International Journal of Science Technology and Engineering.

[8] Juan C Ramallo (2008) "Smart'' Base Isolation Systems Journal of Engineering Mechanics, Vol. 128, No. 10, October 1, 2002. ©ASCE.

[9] Aung Chan Win, Analysis and Design of Base Isolation for Multi-Storied Building, GMSARN International Conference on Sustainable Development: Issues and Prospects for the GMS 12- 14 Nov.2008

[10] Todd W. Erickson1 and Arash Altoontash2," Base Isolation for Industrial Structures; Design and Construction Essentials", ASCE, Structures Congress, (2010).

[11] H. W. Shenton1 III and A. N. Lin2,Relative Performance of fixed based and base isolated concrete frame", ASCE, Journal of Structural Engineering " VOL.119,NO- 10(1993).

[12] Dr Manjunath N Hegde et al (2016),Comparison of Seismic Behavior of Building with Fixed Base, Base Isolator and Shear Wall, International Research Journal of Engineering and Technology (IRJET) e-ISSN: 2395 -0056 Volume: 03 Issue: 10 | Oct -2016

[13] Newmark, N.M. and Rosenblueth, E.: Fundamentals of Earthquake Engineering, Prentice-Hall 1971, pp. 225-228, and 343- 345.

[14] Skinner, R.I., Kelly, J.M., and Heine, A.J., Hysteretic Dampers for Earthquake Resistant Structures, Int. J. Earth. Engg Struct. Dyn., Vol. 3, No.3, 1975.

[15] Skinner, R.I., Kelly, J.M., and Heine, A.J., Energy Absorption Devices for Earthquake Resistant Structures, Proc. 5th Wld. Conf. Earth quake. Engg, Session 8C, Rome, Italy (1973).

[16]] IS 1893 (Part 1): 2002 "Criteria for Earthquake Resistant style of Structures"

[17] Fabio De Angelis (2016) Nonlinear dynamic analysis for multi-storey RC structures with hybrid base isolation systems in presence of bi-directional ground motions Composite Structures 154 (2016) 464–492

[18] Garevski, M., Kelly, J.M. (2001). Evaluation of the Proper Functioning of the Rubber Isolators of the Primary School 'Pestalozzi' in Skopje Under Strong Earthquake", IZIIS-Skopje.

E-ISSN 2581 – 7957
P-ISSN 2277 – 3916

CVR Journal of Science and Technology, Volume 26, June 2024
DOI: 10.32377/cvrjst2604

Implementation of 5G New Radio Secondary Synchronization on FPGA

Dr. Aytha. Ramesh Kumar[1] and Dr. K. Lal Kishore[2]

[1]Associate Professor, VNRVJIET/ ECE Department, Hyderabad, India.
Email: rameshkumar_a@vnrvjiet.in
[2]Professor, CVR College of Engineering / ECE Department, Hyderabad, India.
Email: lalkishore@cvr.ac.in

Abstract: 5th Generation New Radio (NR) cellular technology operates at low latency, and higher bandwidths, and makes use of a large number of antennas. NR communication is compatible with a wide range of machine- and human-centered applications. The cell search procedure plays a crucial role in establishing a synchronized connection with the base station (gNodeB) when the user equipment (UE) is enabled, or in the on state. The procedure for cell search finds the physical cell identity of the base station with primary synchronization and secondary synchronization for 3rd Generation Partnership Project (3GPP) 5G NR standards. This paper focuses on identifying the secondary synchronization of Physical Cell Identity (PCI) in the 3rd Generation Partnership Project (3GPP) 5G NR system. Field Programmable Gate Arrays are reprogrammable, flexible, reconfigurable computing circuits and simple to design at very peak frequencies. This suggested architecture employs Secondary Synchronization Signal detection and aims for low power consumption and high speed. The secondary synchronization block has been designed and executed on the Xilinx Zynq FPGA board.

Index Terms: **5G New Radio, FPGA, Cell search, Physical Cell Identity, Primary and Secondary synchronization (SS).**

I. Introduction

The latest fifth generation of wireless technology is produced by the Third Generation Partnership Project(3GPP) for cellular networks. It provides the ability to interact, connect, engage, and experience the world in ways that are similar to those of its predecessors. It enables communication with exceptionally rapid speed, extremely low latency, and millimeter wavelength signals. The 5G New Radio has a frame period of 10 ms. Although the operating frequency is significantly higher than for LTE, the frame structure and OFDM technology are identical to those of the Advanced LTE frame. The 5th Generation NR offers a myriad of applications like signal processing, multimedia, bio-medical, augmented reality, virtual reality, manufacturing, Internet of Things, and transportation, etc.[1]

In 5G New Radio communication, Cell search and signal synchronization are essential elements. The establishment of communication between the base station (gNodeB) and the User Equipment (UE) will be effective if the synchronization is quick and efficient. The synchronization avoids delay spread, inter-symbol interference, and inter-channel interference problems at high frequencies.

Cell search comprises the identification of both primary synchronization signals (PSS) and secondary SSS signals. The Physical Cell Identity is identified, which is then utilized for further demodulation.

This paper primarily focuses on SSS detection for cell identity to establish communication between UE and the base station and the given system is implemented in the Field Programmable Gate Array. The fundamentals of primary synchronization and secondary synchronization are deliberated. Also, the SSS detection is executed using the synchronization block for the 5 New Radio framework [3][4].

Aymen Omri, et al. explained and examined the synchronization process in 5G NR systems. Initially, they discussed 5G NR physical layers, the necessary synchronization techniques, and various synchronization algorithms used for 5G NR that have not been implemented.

J.-C. Lin, "Synchronization Requirements for 5G: An Overview of Standards and Specifications for Cellular Networks," has addressed the importance, requirements, and challenges of synchronization for wireless communications and specified the importance of timing synchronization, frequency synchronization, and space synchronization for the 5G communication.

Chunjing Hu and Yueliang Zhang proposed the algorithm for 5G NR synchronization signal (NR-PSS) detection and implemented it on a field programmable gate array. They reduced the number of multipliers and transformed multiplication into the shift using a preprocessing strategy that reduced the difficulty of the FPGA hardware.

Peng Wang and Fedrick Berggren," Secondary Synchronization Signal in 5G New Radio" proposed a double detection threshold algorithm and simulated it. The 5G NR SSS simulation results are better than LTE SSS but have not been implemented in FPGA.

The proposed architecture is developed by utilizing Verilog HDL with Xilinx VIVADO 2016.4 and executed in the Xilinx ZYNQ FPGA board. The principle of synchronization and the 5G NR frame structure will be discussed thoroughly in upcoming segments.

This paper discussed 5G NR frame structure, synchronization signal for 5G, 5G NR SSS detection algorithm, implementation of 5G NR, simulation results, and conclusion discussed in the coming sections.

Received on 23-03-2024, Revised on 22-04-2024, Accepted on 22-05-2024.

CVR Journal of Science and Technology, Volume 26, June 2024
DOI: 10.32377/cvrjst2604

II. 5G NR FRAME STRUCTURE

The illustration of the 5G New Radio (NR) frame is shown in Figure 1. The frame period comprises 10 ms and it is subdivided into ten sub-frames with 1 ms. This sub-frame is mathematically shown in equation 1.

Sub frame=Slot2μ (1)

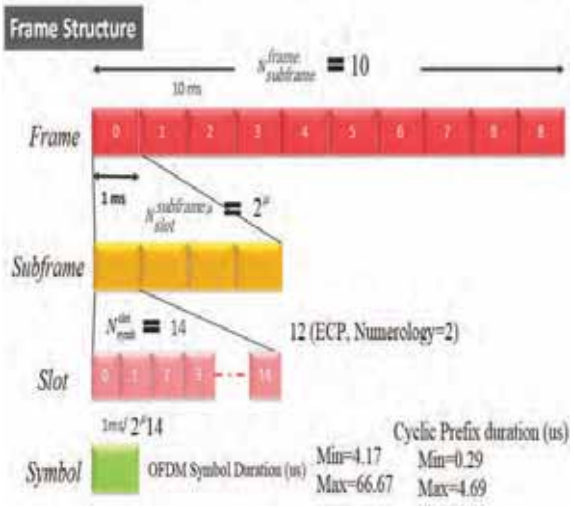

Figure 1. 5G Frame Structure

Each sub-frame is split into slots, with every sub-frame containing 14 slots [5]. Each slot is further divided into symbols, which occupy a small portion of the entire 10ms framework [1]

The frame's mathematical definition is as follows:

Frame=Subclass = 2 μ *14 *10 (2)

When the subcarrier spacing μ =2, then

one symbol = 10 sub-symbols.

One sub-symbol = 2 μ spacing = 2 spaces

One space = 14 OFDM images

symbol = 2*10*14 = 280 OFDM images [6].

Orthogonal Frequency Division Multiplexing (OFDM) images are optimized for the 5G New Radio time frame, making them highly visible at high frequencies, especially with short symbols characteristic of millimeter waves. The synchronization signals PSS and SSS are utilized in the 5G NR system for determining the radio frame boundary and detecting the cell identity (ID) for UE, which is similar to 4G systems. In 5G NR systems, each radio cell is uniquely identified by a cell ID chosen from a pool of 1008 IDs. These IDs are organized into 336 distinct groups. Every group is identified by cell ID group, NID(1)∈ {0,1, …,335}, and comprises three dispa rate segments, specified by the cell ID sector, NID(2)∈ {0,1,2}.

The hierarchical Physical Cell Identity is shown in Figure 2.

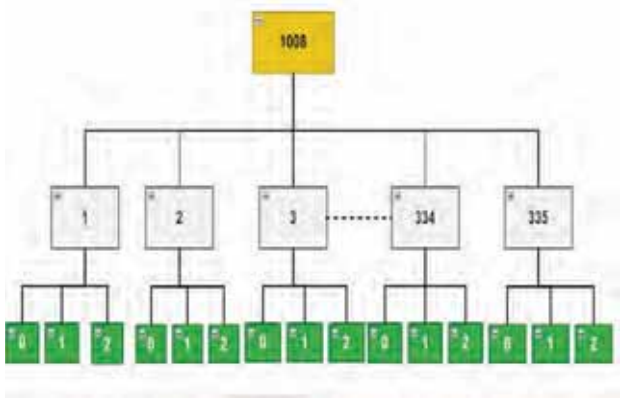

Figure 2: Hierarchy of PSS and SSS

$NID^{(1)}$and $NID^{(2)}$ values from the SSS and PSS, respectively, can be detected by the UE. The UE then uses that information to calculate the serving cell ID in the manner shown below:

$$N_{ID}^{cell} = 3* N_{ID}^{(1)} + N_{ID}^{(2)} \quad (4)$$

Where $N_{ID}^{(1)} \in \{0,1, \dots ,335\}$ and $N_{ID}^{(2)} \in \{0,1,2\}$

III. SYNCHRONIZATION SIGNAL

The initial stage when the user needs to access the mobile network is the 5G NR synchronization process. The primary purpose of this process is to detect the primary and secondary synchronization signals (PSS and SSS). Synchronization is essential for finding a high-quality signal against fading channels, the Doppler effect, inter-channel interference, multi-path interference, and inter-symbol interference scenarios. [7][13]

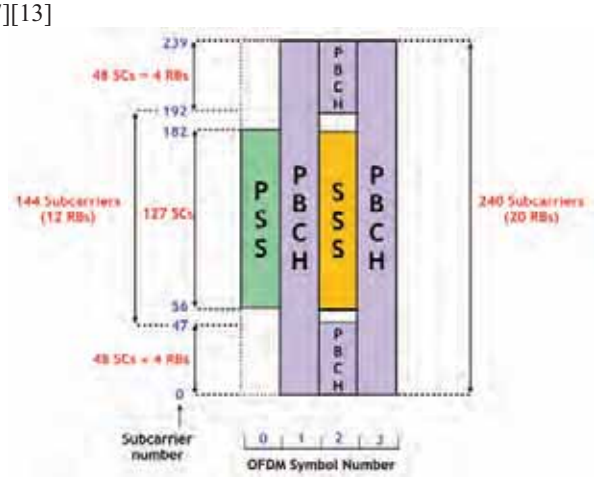

Figure 3: Synchronization Signal block diagram

The synchronization signal block diagram is shown in Figure 3 above. After the generation of PSS, the OFDM symbol0 is generated, and with the PSS value, the SSS value will be calculated at OFDM symbol2.

Physical cell identification of a base station (gNodeB) can be identified by first detecting the PSS value and then determining the SSS value. Figure 4 illustrates the block diagram for finding PCI.

CVR Journal of Science and Technology, Volume 26, June 2024
DOI: 10.32377/cvrjst2604

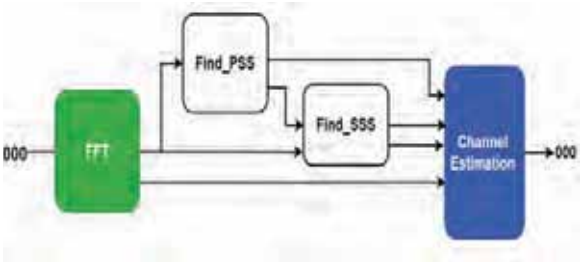

Figure 4: Procedure for finding Physical Cell Identity

The UE first calculates the PSS value and then the SSS value from the received signal will be calculated. PSS provides a radio frame boundary and SSS provides a subframe boundary.

With PSS and SSS values, the Physical layer Cell ID (PCI) will be calculated. The procedure for cell identity calculation is similar, but the number of code groups for SSS is different for finding PCI value compared to LTE.

3.1. Primary Synchronization Signal

The 5G-New Radio (NR) primary synchronization signal is a physical layer-specific signal that determines the radio frame boundary as well as detects the cell ID sector for UEs, e.g., $NID^{(2)}$. the 5G NR PSS, is specifically allocated to the first symbol of each SSB, and 127 subcarriers and it consists of one of three 127-symbol m-sequences PSS has subcarriers with lists ranging from 57 to 183 and is always located in the synchronization block's principal OFDM image. Since the UE oscillator is inaccurate and causes a mismatch with the system reference frequency, the primary goals of PSS are coarse frequency correlation as well as initial symbol alignment. In the time domain, a matched filter of length N= 256 first finds the PSS. To determine the PSS value $NID^{(2)}$, the correlated outputs of the three matched filters of three sectors are maximized.[5]

3.2. Secondary Synchronization Signal

The 5G NR SSS identifies the cell ID group $NID^{(1)}$ and frame identity. However, it is assigned to the third symbol of every SSB, along with the 127 subcarriers, and comprises one of the 336 127-symbol gold sequences. The following definition refers to the 336 potential gold sequences for the SSS:

After PSS detection, the signal proceeds via an OFDM demodulator, recovering the signal from the subcarrier positions in the frequency domain. After that, the receiver can identify the $NID^{(1)}$using SSS detection. Similar to PSS, SSS is always positioned within the third OFDM image of the synchronization block and uses subcarriers that have files ranging from 57 to 183, as shown in Figure 5. [15]

Figure 5. 5G NR Secondary Synchronization Signal Detection Algorithm

The 5G NR Primary SS, however, is allocated to the third image of each SSB and on 127 sub-carriers. It consists of one of three 336 127-image gold successions. The following illustrates the 336 potential gold groupings for the SSS [6]:

$$d_{SSS}= [1 - 2X_0((n+m_0) \bmod 127)] [1 - 2X_1((n+m_1) \bmod 127] \quad (4)$$

From the above equation 4, SSS ($N_{ID}^{(1)}$is generated by Gold sequence which is derived from a combination of two M-sequences m0 and m1.

$$m0 = 15[N_{ID}^{(1)} / 112] +5 N_{ID}^{(2)} \quad (5)$$

$$m1 = N_{ID}^{(1)} \bmod 112; 0 \leq n < 127 \quad (6)$$

Where

$$X_0(|i + 7|) = (X_0(|i + 4|) + X_0(i)) \bmod 2. \quad (7)$$

$$X_1(|i + 7|) = (X_1(|i + 1|) + X_1(i)) \bmod 2. \quad (8)$$

And Initial state:

$[X_1(0)\ X_1(1)\ X_1(2)\ X_1(3)\ X_1(4)\ X_1(5)\ X_1(6)] = [1\ 0\ 0\ 0\ 0\ 0\ 0]$
$[X_0(0)\ X_0(1)\ X_0(2)\ X_0(3)\ X_0(4)\ X_0(5)\ X_0(6)] = [1\ 0\ 0\ 0\ 0\ 0\ 0]$

For 5G NR SSS detection, the suggested block diagram is shown in Figure 6. As inputs, the PSS ($N_{ID}^{(2)}$) and pre-SSS are provided.

The pre-SSS signal data is divided into odd and even index blocks in the proposed design for determining SSS. The data sets are then divided into the SSS X0(m0) block and the SSS X1(m1) block.

The SSS block will process the PSS ($N_{ID}^{(2)}$)) data and the even-indexed SSS data by extracting the value m0 from the input signal using the procedure mentioned above from the SSS Generation equations. SSS X1(m1) is nearly identical to the SSS X0(m0) block; to find the value m1 from the input signal, SSS X1(m1) will analyze the odd-indexed SSS data in conjunction with the PSS ($N_{ID}^{(2)}$) information. The outputs of the correlator are fed to the final block, known as the comparator block**.** This block computes the ultimate value of the cell group ID ($N_{ID}^{(1)}$) and finalizes it for the system's output.

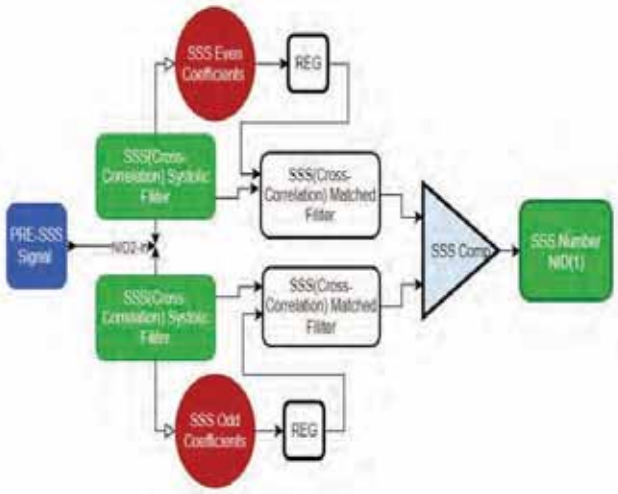

Figure 6. 5G NR SSS detection block diagram

The processing block uses PSS ($N_{ID}^{(2)}$) information and even-indexed SSS data. It extracts the value m0 from the input signal using an algorithm developed from the SSS Generation equations. Similar to the SSS X0(m0) block, the SSS X1(m1) block uses a different algorithm to process odd-indexed SSS data and extract the value m1 together with PSS ($N_{ID}^{(2)}$) information. The outputs of the correlator are fed into the comparator block, the last stage, which generates the system's output by computing the cell group ID ($N_{ID}^{(1)}$) using the previously obtained m0 and m1 values.

The matched filter is designed with Finite Impulse Response Filter. It gives peak output for maximum correlation. [11][12]. The two matched filters' outputs are given to the comparator block. The comparator block will decide the maximum peak value of the SSS number ($N_{ID}^{(1)}$).

After finding the SSS value from the input signal and $N_{ID}^{(2)}$the cell ID will be determined. After finding the cell ID, the next operations are to be performed like the demodulation procedure.

The matched filter is designed with an FIR digital filter. The systolic FIR filter is designed for SSS due to its pipelining and high stability.

3.3 Systolicmatched filter

The systolic FIR filter is an array of processing elements that carries computations on every clock cycle. It is a completely pipelined structure that will offer rapid processing speeds and extremely low latencies. It consists of several processing elements that aim to perform high-speed operations compared to traditional FIR filters within the same period.

The basic definition of the systolic FIR filter is depicted below.

The coefficients are sequenced as {w1, w2, ..., wn}
And the sequences for input {x1, x2, …,xn}

Finally, the resultant sequence is obtained as {y1, y2, …,yn}.

The FIR filter expression is given as:

$$y_i = \sum_{k=0}^{n} w(n)x(k-n) \quad (9)$$

The N tap systolic FIR filter for N=16 taps is designed based on the Direct graph as follows,

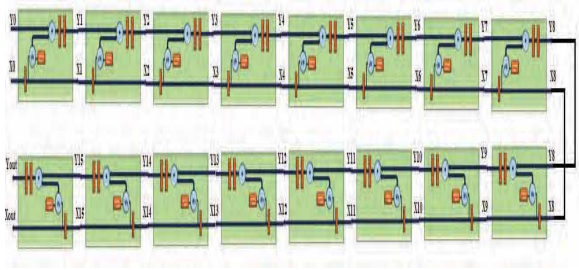

Figure 7: 16 tap Systolic FIR filter block diagram.

16 tap systolic FIR filter consists of 16 processing elements (PE). Each PE consists of a carry select adder, Vedic multiplier, and flip-flops for storage.[12]

The Vedic multiplication algorithm employs a criss-cross technique for n-bit multiplication. It involves splitting the multiplicands into two halves, which are referred to as the Least Significant Bits (LSB) and Most Significant Bits (MSB).

The algorithm is separated into three stages of computation performance. The first stage involves multiplying and providing the product of the LSB bits; the second stage involves multiplying the LSB and MSB bits of both multiplicands in a crisscross fashion and conserving this partial product. The product is obtained in the third stage by multiplying the MSB bits. Ultimately, the final product term is obtained in a single unit step by summing all of the partial products using the corresponding n-bit adder.

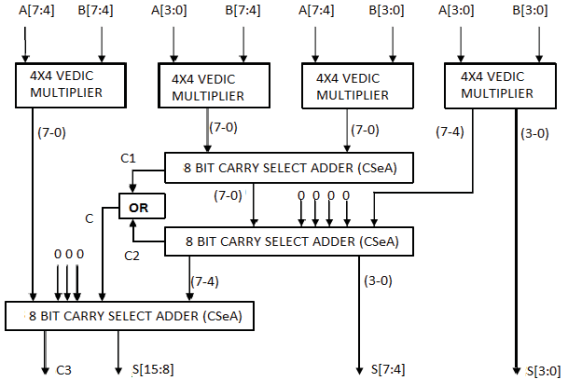

Figure 8: 8-bit Vedic multiplier

The proposed 8-bit Vedic multiplier is designed with a 4 X 4 Vedic multiplier and carries a select adder as shown in Figure 8 above.

The carry-select adder algorithm is implemented in two major stages to perform addition. The general addition is done in the first stage by utilizing the ripple carry process, and the maximum possible carry-in bits are used in the second phase of addition. Consequently, there are two possible outcomes for the carry-in bits: carry-in = 0 and

CVR Journal of Science and Technology, Volume 26, June 2024
DOI: 10.32377/cvrjst2604

carry-in = 1. The determination of the final carry and final sum bits occurs after the second stage has completed its corresponding addition, utilizing the carry-in bits' possibilities. The carry select adder relies on the carry output from the first stage, which feeds into the multiplexer input. By considering the select line bit of the multiplexer, the outcomes are identified or chosen for the addition of the two operands in the second stage. Hereby, the carry select adder is one of the quickest adders that can carry out addition operations in a phase despite the n-bit input.

The carry select adder implementation for the 16-bit data is shown in Figure 9. The proposed carry select adder is a high-speed adder compared to other adder circuits.

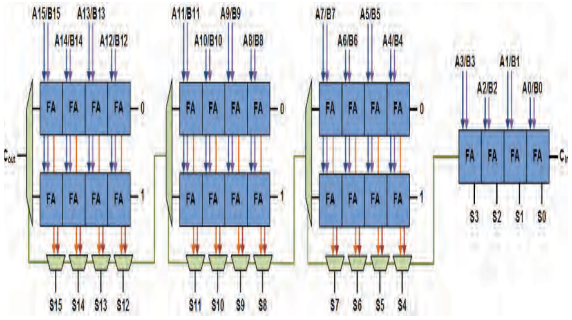

Figure 9. 16-bit Carry Select Adder block diagram.

The proposed systolic FIR is a high-performance and low-power circuit and is considered to be a good choice for the SSS detection system.

IV. Simulation Results

The simulation results for the proposed secondary synchronization block are shown in Figure 10 below. The system processes the SSS input data and $N_{ID}^{(2)}$ value to determine the SSS $N_{ID}^{(1)}$. The data set and the SSS Num value are taken from the system, and a flag head indicates the start of the data symbol. After processing the input data, $N_{ID}^{(1)}$ will be generated and the output flag goes too high to indicate the SSS value is the valid number.

From the simulation results, the calculated secondary synchronization signal value is $N_{ID}^{(1)} = 140(8Ch)$ as shown in Figure 10 below.

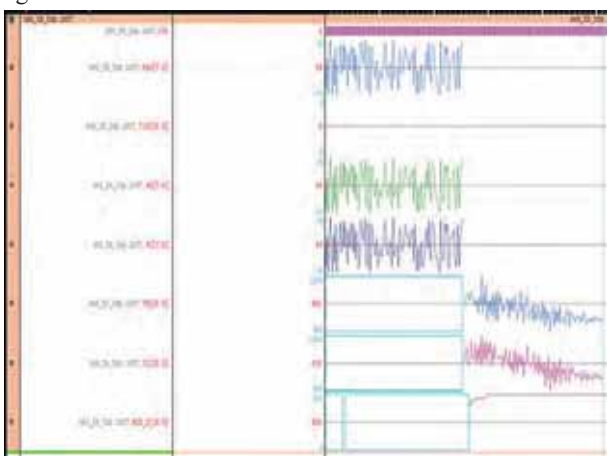
Figure 10: Simulation results of 5G NR SSS.

Finally, the physical cell identity value will be determined with $N_{ID}^{(1)}$) and $N_{ID}^{(2)}$) values. The gate-level schematic diagram for the 5G NR SSS is shown in Figure 11.

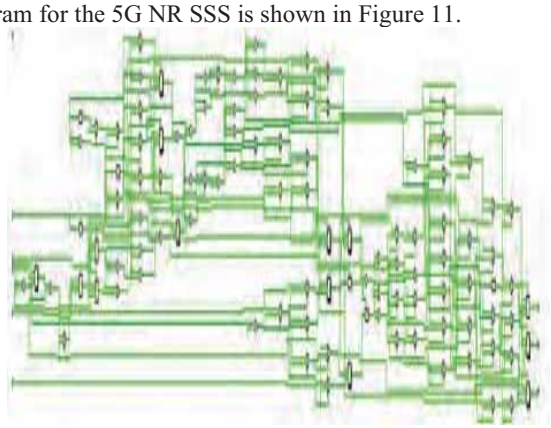
Figure 11. Gate-level schematic diagram of 5G NR SSS

The proposed 5G NR secondary synchronization detection circuit is implemented in the Xilinx ZYNQ board. The FPGA utilization summary is shown in Table 1.

The FPGA utilization summary indicates the resource utilization like flipflops, LUTs, logic blocks, IO blocks, and buffer global clocks, etc.

Table 1: FPGA Utilization Summary

Utilization Summary	Proposed method for SSS		
	Used	Available	Utilization (%)
Number of slice registers	576	17400	3.31
Number of slices LUT'S	773	53200	3.33
Number of flip-flops	264	106400	0.248
No of IOBs	81	200	0.405
No. of BUFGCTRLs	1	32	3.125

From the above FPGA utilization summary, the proposed system uses logic resources with low utilization.

V. Conclusion

The proposed design of a 5G NR Secondary Synchronization Signal for finding Physical Cell Identity is designed, verified, and executed on the Xilinx ZYNQ FPGA board. The outcomes demonstrate that the stated proposition result in the identification of a 5G NR synchronization signal with the proposed technique and also detects the physical cell identity. Also, from the synthesis report, it is observed that logic utilization is reduced. The proposed system has attained low power dissipation and is run at rapid speeds with a minimum of 200 MHz and a maximum of 4 GHz clock rates.

References

[1] A. Omri, M. Shaqfeh, A. Ali and H. Alnuweiri, "Synchronization Procedure in 5G NR Systems," in IEEE Access, vol. 7, pp. 41286-41295, 2019.

[2] J.-C. Lin, "Synchronization Requirements for 5G: An Overview of Standards and Specifications for Cellular Networks," in IEEE Vehicular Technology Magazine, vol. 13, no. 3, pp. 91-99, Sept. 2018.

[3] S. Lien, S. Shieh, Y. Huang, B. Su, Y. Hsu, and H. Wei, "5G

New Radio: waveform, frame structure, multiple access, and initial access," IEEE Communication Magazine., vol.55, no.6, pp.64-71, June 2017.

[4] Y. Jeon, H. Park, and E. Choi, "Synchronization and Cell Search Procedure in 3GPP 5G NR Systems," 2019 21st International Conference on Advanced Communication Technology (ICACT), Pyeong Chang, Korea (South), pp. 475-478, 2019.

[5] C. Hu and Y. Zhang, "5G NR Primary Synchronization Signal Detection with Low Hardware Resource Occupancy," 2018 IEEE/CIC International Conference on Communications in China (ICCC), Beijing, China, pp. 304-308, 2018.

[6] Riccardo Tuninato, Daniel Gaetano Riviello, Roberto Garello, Bruno Melis and Roberto Fantini," A comprehensive study on the synchronization procedure in 5G NR with 3GPP-compliant link-level simulator", EURASIP Journal on Wireless Communications and Networking, Vol.1, pp.1-29, 2023.

[7] Peng Wang, and Fedrick Berggren," Secondary Synchronization Signal in 5G New Radio", 2018 IEEE International Conference on Communications, July 2018.

[8] 3GPP Technical Specification 38.211v1.0.0, September 2017.

[9] 3GPP. The 3rd Generation Partnership Project. Accessed: Mar. 17, 2019.

[10] Y.-H. You, J. -H. Park and I. -Y. Ahn, "Complexity Effective Sequential Detection of Secondary Synchronization Signal for 5G New Radio Communication Systems," in IEEE Systems Journal, vol. 15, no. 3, pp. 3382-3390, Sept. 2021.

[11] S. Kiruthika and A. V. Starbino, "Design and analysis of FIR filters using low power multiplier and full adder cells," *2017 IEEE International Conference on Electrical, Instrumentation and Communication Engineering (ICEICE)*, Karur, India, 2017, pp. 1-5.

[12] V. Visvanathan, N. Mohanty and S. Ramanathan, "An Area-Efficient Systolic Architecture for Real-Time VLSI Finite Impulse Response Filters," *The Sixth International Conference on VLSI Design*, Bombay, India, 1993, pp. 166-171.

[13] F. Chen, X. Li, Y. Zhang, and Y. Jiang, "Design and implementation of initial cell search in 5G NR systems," in China Communications, vol. 17, no. 5, pp. 38-49, May 2020.

[14] A. Golnari, M. Shabana, A. Nezamalhosseini and G. Gulak, "Design and Implementation of Time and Frequency Synchronization in LTE," in IEEE Transactions on Very Large Scale Integration (VLSI) Systems, vol. 23, no. 12, pp. 2970-2982, Dec. 2015.

[15] A. G. Wassal and A. R. Elsherif, "Efficient implementation of secondary synchronization symbol detection in 3GPP LTE," 2011 IEEE International Symposium of Circuits and Systems (ISCAS), Rio de Janeiro, Brazil, 2011, pp. 1680-1683

E-ISSN 2581 – 7957
P-ISSN 2277 – 3916

CVR Journal of Science and Technology, Volume 26, June 2024
DOI: 10.32377/cvrjst2605

IR Sensor based Smart Parking System

Dr. Humaira Nishat[1] and Shakeel Ahmed[2]
[1]Professor, CVR College of Engineering/ECE Department, Hyderabad, India
Email: humaira.nishat@cvr.ac.in
[2]Sr. Assistant Professor, CVR College of Engineering/ECE Department, Hyderabad, India
Email: shakeel.be@gmail.com

Abstract: **Nowadays congestion of traffic level increased with the increase in population. As the population increases, the utilization of vehicles also increases. It's becoming a difficult task to find a slot to park the vehicle. To overcome this problem, a smart parking system is introduced. Previously, there were some approaches to this system where Bluetooth and GPS tracker were used to find the empty slots, and different sensors were used for indoor and outdoor parking. In some approaches there was no security for the user's details. Whereas in the proposed system, every slot has a number which makes it easier for the user to find out the empty slot. IR sensors are used to detect the vehicle and the empty slot is displayed on LCD as well as cloud server where the user's details are secured. Smart parking system is an IoT based system which includes Raspberry pi, LED display, Cloud Server, Monitor and IR Sensors that are available in each parking slot. The proposed system leverages the advantages of IR sensor technology to accurately detect the presence of vehicles in parking spaces, provides real-time information to the users, and improves overall parking efficiency. The paper discusses the system architecture, sensor deployment strategies, and implementation, thereby showcasing the potential benefits of IR sensor-based smart parking systems.**

Index Terms: **camera, cloud, parking, Raspberry Pi, sensors, vehicles**

I. Introduction

Parking is one of the most common human activities on our planet, and it has become more important in recent years as car ownership has increased. It is found that approximately by 2050 most of the cities would be accommodating two thirds of the world's population. Due to rapid urbanization, there is increasing concern over traffic congestion in many parts of the world. In dense urban areas, many drivers have difficulty finding a parking space when they need one. A parking system that can be used to help drivers find parking spaces could solve this problem, allowing them to park their cars more easily and avoid wasting time. A smart parking system could also help save parking facilities from overcrowding. This would be useful in city centers and other large urban areas where many cars must be parked to prevent them from blocking roads and creating traffic bottlenecks. Once a space is available, the car can be parked and removed from the system, making the available space available for other cars to use. This would reduce traffic congestion and allow for a more streamlined parking process.

II. Related Work

There are previous works on this topic where they had different approaches to locate the available parking lot. In paper [1], authors have worked with the same principle, but ultrasonic sensors are used to detect vehicles. Though both ultrasonic and IR sensors are used for detecting objects, IR sensors give the sensed information faster than ultrasonic sensors to locate the available area.

In paper [2], authors have used some simulation models. The work is based on an RFID reader for each vehicle entering the parking area. The proposed system is designed to detect and find a parking location for the user's vehicle. This system creates a wireless sensor network, and the user must wait for confirmation of parking slot through notification from server, it is a little time-consuming process.

In paper [3], authors have used ultrasonic sensors and GPS using MQTT protocol for simulation of the work. The work is not implemented in real time and since it uses ultrasonic sensors, the overall performance of the system is low compared to the proposed system.

Paper [4] provides an idea about smart parking systems using IoT and cloud, but the user must pay the toll fee to use the service. Thus, the proposed method of smart parking system using IR sensors overcomes all the problems discussed above.

Paper [5] uses convolutional neural network tool to train the algorithm deeply. It uses image processing and segmentation for capturing the real time images of the parking slot and displaying the information of its occupancy. It uses MATLAB for validating the approach.

In paper [6], the authors have created a mobile application enabling the users to verify parking space availability and make reservations accordingly. The app also provides real-time 'parking service payment' based on the duration of parking. Moreover, it detects the arrivals of vehicles at the entrance for automated gate opening. This feature empowers the users to conveniently check parking availability online from any location, ensuring hassle-free parking experience.

Paper [7], provides a comprehensive review and analysis on multi-approach-based Smart Parking Systems (SPS) which will emerge as dominant in future smart cities, with IoT serving as the backbone. The user interface is anticipated to be smartphone application-based, offering features such as parking supervision, online payment, parking reservation, and vehicle guidance. Sensor selection in SPS will be contingent upon various indoor and outdoor conditions, with installation ease (easy installation), privacy, sensing method, and sensor coverage area emerging as

Received on 20-02-2024, Revised on 21-03-2024, Accepted on 20-04-2024.

CVR Journal of Science and Technology, Volume 26, June 2024
DOI: 10.32377/cvrjst2605

primary considerations. Data communication protocol security will also be a significant concern in future SPS systems, prompting increased emphasis on wireless communication protocols to ensure data security.

Paper [8], introduces an efficient method for detecting vacant spaces and managing vehicle movement within complex multistoried parking structures. It utilizes IR sensors to detect vehicles and provides real-time feedback. The fully automated smart car parking system is simple and does not necessitate extensive lines of code or expensive equipment. It's a straightforward circuit designed precisely for its intended purpose.

This automated system efficiently identifies available parking spaces and guides drivers to their desired spots using visual cues, thereby reducing search time. It proves beneficial for malls, multi-storey parking facilities, IT hubs, and other parking areas, significantly reducing the need for manual labor.

The authors have done extensive research work in [9] and a technical analysis of smart parking solutions, focusing on the systems and sensors documented in existing literature is discussed. The review aims to offer comprehensive insights into the development of smart parking solutions with a thorough examination of the current landscape of smart parking systems including categorizing these systems based on advanced vehicular detection technologies. The work also presents clear explanations of communication modules involved in these solutions.

Authors in paper [10] introduce a Smart Parking Energy Management solution designed for structured environments like multi-storied office parking areas. The system proposes the integration of cutting-edge Internet of Things technology with advanced Honeywell sensors and controllers to establish a systematic parking management system for users. Empty parking spaces are indicated using lamps, guiding users to available spots and eliminating the need for extensive search. Occupied parking spaces are digitally stored in the cloud, accessible to the central system to direct incoming vehicles to vacant spots. Automatically controlled light brightness helps in reducing energy consumption while providing adequate illumination to the users within the parking area. The fully automated system reduces the need for manual intervention, enhancing the aesthetic appeal of the parking area.

Paper [11] introduces a smart parking system aimed at addressing current parking challenges at an affordable cost. The system integrates the latest advancements in Information and Communication Technologies and comprises four layers: Application, Middleware, Networking, and Sensor layer. It promotes environmental sustainability by reducing harmful emissions during parking and operates as a computerized system pre-programmed without requiring human intervention. The paper also emphasizes the comparison between traditional parking systems and smart parking systems utilizing IoT. Furthermore, it presents a framework for the implementation of a smart parking system.

The paper is organized as follows: Section III describing the proposed methodology followed with implementation of the work in section IV, results and conclusions in V and VI respectively.

III. Proposed Method

The proposed architecture is partitioned into three sections. The first section consists of the parking area where we have IR sensors placed in their respective slots along with the Raspberry Pi module. The sensors give us the information about the availability of the parking slot. In the parking area, cameras are placed for live view of the available slot, an LED display is also employed at certain height at the entrance so that the user will have a view of the slot status from a far distance. The monitor is placed at the entrance of the parking lot. The second section comprises the cloud server. One xyz online cloud server is used to store the data that is being transmitted by the sensors. The third section is meant for the users. The user is given access to the server, he/she can login to the server and check for the available parking slots. There is an LCD display that shows all the slots. If they are occupied, it shows ‘1’ otherwise, it displays’0’ (Example: s1-0 s2-1 s3-1 s4-0 s5-1). It is placed in the parking area alongside the monitor so that the users can have easy access to the free slots. Relays are also used in each slot that glows ‘On’ and ‘OFF’ based on slot occupancy. Figure 1 gives the proposed system architecture.

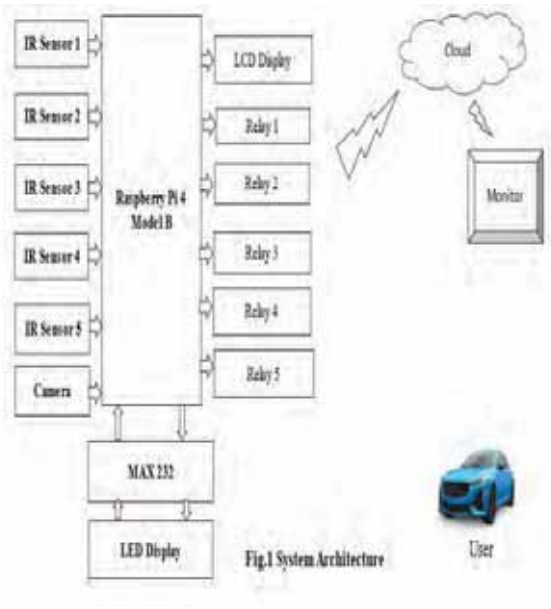

Figure 1. System Architecture.

The module includes:

A. *Raspberry Pi*

The Raspberry Pi as shown in figure 2 is an affordable, credit-card-sized computer that can be plugged in to any computer. It possesses the capability of performing various tasks akin to a desktop computer, including internet browsing, playing high-definition videos, word processing, and gaming. It is widely used to make gaming devices, fitness gadgets, weather stations, and much more.

CVR Journal of Science and Technology, Volume 26, June 2024
DOI: 10.32377/cvrjst2605

Figure 2. Raspberry Pi.

B. IR Sensor

An Infrared (IR) sensor (shown in figure3) is an electronic device designed to detect and measure IR radiation emitted by objects. Objects with temperatures higher than 5° emit IR radiation. IR sensors are primarily employed for motion detection and temperature measurement. They can be classified into two types: Active Infrared Sensors and Passive Infrared Sensors.

Figure 3. IR Sensor.

C. LCD Display

An LCD serves as a display mechanism for showcasing information on various devices such as machines, clocks, railway departure indicators, and more. A dot matrix controller translates processor instructions into signals, activating or deactivating lights within the matrix to generate the desired display. This display comprises a dot matrix of lights organized in a rectangular pattern, allowing for the presentation of text or graphics by selectively turning on or off specific lights. LCD display is shown in figure 4.

Figure 4. LCD Display.

D. IoT-AWS Software

IOT represents the prominent technology of our time, where devices interconnect via the internet, enabling data transfer without direct human-to-human or human-to-computer interaction. The internet connectivity among sensors, computational devices, and storage units can be established through either wired or wireless connections. AWS, an acronym for Amazon Web Services, stands as the foremost cloud provider in the market, offering developers access to over 170 AWS services from any location, as needed.

IV. Implementation

This section of the paper demonstrates the flow of implementation of this project in real life.

A. Section I: Parking Area

With the help of daughter board, the IR sensors are connected to the power supply. The sensors are then placed in their respective slots based on their numbers. The range of these sensors can be altered for future use. Whenever there is a vehicle in the slot the sensors sense it and send a message saying there is an object present. This is further updated in the cloud server.

B. Section II: Cloud Server

Amazon AWS cloud server is used in the work. The server takes the message from the sensor and displays the information accordingly. It displays “1” if the slot is occupied else “0”.

C.Section III: User Interface

The user is given the login credentials to the website, and he/she can access the site whenever he wishes. The user can see whether the slot is occupied or not and can park according to his will.

In addition to the server, there is an LED display at the entrance of the parking lot at a certain height which gives the same information of the slots from afar. The sensors are vulnerable to detect any object in addition to the vehicles, thus, to avoid any error, a camera is placed in the parking area which gives the live streaming and is displayed on the monitor at the entrance gate.

V. Results

Results are shown in the form of pictures taken at different times as per the slot occupancy.

E-ISSN 2581 – 7957
P-ISSN 2277 – 3916

CVR Journal of Science and Technology, Volume 26, June 2024
DOI: 10.32377/cvrjst2605

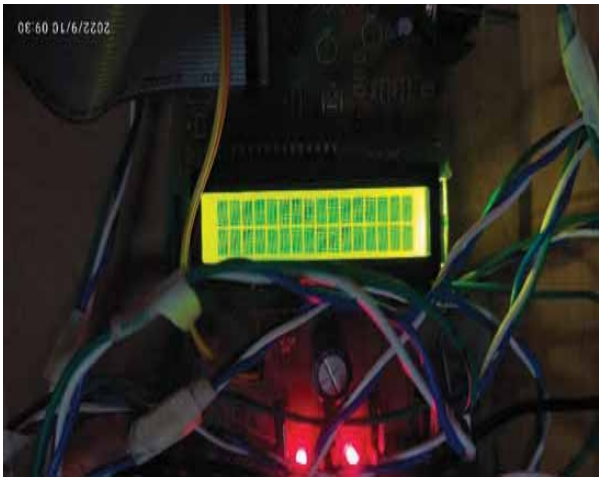

Figure 5. LCD Display.

Figure 5 shows the LCD display, showing the slot occupancy at a particular time. If a slot is occupied, it is represented as F otherwise E.

Figure 6. LED Display.

Figure 6 displays the slot occupancy as 1 or 0 for being occupied or empty.

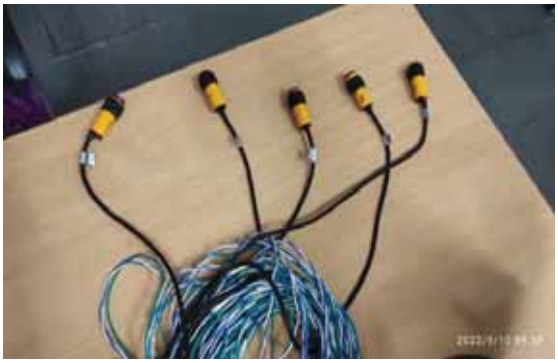

Figure 7. LED Display.

Figure 7 shows the five IR sensors used in the work. These sensors can cover ten meters in detecting an object.

Figure 8. Raspberry Pi.

Figure 8 shows the Raspberry Pi used in the work for receiving the inputs from the sensors, processing it, and transmitting the data to the cloud.

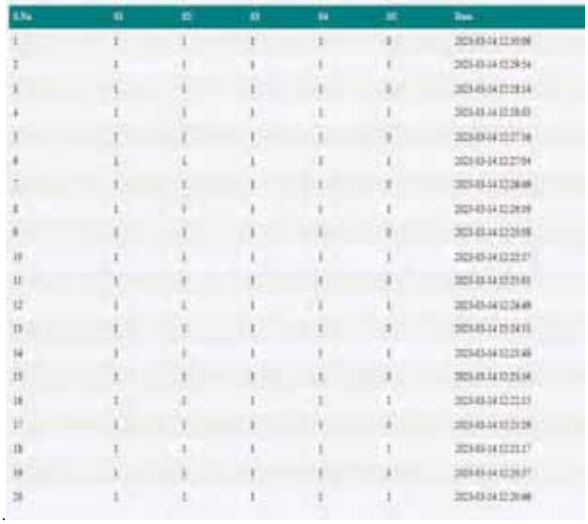

Figure 9. IoT Server data on Monitor with timestamp

Figure 10. IoT server data on Monitor with Timestamp.

Figures 9 and 10 give the data received in the cloud at different time instances regarding the occupancy of the slots with time stamps (date and time).

VI. Conclusions

In conclusion, this smart parking system allows the users to easily access the parking lot irrespective of the place they are in. This paper aims to provide an in-depth understanding of the design, implementation, and optimization of a smart parking system using IR sensors. By leveraging the capabilities of IR sensor technology, this system offers accurate and real-time vehicle detection, enhancing parking space utilization and improving the overall parking experience.

References

[1] A. Gupta, P. Rastogi and S. Jain, "Smart Parking System using Cloud based Computation and Raspberry Pi," 2018 2nd International Conference on I-SMAC (IoT in Social, Mobile, Analytics and Cloud) (I-SMAC)I-SMAC (IoT in Social, Mobile, Analytics and Cloud) (I-SMAC), 2018 2nd International Conference on, Palladam, India, 2018, pp. 94-99, doi: 10.1109/I-SMAC.2018.8653764.

[2] T. N. Pham, M. -F. Tsai, D. B. Nguyen, C. -R. Dow and D. -J. Deng, "A Cloud-Based Smart-Parking System Based on Internet-of-Things Technologies," in IEEE Access, vol. 3, pp. 1581-1591, 2015, doi: 10.1109/ACCESS.2015.2477299.

[3] Juwita, Putri & Fadhil, Radya & Damayanti, Tri & Ramadan, Dadan. (2020). Smart parking management system using SSGA MQTT and real-time database. TELKOMNIKA (Telecommunication Computing Electronics and Control). 18. 1243. 10.12928/telkomnika.v18i3.14869.

[4] Sayed, Fauziya. (2021). Smart Parking System using IoT and Cloud. International Journal for Research in Applied Science and Engineering Technology. 9. 853-856. 10.22214/ijraset.2021.35084.G. Eason, B. Noble, and I. N. Sneddon, “On certain integrals of Lipschitz-Hankel type involving products of Bessel functions,” Phil. Trans. Roy. Soc. London, vol. A247, pp. 529–551, April 1955.

[5] Joshi, Niravkumar, Alsheikhy, Ahmed A., Shawly, Tawfeeq, Said, Yahia F., Lahza, Husam, An Intelligent Smart Parking System Using Convolutional Neural Network, Journal of Sensors 1687-725X, https://doi.org/10.1155/2022/7571716 DOI. 10.1155/2022/7571716, 2022 2022/11/21, , SP - 7571716, VL - 2022

[6] Tanti, Hardik & Kasodariya, Pratik & Patel, Shikha & Rangrej, Dhaval. (2020). Smart Parking System based on IOT. International Journal of Engineering Research and. V9. 10.17577/IJERTV9IS050041.

[7] Abrar Fahim, Mehedi Hasan, Muhtasim Alam Chowdhury, Smart parking systems: comprehensive review based on various aspects, Heliyon, Volume 7, Issue 5, 2021, e07050, ISSN 2405-8440, https://doi.org/10.1016/j.heliyon.2021.e07050.

[8] Joshi, Aashish. (2020). Smart Car Parking System. International Journal of Engineering Research and. V9. 10.17577/IJERTV9IS090305.

[9] Biyik, C.; Allam, Z.; Pieri, G.; Moroni, D.; O’Fraifer, M.; O’Connell, E.; Olariu, S.; Khalid, M. Smart Parking Systems: Reviewing the Literature, Architecture and Ways Forward. Smart Cities 2021, 4, 623-642. https://doi.org/10.3390/smartcities4020032

[10] D. Ashok, A. Tiwari and V. Jirge, "Smart Parking System using IoT Technology," 2020 International Conference on Emerging Trends in Information Technology and Engineering (ic-ETITE), Vellore, India, 2020, pp. 1-7, doi: 10.1109/ic-ETITE47903.2020.457.

[11] W. Z. Al Qaidhi and M. Sohail, “Smart Parking System using IOT”, J Stud Res, Jul. 2020.

E-ISSN 2581 – 7957
P-ISSN 2277 – 3916

CVR Journal of Science and Technology, Volume 26, June 2024
DOI: 10.32377/cvrjst2606

GSM-Enabled Home Automation and Security System: A Comprehensive Investigation and Implementation

N. Swapna[1], V. Sreelatha Reddy[2], K.Uday[3]
[1]Assistant Professor, Guru Nanak Institutions Technical Campus/ECE Department, Hyderabad, India
Email: swapnan.ecegnitc@gniindia.org
[2,3] Sr. Assistant Professor, CVR College of Engineering/EIE Department, Hyderabad, India
Email: srilathareddy.cvr@gmail.com, k.uday@cvr.ac.in

Abstract: **This research project focused on integrating home control and security through advanced Home Automation Systems. A thorough analysis and practical implementation of home automation technology were conducted, utilizing Global System for Mobile Communication (GSM) modems to manage various home appliances, including fans, air conditioning systems, and security systems. The system relied on Short Message Service (SMS) text messages for control and monitoring. Key features included an entrance security mechanism to promptly notify homeowners of unauthorized access, bolstering overall security. Additionally, an anti-theft reporting system employed alarms and SMS notifications to inform owners of security breaches. The system also integrated safety protocols for fire or gas leakage, dispatching SMS notifications and activating alarms to alert homeowners. The use of GSM technology provided wireless access to control connected devices, enhancing system efficiency and convenience. This research contributed to the smart home technologies field by presenting an advanced system that harmonized automation, security, and safety, with potential applications across diverse residential settings. While numerous home automation systems were available in the market, the significance of the proposed home automation system lay in its advanced features and comprehensive approach to integrating control and security functions. Unlike many existing systems, which may have offered basic automation capabilities, the proposed system went beyond simple automation by seamlessly integrating security measures using GSM technology. This allowed homeowners to effectively manage a wide range of home appliances, including fans, air conditioning systems, and security systems, all through the convenience of SMS text messages. Key features of the proposed system, such as the entrance security mechanism and anti-theft reporting system, addressed critical security concerns and provided homeowners with real-time notifications of unauthorized access or security breaches. Additionally, the integration of safety protocols for fire or gas leakage further enhanced the system's utility and value by prioritizing homeowner safety. Moreover, the utilization of GSM technology offered wireless access to control connected devices, significantly enhancing system efficiency and convenience compared to traditional wired systems. This wireless connectivity ensured that homeowners could remotely monitor and control their home environment from anywhere, at any time, providing them with peace of mind and control over their living space. Overall, the proposed home automation system represented a significant advancement in the field of smart home technologies by offering a comprehensive solution that harmonized automation, security, and safety. Its potential applications across diverse residential settings underscored its importance and relevance in meeting the evolving needs of modern homeowners.**

Index Terms: **Short Message Service (SMS), GSM modems, Safety protocols, Gas leakage detection.**

I. Introduction

The escalating prevalence of wireless communication has spurred the utilization of mobile phones for remote household appliance control and security feedback. This paper outlines a system for remotely controlling various household appliances and monitoring home safety and security through SMS notifications. The controller proves particularly advantageous in scenarios where wired connections are impractical, allowing for the seamless ON and OFF switching of devices from any location worldwide. The microcontroller plays a pivotal role in receiving SMS commands and subsequently controlling home appliances accordingly. It provides feedback in case of a security breach, gas leakage, or fire incident. This proposed solution is characterized by its user-friendly interface, simplicity, security, and robustness. Additionally, it provides the convenience of management via dedicated Android mobile applications. The system outlined in this paper presents a simple yet efficient method for remote control of home appliances, as well as enhancing security and safety through GSM SMS.

A. Objective

This home automation project aims to enable remote control of household appliances using a basic GSM-based phone. It eliminates the need for a smartphone, allowing users to operate and manage home electronic devices effortlessly with a standard GSM phone. The project centers around a dedicated Controller responsible for overseeing the entire process. GSM wireless communication is the key technology employed for the remote control of home appliances. By sending specific commands via SMS from the GSM phone, users can seamlessly switch ON or OFF various household electronic devices. The Controller receives these commands through the GSM module and subsequently sends signals to relays with the assistance of a relay driver, facilitating the efficient control of home appliances based on user instructions.

B. Motivation

This research involves an in-depth examination of existing literature and case studies to create a comprehensive overview of GSM-based home automation and security systems. By synthesizing this information, our goal is to present a thorough and insightful analysis. The integration of

Received on 05-03-2024, Revised on 04-04-2024, Accepted on 04-05-2024.

CVR Journal of Science and Technology, Volume 26, June 2024
DOI: 10.32377/cvrjst2606

a GSM module into the system is a key aspect, enabling communication with mobile networks. Various sensors have been incorporated into the system for both security and automation purposes. These sensors are connected and configured to the microcontroller to provide real-time data. By linking the GSM module to the microcontroller, the system facilitates the control and monitoring of home appliances, allowing users to check their status.To implement the necessary logic for controlling and monitoring devices based on sensor inputs and user commands, code can be developed using KIEL software. Additionally, security features have been implemented in the logic, including the capability to send SMS alerts or make phone calls in the event of security breaches. The overall design ensures a robust and integrated GSM-based home automation and security system.

II. Literature Review

Safial Islam Ayon et al. [1] stress security's pivotal role in home automation, introducing a fully automated smart security box to promptly alert authorized users of unauthorized breaches. This device, praised for its advanced security, affordability, and user-friendly design, utilizes Arduino and GSM technology for robust detection and notification. Despite its advantages, challenges such as susceptibility to GSM network outages and integration limitations with existing setups should be acknowledged. Additionally, a comparative analysis with solutions like the GSM-Enabled Home Automation and Security System: A Comprehensive Investigation and Implementation could offer valuable insights into its efficacy and suitability within the broader smart security landscape.

In their recent study, Ahmed Faraz Husain et al. [2] explored wireless sensor networks (WSNs) potential applications, particularly in security systems for businesses like banks, jewellery, and electronic stores. They propose a novel security system utilizing Zigbee technology to enhance security at these establishments. The system provides three levels of security: at the main door locker, upon entry, and when accessing the cash locker. It comprises Zigbee modules, a microcontroller, a voltage regulator, and sensors to detect abnormal activities, especially at night. Alerts are sent via Zigbee to a GSM module, which notifies the owner or designated recipient. The authors justify Zigbee's choice due to its reliability, low power consumption, simplicity, and flexibility. This system highlights wireless technologies' ability to replace complex wired systems, offering extensive coverage, reliability, remote control, real-time service, and user-friendliness. Comparing this system with the GSM-Enabled Home Automation and Security System: A Comprehensive Investigation and Implementation, drawbacks and limitations should be considered. For instance, Zigbee's potential drawbacks may include range limitations and interference from other devices. A comparative analysis could reveal whether Zigbee outperforms GSM in reliability, scalability, and integration. Moreover, differences in addressing security concerns, such as intrusion detection and emergency notifications, could be highlighted. Such analysis would aid stakeholders in making informed decisions regarding security system implementations.

Neha R. Ghate et al. [3] proposed a smart home security monitoring system. This system uses Radio Frequency (RF) technology to monitor the status and security of the electrical system, and it also contributes to energy conservation. The technology used in this research includes the Global System for Mobile Communications (GSM), Frequency Hopping Method, and PIC18F452 Microcontroller. The system employs a Time Password (OTP) concept to provide a reliable, efficient, and safe environment for occupants. The OTP serves as a communication tool between the hardware and the software. A Graphical User Interface (GUI) is developed and configured to facilitate the OTP service. The auto-generated OTP is sent to the homeowners, and if there is an attempt to breach security, the OTP session will expire. Frequency Hopping is defined as a communication scheme between a transmitter and a receiver, where the system changes the frequency during transmission at regular intervals. This allows the RF channel used for signaling channel (SDCCH) time slot or traffic channel (TCH) time slots, to change frequency every TDMA frame (4.615 ms). The frequency is changed on a per-burst basis, meaning all the bits in a burst are transmitted at the same frequency.

Vishaka D. Vaidya et al. [4] emphasize the growing significance of home automation and security systems in modern lifestyles, highlighting their capacity to streamline tasks and provide peace of mind. They commend wireless smart home systems for their versatility, portability, and cost-effectiveness, enabling remote appliance control and enhancing security measures. While automation primarily focuses on managing lights, fan speed, and other devices, security features include gas leakage detection and intrusion prevention, catering especially well to the needs of the elderly, handicapped, and busy individuals by providing real-time alerts through mobile technology. Although the study conducts a comparative analysis of smart home systems utilizing various technologies like GSM, Bluetooth, IoT, and PIC Microcontroller with ZigBee modulation, it does not explicitly address the drawbacks of the proposed system or compare it with existing literature. A comparison with "GSM-Enabled Home Automation and Security System: A Comprehensive Investigation and Implementation" could reveal differences in methodology, technology integration, and system performance, offering a comprehensive understanding of their strengths and weaknesses and aiding in selecting the most suitable approach for home automation and security needs.

Ebrahim Abidi et al. [5] presented a remote development of a voice-controlled home security system for smart home automation. This system uses an Arduino Mega, GSM SIM900A, Bluetooth module, and HC-SR04 ultrasonic sensor. A microcontroller is programmed to control up to four home appliances via Bluetooth technology and transmit the received signal from the sensor to the user's smart phone. The authors note that while there have been many commercial and research projects on smart homes, most of these products use remote controls with touch screen buttons. They propose a wireless remote control for home devices that can be voice-controlled, providing support for the elderly, disabled, and enhancing home security. The proposed system is designed to recognize human voice commands using a voice reader

CVR Journal of Science and Technology, Volume 26, June 2024
DOI: 10.32377/cvrjst2606

Android application to control home appliances. Another key feature of this project is the detection of movement using an ultrasonic sensor. The sensor signal is converted into a message and sent to the mobile user via a GSM module. The system, which has an accuracy rate of over 95%, allows users to control their electrical loads using voice commands. To operate the system, the Arduino Mega must be powered by a 12V DC adapter and all AC power loads must be connected to the electricity. The proposed prototype of the smart home automation system has been implemented and tested on hardware, enabling users to control a certain number of home appliances using voice.

Malti Bansal et al. [6] proposed a Smart IoT-based Integrated Home Security System. This all-in-one system uses various sensors and modules to monitor the user's property and always ensure its safety. The system operates 24x7, regardless of whether the user is at home or not. It is designed to detect fire breakouts, gas leakages, or intruders, and informs the user in real-time via SMS. In addition to these features, the system also includes a camera that records ongoing events. These recordings are not stored locally but are uploaded to the cloud to minimize system costs. The user can access, view, or download these recordings at any time. In summary, the author has proposed and designed a 24x7 smart IoT-based integrated home security system that ensures safety and offers real-time updates.

Ahmed et al. [7] discussed the importance of energy conservation and proposed a system to prevent energy wastage. This system uses Raspberry Pi 3 and the WeMOS D1 mini as the main devices, supported by various microcontrollers like PIR sensors and gas sensors. The system works by ensuring the presence of humans before supplying power. If the PIR sensor does not detect a human for a certain period, the Raspberry Pi controls the relay module to disconnect the power, turning off lights and fans that may have been left on unintentionally. Conversely, when the PIR sensor detects the presence of a human or animal in a room, it turns on the power (e.g., lights, fans) through the relay module and informs the user about the presence. Additionally, if a gas sensor detects a gas leakage, it alerts the WeMOS, which then sends a signal to the Raspberry Pi. The Raspberry Pi immediately informs the user through the GMS module. This system allows users to prevent unauthorized access to their homes and protect their homes from potential accidents, contributing to a safer and more energy-efficient living environment.

Hakar Mosin et al. [8] came up with the significant evolution of network technologies in home environments. This evolution has enabled the use of digital technologies as home appliances, which can be remotely accessed and controlled using existing network infrastructure, leading to a direct integration of computing systems with the physical world. A key part of this network evolution is the Internet of Things (IoT), which expands the services provided by the internet. IoT can be applied in various fields, with home automation being one of its applications. This approach increases the connectivity between devices within and outside the home, enabling the automation of home appliances. The paper presents the design and implementation of a secure and automated house using a hybrid communication system, which includes IoT and mobile communication methods. The system uses an Arduino Microcontroller, GSM Shield, Ethernet Shield, and a variety of sensors. With the advancement of IoT, there is an increasing demand for real-time security. The proposed system secures the house via electronic devices and sensors, protecting it from various intrusions such as motion within the house and disasters like fire and gas leakage. The paper focuses on designing a robust and reliable home automation system to address these issues and alert the homeowner via a message when suspicious activities occur. The results contribute to the field of IoT by providing an efficient and reliable solution that considers various aspects, including fast processing, system cost, robustness, and precision, catering to modern technological needs.

Soniya Devar et al. [9] put forward the rapid expansion of smart home automation in the current era of robotics. This automation plays a crucial role in safety systems. A multitude of sensors are integrated into an Automated Smart Home system to manage and operate various functions such as flame detection and water level tracking, using technologies like Bluetooth and ZigBee. The existing system can be expanded to monitor a child returning from school and to enhance security systems. The author proposes a design for the smart home system that is particularly effective for individuals with mobility issues, enabling them to control every system with minimal effort. This proposed system aims to monitor children, control home lighting, regulate windows, and manage terrace gardening using the power of the Internet of Things.

A project by Chetana Nayyar, [10] aims to develop an efficient, low-cost automated energy management system for homes, which also includes a surveillance feature. The system was designed after evaluating the utility features of existing surveillance and energy management systems, with the goal of enhancing these features. The system provides a cost-effective solution for household energy management and includes features to respond to natural disasters like fires. The system is built on an Arduino UNO microcontroller board and uses embedded C as the programming language, facilitating easier coding for new features. This project represents an attempt to improve home automation and security while keeping costs low.

III. Implementation

The Home Automation and Security System using GSM is meticulously crafted, with each component serving a crucial function in creating a versatile and secure smart home solution.

The power supply section, comprising a transformer and LM7805 IC, ensures a stable +5V power source essential for all components' proper functioning. These components were carefully chosen to guarantee reliable power distribution, thereby mitigating potential damage from voltage fluctuations, and enhancing the system's longevity.

At the heart of the system, the microcontroller acts as the central processing unit, orchestrating operations, processing inputs, and controlling output devices. Its selection was deliberate, choosing a microcontroller with ample processing power, memory, and I/O peripherals to meet the system's

CVR Journal of Science and Technology, Volume 26, June 2024
DOI: 10.32377/cvrjst2606

diverse functionalities. This choice directly impacts system performance, responsiveness, and overall intelligence.

Facilitating communication with mobile networks, the GSM modem enables remote monitoring and control of the system. Chosen for compatibility and ease of integration, the GSM modem enhances system connectivity and accessibility. Integration of the GSM modem enables timely alerts and remote control via SMS or phone calls, enhancing system functionality and user convenience.

The driver circuit serves as an interface between the microcontroller and output components, regulating current flow for devices like lights and fans. Carefully selected for efficient current regulation and compatibility, the driver circuit ensures precise control of output devices. This optimization of power distribution enables seamless automation and reliable operation of output devices, enhancing system versatility and efficiency.

The LCD provides a user-friendly interface, displaying relevant information and feedback. Selected for versatility, low power consumption, and ease of integration, the LCD enhances user interaction and system accessibility. Its integration improves the user experience by providing real-time updates and status indicators, contributing to overall user satisfaction and system usability.

Sensors deliver real-time data on environmental conditions and security threats, enabling prompt system responses. These sensors are chosen based on sensitivity, accuracy, and suitability for detecting specific threats or events. Their integration enhances system intelligence and responsiveness, enabling proactive detection and mitigation of security risks and environmental hazards.

In addition to component selection, the system's intelligence lies in its code implementation using software like KIEL, enabling efficient device control via SMS commands sent through the GSM module. Thorough testing and debugging ensure robust functionality, supported by comprehensive documentation for ease of operation and troubleshooting. Continuous monitoring post-deployment allows for updates and improvements, ensuring the system remains reliable and effective in providing a secure and smart living environment.

A.Block Diagram

Power Supply: The power supply section is responsible for providing a stable +5V for the components to operate. The IC LM7805 is utilized to ensure a constant power output of +5V. The AC voltage, typically 220V, is connected to a transformer, which steps down the AC voltage to the desired DC output level.

Microcontroller: A microcontroller is a compact integrated circuit designed to control specific operations within an embedded system. It typically includes a processor, memory, and input/output (I/O) peripherals on a single chip.

GSM Modem: A GSM modem is a specialized type of modem that accepts a SIM card and operates based on a subscription to a mobile operator, similar to a mobile phone. From the mobile operator's perspective, a GSM modem appears just like a mobile phone.

Driver Circuit: A driver IC is a circuit or component used to regulate current flow and control another circuit or component. Acting as an interface between a microprocessor or microcontroller and the output component, the driver IC receives image data and delivers precise analog voltages to activate pixels on a display.

LCD: A liquid-crystal display (LCD) is a flat-panel display or electronically modulated optical device that utilizes the light-modulating properties of liquid crystals combined with polarizers. Liquid crystals themselves do not emit light; instead, a backlight or reflector is used to produce images in color or monochrome.

Light: An electric light, lamp, or light bulb is an electrical component that generates light. It represents the most common form of artificial lighting.

Fan: A fan is a powered machine designed to create airflow. It consists of a rotating arrangement of vanes or blades, typically made of wood, plastic, or metal, which act on the air. The rotating assembly of blades and hub is known as an impeller, rotor, or runner.

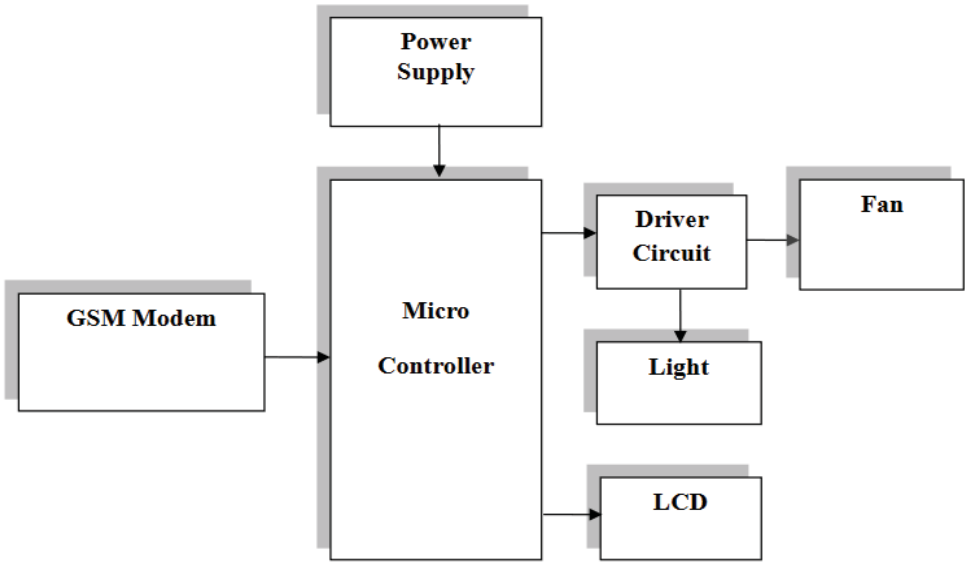

Fig. 1. Block diagram of GSM based home automation.

E-ISSN 2581 – 7957
P-ISSN 2277 – 3916
CVR Journal of Science and Technology, Volume 26, June 2024
DOI: 10.32377/cvrjst2606

B. Schematic Diagram

In Fig 2 is a schematic diagram for a Home Automation and Security System using GSM, diverse components and their connections are intricately laid out, offering a holistic view of the system architecture. At its core, the diagram would feature a power supply section incorporating a transformer and LM7805 IC, illustrating their connections to provide a stable +5V power source. The microcontroller, serving as the brain of the system, would be prominently displayed with detailed connections showcasing its role in managing system operations, including processor functions, memory utilization, and interactions with various I/O peripherals. Integrated into the system is the GSM modem, visually represented with connections that highlight its communication capabilities with mobile networks through a SIM card. A crucial aspect of the schematic would be the driver circuit setup, portrayed to showcase its function as an intermediary between the microcontroller and different output components. This circuit regulates current flow, controlling devices such as lights and fans. Additionally, the schematic would include an illustration of the LCD connections, demonstrating their integration with the microcontroller for displaying pertinent information in a user-friendly format. The inclusion of sensors, such as motion detectors and gas sensors, would be visually represented, indicating their connections to the microcontroller for real-time data acquisition. The diagram would further elucidate the implementation of code for device control via SMS commands through the GSM module, possibly using a flowchart to represent the logical sequence.

Security logic implementation is another critical aspect, with the schematic featuring connections and pathways that depict the system's response to security breaches, fire incidents, or gas leakages. The optional integration for Android mobile control might be presented with connections to both the microcontroller and GSM module.

The testing and debugging phase would be outlined in the schematic, showcasing a flowchart or series of steps to ensure the system's robust functionality. Sections for comprehensive documentation, including circuit diagrams and code snippets, would be visually indicated along with a user manual section for operational guidance and troubleshooting. Lastly, the continuous monitoring and updates segment will be depicted, illustrating the ongoing phase for system evaluation and potential enhancements post-deployment, ensuring the longevity and efficiency of the Home Automation and Security System using GSM.

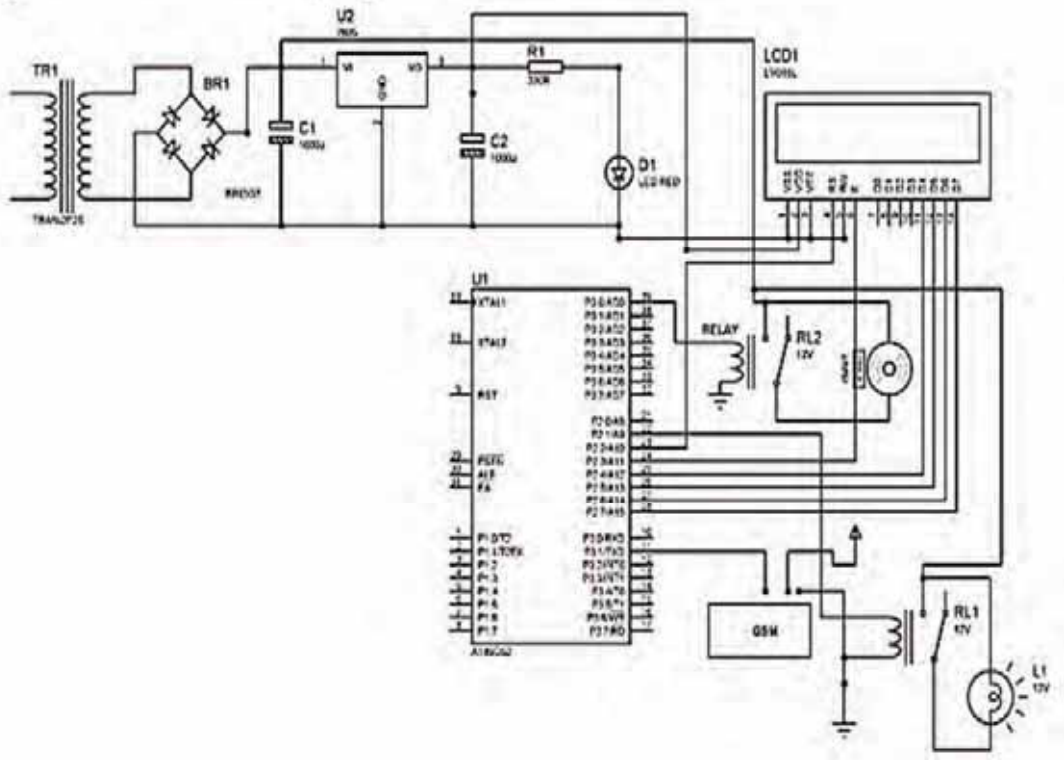

Fig 2. Schematic Diagram of GSM based home automation.

IV. RESULTS

The project's operational framework is delineated into three distinct facets: home automation, home safety, and the security system. The mechanism is initiated by employing a basic GSM-based phone to transmit SMS commands to the integrated GSM modem within our project setup.

Upon receiving the SMS, the microcontroller undertakes the task of extracting the message contents, deciphering the instructions embedded within. This decoded information is

CVR Journal of Science and Technology, Volume 26, June 2024
DOI: 10.32377/cvrjst2606

then employed to control the relay module, allowing for the activation or deactivation of appliances as per the owner's directives.

In the domain of home safety, the project integrates sophisticated sensors, including a smoke detector and an LPG gas detector. These sensors play a pivotal role in identifying the presence of gas or smoke. Once a potential hazard is detected, the sensors promptly communicate this feedback to the microcontroller.

Subsequently, the microcontroller orchestrates a multi-faceted response, including the dispatch of an SMS alert to the homeowner and the activation of an audible alarm. The results of this project demonstrate a seamless integration of home automation features, allowing for the remote control of appliances through simple SMS commands. Simultaneously, the home

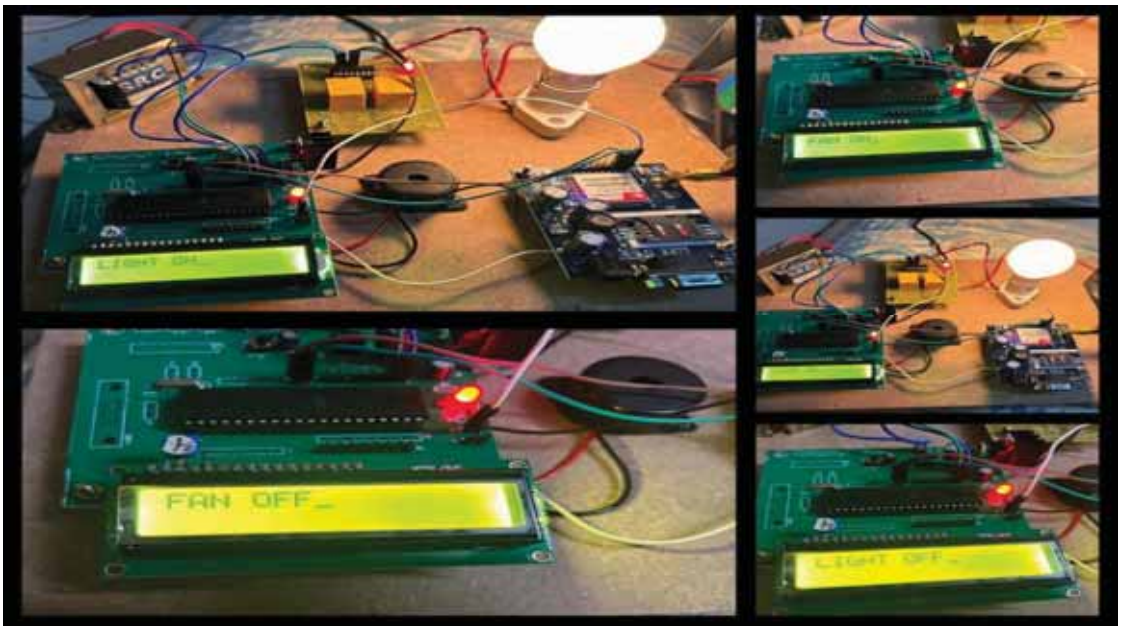

Fig 3. Hardware Setup of the system

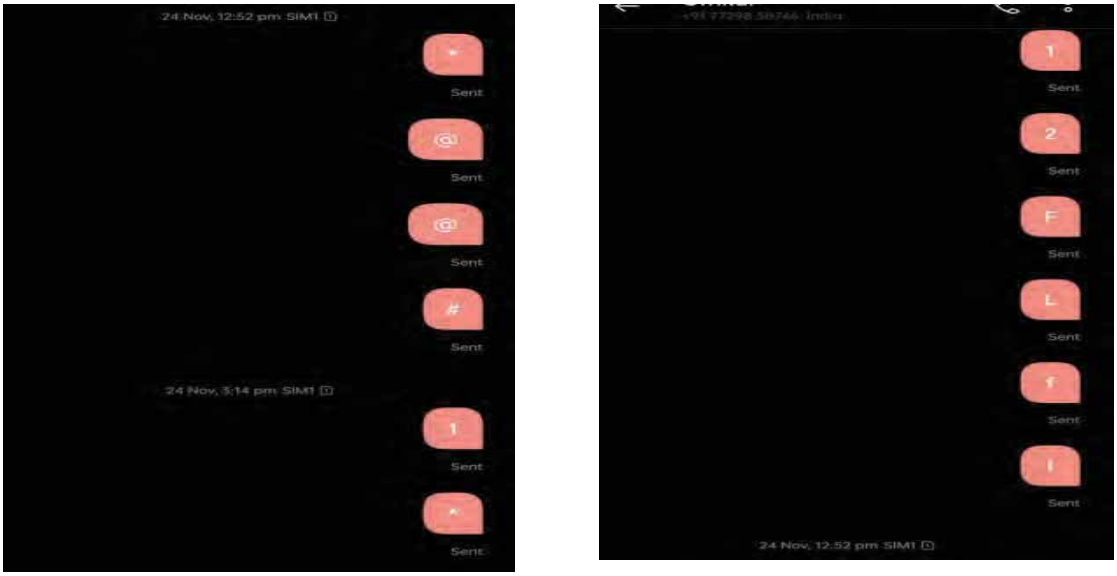

Fig.4. Android phone data

CVR Journal of Science and Technology, Volume 26, June 2024
DOI: 10.32377/cvrjst2606

V. Conclusions

This paper explores our cost-effective GSM-based home automation, safety, and security system, presenting a user-friendly solution that proves both practical and economical. The system offers a straightforward means of managing household appliances, enabling control through a simple SMS or an Android application. Notably, the versatility of The researcher's approach allows users to control devices with ease, whether through the safety-enhanced Android application or by sending a conventional SMS to the GSM modem in the absence of a smartphone. An overarching advantage of our system lies in its accessibility and ease of installation for safety and security features. The system can promptly alert the homeowner about potential fire hazards, gas leakages, or unauthorized access, providing peace of mind even when the owner is away from home. This dual functionality, blending convenience with enhanced safety measures, positions our GSM-based home automation and security system as a practical and inclusive solution for modern households.

References

[1] Safial Islam Ayon and Abu Saleh bin Shahadat, 2019 International Conference on Robotics, Automation, Artificial-intelligence, and Internet-of-Things (RAAICON), "Smart Security Box using Arduino and GSM Module", 29 November-1 December 2019, Dhaka, Bangladesh.

[2] Ahmad Faraz Hussain, Faheem Ajaz, Noman Ahmed, Hima Stephen, Yunfeng Li, A B M Mazharul Mujib, Jehangir Arshad and Polash K. Das, 20121 International Conference on Advance Computing and Innovative Technologies in Engineering (ICACITE), "Zigbee and GSM Based Security System for Business Places", 2021.

[3] Neha R. Ghate and K.V. Kale, IEEE International Journal of Computer Science, and Information Technology, "Smart Home Safety device using frequency hopping approach based on GSM generation", 2020.

[4] Vishaka D. Vaidya and Pinki Vishwakarma, Department of Computer Engineering, "A Comparative Analysis on Smart Home System to Control, Monitor and Secure Home, based on technologies like GSM, IoT, Bluetooth and PIC Microcontroller with Zigbee Modulation", 2021.

[5] M. Ebrahim Abidi, Ani Liza Asnawi, N.FM. Azmin, A.Z. Jusoh, S. Noorjannah Ibrahim, Huda Adibah Mohd Ramli and Norun Abdul Malek, 2018 7th International Computer and Communication Engineering (ICCCE), "Development of Voice Control and Home Security for Smart Home Automation", 2018..

[6] Malti Bansal, Navodit Adarsh, Nitin Kumar and Monika Meena, Proceedings of the Fourth International Conference on Inventive Systems and Control (ICISC 2020), "24*7 Smart IoT based Integrated Home Security System", 2020.

[7] Ahmed Imteaj, Tanveer Rahman, Hosna Ara Begum and Mohammed Shamsul Alam, Proceedings of the 2017 4th International Conference of an Advances in Electrical Engineering (ICAEE) 28-30 September, Dhaka, Bangladesh, "IoT based Energy Economic Home Automation System using Raspberry Pi 3", September 2017.

[8] Hakar Mosin Saber and Nawzad Kamaran Al-Salihi, Department of Computer Engineering, "IoT: Secured and Automated House", 2018.

[9] Soniya Devar, Rohit Gaikwad, A.B. Gavali, Vaibhavkumar Yadav and Shubham Borate, 2017 2nd International Conference for Convergence in Technology (I2CT), "Smart Home Automation using Virtue of IoT", 2017.

[10] Chetana Nayyar, B. Valarmathi and K. Santhi, International Conference on Communication and Signal Processing, April 6-8, 2017, "Home Security and Energy Efficient Home Automation System using Arduino", April 2017.

[11] Prabhakar Gantella, M. Javed Idrisi, Abdulhafiz Ahmed Mustofa and Yohannes Alemayehu Dagnew, Journal of Computer Networks and Communications, Volume 2023, Article ID 8571506, 12 pages, "SECHA: A Smart Energy-Efficient and Cost-Effective Home Automation System for Developing Countries", 2023.

[12] Aderonke Ikuomola, Department of Mathematical Sciences, "A Secured GSM-Based Remote Controlled Home Automation System", April 2020.

[13] Azwan Aziz, Maslan Zainon, Jamil Alsayayedh and Sy Najib Sy Salim, Article in ARPN Journal of Engineering and Applied Sciences, January 2021, "Development of Programmable Home Security using GSM System for Early Detection", January 2021.

[14] E. Isa, N. Sklavos, Journal of Engineering Science and Technology Review, 15 January 2016, "Smart Home Automation: GSM Security System Design and Implementation", January 2016.

[15] Nikolas Sklavos, Eleni Isa, Computer Engineering and Infornatics Department, "Smart Home Automation GSM Security System Design and Implementation, 2019.

E-ISSN 2581 – 7957
P-ISSN 2277 – 3916

CVR Journal of Science and Technology, Volume 26, June 2024
DOI: 10.32377/cvrjst2607

Enhanced Safety Measures for Accident Prevention in Mountainous Regions

V. Shekar Reddy
Asst Professor, JBIT College of Engineering/ ECE Department, Hyderabad, India
Email: vsreddyinfo14@gmail.com

Abstract: **In mountainous terrains, road safety is a paramount concern exacerbated by challenging conditions such as sharp turns and obscured visibility due to deep excavations. Forward Collision Warning (FCW) systems, employing ultrasonic sensors, serve as critical tools in identifying potential hazards, including vehicles, and issuing timely alerts to drivers. This paper introduces a controller-based approach integrating Arduino Nano and Atmega328 microcontrollers, with a specific emphasis on ultrasonic sensors, to address accident mitigation on mountainous roadways. Developing nations confront substantial road safety hurdles, with accidents emerging as a primary cause of fatalities. Embracing road design methodologies observed in developed nations like the Netherlands and Denmark holds promise for enhancing safety standards. Notably, buses and trucks are disproportionately vulnerable to accidents owing to deficient safety protocols, leading to significant loss of life. Deploying daytime lighting, high-mounted stop lamps, reflectors, and vivid attire has proven effective in mitigating accidents attributable to poor visibility. The proposed solution advocates for the strategic placement of ultrasonic sensors and LED lights ahead of and following sharp curves, respectively. Upon vehicle detection, the sensor activates the LED light, alerting oncoming traffic and empowering drivers to adjust their speed accordingly. This proactive strategy aims to curtail accidents and elevate road safety levels across mountainous regions.**

Index Terms**: Forward Collision Warning (FCW), Mountainous terrains, high-mounted stop lamps, LED lights.**

I. Introduction

India's staggering prevalence as the global epicenter of road accidents underscores the urgent necessity for robust preventive strategies. Primary contributors to these incidents include excessive speeds and insufficient awareness of nearby vehicles, particularly in hazardous hairpin bends. With an annual toll of 137,000 lives lost to road mishaps in India, averaging a harrowing 377 fatalities per day, the gravity of the situation cannot be overstated.

Conventional safety measures, such as horn alerts, often fall short, especially during adverse weather conditions or when drivers disregard auditory warnings. Therefore, innovative solutions are imperative to address these multifaceted challenges comprehensively.

In tackling the inherent risks of mountainous and curved terrains, sensor-based accident prevention systems present as promising interventions. By strategically deploying ultrasonic sensors on both sides of curves, complemented by LED lights post-curve, potential hazards can be swiftly identified and communicated to drivers.

Operating as obstacle detectors, ultrasonic sensors emit pulses that interact with passing vehicles. Upon detection, the sensor triggers the illumination of an LED light opposite to the curve, effectively notifying drivers about the approaching traffic. Conversely, in the absence of vehicles, the sensor remains inactive, and the light remains unlit. This instantaneous visual feedback empowers drivers to make informed decisions, potentially averting accidents or mitigating their severity.

The adoption of sensor-based light systems holds efficacy in scenarios where driver visibility is compromised, thereby bolstering safety along mountainous and curved roadways. The implementation of this innovative approach harbors significant promise in saving lives by proactively preventing accidents and nurturing a culture of safer driving practices.

A. Objective

In developing countries, road accidents are a leading cause of fatalities, particularly in regions characterized by mountainous terrain and curved roadways. The challenging topography often presents tight curves and narrow roads, obstructing visibility and increasing the risk of accidents. In such scenarios, drivers may struggle to perceive vehicles approaching from the opposite direction.

To address this critical safety concern, our objective is to develop a proactive solution that alerts drivers to oncoming vehicles on curved roads. We propose the installation of ultrasonic sensors on one side of the road before the curve, coupled with LED lights positioned after the curve. When a vehicle approaches from one side of the curve, the ultrasonic sensor detects its presence and triggers the illumination of the LED light on the opposite side. This visual cue serves as an alert to drivers, prompting them to adjust their speed accordingly.

We aim to evaluate the effectiveness of this sensor-based warning system in enhancing road safety and reducing the incidence of accidents in mountainous and curved road environments. By providing timely and clear visual indications of potential hazards, we anticipate that this solution will empower drivers to make informed decisions, ultimately mitigating the risk of collisions and saving lives.

B. Motivation

The mountainous regions pose unique challenges for road safety, characterized by winding roads, steep gradients, and limited visibility. In these environments, the risk of accidents is heightened, leading to tragic consequences

Received on 12-03-2024, Revised on 11-04-2024, Accepted on 11-05-2024.

CVR Journal of Science and Technology, Volume 26, June 2024
DOI: 10.32377/cvrjst2607

including loss of life and property damage. Despite efforts to improve road infrastructure and safety regulations, accidents continue to occur with alarming frequency.

Our motivation stems from the urgent need to address this pressing issue and implement enhanced safety measures tailored specifically for mountainous regions. By developing innovative solutions and leveraging advancements in technology, we aim to mitigate the risks associated with driving in these challenging terrains.

The title "Enhanced Safety Measures for Accident Prevention in Mountainous Regions" encapsulates our commitment to implementing proactive strategies aimed at preventing accidents and safeguarding the lives of road users. Through this research, we seek to contribute to a safer transportation environment in mountainous areas, ultimately reducing the incidence of accidents and minimizing their impact on communities.

II. Literature Review

Amar Shitole et al. [1] discussed that in developing countries, mountainous terrain poses significant road safety challenges due to tight curves and narrow roads, leading to reduced visibility and increased collision risks. Traditional measures like daytime lights and reflectors have limited effectiveness, especially on such roads. A new solution suggests using ultrasonic sensors and LED lights. Placing sensors before curves and LEDs after, the system detects approaching vehicles and illuminates lights, alerting drivers to slow down. This innovative approach shows promise in improving visibility and reducing accidents. Overall, addressing road safety in developing countries requires tailored solutions. While the proposed sensor-LED system holds potential, further research and testing are necessary to validate its effectiveness in real-world conditions.

Dwaipayan Saha et al. [2] the escalating occurrence of road accidents has become a critical issue, demanding the establishment of robust accident prevention measures. This study focuses on the design and implementation of a smart road safety and prevention system aimed at mitigating road accidents. At the core of this system lies the integration of sensors with Arduino technology, enabling the incorporation of IR sensors, buzzers, and RGB LED lights for signaling purposes. Additionally, the system incorporates a vehicle counter to monitor traffic flow efficiently. The primary objective of this research is to develop a proactive safety solution specifically tailored to address the challenges posed by curved and narrow roads, to reduce accident rates.

Anand M. G. et al [3] highlight in their study that in developing countries, accidents pose a significant threat to life, especially on curved roads like U-turns, hairpin bends, and narrow mountainous paths where visibility is severely restricted. The paper emphasizes the alarming number of fatalities caused annually due to drivers' inability to perceive approaching vehicles from the opposite direction. To tackle this challenge, the authors propose a technological solution aimed at alerting drivers about oncoming vehicles. Their approach involves the strategic placement of ultrasonic sensors on one side of the road before a curve and LED lights on the opposite side. These sensors detect vehicles approaching the curve, triggering the illumination of LED lights to notify drivers. The primary objective of this research is to mitigate accidents on curved roads by implementing a system that effectively communicates with drivers through LED lights, activated by ultrasonic sensors integrated with Arduino UNO microcontrollers. Such innovative measures hold the potential to significantly reduce fatalities on hazardous curved roads.

Rohit Pautare et al. [4] shed light on the challenges faced by residents in hilly regions, exacerbated by increasing traffic congestion and frequent disruptions like landslides and floods. These regions are particularly vulnerable to such calamities, resulting in substantial loss of life and property. Moreover, as popular tourist destinations, these areas witness a surge in visitors during peak seasons, further complicating matters as tourists are often unfamiliar with the treacherous terrain, including sharp turns and bridge breaks, increasing the risk of accidents. Any natural disaster occurring during peak tourist periods amplifies the potential for tragedy. To address these issues, significant research is being conducted, with Wireless Sensor Network and Internet of Things emerging as promising solutions. This paper explores various techniques aimed at tracking and mitigating these hazardous incidents, ultimately aiming to minimize loss and prevent catastrophic outcomes.

In their study, Ichita Mhatre et al. [5] emphasize the importance of implementing a vehicle accident prevention system to enhance safety on mountain roads. They highlight the alarming frequency of accidents and fatalities on these roads, including incidents where vehicles fall off cliffs and are unable to be located thereafter. Such accidents not only result in human casualties but also impose significant financial burdens on individuals and governments alike. Moreover, the narrowness of mountain roads exacerbates the impact of accidents, often leading to prolonged road closures. To address these challenges, the authors propose a model that utilizes sensors to detect oncoming traffic from both directions and alert drivers accordingly. This system, equipped with LED indicators, aims to significantly reduce accidents, and serve as a crucial advancement in vehicle safety on mountain roads. By implementing this system, which provides warnings to drivers in blind spots, it has the potential to greatly enhance safety measures and mitigate the risks associated with mountainous terrain.

Ranga Sreedhar et al. [6] focus on reducing accidents on hilly and slippery roads, particularly addressing the challenges posed by curved roads where drivers may not have visibility of vehicles approaching from the other end. They highlight the increased risk of accidents, especially at night, due to the intensity of headlights from oncoming vehicles. This issue is exacerbated on both curved and mountainous roads, resulting in numerous fatalities. To mitigate these risks, the authors propose a solution involving the placement of an ultrasonic sensor on one side of the road before a curve, coupled with an LED light positioned after the curve. When a vehicle approaches the curve, the sensor detects its presence, triggering the illumination of the LED light on the opposite side, thereby alerting drivers to oncoming traffic. This proactive approach has the potential to significantly enhance road safety and prevent accidents on challenging terrains.

CVR Journal of Science and Technology, Volume 26, June 2024
DOI: 10.32377/cvrjst2607

In their research, Najbin Momin et al. [7] aim to develop a system that effectively prevents accidents by providing indications through lamps or buzzers. The frequency of accidents has surged in recent times due to factors such as globalization, lack of attention, drowsiness, and excessive vehicle speed. Particularly on curved roads, vehicles on one side are unable to anticipate approaching vehicles from the other side, leading to potential collisions. To address this issue, the authors have devised a straightforward system employing microcontrollers and ultrasonic sensors. This system offers alerts about oncoming vehicles from the opposite side using lamps installed on both sides of the road. By strategically placing ultrasonic sensors on both sides of the road, with four sensors in total (two on each side), the system effectively detects approaching vehicles. When vehicles are detected on one side, the corresponding lamp or buzzer on the opposite side is activated. For instance, if vehicles are approaching from the left side, the left-side sensors (1L and 2L) are triggered, signalling the controller to activate the lamp or buzzer on the right side. This visual or auditory alert prompts vehicle occupants to be cautious, thereby averting potential accidents.

In their study, Swapnil V. Vanmore et al. [8] address the rising incidence of accidents involving commercial vehicles on highways, primarily attributed to driver unconsciousness and confusion, accounting for 80% of cases. The authors propose a cost-effective solution to this pressing issue, recognizing that traditional intelligent security systems may be financially out of reach for many consumer-class commercial vehicle owners. Their solution involves the implementation of a stationary radar system based on ultrasonic sensors, which provides both accident prevention and detection capabilities. Central to this system are ultrasonic sensors and accelerometers, which play pivotal roles in accident prevention and accurately locating stationary objects, if necessary. The primary objective of their research is to develop a real-time security system capable of detecting stationary objects within a 180-degree front phase while considering the dimensions of the wheel track. This innovative approach holds promise in enhancing safety measures for commercial vehicles on highways, offering an affordable yet effective means of accident prevention and detection.

III. Implementation

The implementation of the enhanced safety measures system for accident prevention in mountainous regions involves the integration of critical hardware and software components to create a comprehensive safety infrastructure. Anchored by two central microcontrollers, the Arduino UNO and Arduino Nano, the system orchestrates communication and coordination among various components.

Key hardware components include Ultrasonic Sensors for vehicle/object detection, sets of LED lights for visual indication, an RF Module for wireless communication, a DC Motor for vehicle ignition control, and buzzers for auditory alerts. These components are strategically deployed both within the vehicle and along curved regions of hilly terrains, each part with its respective block diagram.

The software aspect involves programming the Arduino microcontrollers using the Arduino IDE and leveraging code libraries for interfacing with sensors, LED lights, RF modules, and other components. Through meticulous testing, calibration, and integration, the system is fine-tuned to ensure seamless functionality and performance.

Field testing in real-world mountainous environments validates the system's effectiveness under diverse conditions, with data and feedback informing continuous improvement efforts. Detailed documentation of the implementation process facilitates future maintenance and troubleshooting, ensuring the sustained functionality of the safety system.

The implementation of the enhanced safety measures system aims to proactively prevent accidents and enhance safety in mountainous regions, ultimately saving lives and reducing the incidence of accidents.

A. Block Diagram

Fig 1 of the transmitter component of the system is responsible for detecting vehicles approaching the curve in hilly areas and relaying this information to the central control unit. It comprises two Ultrasonic Sensors positioned strategically to calculate the distance between the sensors and the vehicles on either side of the curve. These sensors continuously monitor the surrounding environment and provide real-time data to the ATmega328 microcontroller.

Upon receiving data from the Ultrasonic Sensors, the ATmega328 microcontroller processes this information and determines the appropriate response based on the calculated distances. Depending on the proximity of vehicles to the curve, the microcontroller generates signals to control the LED lights, which include indicators such as red, green, and yellow lights. These LED lights serve as visual cues to alert drivers of potential hazards and help regulate traffic flow.

In scenarios where the distance between two vehicles is critically close, indicating an imminent collision risk, the ATmega328 microcontroller activates the RF transmitter. This transmitter sends out a signal to alert the receiving vehicle's system, triggering necessary precautions to prevent accidents.

The ranges of transmitter and receiver are 433MHz radio frequency (RF) modules and are widely used in different wireless projects and products. The normal range of most RF transmitter and receiver modules is below fifty meters and up to 100 meters in standard conditions (open place). When the vehicles are very close to the curve from either sides which is measured by sensor, signals should be sent from the transmitter (present outside the vehicles, setup will be present on the curve) to the receiver(present in the vehicles) so that vehicles' motors will be turned off or slowed down by which sudden crashes can be prevented. The transmission part setup is present on the sharp curve, which is properly shielded. It also has sensors on each side of the curve connected to the transmitter part. DC power supply is used which is of 5V to 12V range. In the project prototype batteries are used. According to real life implementation, having components that require high power supply batteries with high capacity can be used.

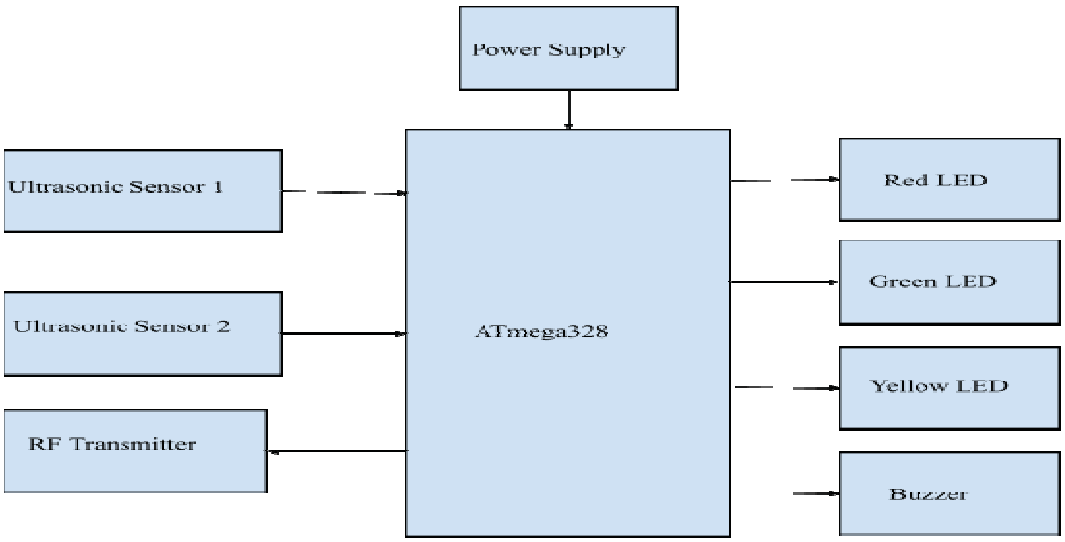

Fig. 1. Block diagram of Transmitter section.

Fig 2. Description of the receiver component of the system acts as the vehicle's interface, responding to signals transmitted by the transmitter unit. It consists of an RF receiver designed to capture signals sent by the RF transmitter from nearby vehicles. Upon receiving a signal, the RF receiver forwards the data to the ESP32 dual-core microcontroller.

The ESP32 microcontroller processes the incoming signal and initiates appropriate actions based on the transmitted data. Upon detecting a signal indicating a vehicle's proximity to the curve, the ESP32 microcontroller activates a relay mechanism connected to the vehicle's ignition system. This relay, in turn, triggers the vehicle's motor, allowing for automatic ignition or shutdown as needed.

By integrating these transmitter and receiver components into the system architecture, the safety system can effectively detect and respond to potential hazards on mountainous roads. The collaborative operation of these components ensures timely alerts and interventions, ultimately enhancing road safety and preventing accidents in challenging terrain.

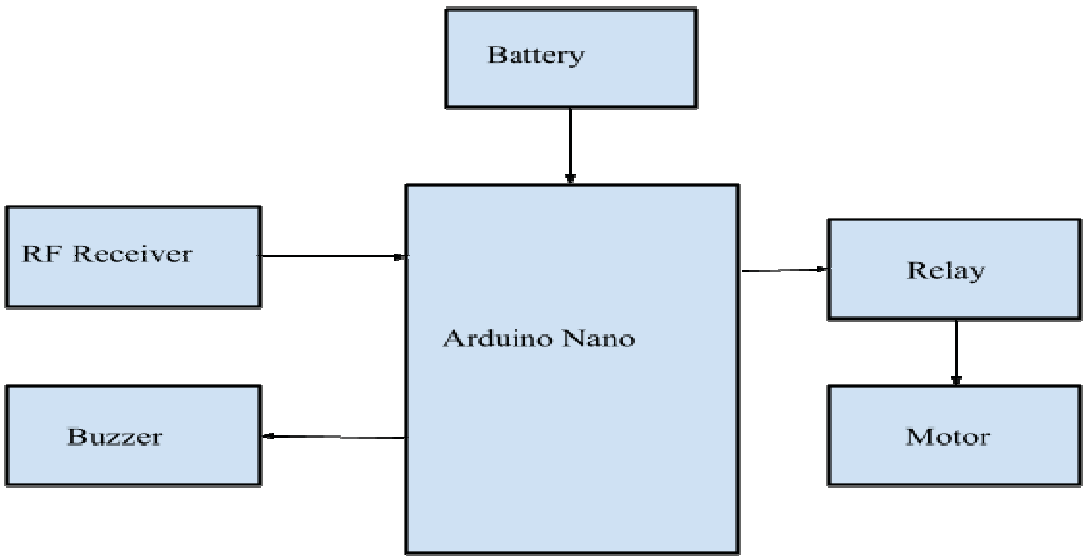

Fig. 2. Block diagram of Receiver section.

B. Schematic Diagram

Fig 3,4 is the schematic diagram for Enhanced Safety Measures for Accident Prevention in Mountainous Regions,

The hardware setup for the enhanced safety measures system involves meticulous wiring and connections to

ensure proper functionality. Firstly, the Ultrasonic Sensors are integrated into the system, with their VCC and GND pins connected to the 5V and GND pins, respectively. Additionally, the trig and echo pins of the sensors are linked to the Arduino UNO for data transmission and reception. Next, the buzzer's positive terminal is connected to the Arduino, while the negative terminal is grounded to complete the circuit. Moving on to the LEDs, their positive pins are interfaced with the Arduino to receive control signals, while the negative pins are connected to the ground for proper grounding. The RF transmitter is then integrated, with its GND and TE pins connected to the ground, and the VCC pin receiving power from the 5V source. Finally, the D0 pin of the RF transmitter is linked to the Arduino for data transmission. To ensure a stable power supply, an adapter is connected to the voltage regulator, which distributes a constant 5V supply to all components, ensuring consistent and reliable operation of the system. To ensure proper functionality and connectivity, the RF Receiver component is configured with attention to detail. Its GND and VCC pins are appropriately connected to the ground and 5V power source, respectively, ensuring stable power distribution. The RF Receiver's D0 pin, responsible for data transmission, is carefully linked to the A0 pin of the Arduino Nano, facilitating seamless communication between the receiver and the microcontroller.

In addition, the system incorporates a Buzzer for auditory alerts, with its positive terminal connected to the Nano for activation and the negative terminal grounded for proper operation. The relay, essential for controlling motor ignition, is meticulously integrated into the setup. Its VCC pin receives power from the Nano's ICSP pin, while the GND pin is connected to the ground for circuit completion. The relay's IN pin, responsible for triggering motor activation, is appropriately linked to D2 of the Nano, enabling precise control over the ignition mechanism.

Furthermore, the motor, vital for vehicle ignition, is effectively incorporated into the system. Its negative pin is securely grounded, ensuring proper electrical flow and functionality. Finally, to provide a reliable power supply to all components, a battery is connected to a voltage regulator, ensuring consistent and uninterrupted operation of the entire system.

Through meticulous configuration and integration, each component of the RF Receiver setup contributes to the overall functionality and effectiveness of the enhanced safety measures system, enhancing accident prevention and ensuring safety in mountainous regions.

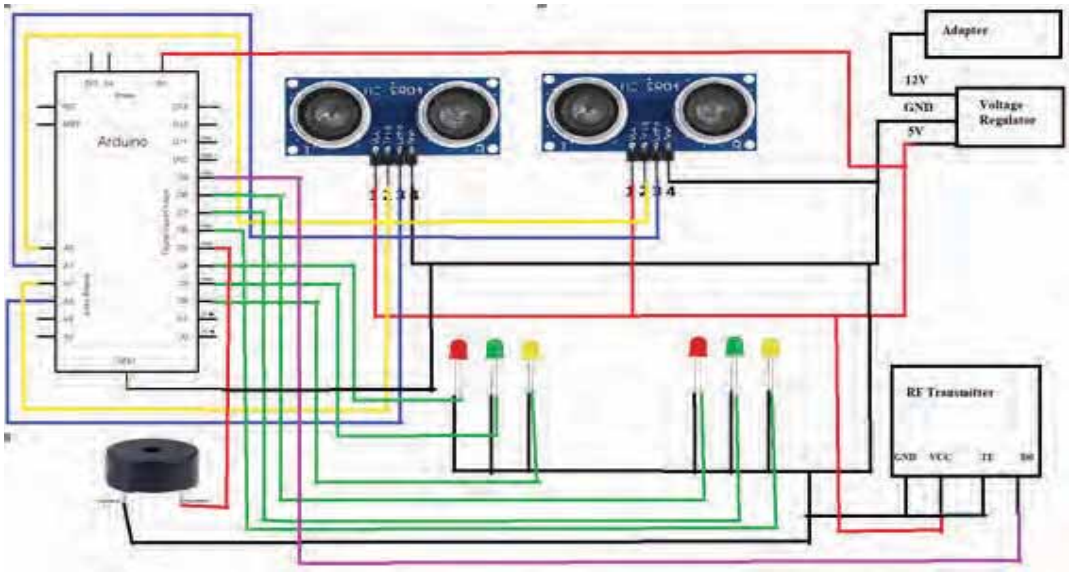

Fig 3. Schematic Diagram of Transmitter section.

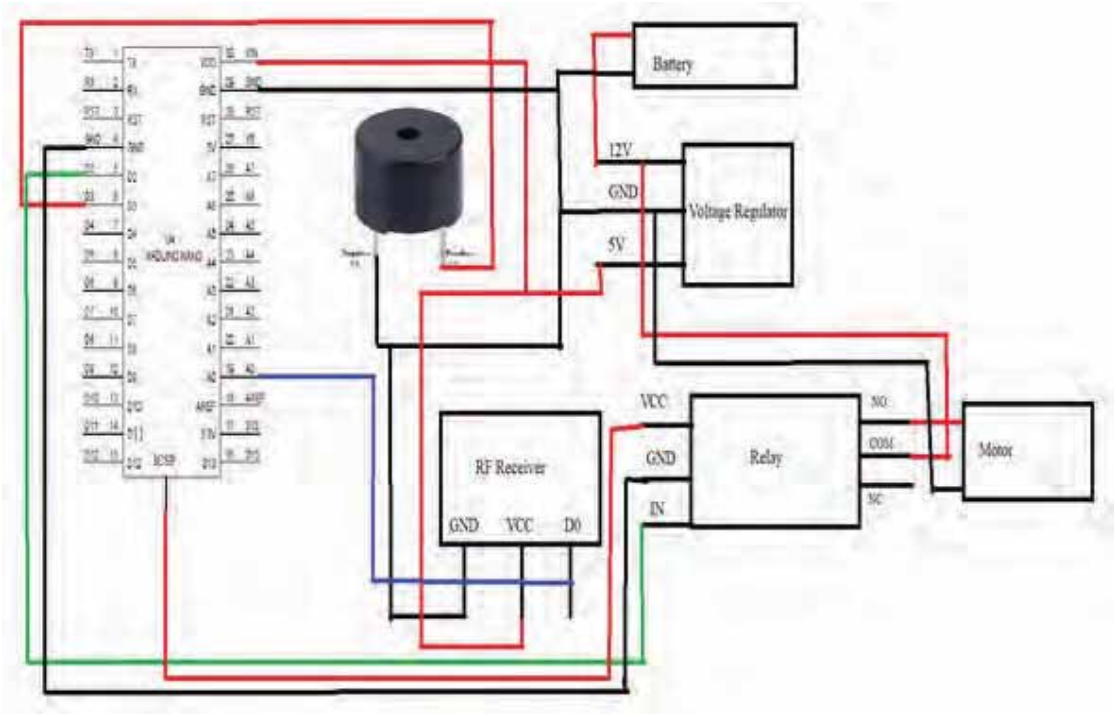

Fig 4. Schematic Diagram of receiver section.

C. *Flow Chart*

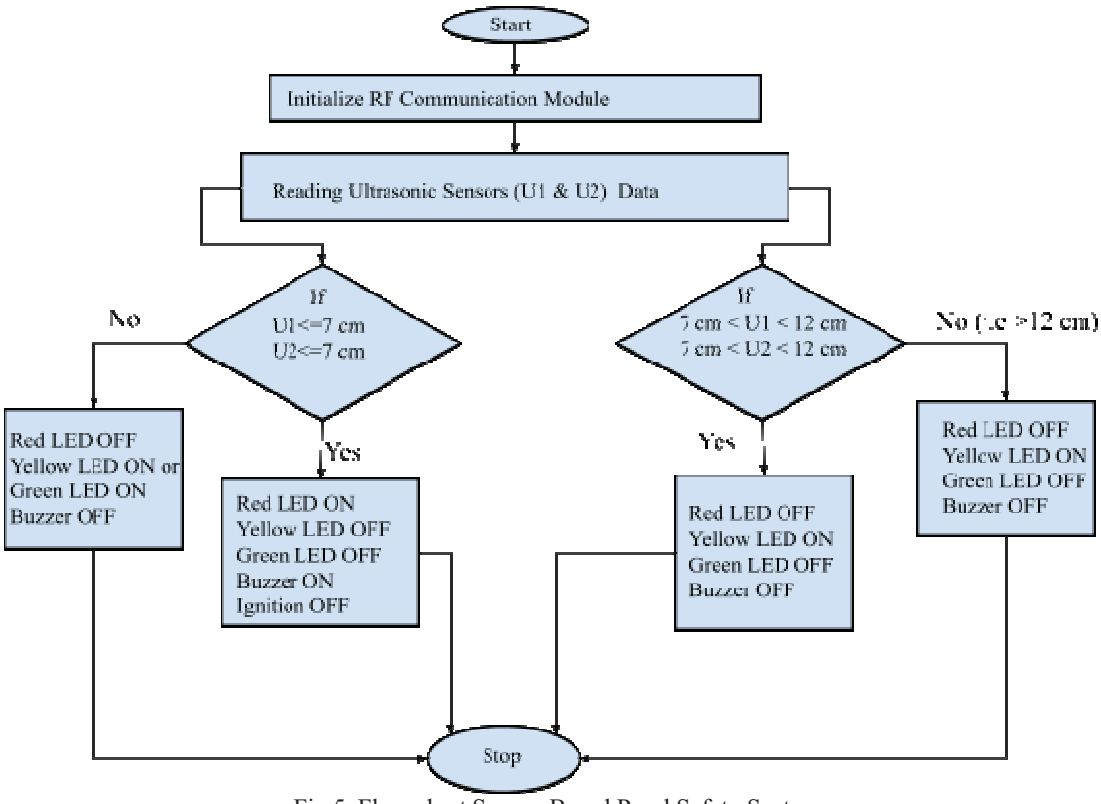

Fig 5. Flow chart Sensor-Based Road Safety System.

CVR Journal of Science and Technology, Volume 26, June 2024
DOI: 10.32377/cvrjst2607

Fig 5 is the implementation steps for Sensor-Based Road Safety System

Step 1: Data Acquisition with Ultrasonic Sensors

In the initial step, ultrasonic sensors are deployed to gather distance data from their surroundings. Specifically, Ultrasonic Sensor 1 and Ultrasonic Sensor 2 are responsible for capturing distance information.

Step 2: Red LED Activation for Close Proximity Warning

If the distance reading from either Ultrasonic Sensor 1 or Ultrasonic Sensor 2 falls below 7 cm, the Arduino microcontroller interprets this as a critical proximity situation. Consequently, the system sends signals to activate the Red LED on the opposite side of the curve, serving as an immediate warning for drivers.

Step 3: Yellow LED Activation for Caution

In scenarios where the distance reading from either Ultrasonic Sensor 1 or Ultrasonic Sensor 2 is greater than 7 cm but less than 12 cm, the Arduino issues signals to activate the Yellow LED on the opposite side of the curve. This signals caution to drivers, alerting them to the presence of a nearby vehicle.

Step 4: Green LED Activation for Safe Distance

When the distance reading from either Ultrasonic Sensor 1 or Ultrasonic Sensor 2 exceeds 12 cm, the Arduino responds by sending signals to activate the Green LED on the opposite side of the curve. This indicates a safe distance for drivers, promoting a smooth and secure passage.

Step 5: Emergency Response for Critical Conditions

If both Ultrasonic Sensor 1 and Ultrasonic Sensor 2 record distances below 7 cm simultaneously, the Arduino initiates emergency measures. This involves signaling the activation of Red LEDs on both sides of the curve, activating a Buzzer for audible alerts, and crucially, deactivating the motor to halt the vehicle. This comprehensive response ensures heightened safety during exceptionally hazardous conditions.

These systematic steps in the implementation of the sensor-based road safety system contribute to creating a proactive and responsive environment for drivers, enhancing overall road safety and preventing potential accidents, especially on curved roads.

limited visibility and the risk of accidents on curved roads. The integration of LED lights as visual indicators contributed to increased driver awareness and proactive measures to mitigate the likelihood of collisions with vehicles approaching from the opposite direction. Overall, the project's outcome signifies a promising step towards improving road safety in mountainous regions through the implementation of innovative technologies and enhanced safety measures.

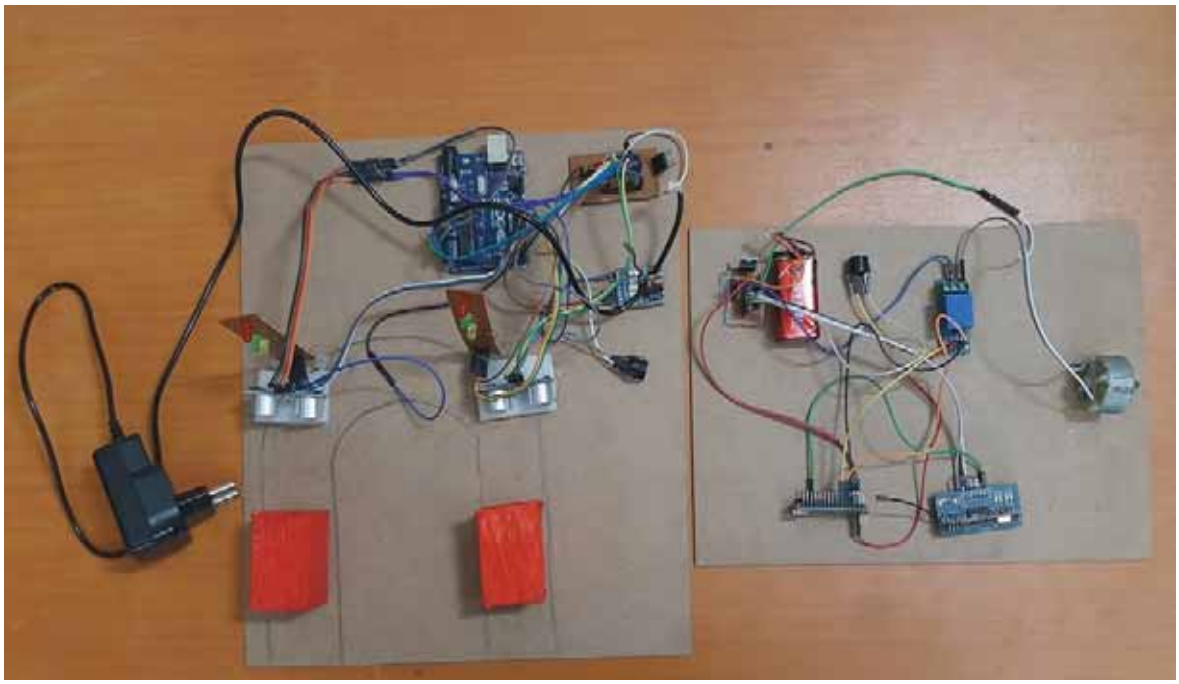

Fig 6. Hardware Setup of the system

CVR Journal of Science and Technology, Volume 26, June 2024
DOI: 10.32377/cvrjst2607

IV. CONCLUSIONS

In today's world, the frequency of accidents has surged due to bystanders not assisting when accidents occur, even when they happen right in front of their eyes. Our primary objective of this project is to mitigate accidents through the implementation of sensor-based technology. In the event of a person being involved in an accident, they shouldn't have to rely on others for help. Instead, they can safely navigate through curves or hilly roads with the assistance of LED lights signaling alerts.

The focus of this endeavor is to reduce the number of accidents on curved roads. This can be achieved by warning drivers through the illumination of LED lights when a vehicle approaches from the opposite side of the curve. The detection is facilitated by an Ultrasonic sensor interfaced with the Arduino UNO microcontroller. This proactive approach has the potential to save countless lives on curved roads. Moreover, this project not only serves to alert drivers in advance but can also automatically halt vehicles, when necessary, thereby preventing accidents effectively.

REFERENCES

[1] Sensor Based Accidents Prevention System for Hilly Region, International Journal of Advanced Research in Science, Communication and Technology (IJARSCT), June 2021.

[2] Smart Safety and Accident Prevention System for Mountain Roads, International Journal of Computer Sciences and Engineering (IJCSE), February 2020.

[3] Sensor Based Accident Prevention System in Curving, International Journal of Advance Research and Innovative Ideas in Education (IJARIIE), February 2019.

[4] Review on Safety in Hilly Regions, Journal of Engineering Sciences (JES), July 2020.

[5] Vehicle Accident Prevention System for Mountain Roads, International Research Journal of Engineering and Technology (IRJET), June 2020.

[6] Diminishing Road Accidents on Sharp Curves Using Arduino, International Journal of Advanced Research and Publications (IJARP), November 2017.

[7] Najbin Momin, Dr.M.S. Patil, Accident Control System Using Ultrasonic Sensor, International Journal of Innovative Research in Electrical, Electronics (IJIREE), Instrumentation and Control Engineering, October 2017.

[8] Sensor Based Accident Prevention System, International Journal of Innovative Research in Electrical, Electronics, Instrumentation and Control Engineering (IJIREEICE), June 2016.

E-ISSN 2581 –7957
P-ISSN 2277 – 3916

CVR Journal of Science and Technology, Volume 26, June 2024
DOI: 10.32377/cvrjst2608

Area-Delay-Power Efficient VLSI Architecture 2D FIR Filter using Modified Multipliers and Adders

Dr. Venkata Krishna Odugu[1]. Dr. B Janardhana Rao[2] and Dr. G Harish Babu[3]
[1]Associate Professor, CVR College of Engineering/ECE Department, Hyderabad, India
Email: venkatakrishna.odugu@gmail.com
[2]Associate Professor, CVR College of Engineering/ECE Department, Hyderabad, India
Email: janardhan.bitra@gmail.com
[3]Sr. Assistant Professor, CVR College of Engineering/ECE Department, Hyderabad, India
Email: harish.sidhu12@gmail.com

Abstract: **In this paper, a low power, area, and delay 2D Finite Impulse Response (FIR) filter architecture is derived from an analysis of a memory-efficient design. The completely direct-form 2D FIR filter is where the idea of parallel processing is first presented. As a result, the FIR filter may make better use of its memory by reusing its contents. With a block size of L and a filter length of N, a non-separable 2D FIR filter structure is developed and implemented. The FIR filter's arithmetic module makes use of high-speed, low-power multipliers and Carry Look Ahead (CLA) adders, with the output calculated by a pipelined adder unit. Verilog HDL code is used to represent the proposed architecture, and the CADENCE environment's NC Simulator and RTL Compiler synthesis tool are used to verify the design. Existing memory-efficient 2D FIR filter hardware architectures are compared to the produced area, power, and delay reports. Using Modified CLA (MCLA) adders and pipelining, we were able to cut down on power consumption by 44% and delay by 20%.**

Index Terms: **Memory reuse, 2D-FIR filter, Low Power Multiplier, Parallel Prefix Adder, Carry Look Ahead adder, and pipelining.**

I. Introduction

The most common applications for 2D digital filters are in image and video processing as well as bio-medical signal processing [1]. In biometric systems, 2D filters are sought after for use in feature extraction [2] and face recognition [3]. While the idea of a 2D filter may be used to both FIR and Infinite Impulse Response (IIR) fits, the stability and simplicity of the construction make 2D FIR filters more widely used. Some research is done on current architectures to implement a memory-efficient and less hardware-complex 2D FIR design. In [4], we learn about the 2D symmetry filters. Several symmetrical IIR and FIR filters are described, along with a study of their hardware metrics and VLSI (Very Large Scale Integration) designs. Here, after the requisite symmetry is achieved, the un-symmetric frequency response is split into sub-components. IIR and FIR filters with reduced multiplier counts and four-fold symmetry are presented in this study.

New 2D VLSI filter designs based on sub-filter blocks with a local connectivity structure and no global broadcasting are derived from the specified generalized formulae in [5]. With this study, we are able to create IIR filters with decoupled numerators and FIR filters with quadrant symmetry, both of which have the advantage of requiring fewer multipliers.

For 2D FIR filters, many systolic topologies are used for optimization of area, power, and latency. There aren't many studies that thoroughly investigate the idea of 2D Filters. To construct 2D systolic FIR and IIR filters, the authors of [6] develop a novel systolic transformation approach and modify reordering algorithms. Lower quantization error, local broadcast, no latency, and good critical routes are all accomplished by the combination of these two methods.

By rearranging the delay components and summing them up, novel VLSI systolic array FIR and IIR filter architectures [7] may be produced. A low-latency, locally broadcast architecture with a suitable number of multipliers and delay components is provided in this.

One-dimensional (1D) and two-dimensional (2D) filter bit-level VLSI designs are explored in [8]. These architectures are consistent, modular, and adaptable to a wide variety of specialized setups. Throughputs and hardware utilization are enhanced with reduced delay as a result of our effort. The modularity and simplicity of these structures make them suitable for optimization.

To counteract the worldwide signal broadcast, these preexisting works incorporate several delay or storage devices along the data stream. In current architectures, memory complexity is a serious problem. Memory's complexity impacts the building's footprint and energy needs [9]. In [10], a memory-centric 2D FIR filter is presented, although it incurs a power and latency cost in non-separable and separable models. The hardware modules in this architecture are L times more powerful than in prior efforts, but the throughput is only L times higher. The greater density of hardware components translates into higher requirements for both space and energy.

In this work, we offer a memory-efficient, low-power, small-area, and low-delay design for a 2D FIR filter. The completely direct-form 2D FIR filter presented here takes advantage of block-based input processing to minimize data storage and maximize memory reuse. Registers are located only in the input data route in the completely direct-form construction, whereas in the entirely transpose-form structure, they are located at the intermediate signal level [10]. Various area and power efficient 2D FIR filter using parallel processing and single input processing filter architectures are presented in the works [11-14].

Received on 18-10-2023, Revised on 17-11-2023, Accepted on 17-12-2023.

CVR Journal of Science and Technology, Volume 26, June 2024
DOI: 10.32377/cvrjst2608

The original, totally direct-form structure is transformed into an efficient block-based design that takes advantage of previously allocated memory. The following key contributions of this work are:

- Bypass Zero Feed Multiplicand Directly (BZ-FMD) multiplier is used to improve the Functional Unit (FU) in the arithmetic module of the 2D FIR filter design.
- Power consumption is dominated by dynamic power in VLSI design. In the suggested multiplier, the decrease in switching activities lowers the dynamic power.
- For the speedy addition of partial products, the multiplier's performance is further enhanced with a parallel prefix adder.
- Using CLA's fast adder logic, we have created this lightning-quick parallel prefix adder. In order to improve the standard CLA's efficiency in terms of speed, area, and power, it changes. These MCLAs are also used to add the filter at the end.
- The final addition of the FIR filter is computed using MCLAs, a pipelined addition procedure. Overall, the 2D FIR filter structure uses less energy and complete computation time thanks to MCLA adders and pipelining ideas.

The remaining sections of this paper is described as follows: In section 2, we propose the design of a 2D FIR filter, which eliminates computational redundancy. The suggested architecture for implementing a 2D FIR filter and its constituent sub-modules is outlined in section 3. Sections 4 and 5 explain the results and conclusions of the synthesis.

II. Memory Reuse

The suggested 2D FIR filter architecture takes into account the entirely direct-form structure. The FIR filter's memory reuse is investigated by analyzing the input data flow of the direct-form structure. The redundancy of input samples is displayed in Fig. 1 for the filter length N = 4, which is useful for comprehending the memory reuse idea. If the computation of the output at the m^{th} row is taken into account, the results are y(m, n), y(m,n+1), y(m,n+2), and y(m,n+3). Four columns and four rows of 2D input are needed for the 4 x 4 filter, totaling 16 samples. Serial-In-Parallel-Out (SIPO) Shift Register Blocks (SRB) and shift registers are utilized to provide row and column history samples, respectively.

Fig.1. Data flow in the fully direct form structure for N=4 with four outputs *{ y(m,n), y(m,n+1), y(m,n+2), y(m,n+3)}*, [10].

In a totally direct data flow, only 28 of the 64 samples are unique, while the other 36 are repeated four times. The outputs y(m,n), y(m,n+1), y(m, n+2), and y(m, n+3) are emphasized in Fig.1 along with their associated duplicate samples. Direct-form structures can eliminate redundancy through parallel computing or by employing a block-based structure. To calculate a precise result, it is necessary to examine previous sample values. Every clock cycle [10] allows access to the SRBs and the retrieval of these historical samples.

III. Implementation of Proposed 2D FIR Filter Architecture

To eliminate unnecessary repetition in the filter's data flow, the suggested block-based FIR filter is constructed in a methodical design. In order to save on storage space in relation to the input data flow, the memory reuse concept is implemented to cut down on redundant sample data. The filter length is N = 8, and there are blocks of size L = 4.

Figure 2 depicts the construction of a 2D FIR filter that uses non-separable blocks. Parallel inputs of size L are used to construct the fully direct form based 2D FIR filter. The two primary components of this design are the memory and arithmetic modules.

P = M/L = 512/4 = 128, hence the memory module has an array of 28 shift registers with a capacity of 128 words and 8 input register units (IRU). Every four of the 28 shift registers form a cluster called an SRB. Seven SRBs (SRB1, SRB2,.... SRB7) are needed for this design.

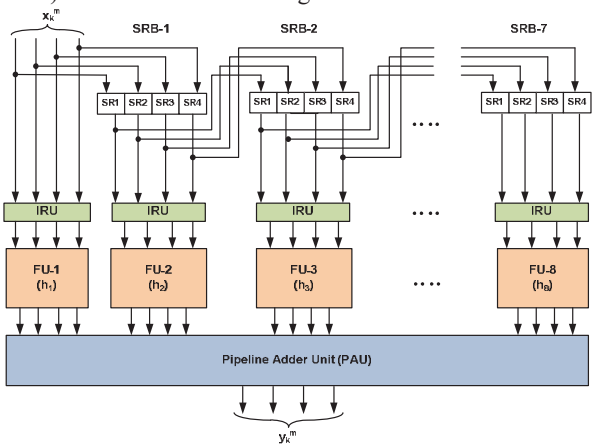

Fig. 2. Block-based non-separable 2D FIR filter architecture.

Each time the clock ticks, the filter processes the block of 4 inputs and generates 4 outputs. This is how the 512 by 512 input picture matrix is processed in serial sequence, block by block, to produce the outputs [15]. By organizing the image into blocks, we may finish it in MP = 512 x 128 clock cycles rather than the usual MP = 512 x 512. Throughput is raised while latency is decreased. Each time the clock ticks, the SRB component supplies N minus one, or seven, input blocks, which correspond to N minus one, or seven, successive input rows.

Eight IRUs are sampled based on the previous seven input blocks and the current input block. For the case of L = 4 and N = 8, Fig. 3 depicts the register layout on the inside that would be used for redundancy-avoiding logic. To generate input vectors of length 8, it uses a total of 7 registers, or D-Flip Flops (N - 1). The input samples, totaling 8 points, come

E-ISSN 2581 –7957
P-ISSN 2277 – 3916

CVR Journal of Science and Technology, Volume 26, June 2024
DOI: 10.32377/cvrjst2608

from both the past and the present. Since L= 4 and N= 8, each of the 8 - IRUs produces a 4 x 8 matrix of [Ak]; the first IRU gets input samples from the current block and applies this matrix to the FU. Seven identical IRUs produce equivalent 7-FUs with 4x8 matrices.

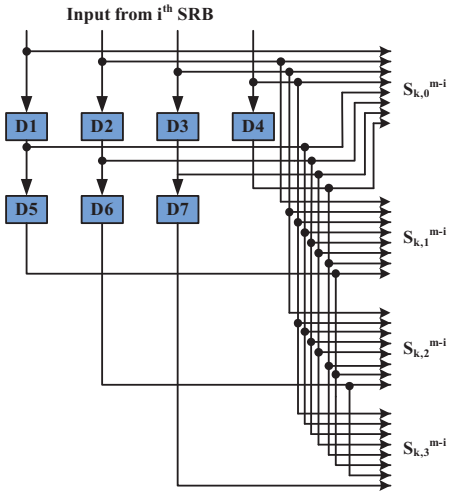

Fig. 3. The internal structure of IRU.

A. *Arithmetic Module*

The arithmetic module begins with the FU block. To multiply the input vectors by the filter coefficients, N = 8 FUs are needed [h_i]. Each of the eight IRUs sends FU four input vectors. The (i + 1)th FU takes the input vector and the (i + 1)th row of the impulse response matrix from the (i +1)th IRU and calculates the inner product of the two. The notation for the FU output matrix is [V_i].

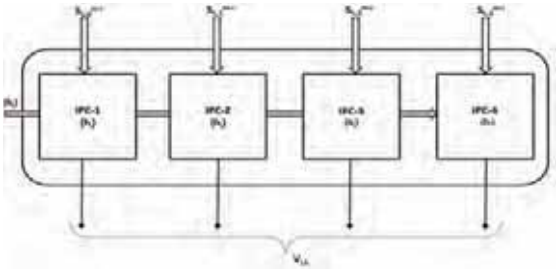

Fig. 4. The Internal block diagram of FU.

Fig.4 shows how FU is put together on the inside. There are four inner product cells (IPC) in FU. IPC is used to multiply the input vectors and the impulse response matrix elements that go with them. Figure 5 shows IPC's core reasoning for putting things together. An adder circuit is used to add the 8 partial products together to get the 8-point core product.

B. *Multiplier Implementation*

Each IPC needs N multipliers and N-1 adders to combine the input samples and filter coefficients. In this part, we will talk about the improved multiplier and adder circuits. The basic process of multiplication is made up of two steps: making partial products and adding them together. The swapping in a multiplier or any other circuit affects how much power it uses. The general dynamic power in the VLSI circuits is shown by Equation (12.

$$P_{Dynamic} = \alpha . C_L . f_{clk} V_{DD}^2 \quad (1)$$

Where C_L is Load capacitance, f_{clk} is clock frequency, V_{DD} is the power supply and α represents switching activity. The number of switching activities represents the power consumption of the circuit.

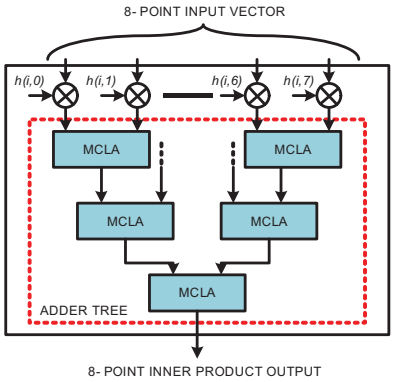

Fig. 5. Internal combinational logic diagram of IPC.

The traditional shift-add multiplier is changed, and a new multiplier is made using the Bypass Zero, Feed A Directly (BZ-FAD) method. This method is described in [15]. The switching activities of the BZ-FAD multiplier depend on (i) moving the bits of the multiplier, (ii) switching the bits of the partial product, (iii) switching the activities of the adder, and (iv) switching the activities of the multiplexer for the final addition. Bypass Zero, Feed Multiplicand Directly (BZ-FMD) is a change to the BZ-FAD that cuts down on delay and cuts down on the number of hardware blocks [16].

Figure 6 shows how the BZ-FMD multiplier is put together. It has an adder, an expander, a product register, a feed register, and a driver. Some parts of the BZ-FAD multiplier are taken out to cut down on delay and space. To make things less complicated, a binary counter is used instead of a ring counter and is put in the control block.

At first, the supervisor checks to see if the 0th bit of the multiplier is a '0' or a '1'. Instead of a ring counter, the driver has a synchronous binary counter that checks each bit and adds one to it every time the clock goes around. The managing block is in charge of everything in the adder, multiplexer, and feed register blocks. The input from the feed register is sent to the adder block or multiplexer through the control block. The multiplier bit decides the output of the multiplexer it should be the feeder register value of a previous partial product or adder output. The adder processing is skipped for the multiplier bit as '0' and the feeder register feeds the previous partial product value directly to the MUX. Otherwise, the sum of the multiplicand value and the previous partial product is directly given to MUX. The switching activity required for the zero-bit addition is eliminated and directly the multiplicand is fed to MUX.

CVR Journal of Science and Technology, Volume 26, June 2024
DOI: 10.32377/cvrjst2608

The multiplier structure effectively reduces the switching activities associated with the shifting of the partial product. In this particular multiplier, the upper half of the partial product bits undergo a rightward shift during processing, but the lower half of the partial product bits are retained and immediately put in the product register. Traditionally, the complete partial product is subjected to a rightward shift, however, in the suggested multiplier, only half of the bits representing the product undergo a shift. The suggested multiplier reduces the switching actions for partial product shifting by 50%.

The proposed multiplier design aims to minimize the switching activities associated with the shifting of multiplier bits, addition, and shifting of partial products. The decrease in switching activity results in a significant reduction in dynamic power usage. This paper presents the implementation of an 8-bit multiplier for the purpose of multiplying filter coefficients and input samples.

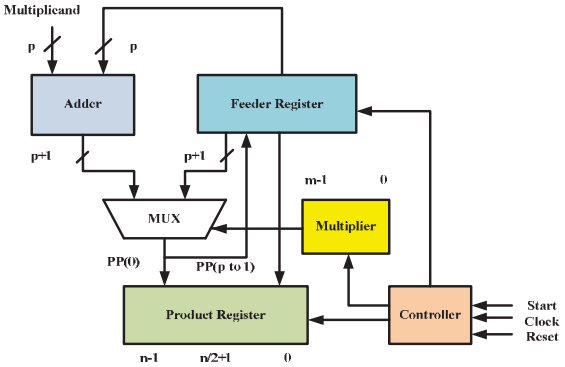

Fig.6. Architecture of multiplier.

C. Parallel Prefix adder based on Modified CLA (MCLA)

The process of multiplication involves a mix of shifting and summing. Higher bit multiplication necessitates the utilization of multiple adders. Therefore, the efficiency of the multiplier is contingent upon the performance of the adder as well. In the implementation of the N-tap filter, the addition of individual tap outputs and the calculation of the final filter output necessitates the use of N adders. The implementation of adder optimization is necessary to mitigate power consumption and delay. This section is a detailed description of a modified high-speed Carry Look Ahead (CLA) adder. The CLA equation has been updated in order to optimize hardware utilization and enhance performance and power efficiency. In this study, the 8-bit and 16-bit parallel prefix MCLA adders are given. The utilization of 8-bit Modified Carry Look-Ahead (MCLA) units is common in the process of adding partial products inside a multiplier. Additionally, 16-bit MCLA adders are employed in the construction of an adder tree.

The Modified Carry Look-Ahead (MCLA) algorithm replaces the usual carry ci with a modified carry. Following the computation of propagating and generating terms, a parallel prefix addition technique is employed to minimize the time required [17]. In this Modified CLA (MCLA), a modified carry M_i is determined in the place of conventional carry c_i. After the calculation of propagating and generate terms, a parallel prefix addition concept is used to reduce the time [17].

The modified carry M_i and sum$S_i$of the MCLA is given by equations (2) and (3) respectively.

$$M_i = g_i + g_{i-1} + p_{i-1}.g_{i-2} + p_{i-1}.p_{i-2}.g_{i-3} + \cdots + p_{i-1}.p_{i-2} \ldots . p_1.g_0 \quad (2)$$

Where g_i and p_i are generating and propagate terms in equation (2). This equation is modified to improve the efficiency of the adder. The real carry is given by the equation

$$c_i = M_i.p_i \quad (3)$$

The modified carry for even and odd bit positions are different. The M_i for even and M_{i+1} for odd given by equations (4) & (5),

$$M_i = (G_i^*, P_{i-1}^*) \odot (G_{i-2}^*, P_{i-3}^*) \odot \ldots\ldots\ldots . \odot (G_0^*, P_{-1}^*) \quad (4)$$

$$M_{i+1} = (G_{i+1}^*, P_i^*) \odot (G_{i-1}^*, P_{i-2}^*) \odot . \ldots\ldots\ldots . \odot (G_1^*, P_0^*) \quad (5)$$

The true carry is calculated by first calculating the modified carries for the even and odd bit locations. Employing a Formula (3). The equation (6) is used to determine the total.

$$S_i = d_i \oplus (p_{i-1}.M_{i-1}) \quad (6)$$

Only the least significant bits are used in the aforementioned carry computation algorithms. What follows is a parallel computation of the upper half of the bits carry. The modified carry is calculated in this manner by plugging in values for the intermediate propagate term and the intermediate generate term into Equation (7).

$$c_i = \left(G_{i:k} + P_{i-1:k-1}.G_{k-1:j+1}\right).p_i \quad (7)$$

Equation (8) describes the carry of the eighth bit in a 16-bit adder.

$$M_8 = (G_{8:7}, P_{7:6}) \odot (G_{6:3}, P_{5:2}) \odot (G_{2:-1}, P_{1:-2}) = \left(G_{8:7} + P_{7:6}.G_{6:-1}, P_{7:6}.P_{5:-2}\right) \quad (8)$$

The remaining upper half bits carries are determined using the equations from (9) to equation (1).

$$c_8 = (G_{9:8} + P_{7:6}.G_{6:-1}).p_8 \quad (9)$$

$$c_9 = (G_{9:8} + P_{8:7}.G_{7:0}).p_9 \quad (10)$$

$$c_{10} = (G1_{10:7} + P_{9:6}.G_{6:-1}).p_{10} \quad (11)$$

$$c_{11} = (G_{11:8} + P_{10:7}.G_{7:0}).p_{11} \quad (12)$$

$$c_{12} = (G_{12:7} + P_{11:6}.G_{6:-1}).p_{12} \quad (13)$$

$$c_{13} = (G_{13:8} + P_{12:7}.G_{7:0}).p_{13} \quad (14)$$

$$c_{14} = (G_{14:7} + P_{13:6}.G_{6:-1}).p_{14} \quad (15)$$

$$c_{15} = (G_{15:8} + P_{14:7}.G_{7:0}).p_{15} \quad (16)$$

Taking into account [13] the above-mentioned modifications to the CLA equations, we design and build 8-bit and 16-bit parallel prefix adders, examples of which are

illustrated in Figs.7 and 8, respectively.

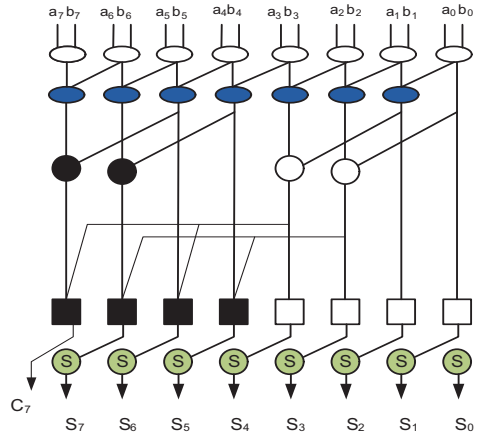

Fig.7. The 8-bit parallel prefix MCLA adder for multiplication

In Fig. 9, we see the logic cells that are needed to perform a simultaneous prefix sum of 8-bit and 16-bit adder structures. The AND, OR, and XOR logic gates are used to implement all of the logic cells.

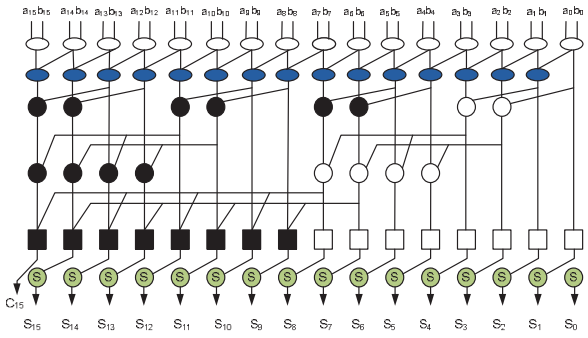

Fig.8. The 16-bit Parallel Prefix MCLA adder for filter outputs summation.

The adder block utilizes a specialized MCLA adder. To compute the sum of IPC, the MCLA adders are organized in a tree structure known as an Adder Tree (AT).

Pipeline Adder Unit (PAU) refers to the FIR filter's last adder block, which functions as the second block of the arithmetic module and generates the filter's output. D-FFs and MCLAs make up the PAU, which performs the final addition of the vectors generated by the FUs. Fig. 10 depicts an inside perspective of the PAU. Parallel processing optimizes the data flow in the input channel, while pipeline computing expedites the computation of the final output. The power consumption and critical route latency of VLSI designs can be minimized by employing pipelining and parallel processing [18, 19].

It takes one clock cycle to generate an output for each 4-sample input block. The delay of all arithmetic blocks is used to determine the minimum clock period used to define each clock cycle. This design has a clock period of $T = T_M + T_{PAU} + T_{MCLA} (2\log_2 N - 1)$, where T_M is the time needed to compute one multiplier, T_{PAU} is the time needed for the PAU, and T_{MCLA} is a delay of the MCLA adder in the adder tree. It takes 128 clock cycles to process a single row of the input picture, and just 128M cycles to process the full image matrix (where M is the size of the image matrix in bytes

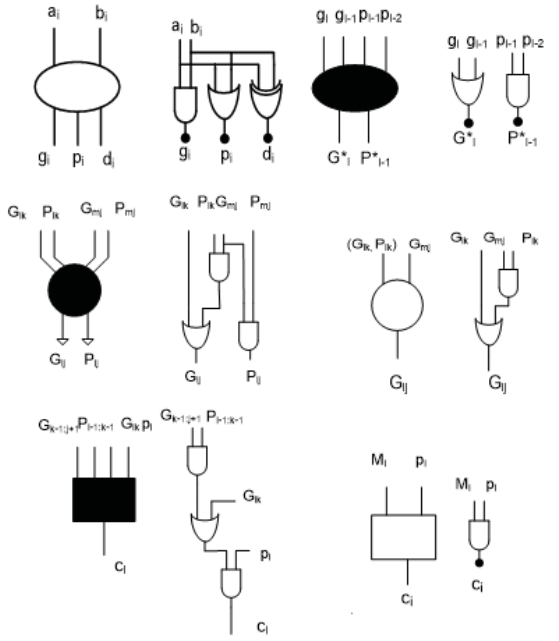

Fig.9. Internal logic cells are used in MCLA adder

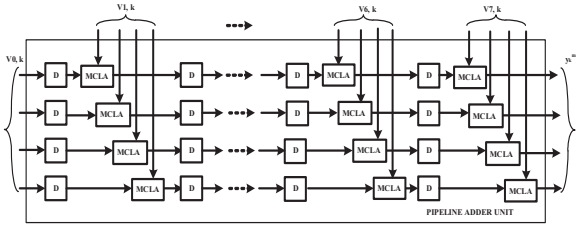

Fig.10. Pipeline Adder Unit (PAU) of 2D FIR structure.

IV. Implementation Results

The block-based, non-separable structure has $LN^2 = 4 \times 64 = 256$ multipliers, $L (N^2 - 1) = 4 \times 63 = 252$ MCLAs, and $[(M + N) (N - 1)] = 512 + 8 \times 7 = 28672$ registers. Every time the clock goes around, this structure sends out four signals. Non-separable structure's memory reuse efficiency is $L–1 = 3$, and its memory bandwidth per output (MBWPO) is $(L+N)(N–1)/L = 21$. The MBWPO costs 3 times less than the buildings that are already there [10].

The proposed 2D FIR filter design is written in HDL for block sizes L = 2 and 4 and filter sizes N = 4 and 8. The NCSim model from CADENCE tools is used to test the code. CADENCE tools' Encounter RTL translator is used to make the synthetic HDL code in the TSMC 90nm CMOS technology library. The synthesis of design is done with the TSMC 45nm CMOS library's general building blocks library, and D-FFs are used as registers and shift registers. The width of the original sample signal is thought to be b = 8 bits, and the width of the signal in the middle is d = 16 bits.

In Table I, the suggested non-separable 2D FIR filter design with block sizes of L = 2 and 4 and filter lengths of N = 4 and 8 is compared with known 2D FIR filter architectures. For reference, an FIR filter with N=4 blocks of size L= 4 is also put in place. Fig.11 is a picture that shows how the proposed design compares in terms of power to current 2D FIR filter architectures.

TABLE I
COMPARISON OF THE AREA AND POWER PARAMETERS OF DIFFERENT NON-SEPARABLE FIR FILTER ARCHITECTURES (L = 4)

Structure	Length of the filter (N)	Area (μm^2)	Power (mW)		
			Static	Dynamic	Total
Proposed 2D FIR	4	32598	0.2985	2.9856	3.2841
	8	40215	0.4215	3.9547	4.3762
Khoo [5]	4	1009878	3.9107	4.9441	8.8548
Mohanty*et. al* [10]	4	791361	2.8016	3.2918	6.0934

When comparing structures [10], we find that when N is equal to 4, total power consumption is decreased by 44%, and when N is equal to 8, total power consumption is reduced by 20%. Power consumption is reduced by 62% in the suggested design compared to the [5] architecture. As can be shown in Table I, the space savings is more than that of current structures. Table II displays a comparison of the power of non-separable FIR filters of filter orders N = 4 and N = 8.

TABLE. II
COMPARISON OF POWER FOR BLOCK SIZE L = 2 AND 4

Structure	N	L	Area (μm^2)	Power (mW)		
				Static	Dynamic	Total
Proposed Non-separable FIR filter	4	2	12654	0.1985	1.1254	1.3239
		4	32598	0.2985	2.9856	3.2841
	8	2	21478	0.2014	2.0146	2.2130
		4	40215	0.4215	3.9547	4.3762

Using an RTL compiler synthesis tool, we compare the suggested design using MCLA adders for the multiplier and adder block against the same design using regular CLA adders. Figures 12 and 13 provide visual comparisons of power, area, and delay between the proposed design and MCLA and CLA, respectively.

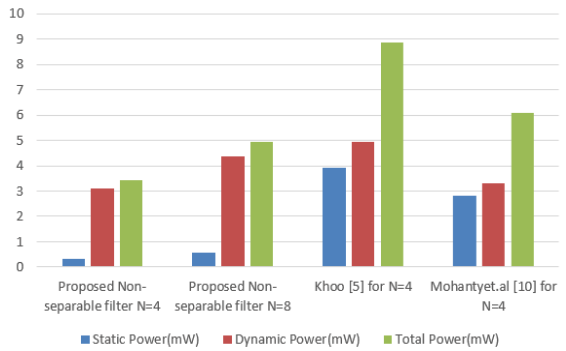

Fig.11. Graphical Comparison of power between proposed and existing structures.

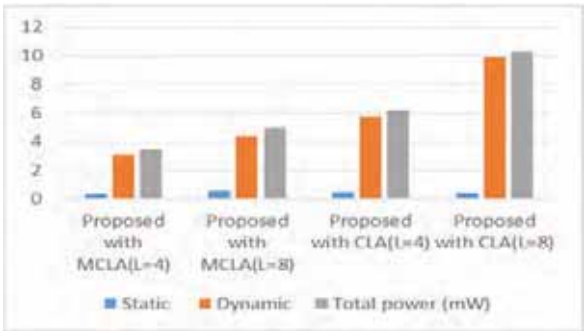

Fig.12. Comparison graph of power for the proposed design with MCLA and with CLA

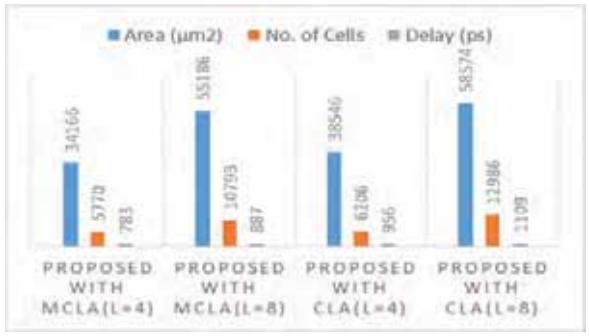

Fig.13. Comparison graph of area and delay for the proposed design with MCLA and with CLA for N = 8

V. CONCLUSION

An organized approach is taken to realize a 2D FIR non-separable filter architecture with minimal power, area, and delay memory consumption. By employing a block-based model for output assessment in parallel, we can boost throughput by a factor of L. Memory reuse in a completely direct-form structure helps minimize the amount of storage space needed. Parallel prefix adders and low-power BZ-FMD multipliers are used to realize the suggested filter architecture. In order to create a parallel prefix adder, the MCLA addition idea is utilized. Reduced power consumption and a shorter critical path are achieved by the use of parallel processing and pipelining techniques in the filter's final addition. The non-separable 2D FIR filter using MCLA achieves superior power and area results compared to the state-of-the-art FIR architectures. The designs are developed and synthesized in RTL Compiler tools from the TSMC 45nm CMOS library, with the input image size set at 512 by 512, the input block size set at L = 2 and 4, and the filter length set at N = 4 and 8. The suggested MCLA adders in the 2D FIR filter structure resulted in a 50% reduction in power consumption and a 20% reduction in delay compared to the standard 2D FIR filter. The experimental findings demonstrate that the suggested design outperforms the state-of-the-art in terms of area, latency, and power efficiency in the context of memory-efficient architectures.

REFERENCES

[1] H. Mohammadzade, L. T. Bruton, "A simultaneous div-curl 2D Clifford Fourier Transform filter for enhancing vortices, sinks, and sources in sampled 2D vector field images," in Proc. IEEE International Symposium on Circuits and Systems, May. 2007, pp. 821- 824.

[2] T. Barbu, "Gabor filter based face recognition technique," in *Proc. Rmanian Acad. Ser. A*, 2010, vol. 11, no. 3/2010, pp. 277–283.

[3] S. E. Grigorescu, N. Petkov, and P. Kruizinga, "Comparison of texture features based on Gabor filters," *IEEE Trans. Image Process.*, vol. 11, no. 10, pp. 1160–1167, Oct. 2002.

[4] P. Y. Chen, l. D. Van, H. C. Reddy, and C. T. Lin, "A new VLSI 2-D four-fold-rotational-symmetry filter architecture design", in Proc. IEEE Int. Symp. Circuits Syst. (ISCAS), May 2009, pp. 93-96.

[5] I. H. Khoo, H. C. Reddy, L. D. Van, and C. T. Lin, "Generalized formulation of 2-D filter structures without global broadcast for VLSI implementation", in Proc., *IEEE MWSCAS, Seattle, WA, USA*, Aug. 2010, pp. 426-529.

[6] L. D. Van, "A new 2-D systolic digital filters architecture without-global broadcast", IEEE Trans. Very Large Scale Integr. Syst., vol. 10, no. 4, pp. 477-486, Aug. 2002.

[7] Van, Lan-Da, et al. "A new VLSI architecture without global broadcast for 2-D digital filters." 2000 *IEEE International Symposium on Circuits and Systems. Emerging Technologies for the 21st Century. Proceedings (IEEE Cat No. 00CH36353)*. Vol. 1. IEEE, 2000.

[8] Mohanty, B. K., and P. K. Meher. "High throughput and low-latency implementation of a bit-level systolic architecture for 1D and 2D digital filters." *IEE Proceedings-Computers and Digital Techniques* 146.2 (1999): 91-99.

[9] B. K. Mohanty and P.K. Meher, "A high-performance FIR Filter Architecture for Fixed and Reconfigurable Applications", IEEE Trans. On VLSI Systems, vol. 24, issue 2, pp. 444-452, 2016.

[10] B. K. Mohanty and P.K. Meher, and A. Amira, "Memory Footprint Reduction for Power-Efficient Realization of 2-D Finite Impulse Response Filters", in *IEEE Trans Circuits Syst. I*, vol. 61, no. 1, Jan. 2014.

[11] Odugu, Venkata Krishna, C. Venkata Narasimhulu, and K. Satya Prasad. "Design and implementation of low complexity circularly symmetric 2D FIR filter architectures. " *Multidimensional Systems and Signal Processing* 31 (2020): 1385-1410.

[12] Odugu, Venkata Krishna, and Satya Prasad K. "An efficient VLSI architecture of 2-D finite impulse response filter using enhanced approximate compressor circuits." *International Journal of Circuit Theory and Applications* 49.11 (2021): 3653-3668.

[13] Odugu, Venkata Krishna, C. Venkata Narasimhulu, and K. Satya Prasad. "Implementation of Low Power Generic 2D FIR Filter Bank Architecture Using Memory-based Multipliers." *Journal of Mobile Multimedia* (2022): 583-602.

[14] Odugu, Venkata Krishna, C. Venkata Narasimhulu, and K. Satya Prasad. "A novel filter-bank architecture of 2D-FIR symmetry filters using LUT based multipliers." *Integration* 84 (2022): 12-25.

[15] M. Mottaghi-Dastjerdi, A. Afzali-Kusha, and M. Pedram, BZ-FAD: A low-power low area multiplier based on shift-and-add architecture, IEEE Trans. Very Large Scale Integration (VLSI) Systems. (2009) 302–306.

[16] Pinto, Rohan, and Kumara Shama. "Low-Power Modified Shift-Add Multiplier Design Using Parallel Prefix Adder." *Journal of Circuits, Systems and Computers* 28.02 (2019): 1950019.

[17] Poornima N and V S KanchanaBhaaskaran, Area efficient hybrid parallel prefix adders, J. Procedia Materials Science. 10 (2015) 371–380.

[18] A. P. Vinod and E.M. Lai, "Low power and high-speed implementation of FIR filters for software defined radio receivers" IEEE Trans. Wireless Commun., vol. 7, no. 5, pp. 1669-1675, Jul. 2006.

[19] O. Venkata Krishna, C. Venkata Narasimhulu and K. Satya Prasad "Design and Implementation of Block Based Transpose Form FIR Filter" in IJCA, Issue 8 Volume 1, Jan-Feb. 2018.

E-ISSN 2581 – 7957
P-ISSN 2277 – 3916

CVR Journal of Science and Technology, Volume 26, June 2024
DOI: 10.32377/cvrjst2609

Comparative Analysis of 5-Level and 7-Level Single-Phase Cascaded H-bridge Multilevel Inverters

Dr. S. Venkateshwarlu[1], N. Koushik[2], V. Ravi Prasad[3], Ch. Sai Karthik[4]
[1]Professor, CVR College of Engineering/EEE Department, Hyderabad, India
Email: svip123@gmail.com
[2]UG Student, CVR College of Engineering/EEE Department, Hyderabad, India
Email: sharmanmk321@gmail.com
[3]UG Student, CVR College of Engineering/EEE Department, Hyderabad, India
Email: vundruraviprasad@gmail.com
[4]UG Student, CVR College of Engineering/EEE Department, Hyderabad, India
Email: saikarthikchevula@gmail.com

Abstract: **The demand for high-performance, efficient, and reliable power electronic systems has been steadily increasing in various industrial applications, including renewable energy systems, electric vehicles, and smart grids. In response to this demand, the Cascaded H-Bridge Multi-level Inverter (CHB-MLI) has emerged as a promising solution, offering advantages such as improved voltage waveform quality, reduced harmonic distortion, and enhanced power handling capabilities. The CHB-MLI is characterized by its modular structure, comprising multiple H-bridge cells cascaded in series. Each H-bridge cell operates with a separate DC power source, enabling the generation of stepped voltage levels at the inverter output. By intelligently controlling the individual H-bridge cells, the CHB-MLI achieves the synthesis of a high-quality multilevel output voltage waveform. The different multi-level inverter topologies are Diode-Clamped MLI, Capacitor-Clamped MLI and Cascaded H-bridge MLI. This paper focused on key aspects like design, simulation, control strategies, performance evaluation, overall comparison and analysis of 5-level and 7-level CHB-MLIs. By addressing these aspects, this paper aimed to contribute to the advancement of power electronics technology and promote the adoption of the CHB-MLI in real-world applications, fostering energy efficiency and sustainability in power conversion systems.**

Index Terms: **Inverter, Multi-level inverter, CHBMLI, switching, SPWM, MCSPWM, gate signal, waveform, harmonics, THD, MATLAB.**

I. Introduction

A. General Concept

To start off, an inverter, in simple terms, is a very widely used power electronic converter which converts fixed DC input to variable AC output. Any inverter uses power electronic switches like SCR or IGBT or MOSFET (based on the application) for its operation. The output of the inverter is varied by varying the switching sequences and firing angles of the switches. Inverters are of 1-phase as well as 3-phase. Figure 1 shows a general classification of Inverters.

B. Classification of inverters

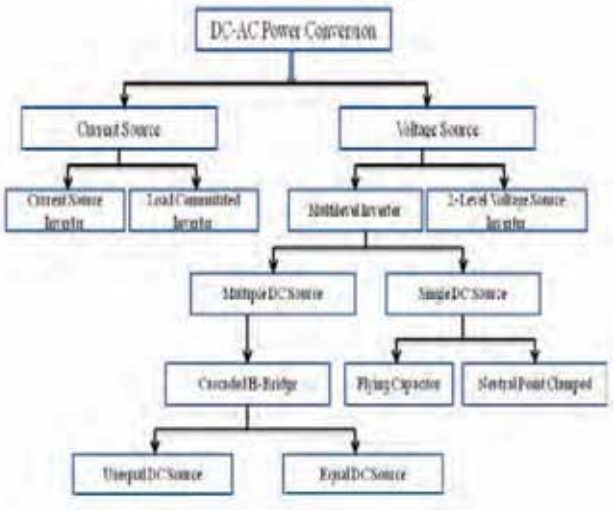

Figure 1. General classification of Inverters

C. Fulfilling the purpose of an Inverter

The main aim of any DC-AC converter is to obtain a smooth variable AC waveform at the output side. This can be achieved by increasing the number of levels in the output waveform. In a simple 3-level inverter with four switches, the possible output values are +Vdc, 0, -Vdc (for a given DC source Vdc). There is an immediate transition in the levels of the waveform whilst it reaches its peak value, which does not give us an output which is near-sinusoidal in nature. As we increase the number of levels, the transition takes place step wise and as a result, we get to observe a waveform which is nearer to a sinusoidal form. The Total Harmonic Distortion (THD) is lesser in those waveforms which are almost sinusoidal in nature. In simple words, the more the number of levels, the better.

Received on 19-03-2024, Revised on 18-04-2024, Accepted on 18-05-2024.

CVR Journal of Science and Technology, Volume 26, June 2024
DOI: 10.32377/cvrjst2609

D. Circuit design requirements

In the case of a CHBMLI, if N is the number of levels in the output waveform, then, Table I shows the design requirements based on the number of levels.

TABLE I.
DESIGN REQUIREMENTS BASED ON NO. OF LEVELS

Design Requirements	Formula
No of Bridges	(N-1)/2
No of Sources	(N-1)/2
No of Switches	2(N-1)
No of carrier waves required (PWM control)	N-1

II. LITERATURE SURVEY

[1] provides an overview of cascaded multilevel inverters, discussing various topologies, control techniques, and applications. It offers insights into the design considerations and performance characteristics of these inverters, serving as a foundational resource for understanding the technology. [2] This work from the University of Tennessee delves into the intricacies of multilevel power converters, covering fundamental principles, control strategies, and emerging trends. It provides comprehensive coverage of multilevel converter architectures and their applications in power electronics systems. [3] The research evaluates the performance of a five-level inverter in the context of solar grid-connected systems. It investigates the efficiency, reliability, and grid integration aspects of the inverter, offering valuable insights into its practical implementation and potential advantages for renewable energy applications.[4] focuses on the simulation of cascaded H-bridge multilevel inverters for photovoltaic (PV) applications. It explores the suitability of multilevel inverter topologies for PV systems, analysing factors such as output waveform quality, efficiency, and grid compatibility through simulation-based experiments.[5] provides a comprehensive overview of multilevel inverter topologies and control strategies. It synthesizes existing research on the subject, highlighting key advancements, challenges, and future directions in the field of multilevel power electronics, offering valuable insights for researchers and practitioners alike. [6] proposes a new cascaded H-bridge multilevel inverter design with improved efficiency. It presents novel circuit configurations or control techniques aimed at enhancing the performance of multilevel inverters, potentially addressing issues such as voltage levels, switching losses, and overall system efficiency. [7] present a comprehensive survey of multilevel inverter topologies, control techniques, and applications, providing a foundational understanding of the field. Kuriakose and Anooja [8] compare the performances of switched DC sources inverters and cascaded H-bridge inverters, contributing to the understanding of different inverter configurations. [9] proposes a symmetrical multilevel cascaded H-bridge inverter using a multicarrier SPWM technique, adding to the repertoire of control strategies for multilevel inverters. [10] offer a comparative analysis of SVPWM and SPWM schemes for NPC multilevel inverters,

enhancing knowledge on modulation techniques. [11] provided a detailed comparative analysis of multi-pulse and multilevel topologies for STATCOM, contributing insights into power quality improvement strategies. [12] introduces a modified hybrid multi-carrier PWM technique for cascaded H-bridge multilevel inverters, advancing PWM modulation methods. [13] discuss the generation of triggering signals for multilevel converters, addressing control aspects crucial for inverter operation. [14] offer a comprehensive review of different multilevel inverter topologies, modulation, and control strategies for grid-connected photovoltaic systems, providing insights into system integration. [15] present multi-carrier PWM strategies for multilevel inverters, contributing to the advancement of modulation techniques in the field.

This literature survey amalgamates diverse perspectives from research articles, surveys, and experimental studies, providing a comprehensive understanding of multilevel inverter technologies, control methodologies, different topologies for their applications, and ongoing research endeavours in the field.

III. 5-LEVEL CHB-MLI

A. Circuit Description

A 5-level CHBMLI has two H bridges connected in series i.e. eight switching devices operate to produce the desired 5 levels in the output waveform. In this case, the reference sine wave is compared with four triangular carrier waves. The frequency of the reference wave is 50Hz whereas that of the carrier waves is in KHz.

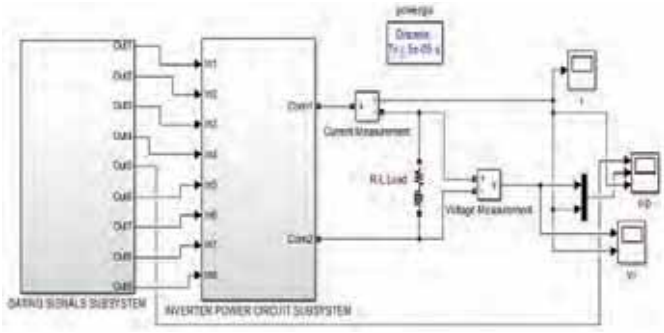

Figure 2. Simulation circuit diagram of 5-Level CHBMLI

Figure 2 shows the MATLAB simulation circuit of a 5-Level CHBMLI which includes the gating pulses subsystem, power circuit subsystem, an R-L Load with V&I measurement blocks and oscilloscopes to observe the waveforms.

CVR Journal of Science and Technology, Volume 26, June 2024
DOI: 10.32377/cvrjst2609

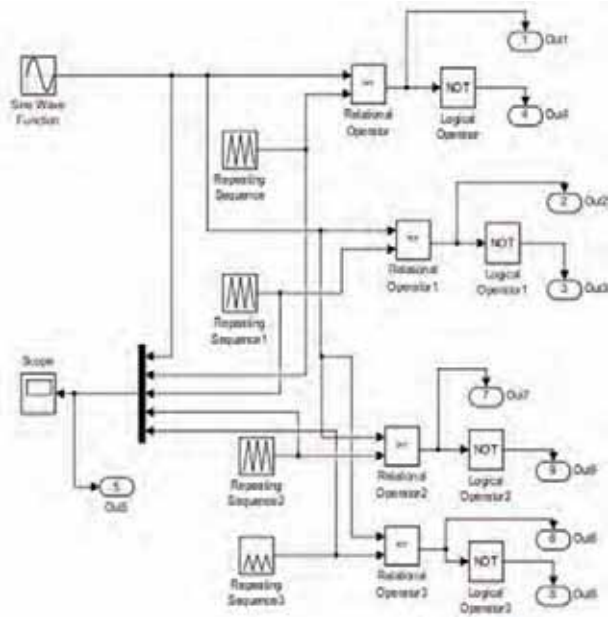

Figure 3. Gating signals subsystem

Figure 3 shows the gating signals subsystem of the 5-Level CHBMLI.

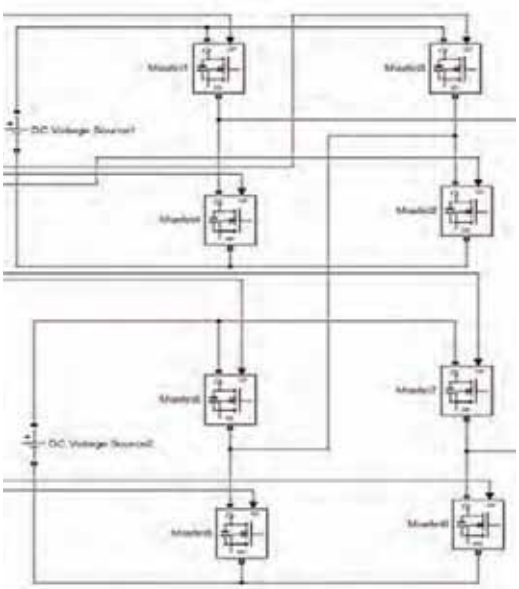

Figure 4. Cascading connections of the two bridges (Power circuit)

Figure 4 shows two H-Bridges in a cascaded fashion. The input fed to the bridges is DC. The switching devices used for the simulation are MOSFETs. The positive end is connected to the Drain terminals of the switches 1,3. The negative is connected to the Source terminals of the switches 2,4. The source of the upper switch is connected to the drain of the switch present below it in the same leg. The switch connections are the same for the second bridge as well. Since both bridges are connected in series, there is a connection between the 2nd leg of bridge-1 and 1st leg of bridge-2. However, the load is connected across the two bridges. One end of the load is connected to a point somewhere in between switches 1,4 of bridge-1 and another end is connected to a point in between the switches 6,7 of bridge-2.

IV. 7-Level CHB-MLI

A. Circuit Description

A 7-level CHBMLI has three H bridges connected in series i.e. twelve switching devices operate to produce the desired 7 levels in the output waveform. In this case, the reference sine wave is compared with six triangular carrier waves. The frequency of the reference wave is 50Hz whereas that of the carrier waves is in KHz.

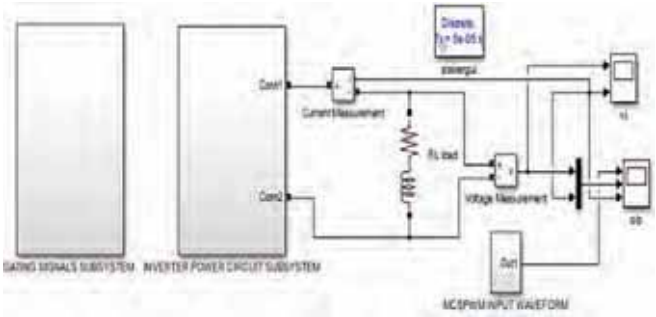

Figure 5. Simulation circuit diagram of 7-Level CHBMLI

Figure 5 shows the MATLAB simulation circuit of a 7-Level CHBMLI which includes the gating pulses subsystem, power circuit subsystem, an R-L Load with V&I measurement blocks and oscilloscopes to observe the waveforms.

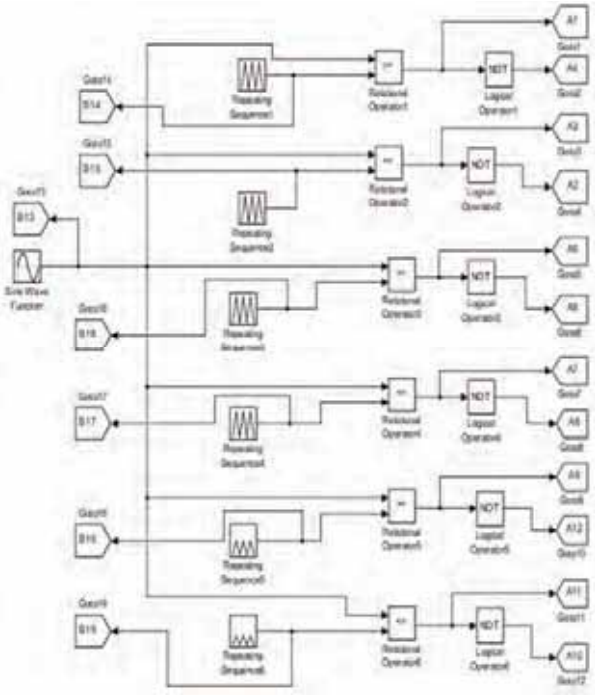

Figure 6. Gating signals subsystem

CVR Journal of Science and Technology, Volume 26, June 2024
DOI: 10.32377/cvrjst2609

Figure 6 shows the gating signals subsystem of the 7-Level CHBMLI.

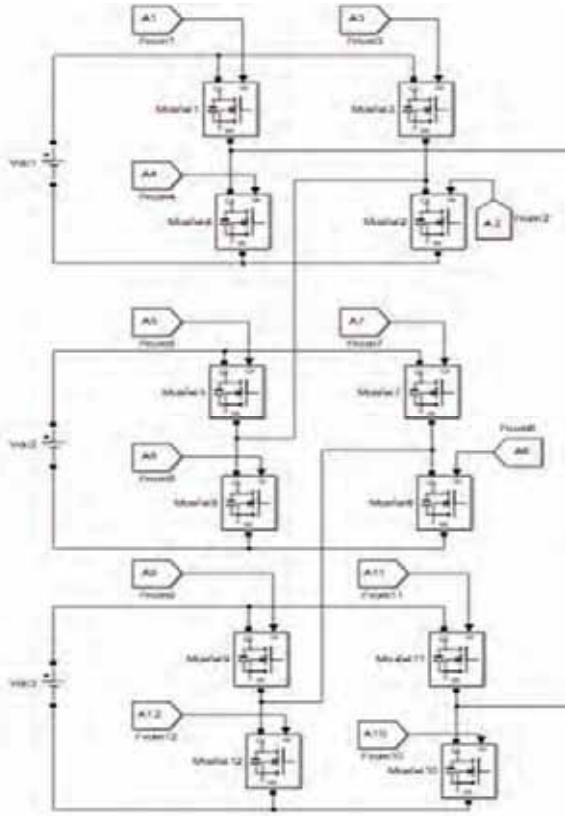

Figure 7. Cascading connections of the three bridges (Power circuit)

Figure 7 shows three H-Bridges in a cascaded fashion. The input fed to the bridges is DC. The switching devices used for the simulation are MOSFETs. The positive end is connected to the Drain terminals of the switches 1,3. The negative is connected to the Source terminals of the switches 2,4. The source of the upper switch is connected to the drain of the switch present below it in the same leg. The switch connections are the same for the second and third bridge as well. Since all three bridges are in series, there is a connection from 2nd leg of bridge-1 to 1st leg of bridge-2, 2nd leg of bridge-2 to 1st leg of bridge-3. However, the load is connected across the first and last bridges. One end of the load is connected to a point somewhere in between switches 1,4 of bridge-1 and another end is connected to a point in between switches 10,11 of bridge-3.

V. Control Strategies

The power electronic switching devices operate i.e. conduct when the gate signal is provided. To trigger the gate terminal, various methods are used. The technique used for this analysis is Multi-carrier Sinusoidal Pulse Width Modulation (MCSPWM). It is an extension of conventional SPWM, which is commonly employed in power inverters to generate AC output from a DC source.

Basic SPWM: In SPWM, a high-frequency carrier signal is modulated by a low-frequency reference signal (sine or triangle wave).The modulation alters the width of the pulses in the carrier signal to create a waveform that approximates a sine wave.

MCSPWM: MCSPWM extends the concept by using multiple carrier signals instead of just one.The idea is to have several carrier waves with different frequencies, each modulated by the same low-frequency reference signal.These carriers are typically evenly spaced in frequency.

Advantages of MCSPWM:

Reduced Harmonics: By using multiple carriers, the modulation spectrum is distributed across different frequencies, resulting in reduced harmonic content in the output waveform.

Improved Performance: Multi-carrier SPWM can provide better harmonic performance compared to single-carrier SPWM, leading to lower Total Harmonic Distortion (THD) in the output waveform.

Based on the control strategy used, the switching gate pulses will be generated and based on this switching, the desired output is achieved.

Figure 8 shows the concept of MCSPWM using a sinusoidal reference signal and two triangular carrier signals.

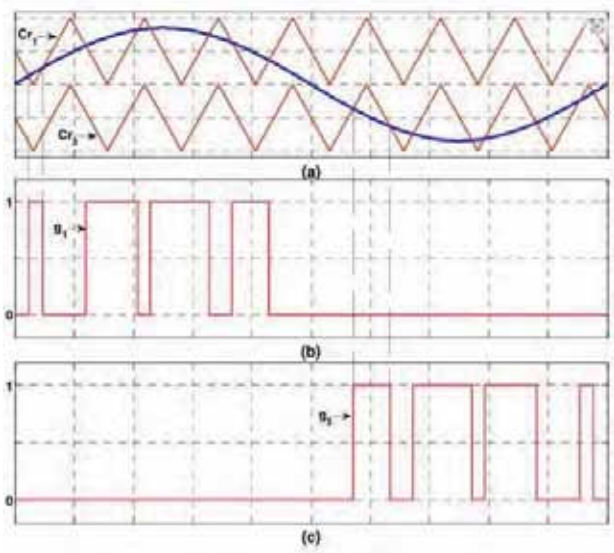

Figure 8. Concept of MCSPWM using a sinusoidal reference wave and two triangular carrier waves

E-ISSN 2581 – 7957
P-ISSN 2277 – 3916

CVR Journal of Science and Technology, Volume 26, June 2024
DOI: 10.32377/cvrjst2609

VI. Switching Sequences

A. Switching sequence of 5-Level CHBMLI

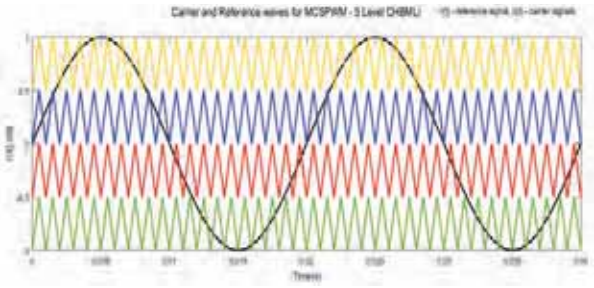

Figure 9. MCSPWM for 5-Level CHBMLI

Figure 9 represents the MCSPWM technique used for the simulation of a 5-Level CHBMLI. As shown in figure 3, a common sinusoidal reference signal (whose frequency is 50Hz and peak value is 1) and since it is a 5-level inverter, 4 carrier signals (2 per each bridge, which are triangular with 2KHz frequency, peak value as 1/2) have been considered. At every instant, the reference and carrier signals are compared with the help of a relational operator and if the reference is greater than the carrier signal, in that case the switches which are not subjected to a NOT operator are turned on and otherwise, the switches which are subjected to a NOT operator are turned on. This is the same for both the bridges.

B. Switching sequence of 7-Level CHBMLI

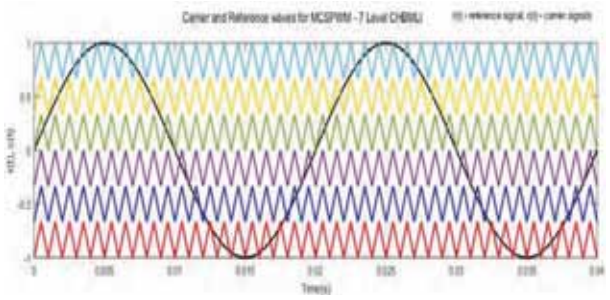

Figure 10. MCSPWM for 7-Level CHBMLI

Figure 10 represents the MCSPWM technique used for the simulation of a 7-Level CHBMLI. As shown in figure 6, a common sinusoidal reference signal (whose frequency is 50Hz and peak value is 1) and since it is a 7-level inverter, 6 carrier signals (2 per each bridge, which are triangular with 2KHz frequency, peak value as 1/3) have been considered. At every instant, the reference and carrier signals are compared with the help of a relational operator and if the reference is greater than the carrier signal, in that case the switches which are not subjected to a NOT operator are turned on and otherwise, the switches which are subjected to a NOT operator are turned on. This is the same for all the three bridges.

For any inverter, the switching order typically follows the modulation index and carrier wave phase relationships to minimize harmonic distortion and maintain waveform fidelity. In this context, switches are activated or deactivated in a pattern that aligns with the modulation scheme, ensuring the desired voltage levels are achieved at the output. The specific switching sequence for these configurations would involve a precise timing mechanism to synchronize the reference and carrier signals and optimize the inverter's performance while meeting system requirements and constraints.

However, the generalized switching of 5-Level and 7-Level CHBMLIs in case of using a microcontroller is determined by a code which works as per the switching sequences shown in the following tables II and III

TABLE II
GENERALIZED SWITCHING SEQUENCE OF 5-LEVEL CHBMLI

Switching sequence								Vdc
S1	S2	S3	S4	S5	S6	S7	S8	
1	1	0	0	1	1	0	0	2Vdc
1	1	0	0	0	0	0	0	Vdc
0	0	0	0	0	0	0	0	0
0	0	1	1	0	0	0	0	-Vdc
0	0	1	1	0	0	1	1	-2Vdc

TABLE III
GENERALIZED SWITCHING SEQUENCE OF 7-LEVEL CHBMLI

Switching sequence												Vdc
S1	S2	S3	S4	S5	S6	S7	S8	S9	S10	S11	S12	
1	1	0	0	1	1	0	0	1	1	0	0	3Vdc
1	1	0	0	1	1	0	0	1	0	1	0	2Vdc
1	1	0	0	1	0	1	0	1	0	1	0	Vdc
0	0	0	0	0	0	0	0	0	0	0	0	0
0	0	1	1	0	1	0	1	0	1	0	1	-Vdc
0	0	1	1	0	0	1	1	0	1	0	1	-2Vdc
0	0	1	1	0	0	1	1	0	0	1	1	-3Vdc

VII. Simulation Results

A. 5-Level CHBMLI

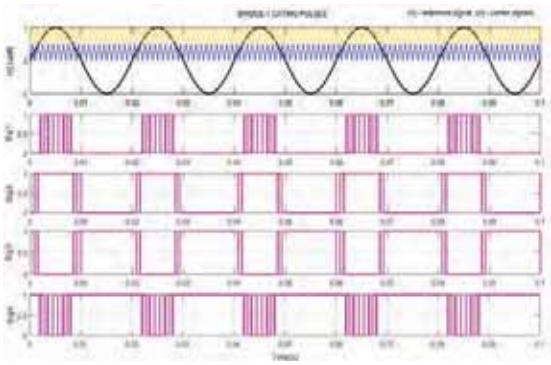

Figure 11. Gating pulses for switches 1,2,3,4

CVR Journal of Science and Technology, Volume 26, June 2024
DOI: 10.32377/cvrjst2609

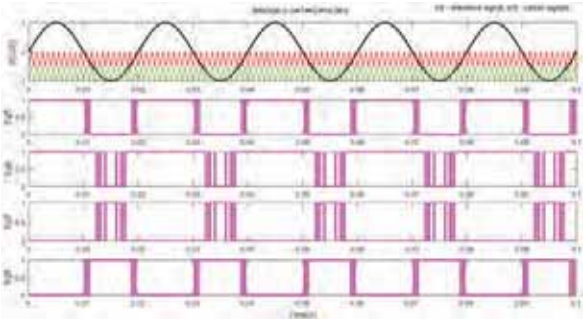

Figure 12. Gating pulses for switches 5,6,7,8

Figures 11,12 represent the switching or gating pulses for the 8 switches present in the 5-Level CHBMLI. These gate signals are generated as per the explanation mentioned in VI. A

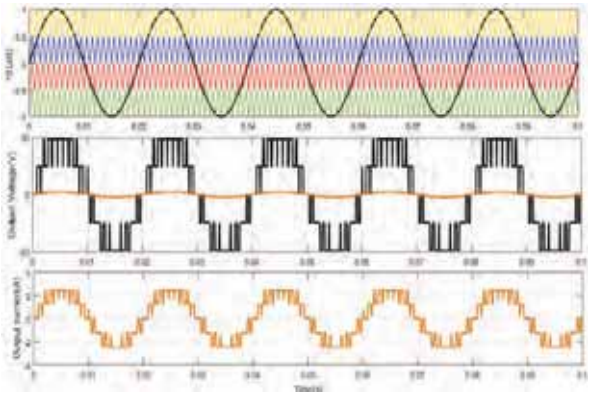

Figure 13. Output Voltage and Current waveforms of 5-Level CHBMLI

Figure 13 represents the simulated 5-level output voltage and current waveform of a 5-Level CHBMLI for a sample R-L load (R=20Ω, L= 0.5mH) and DC input of 25V to each bridge.

B. 7-Level CHBMLI

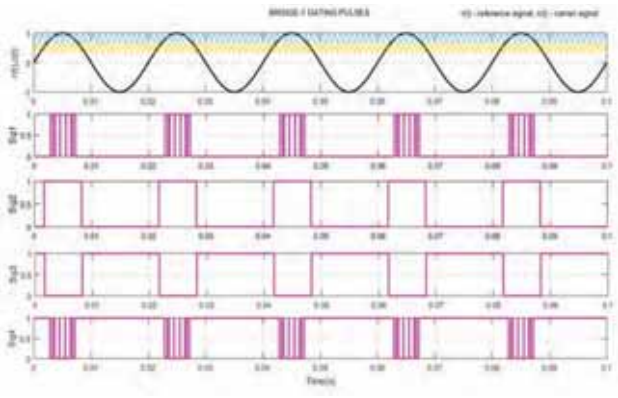

Figure 14. Gating pulses for switches 1,2,3,4

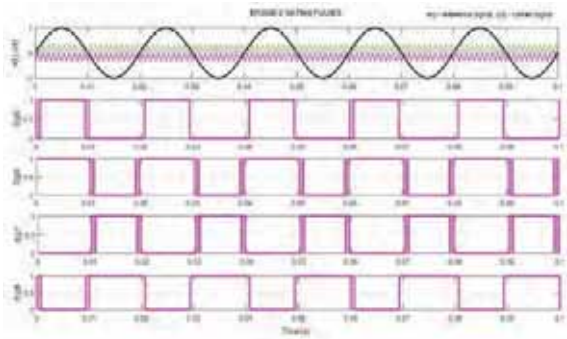

Figure 15. Gating pulses for switches 5,6,7,8

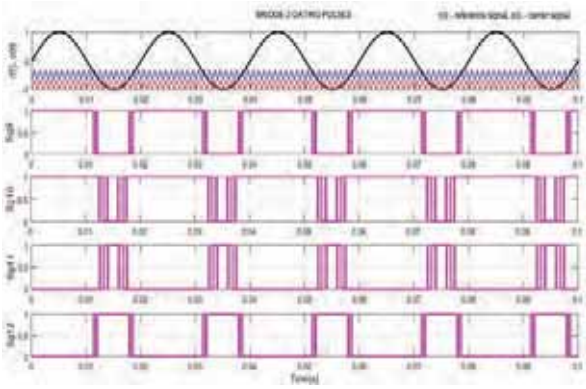

Figure 16. Gating pulses for switches 9,10,11,12

Figures 14,15,16 represent the switching or gating pulses for the 12 switches present in the 7-Level CHBMLI. These gate signals are generated as per the explanation mentioned in VI. B

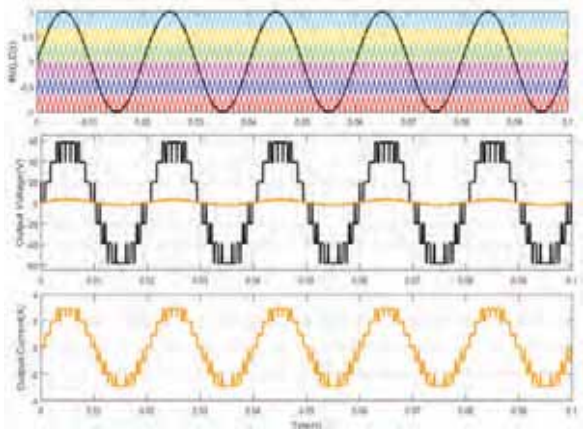

Figure 17. Output Voltage and Current waveforms of 7-Level CHBMLI

Figure 17 represents the simulated 7-level output voltage and current waveform of a 7-Level CHBMLI for a sample R-L load (R=20Ω, L= 0.5mH) and DC input of 20V to each bridge

All the simulations have been performed using MATLAB Simulink, version- R2015a.

C. FFT Analysis for % THD

In MATLAB, a time-domain signal can be converted into its frequency-domain representation using the FFT-Analysis tool. This tool facilitates spectral analysis tasks such as identifying peak frequencies, measuring frequency components' magnitudes, calculating spectral density, and estimating total harmonic distortion (THD). In this simulation, two cycles of the output waveforms have been considered for THD analysis.

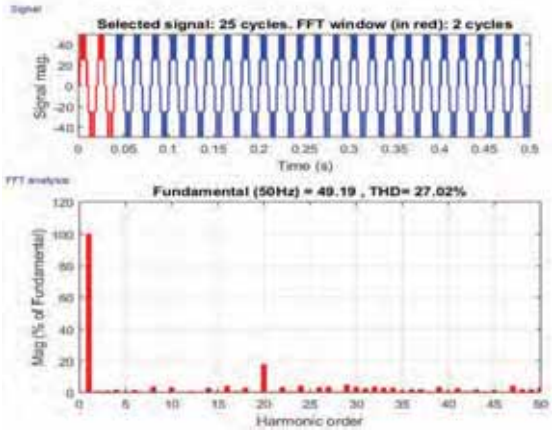

Figure 18. THD in 5-Level CHBMLI output voltage waveform

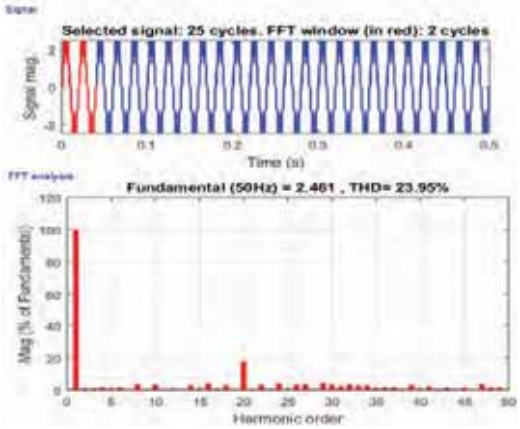

Figure 19. THD in 5-Level CHBMLI output current waveform

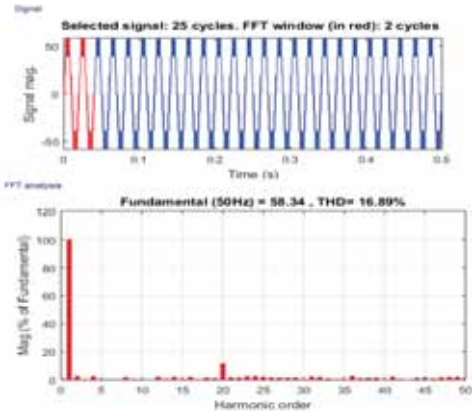

Figure 20. THD in 7-Level CHBMLI output voltage waveform

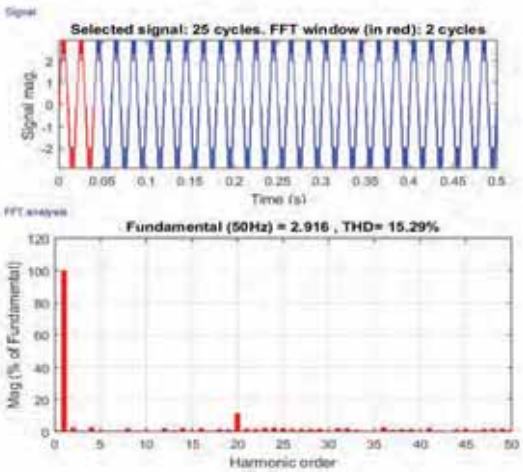

Figure 21. THD in 7-Level CHBMLI output current waveform

Figures 18,19,20,21 represent the %THD in the output voltage and current waveforms of 5-Level and 7-Level CHBMLIs respectively. Figure 22 shows the %THD comparison between the output V&I waveforms of 5-Level and 7-Level CHBMLIs respectively.

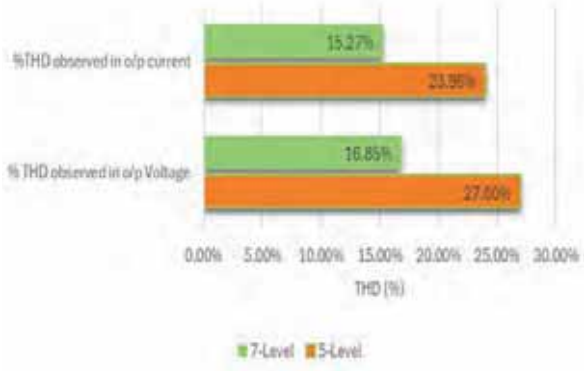

Figure 22. Comparison of %THD in 5-Level and 7-Level CHBMLIs

VIII. CONCLUSIONS

1. A 7-level cascaded H-bridge multilevel inverter offers higher voltage resolution compared to a 5-level inverter, resulting in finer control of the output voltage waveform.
2. The additional voltage levels in a 7-level configuration enable better approximation of sinusoidal waveforms, effectively reducing total harmonic distortion.
3. The finer voltage steps in a 7-level inverter contribute to improved power quality by minimizing voltage fluctuations and waveform distortion. This is particularly advantageous for applications demanding high-quality power supply, such as renewable energy systems and uninterruptible

CVR Journal of Science and Technology, Volume 26, June 2024
DOI: 10.32377/cvrjst2609

power supplies (UPS), grid-tied inverters and motor drives.

4. Implementing a 7-level cascaded H-bridge inverter involves more H-bridge cells and additional circuitry compared to the 5-level counterpart, increasing the complexity and cost of the system.
5. The 7-level inverter may subject its semiconductor devices to higher voltage stress compared to the 5-level counterpart, potentially impacting reliability and lifespan, which necessitates robust device selection and protection strategies.
6. The choice between the 5-level and 7-level cascaded H-bridge inverters depends on the specific application requirements, such as desired output quality, cost constraints, efficiency considerations, and available semiconductor technology. For applications where high-quality output waveform is critical and cost is not a limiting factor, the 7-level inverter may be preferred, while the 5-level inverter could offer a more cost-effective solution for less demanding applications.

REFERENCES

[1] Mariusz Malinowaski, Senior Member, IEEE, K.Gopakumar, Senior Member, IEEE, Jose Rodriguez, Senior Member, IEEE, and Marcelo A. Perez, Member IEEE "A Survey on Cascaded Multilevel Inverters".

[2] Surin Khomfoi and Leon M. Tolbert, "Multilevel Power Converters," The University of Tennessee, pp-31.1-31.50.

[3] Jaysing Ashok Kshirsagar and K. Vadirajacharya, "Performance evaluation of five level inverter for solar grid connected system," International Journal of Current Engineering and Technology, ISSN 2277 – 4106, issue-3, April 2014, pp. 222-225.

[4] Penugonda V. V. N. M. Kumar, P. M. Kishore, R. K. Nema, "Simulation Of Cascaded H-Bridge Multilevel Inverters For PV Applications," ICGSEE-2013 International Conference on Global Scenario in Environment and Energy, International Journal of Chem Tech Research IJCRGG, ISSN : 0974-4290 vol.5, no.2, June 2013, pp. 918-924.

[5] Bindeshwar Singh, Nupur Mittal, Dr. K.S. Verma, Dr. Deependra Singh, S.P. Singh, Rahul Dixit, Manvendra Singh and Aanchal Baranwal, "Multi-Level Inverter: A Literature Survey On Topologies And Control Strategies," International Journal of Reviews in Computing, ISSN: 2076-3328 E-ISSN: 2076-3336, July 2012, vol. 10, pp. 1-16.

[6] Gobinath.K1, Mahendran.S2, Gnanambal.I3 "New cascaded H-bridge multilevel inverter with improved efficiency." International journal of advanced research in Electrical, Electronics and Instrumentation Engineering Vol.2, issue 4, April 2013.

[7] J. Rodriguez. J.-S. Lai, and F.Z. Peng, "Multilevel inverters: A survey of topologies, controls and applications," IEEE Trans. Ind. Electron, vol. 49, No. 4, pp. 724-738, Aug.2002.

[8] Mithun Kuriakose, Anooja V S "Comparison of Performances of Switched DC Sources Inverter and Cascaded H bridge Inverter", International Journal of Science, Engineering and Technology Research, Volume 3, Issue 9, September2014.

[9] Sanjay P.S., Tanaji P.R. and Patil S.K., 2018. Symmetrical Multilevel Cascaded H-Bridge Inverter Using Multicarrier SPWM Technique. International Conference for Convergence in Technology (I2CT), pp. 1-4.

[10] Srivastava S. and Chaudhari M.A., 2020. Comparison of SVPWM and SPWM Schemes for NPC Multilevel Inverter. IEEE International Student's Conference on Electrical, Electronics and Computer Science (SCEECS), pp. 1-6.

[11] Maurya D.S., Jadhav P.D., Joshi R.S., Bendkhale R.R. and Thakre M.P., 2020. A Detailed Comparative Analysis of Different Multipulse and Multilevel Topologies for STATCOM. International Conference on Electronics and Sustainable Communication Systems (ICESC), pp. 1112-1117.

[12] Sarkar I and Fernandes B G 2014 Modified Hybrid Multi-Carrier PWM Technique for Cascaded H Bridge Multilevel Inverter Annu. Conf. Ind. Electron. Soc. 4318–24

[13] Bashi S M, Mailah N and Kadir Z 2008 Generation of Triggering Signals for Multilevel Converter Eur. J. Sci. Res. 24 548–55

[14] Sinha A, Chandra Jana K and Kumar Das M 2018 An inclusive review on different multi-level inverter topologies, their modulation and control strategies for a grid connected photo-voltaic system Sol. Energy 170 633–57

[15] B.P. Mcgrath and D.G Holmes "Multi carrier PWM strategies for multilevel inverter" IEEE Transaction on Industrial Electronics, Volume 49, Issue 4, Aug 2002, pp. 858-867

E-ISSN 2581 – 7957
P-ISSN 2277 – 3916

CVR Journal of Science and Technology, Volume 26, June 2024
DOI: 10.32377/cvrjst2610

Review on Electric Vehicles Battery Swapping Technology

Dr. G. Sree Lakshmi
Professor, CVR College of Engineering/EEE Department, Hyderabad, India
Email: g.sreelakshmi@cvr.ac.in

Abstract: **The goal of research and development organizations is to intelligently design the architecture of battery swapping stations (BSSs), with the hope of offering a reliable platform for the successful installation of a large fleet of electric vehicles (EVs) and hybrid electric vehicles (HEVs). The BSS can calibrate its subsystem for the deployment of electric vehicles (EVs) by implementing a similar concept to those found in current gas stations, which involve exchanging or swapping out discharged batteries for partially or fully charged ones after a short while. Because it gives the relevant stakeholders a more comprehensive understanding of the business prospects, the BSS approach has emerged as a promising technological alternative to the conventional EV recharging station approach. This paper addresses the introduction to BSS, covering its methods, infrastructure, advantages over charging stations, and main obstacles.**

Index Terms: **Battery Swapping Station (BSS), Battery Charging Stations (BCS), Electric Vehicles (EVs), Hybrid Electric Vehicles (EHVs).**

I. Introduction

Traditionally, EVs are bought with "fixed" batteries, which can only be charged with the power source inside the vehicle. Mass adoption of EVs depends on the availability of sufficient, reasonably priced, easily accessible, and dependable charging networks like ICE vehicles need fueling stations [1]-[2]. In India, initiatives are in place to increase the accessibility of infrastructure for charging. Even so, charging still takes a lot longer than ICE refueling. An alternative is battery swapping, which allows you to charge the batteries independently and entails swapping out discharged batteries for charged ones [3]. As a result, there is very little downtime while the car is in operating mode and charging and battery consumption are disconnected. Battery swapping is more common for smaller vehicles, like 2Ws and 3Ws, because their batteries are smaller and easier to change, as opposed to 4 wheelers and e-buses, though there are also solutions being developed for these other vehicle segments. As long as each swappable battery is actively used, battery swapping has three main benefits over charging: it saves time, space, and money [4]- [5].

The goal of battery swapping policy is to protect the ecosystem's potential for innovation in EV batteries while establishing a framework for increased interoperability.

• Regular charging of e-2W and e-3W devices requires at least three to four hours with current technologies, which is inconvenient and increases range anxiety. This results in a significant amount of vehicle downtime, especially for shared mobility and freight vehicles. On the other hand, because swapping stations have pre-charged batteries, switching out batteries only takes a few minutes [6].

• Charging stations take up more space due to the need for vehicles to park nearby during charging. Battery swapping stations can stack multiple batteries and require minimal parking, making them ideal for urban areas with limited space [7].

• Battery swapping requires more batteries than traditional batteries, but each swappable battery can have a smaller capacity (kWh) due to lower range anxiety [8].

One of the most crucial components for battery leasing and swapping companies is the ability to track the location and performance of batteries. From the swapping stations, it is simple to track and observe the battery swapping process. IoT can be very helpful in tracking and monitoring batteries, as well as preventing theft and loss. The Internet of Things has a particularly noticeable impact on industries like grid-scale energy storage and electric vehicles (EVs). IoT-enabled EV batteries can interact with charging stations to ensure the best possible charging while simultaneously sending vital information for upkeep of the vehicle [9].

The communication protocol is an essential part of a Battery Management System (BMS) that ensures prompt and efficient communication with other systems or components in a particular application. In its most basic form, a communication protocol is a set of rules that define how two or more entities. In this case, electronic devices interact with one another. These rules may regulate data rate, error-checking protocols, data structure and order, and mutual device identification between transmitting and receiving devices [10].

Adoption of communication infrastructure standards (protocols and technology) is crucial for maintaining data stability and security. BIS will define and approve communication standards between batteries and vehicle controllers, chargers, and energy operator servers. To promote "back-end" interoperability in the battery swapping ecosystem, an open standard communication protocol like OCPP can be used. This protocol should allow network switching. The BMS constantly monitors and regulates a number of battery-related parameters, including temperature, voltage, current, and state of health (SoH) and state of charge (SOC). However, in the event of a serious issue, the BMS may receive instructions from the car's central control unit to limit current output, initiate a cooling cycle, or even isolate the battery. This unprocessed data must be sent to this unit. This sharing of information is made possible by the communication protocol [11]-[12].

This paper provides an overview of the most advanced battery swapping technologies and implementations currently on the market. This paper highlights the technical challenges facing this newly proposed model and the potential for

Received on 18-03-2024, Revised on 17-04-2024, Accepted on 17-05-2024.

CVR Journal of Science and Technology, Volume 26, June 2024
DOI: 10.32377/cvrjst2610

technological advancements in the near future. It also presents a redesigned model of battery swapping methodologies that addresses some of the issues that current battery swapping technologies face. The advantage of this battery swapping technology over the state-of-the-art is also emphasized, including mechanical, electrical, and financial ones. In order to commercialize this proposed model, significant differences, advantages, and technological advancements are highlighted. Finally, research opportunities and technical challenges related to this novel model are presented.

II. Methods of Battery Swapping

A. Manual Battery Swapping Station

At a battery-swapping station, batteries are manually inserted and extracted. This process involves manual labor, usually done by hand. These stations are modular and require very little space. These have smaller battery packs and are manageable for one or two people to handle, so they can be used with 2W or 3W batteries [13].

B. Autonomous Battery Swapping Station

At the Autonomous Battery-Swapping Station, the process can be automated entirely or in part. 4W makes use of the robotic arm. More space is necessary before setting up an autonomous battery swapping station, though. This is typically more expensive than doing it by hand. Furthermore, due to their increased weight and size, battery packs require mechanical support. The Ministry of Road Transport and Highways (MoRTH) has approved the sale and registration of electric vehicles (EVs) without batteries. This is a good step that will help battery swapping solutions a lot, even though it seems to take forever. Commercial electric vehicle fleets, especially those in the electric two- and three-wheeler segments, can find it feasible because batteries can currently be changed [14]-[16].

For the first time on a commercial scale, China used the battery swapping technique for electric buses in 2008—that is, during the Summer Olympics. The batteries on about fifty buses that ran various routes were switched. Since then, the bus swapping method has also been widely adopted by China, Japan, South Korea, and other countries. The different swapping techniques are as follows, with distinctions made based on where the robotic arm is being used and where the battery is located within the vehicle:

Sideways Swapping: This is mostly applied to vans and other vehicles where having the sideways position is the most sensible.

Rear Swapping: This is used in cars where the battery is installed backwards. Usually, in the case of cars with a large boot.

Bottom Swapping: This is applicable to vehicles that have their batteries installed at the bottom. At the swapping station, the car is positioned on an elevated platform, and a robotic arm is used to swap the batteries from the bottom using other accessories that are usually found below ground level.

Top Swapping: The most common application of this is in electric bus technology, where the batteries are kept at the top and the rooftop opens upon the bus's arrival to enable the robotic arm to complete the battery swap.

TABLE I
ELECTRIC VEHICLES WITH AND WITHOUT BST

S.No	Manufacturer	Model	Country	Battery Swapping
1.	NIO	NIO ES8	China	Manual
2.	Geely	Geely Geometry EX3	China	Manual
3.	Tesla	Tesla Model S	United States	NO
4.	Nissan	Nissan Leaf	Japan	NO
5.	BMW	BMW i3	Germany	NO

III. Mathematical Model for BSS

The battery swapping station's total charged power and total discharged power are represented by equations 1 and 2:

$$P_{cbss}^{t} = \sum_{b=1}^{B}(P_{cbs}^{t,b}) \quad \forall\, t \in T \tag{1}$$

$$P_{dbss}^{t} = \sum_{b=1}^{B}(P_{dbs}^{t,b}) \quad \forall\, t \in T \tag{2}$$

By adding the power of each battery in the battery swapping station, the total powers are determined. Each battery in the battery swapping station is charged or discharged in the same way as a conventional battery, as demonstrated by:

$$U_{cbs}^{t,b} + U_{dbs}^{t,b} \leq 1 \;\forall\, t \in T; \forall\, b \in B \tag{3}$$

$$P_{cbs}^{t,b} \leq P_{bs}^{r,b} * U_{cbs}^{t,b} \;\forall\, t \in T; \forall\, b \in B \tag{4}$$

$$P_{dbs}^{t,b} \leq P_{bs}^{r,b} * U_{dbs}^{t,b} \;\forall\, t \in T; \forall\, b \in B \tag{5}$$

Each battery's stored energy within the battery swapping station is determined by

$$E_{bs}^{t,b} = E_{bs}^{t-1,b} + \left\{P_{cbs}^{t,b} - \frac{P_{dbs}^{t,b}}{\eta_{bs}}\right\} X\, I_{dur}^{t}$$

$$\forall\, t \in T; \forall\, b \in B \tag{6}$$

Each battery's rated capacity and efficiency are indicated by

$$\eta_{bs}\frac{\sum_{t=1}^{T}\left(P_{dbs}^{t,b}\, X\, I_{dur}^{t}\right)}{\sum_{t=1}^{T}\left(P_{cbs}^{t,b}\, X\, I_{dur}^{t}\right)} \tag{7}$$

$$E_{bs}^{t,b} \leq E_{bs}^{r} \forall\, t \in T; \forall\, b \in B \tag{8}$$

Modeling the process of switching batteries is done by

$$\begin{cases} E_{bs}^{t,b} = 0 \\ P_{cbs}^{t,b} = 0 \;\; \forall\, t \in t_{swap}; \forall\, b \in B \\ P_{dbs}^{t,b} = 0 \end{cases} \tag{9}$$

$$E_{bs}^{t,b} = E_{bs}^{r} \;\forall\, t = (t_{swap} - 1)\; \forall\, b \in B \tag{10}$$

During the battery swapping procedure, the fully charged battery in the station is replaced with a depleted battery from an electric vehicle that pulls up to the station. When a battery needs to be changed, an empty battery is replaced with one that is fully charged. Furthermore, it is not feasible to charge or discharge the battery at this time due to the ongoing swapping process [17]. As such, during the swapping time, the battery's power and energy are set to zero, as shown by Eq. 9. The battery needs to be fully charged during the time period before swapping it out at the next time interval. In order to replace the batteries at the next time interval, the energy management system must ensure that there are sufficient fully charged batteries available at each time interval. This point is expressed in Eq. 10.

CVR Journal of Science and Technology, Volume 26, June 2024
DOI: 10.32377/cvrjst2610

IV. Electric Vehicle Charging Ecosystem

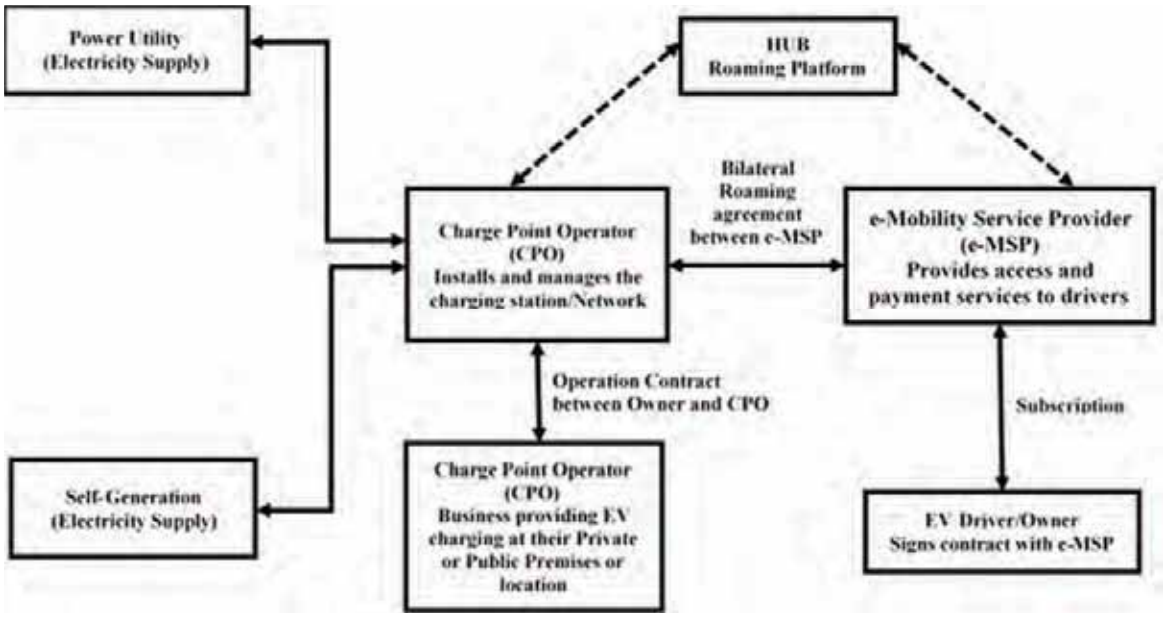

Figure.1. Electric Vehicle Charging Ecosystem

To ensure smooth operation of EVs certain guidelines are needed for EVs charging and Battery Swapping systems which are given as:

- To provide universal access to the infrastructure needed for charging electric vehicles.
- To promote a quicker uptake of electric vehicles by making sure that the environment and infrastructure for charging are secure, dependable, accessible, and reasonably priced.
- To encourage charging rates that are reasonable for both owners of electric vehicles (EVs) and operators of charging stations.
- To create chances for small business owners to get work and income.
- To actively encourage the development of EV charging infrastructure in the first stages and ultimately establish a market for the EV charging industry.
- To promote the adoption of EV Charging Infrastructure by Electrical Distribution Systems.
- To establish consistency and assurance in the direction of the nation's accelerated adoption of EVs.

The electric vehicle charging ecosystem consists of Power Utility, Self-Generation, Roaming Platform (HUB), Charge Point Operator (CPO), e-Mobility Service Provider (e-MSP), Charging Station Owner, EV Driver/Owner [18]-[19].

For effective battery monitoring, data analysis, and safety, the batteries must be BMS-enabled. In order to safeguard the battery against situations like thermal runaway, the battery swapping provider must make sure the proper BMS is in place. In order to guarantee asset security and battery safety, swappable batteries will be outfitted with sophisticated features such as remote monitoring and immobilization capabilities, Internet of Things-based battery monitoring systems, and other necessary control features.

V. BSS Modes

State-of-the-art EV charging studies include models of battery swapping and charging stations to give EVs additional energy. Electric car drivers link their vehicles to a charging station and allow their batteries to run for several hours while in BCS mode. When an electric vehicle is in BSS mode, it just takes a few minutes to replace its depleted battery with a fully charged one. To comprehend the BSS operation models, this investigation will first concentrate on two key areas: the two types of stations (BSS/BCS) and the number of BSSs and BCSs in the business models. Based on various combinations of BSS and BCS, these can be divided into four categories: a single BSS, multiple BSSs, an integrated BSS and BCS, and multiple BSSs and BCSs [20].

Single BSS: The fundamental mode of operation for a single BSS is the most common business mode among commercial BSSs that are currently in use. The workflow is explained in the following. When the battery's state-of-charge (SOC) drops, the EV driver first notifies the BSS; if the request is granted, the driver then visits the BSS. Second, after being exchanged, the battery is mixed with the batch of swapped batteries at the BSS. Third, if there are charging piles at the recharging center, the switched battery is placed on a charger to be charged. Fourth, when the battery reaches its full charge or the termination criterion is satisfied, it is moved to the batch of fully recharged batteries to wait for future swapping. Lastly, the battery of an arriving EV is installed in place of the fully charged battery that was previously installed in the BSS [21]-[22].

CVR Journal of Science and Technology, Volume 26, June 2024
DOI: 10.32377/cvrjst2610

Multiple BSS: There are three ways that the drivers can start a swapping order: by calling one hour ahead of time, by making a reservation (based on a daily schedule), or by just showing up without an appointment. Second, following the EV driver's swapping orders and ongoing battery condition monitoring at each BSS, the control center chooses a potential BSS for the EV based on predefined objective values and constraints. Once assigned, the EV driver can either accept it and visit the BSS to replace it, or they can reject the suggested BSS. In conclusion, updating each BSS's battery queuing and dynamic availability requires real-time communication between the control center and BSSs [23].

Integrated BSS and BCS: This BSS mode is different from the previous two in that it features ten parking ports in the charging section, eight EVs in the recharging mode, and nine EVs in the queuing mode. Here, two distinct types of chargers are displayed: Four 25 kW maximum power slow chargers and six 50 kW maximum power fast chargers are available. The control center is responsible for handling requests from EV drivers, monitoring the BSS and BCS's current status in real time, determining the most efficient way to replace and recharge EVs, and developing the best charging schedule for both BSSs and BCSs. An integrated BSS and BCS station's decision-making process is defined by the combination of centralized and decentralized models: While decentralized models manage swapping or charging requests independently, centralized models take into account drivers' preferences when deciding whether to swap or charge an incoming EV. This helps to minimize station load.

TABLE II
BENEFITS AND BARRIERS OF BATTERY SWAPPING TECHNOLOGY

Aspects	Benefits of Battery Swapping Technology	Barriers of Battery Swapping Technology
Charging Time	When compared to conventional charging, rapid battery replacement minimizes waiting time.	Requires the development of infrastructure, which can be costly and time-consuming.
Battery Life & Health	Batteries can be maintained and charged to achieve ideal conditions and a longer lifespan by switching them out on a regular basis.	Quality control must be strictly adhered to in order to guarantee that all replaced batteries are in good condition.
Vehicle Cost	Possibility of lowering the initial cost of EVs if batteries are leased as opposed to purchased.	Difficulties with standardization could limit compatibility between different car models, which could raise costs.
Environmental Impact	The production of clean energy is ultimately facilitated by centralized charging, which is essential for optimizing the potential of renewable energy sources.	Batteries should be recycled or disposed of properly because improper handling can pose risks to human health and the environment.
Grid Load	Can centralize charging to lessen the burden on the electrical grid during peak hours.	Needs a steady power supply to guarantee that replaced batteries are constantly charged.

VI. BSS CHALLENGES

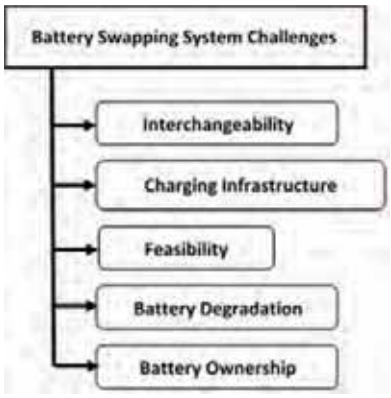

Figure 2. Battery Swapping System Challenges

A. Interchangeability

Cross-platform capability and brand compatibility are prerequisites for technology's success and ascent to prominence in the market. The availability of similar interchangeable battery packs from multiple manufacturers is the only way a battery swapping system has any chance of continuing to be a viable primary option. Consent from the manufacturer is required for this easy fix. But this could also limit the creativity, individuality, and adaptability of goods created solely by a single manufacturer. Furthermore, it will restrict the development of new products because cell manufacturers at the top of the supply chain will be forced to create standardized cells that are comparable to those produced by the next level of manufacturing, which will be the only way to achieve further standardization. It is possible to argue that the battery pack has different power segments, but this would lead to issues with supply and demand as well as potential incompatibilities with cars not built for higher or lower powered battery packs [24]-[25].

B. Feasibility

Currently, the biggest obstacle to battery swapping technology is the battery design. Robustness in removing and reinstalling the battery from the car should be incorporated into its design. There are currently very few cars in India with these kinds of battery pack designs. Hero Maxi, for instance, enables the simple replacement of a discharged battery with a charged one and the independent charging of the discharged battery [26].

C. Infrastructure

The infrastructure required to power the battery packs is much larger, more complex, and expensive than that required for charging. BSSs and charging stations both place equal demands on battery packs in terms of their primary need for charging. The only distinction is that since the former's demand can be managed, the battery packs should always be available for incoming customers and should, therefore, offer charging times that are suitable. Furthermore, for any station to meet its requirements, the stacked quantity of charged battery packs must always exceed the daily demand by a predetermined percentage. It is therefore a feasible plan to have two battery packs for each car, one inside the vehicle and one at the swap station. A national vehicle charging

system makes more financial sense than a national battery swapping system, so even if everything works out, it still seems like a far-off future [27].

D. Battery Degradation

The degradation of battery performance over time has an adverse effect on the maximum battery charge range. Customers will therefore prefer the new battery packs over the alternative of other, comparatively older battery packs because the latter will provide less energy storage owing to deterioration with time, which will be reflected in the EVs' mileage. Customers will therefore only be satisfied with brand-new battery packs, which will significantly shorten each battery pack's operational cycle [28]-[29].

E. Ownership

The battery belongs to the owner of the vehicle; in this scenario, the owner will need to buy a spare battery pack to use as a replacement when the vehicle's battery runs out, which is extremely unlikely to happen. An owner of a vehicle will never have any ownership over a battery pack. This has numerous benefits. EVs are less expensive because the owner of the car does not have to pay for it because he does not own it. Instead, he must pay an extra lease payment in addition to the cost of energy and will never receive his replaced battery back. This can be charged every time a swap is made or at any other frequency that is mutually agreed upon, like once a month. The latter method of calculating the lease amount is more expensive because it includes the service charge for the swapping station and a minimum of two battery packs (instead of just one battery being purchased if the car is charged and already owns one battery). The lease-on-each-swap option is more expensive because there will be greater investment risk associated with swapping stations. Additionally, customers may be persuaded to use fewer swap stations in order to avoid paying these exorbitant fees, particularly if there is a charging option [30]-[31].

VII. Conclusions

BSS strategies are a promising alternative to traditional battery charging stations, offering more business opportunities to dedicated stakeholders. Battery swapping technology for electric vehicles appears to be technically feasible, as evidenced by a number of prototypes and pilot projects. Advances in robotics, automation, and battery design have helped to make the process more efficient and practical. Automation, and battery design have helped to make the process more efficient and practical. In this paper, different types of BSS, mathematical model, BSS modes and the BSS's key challenges, including interchangeability, feasibility, infrastructure, battery degradation, and ownership are discussed briefly. Finally, it is concluded that battery swapping has advantages in terms of convenience and possibly quicker charging times, but its long-term sustainability depends on a number of factors, such as cost-effectiveness, the development of EV ownership models, and technological advancements.

References

[1] J. Han, Y. Zhang, and H. He, "A review of electric vehicle battery swapping technologies, infrastructures, and business models," Journal of Cleaner Production, vol. 257, p. 120470, 2020.

[2] J. Doe and J. Smith, "A Review of Battery Swapping for Electric Vehicles: Opportunities and Challenges," IEEE Transactions on Vehicular Technology, vol. 68, no. 3, pp. 2345-2356, 2020.

[3] International Energy Agency (IEA), "Global EV Outlook 2019: Scaling-up the Transition to Electric Mobility," Paris, IEA, 2019.

[4] BloombergNEF, "Electric Vehicle Outlook 2021," London, BloombergNEF, 2021.

[5] X. Li, L. Lu, M. Ouyang, and J. Li, "Electric vehicle battery swapping system: A critical review of past and future trends," Renewable and Sustainable Energy Reviews, vol. 111, pp. 317-331, 2019.

[6] Deloitte, "Electric Vehicle Trends, Opportunities, and Challenges in an Electrified Future," Deloitte Insights, 2020.

[7] European Environment Agency (EEA), "Electric vehicles and renewable energy: Exploring synergies and assessing challenges," Copenhagen, EEA, 2020.

[8] E. Johnson and D. Brown, "Design and Implementation of a Battery Swapping Station for Electric Vehicles," in Proceedings of the IEEE International Conference on Sustainable Energy Technologies (ICSET), Miami, FL, USA, 2019.

[9] M. Lee and S. Wilson, "Optimization of Battery Swapping Scheduling in Electric Vehicle Fleets," IEEE Transactions on Industrial Electronics, vol. 65, no. 8, pp. 6789-6798, 2018.

[10] C. Liu, X. Chen, F. He, and J. Shen, "Integration and Management of Battery Swapping Stations for Urban Electric Vehicle Systems," IEEE Transactions on Power Systems, vol. 33, no. 3, pp. 3117-3126, 2018.

[11] H. Zhang, X. Zhang, Z. Chen, and X. Hu, "Battery Swapping Technologies for Electric Vehicles: A Comprehensive Review," IEEE Access, vol. 7, pp. 91320-91331, 2019.

[12] Md Tahmid Hussain, Ahmad Bin Afzal, Altaf Hussain Thakurai, Ahmar Azim et al. "Chapter 24 A Comprehensive Review on Electric Vehicle Battery Swapping Stations", Springer Science and Business Media LLC, 2024

[13] T. Chen, Y. Wang, L. Wang, and K. Li, "Battery Swapping Station Design and Optimization for Electric Vehicle Fleets," IEEE Transactions on Transportation Electrification, vol. 4, no. 2, pp. 408-417, 2018.

[14] L. Zhang, S. Lou, Y. Wu, L. Yi and B. Hu, "Optimal scheduling of electric vehicle battery swap station based on time-of-use pricing," 2014 IEEE PES Asia-Pacific Power and Energy Engineering Conference (APPEEC), Hong Kong, China, 2014, pp. 1-6.

[15] T. Boonraksa, P. Boonraksa, W. Pinthurat and B. Marungsri, "Optimal Battery Charging Schedule for a Battery Swapping Station of an Electric Bus Furkan Ahmad with a PV Integration Considering Energy Costs and Peak-to-Average Ratio," in IEEE Access, vol. 12, pp. 36280-36295, 2024.

[16] B. Bairwa, M. Sarvagya, S. Kumar and A. Banik, "Battery Swapping Mobile Service Station for Electric Vehicles Application," 2021 Second International Conference on Smart Technologies in Computing, Electrical and Electronics (ICSTCEE), Bengaluru, India, pp. 1-6, 2021.

[17] H. Yang, C. Guo, J. Ren and J. Sheng, "A Coordinated Charging Strategy on Battery Swapping Station in Microgrid Considering Battery to Grid," 2019 IEEE Innovative Smart Grid Technologies - Asia (ISGT Asia), Chengdu, China, pp. 3322-3326, 2019.

[18] C. Dongdong et al., "Research on standard scheme of battery swapping mechanism for electric commercial vehicle," 2023 International Conference on Electronics and Devices, Computational Science (ICEDCS), Marseille, France, pp. 785-790, 2023.
[19] G. Battapothula, C. Yammani and S. Maheswarapu, "Multi-Objective Optimal Scheduling of Electric Vehicle batteries in Battery Swapping Station," 2019 IEEE PES Innovative Smart Grid Technologies Europe (ISGT-Europe), Bucharest, Romania, pp. 1-5, 2019.
[20] S. S. Kumbhar and V. N. Kalkhambkar, "Optimal Planning of Battery Swapping and Charging Stations for the Urban Cities," 2023 International Conference on Advanced Computing Technologies and Applications (ICACTA), Mumbai, India, pp. 1-6, 2023.
[21] Sujie Shao, Shaoyong Guo, Xuesong Qiu. "A Mobile Battery Swapping Service for Electric Vehicles Based on a Battery Swapping Van", Energies, 2017
[22] Xian Zhang and G. Wang, "Optimal dispatch of electric vehicle batteries between battery swapping stations and charging stations," 2016 IEEE Power and Energy Society General Meeting (PESGM), Boston, MA, pp. 1-5, 2016.
[23] Kriti Yadav, Anirbid Sircar. "A review on electric vehicle transport policy of India with certain recommendations", MRS Energy & Sustainability, 2022
[24] S. Kabir, A. Shufian, R. Islam, M. M. Islam, M. A. Islam and M. S. R. Mahin, "Impact of Grid-tied Battery to Grid (B2G) Technology for Electric Vehicles Battery Swapping Station," 2023 10th IEEE International Conference on Power Systems (ICPS), Cox's Bazar, Bangladesh, pp. 1-6, 2023.
[25] S. Jain, Z. Ahmad, M. S. Alam and Y. Rafat, "Battery Swapping Technology," 2020 5th IEEE International Conference on Recent Advances and Innovations in Engineering (ICRAIE), Jaipur, India, pp. 1-4, 2020.
[26] Furkan Ahmad, Mohammad Alam, Ibrahim Alsaidan, Samir M Shariff. "Battery Swapping Station for Electric Vehicles: Opportunities and Challenges", IET Smart Grid, 2020
[27] H. Wu, G. K. H. Pang, K. L. Choy and H. Y. Lam, "An Optimization Model for Electric Vehicle Battery Charging at a Battery Swapping Station," in IEEE Transactions on Vehicular Technology, vol. 67, no. 2, pp. 881-895, Feb. 2018.
[28] X. Yu, F. Wang and H. Wang, "Optimal Battery Swapping and Charging Strategy Considering On-Site Solar Generation," 2023 IEEE/IAS Industrial and Commercial Power System Asia (I&CPS Asia), Chongqing, China, pp. 1082-1087, 2023.
[29] Md Tahmid Hussain X. Li, Y. Cao, S. Wan, S. Liu, H. Lin and Y. Zhu, "A Coordinated Battery Swapping Service Management Scheme Based on Battery Heterogeneity," in IEEE Transactions on Transportation Electrification, vol. 9, no. 3, pp. 4474-4491, Sept. 2023.
[30] Reza Hemmati. "Integration of electric vehicles and charging stations" , Elsevier BV, 2024.
[31] Hao Wu. "A Survey of Battery Swapping Stations for Electric Vehicles: Operation Modes and Decision Scenarios", IEEE Transactions on Intelligent Transportation Systems, 2022.

E-ISSN 2581 – 7957
P-ISSN 2277 – 3916

CVR Journal of Science and Technology, Volume 26, June 2024
DOI: 10.32377/cvrjst2611

Navigating the Present and Future Dynamics of Electric Vehicle Fast Charging and its Impact on Grid

Dr. M. Chiranjivi[1], Mr. K. Suresh[2] and Mr. M. Siddartha[3]
[1]Associate Prof, Hyderabad Institute of Technology and Management/ EEE Department, Hyderabad, India.
Email: chiranjivimadduluri@gmail.com
[2]Associate Prof, Hyderabad Institute of Technology and Management/ EEE Department, Hyderabad, India.
Email: sureshk.eee@hitam.org
[3]Assistant Prof, Hyderabad Institute of Technology and Management/ EEE Department, Hyderabad, India.
Email: siddartham.eee@hitam.org

Abstract: **As electric vehicle (EV) adoption surges worldwide, the need for fast charging infrastructure becomes paramount. Fast charging technology alleviates range anxiety and bolsters EV practicality. This comprehensive analysis delves into current challenges and future prospects surrounding EV fast charging and its grid impact. Examining the state of fast charging technology, it scrutinizes charging standards, connector types, and power levels across global regions. Emphasis is placed on key market players and the imperative for interoperability and standardization to seamlessly integrate EVs into the power grid. Voltage fluctuations, harmonics, and power factor issues stemming from rapid, high-power charging pose technical hurdles. Solutions like advanced power electronics, grid management tactics, and enhanced communication between EVs and the grid are explored to uphold stability and power quality. Consideration is given to energy sources fueling fast chargers, including renewable integration and environmental repercussions. Economic facets, encompassing infrastructure deployment costs and grid upgrade analyses, are examined amidst escalating electricity demand and potential grid expansion needs. A forward-looking perspective addresses future challenges and opportunities. This includes advancements in battery tech, smart grid solutions, and bidirectional power flow potential between EVs and the grid.**

Index Terms: **Battery electric vehicles (BEVs), Grid, Fast Charging, plug-in hybrid electric vehicles (PHEVs).**

I. Introduction

The global shift to electric mobility has gained tremendous impetus in recent years, with electric vehicles (EVs) emerging as a transformative answer to the environmental and energy concerns connected with traditional internal combustion engine vehicles. The increasing adoption of EVs marks a significant stride in reducing greenhouse gas emissions and decreasing reliance on fossil fuels. A critical component for the widespread acceptance of EVs is the development of efficient and high-speed charging infrastructure, commonly known as "fast charging." [1] Fast charging plays a vital role in alleviating range anxiety, enhancing the practicality of EVs, and promoting their mainstream adoption. This Paper delves into the current issues and future challenges surrounding the fast charging of electric vehicles and its profound implications for grid power quality. While the proliferation of fast charging technology represents a remarkable achievement in the EV domain, it also brings forth a plethora of technical, environmental, and economic considerations that warrant a comprehensive examination. Understanding these issues is imperative for ensuring the seamless integration of electric vehicles into the existing power grid infrastructure.

1.1 The EV Revolution: A Global Shift in Mobility

For years, the transportation industry has significantly added to environmental problems like greenhouse gas emissions, air pollution, and high energy usage. In reaction, nations across the globe are vigorously advocating for the electrification of transportation as a remedy. Electric vehicles (EVs), which include Battery Electric Vehicles (BEVs) and Plug-in Hybrid Electric Vehicles (PHEVs), stand as pioneers in this transformation, presenting cleaner and more effective options compared to conventional gasoline and diesel vehicles.

Several factors have converged to drive the rapid growth of the EV industry. Advances in battery technology, coupled with decreasing costs of lithium-ion batteries, supportive government policies, and a growing awareness of environmental issues, have propelled the adoption of EVs to new heights. As a result, the automotive market is experiencing a surge in EV production, accompanied by an expansion of charging infrastructure to facilitate this transition.

Fast charging technology plays a crucial role in addressing the concerns of EV owners regarding charging time and range limitations [2]. Fast chargers, capable of delivering high power to an EV in a matter of minutes, have become emblematic of the industry's progress. They significantly reduce the inconvenience of lengthy charging times associated with conventional chargers, thus accelerating the adoption of EVs and further driving the growth of the industry.

1.2 The Need for Fast Charging Infrastructure

Fast charging infrastructure plays a pivotal role in establishing EVs as a practical choice for everyday transportation. Unlike traditional chargers that require hours for a full charge, fast chargers can provide a significant range boost in just 15-30 minutes. [3] This remarkable reduction in charging time has the potential to transform

Received on 15-03-2024, Revised on 14-04-2024, Accepted on 14-05-2024.

CVR Journal of Science and Technology, Volume 26, June 2024
DOI: 10.32377/cvrjst2611

how people perceive and utilize EVs in their daily lives, effectively eliminating range anxiety—a significant psychological barrier to EV adoption.

However, as fast charging technology becomes more widespread, it brings forth a new set of challenges. One of the most pressing concerns is its impact on grid power quality. Rapid and high-power charging can result in voltage and current fluctuations, harmonics, and power factor issues, placing stress on existing grid infrastructure and necessitating investments in upgrades. Moreover, the energy sources powering fast chargers, particularly in regions heavily reliant on fossil fuels, raise environmental concerns. As the adoption of EVs will continue to grow, the demand for energy for charging will increase, prompting a closer examination of the sustainability of this transition.

The objective of this paper is to provide an extensive examination of the present concerns and forthcoming obstacles linked with rapid electric vehicle charging and its effects on grid power quality. Furthermore, it will investigate possible remedies and prospects to guarantee the establishment of a sustainable and dependable EV charging infrastructure while maintaining grid stability and power quality.

II. Current Issues Regarding Electric Vehicles' Fast Charging

The rapid growth of Electric Vehicles (EVs) and the increasing demand for fast charging solutions have brought about several pressing issues that need to be addressed for the sustainable integration of EVs into our transportation infrastructure. Here are some current issues regarding electric vehicles' fast charging:[4]

Charging Infrastructure Gap:

As electric vehicle (EV) adoption rises, the development of fast charging infrastructure fails to keep pace, resulting in "charging deserts" in certain areas. This situation can instill range anxiety among EV owners and dissuade prospective buyers from transitioning to electric vehicles.

Uneven Distribution:

Fast charging stations are often concentrated in urban areas, leaving suburban and rural communities with limited charging options. This uneven distribution hinders the accessibility and convenience of EVs for a broader population.[5]

Power Demand Peaks:

Fast charging stations demand a substantial amount of electricity within a brief timeframe, causing localized spikes in power demand during peak charging periods. This strain on local grids can potentially result in power outages or voltage fluctuations.

Grid Capacity:

As more EVs hit the road and require fast charging, the grid's capacity to handle the increased load needs to be upgraded. Without proper upgrades, widespread fast charging could overload local distribution networks.

Intermittent Charging:

The intermittent nature of fast charging (users plugging in and unplugging at different times) can cause sudden and unpredictable fluctuations in power demand. This can challenge grid stability and require careful load management.

Charging Speed vs. Battery Life:

Extremely fast charging can degrade battery health over time. Finding the right balance between fast charging speeds and preserving battery life is crucial for maximizing the longevity of EV batteries is shown in figure 1. [6]

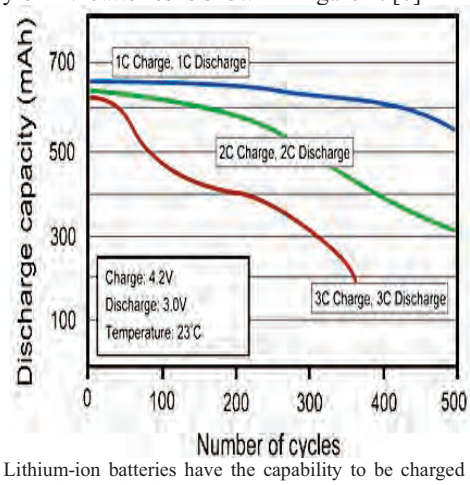

Fig 1. Lithium-ion batteries have the capability to be charged at rates faster than 1C, albeit with a decrease in cycle life.

Energy Source and Environmental Concerns:

The source of electricity for fast charging can impact the overall environmental benefits of EVs. If the electricity comes from fossil fuels, the reduction in emissions may be limited.

Cost: The high upfront costs of installing fast charging stations can be a deterrent for businesses and governments looking to expand charging infrastructure. Balancing the investment needed with the potential revenue from charging services is a challenge.

Compatibility and Standards:

Different fast charging technologies and connector types (e.g., CHAdeMO, CCS, Tesla Superchargers) can lead to compatibility issues and confusion for EV owners, as well as complicate infrastructure development.

Regulatory Barriers:

Regulatory and permitting challenges can slow down the installation of fast charging stations. Streamlining regulations and permitting processes is essential to accelerate infrastructure deployment.

Consumer Behavior and Education:

Shifting consumer's behaviors to adapt to fast charging norms and educating EV users about optimal charging practices to prevent grid strain and maintain battery health is an ongoing challenge.

It's crucial to tackle these present challenges to establish a dependable and user-friendly fast charging infrastructure that facilitates the widespread acceptance of electric vehicles

CVR Journal of Science and Technology, Volume 26, June 2024
DOI: 10.32377/cvrjst2611

and contributes to a more sustainable future for transportation.

Scaling Charging Infrastructure:

The rapid increase in EV adoption necessitates a vast expansion of fast charging infrastructure to meet the growing demand. Developing a network of charging stations that is both widespread and strategically located is essential. The Solution is Collaborative efforts between governments, utilities, and private companies to plan and fund the construction of charging stations in urban, suburban, and rural areas[7]. Incorporating charging stations into existing infrastructure, such as parking lots and highways, can optimize their accessibility.

Load Balancing and Grid Stability:

Coordinating the charging of numerous EVs at fast charging stations simultaneously can lead to concentrated power demand spikes, straining the local grid and causing voltage fluctuations.[8] One solution involves in implementing intelligent charging algorithms that adjust charging rates according to grid conditions, energy demand, and available capacity, thereby overcoming this challenge. Dynamic load management systems can distribute charging loads evenly throughout the day and across multiple stations.

Dynamic Energy Demand:

The unpredictability of EV charging patterns can challenge grid operators' ability to anticipate and meet energy demand, potentially leading to imbalances between supply and consumption. To overcome this Developing advanced predictive models that incorporate data from EV charging behavior, weather patterns, and other variables to forecast energy demand accurately. Utilizing demand-response initiatives that incentivize the owners of electric vehicles to charge during non-peak hours can effectively control energy demand.

Grid Reinforcement and Upgrades:

Expanding the quantity and capacity of fast charging stations may necessitate substantial enhancements to local grid infrastructure to accommodate the increased power requirements. It can be reduced by Prioritizing grid modernization projects that reinforce infrastructure, upgrade transformers, and enhance substation capacity. Close collaboration between utilities and charging network operators is essential to plan these upgrades effectively reduce.

Bidirectional Energy Flow (V2G):

Integrating vehicle-to-grid (V2G) technology introduces challenges in managing bidirectional energy flow between Electric Vehicles (EVs) and the grid, necessitating robust communication and control systems. This complexity can be mitigated by establishing standardized V2G protocols and communication interfaces to ensure compatibility across various vehicle models and charging networks [9]. Additionally, incentivizing EV owners to engage in V2G programs can promote their active participation. This information is depicted in Figure 2.

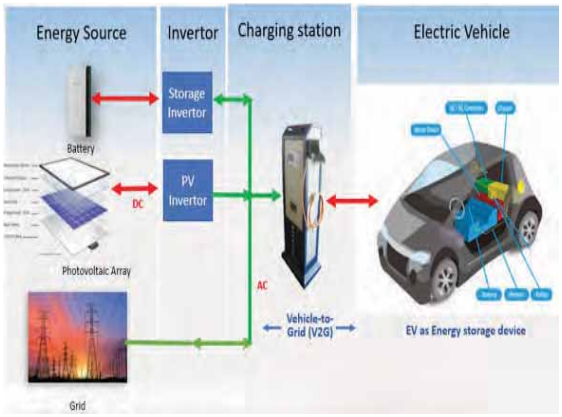

Fig 2. Bidirectional_EV-chargers-explained-V2H-V2G

III. Types of Electric Vehicles Fast Charging

DC Fast Charging (DCFC): Examining the technical aspects of DC fast charging involves supplying direct current to the electric vehicle battery at elevated voltages, facilitating rapid charging. DC fast charging, also referred to as Level 3 charging, delivers significantly higher power input to electric vehicles compared to Alternating Current (AC) charging. It predominantly relies on three primary components [10]. DC fast chargers feature high-power electronics that convert AC power from the grid into DC power for efficient and rapid charging. Charging power levels can vary from 50 kW to 350 kW and beyond, enabling a substantial charge within a short duration. Below figure is an illustration of the DC fast charging station for electric vehicles

Fig 3. DC Fast Charging Station

3.1 Benefits of DC Fast Charging

a. Reduced Charging Time: A key benefit of DC fast charging lies in its remarkable reduction of charging duration. Unlike conventional Level 2 AC chargers, which may require hours to fully charge an electric vehicle (EV), DC fast chargers can offer a significant charge increase in just 30 minutes or less. This effectively alleviates concerns about range anxiety and enhances the practicality of EVs for long-distance travel.

b. Convenience: DC fast chargers are strategically located along major highways and in urban areas, making long-distance travel more accessible for EV owners. Convenience stores, shopping centers, and rest areas often host these chargers, providing a seamless charging experience.

c. Grid Stability: DC fast charging can be integrated into smart grid systems, enabling dynamic charging rates and load balancing. This helps to manage the grid's demand and reduce peak load impact.

3.2 The Future of DC Fast Charging

The future of DC fast charging looks promising, with advancements in charger technology, battery management, and grid integration. High-power chargers capable of delivering 350 kW and beyond are being developed, further reducing charging times. Additionally, bidirectional charging, which allows EVs to supply power back to the grid, holds potential benefits for grid management and energy resilience.

3.3 Ultra-Fast Charging

Delving into advancements in ultra-fast charging technologies that promise even shorter charging times through higher power delivery[11].

Ultra-fast charging for electric vehicles (EVs) represents the cutting edge of EV charging technology, offering significantly faster charging speeds than traditional DC fast chargers. The environmental impact of ultra-fast charging depends on the source of electricity. Like other charging technologies, the transition to renewable energy sources is crucial to minimize the carbon footprint of ultra-fast charging.

3.4 Future Challenges

As the paper unfolds, the spotlight shifts towards the future, shedding light on the innovative strategies, technological advancements, and policy interventions that hold the potential to mitigate the challenges posed by EV fast charging. Taking a forward-thinking approach involves examining the progression of grid management, scalability of charging infrastructure, implementation of smart charging solutions, integration of energy storage, and the emergence of vehicle-to-grid (V2G) technology as a potentially transformative factor. Below is a concise overview.

Charging Speed: Ultra-fast chargers are capable in delivering extremely high-power levels, often exceeding 350 kW and sometimes reaching up to 350 kW or more. This is several times faster than even the most powerful DC fast chargers, which typically offer charging speeds of up to 50-350 kW.

Reduced Charging Time: The high-power output of ultra-fast chargers means that EVs can be charged to a substantial percentage of their battery capacity in just a few minutes. In some cases, a 15–20-minute charge can provide enough energy to extend an EV's range significantly.

Impact on Grid: Due to their high-power requirements, ultra-fast chargers may pose challenges to the local power grid, necessitating grid upgrades or intelligent grid management strategies to accommodate them without causing disruptions.

Battery Compatibility: EVs need to be equipped with batteries that can accept ultra-fast charging to make full use of these chargers. Battery technology and thermal management systems must be capable of handling the high charging currents and dissipating the resulting heat.

Bidirectional Charging: Certain ultra-fast chargers come with bidirectional charging capabilities, enabling electric vehicles (EVs) not just to charge but also to feed energy back into the grid. This feature holds promise in bolstering grid stability and facilitating the implementation of vehicle-to-grid (V2G) applications.

Ultra-fast charging is at the forefront of EV charging technology, providing a solution for EV owners who require rapid charging capabilities. As this technology evolves and becomes more widespread, it has the potential to make long road trips in electric vehicles more practical and to further drive the transition to sustainable transportation.

3.5 Charging Stations and Infrastructure

Power Levels: Discussing the range of power levels offered by fast charging stations, from lower-power stations suitable for home use to high-power stations along highways and in urban areas [12].

Level 1 Charging (120V, AC): Level 1 charging is the most basic and typically involves plugging an EV into a standard household electrical outlet using a portable charging cord [10]. It provides a very low charging power level of about 1-2 kW, suitable for overnight charging at home but not ideal for fast charging.

Level 2 Charging (240V, AC): Level 2 charging stands as the prevalent choice for residential charging. Operating at 240 volts, it offers charging power varying from 3 kW to 22 kW, dependent on the charger model. Widely deployed at residences, workplaces, and public charging stations, Level 2 chargers provide faster charging compared to Level 1 alternatives.

Connector Types: Examining various charging connector types (CHAdeMO, CCS, Tesla Superchargers)[10] and their compatibility with different EV models. Connectors designed for electric vehicles (EVs) serve a vital function by facilitating the charging process and guaranteeing compatibility with diverse charging infrastructure. Below is a concise overview of prevalent connector types used for EVs.

CCS (Combined Charging System): The CCS connector integrates a Type 2 connector with two extra DC pins. This configuration enables both AC and DC charging through a single port. CCS connectors are widely adopted in Europe and North America for DC fast charging, offering compatibility with a broad range of EVs.

CHAdeMO: CHAdeMO connectors are recognized by their unique design and are predominantly used in Japan. They are primarily associated with DC fast charging and are found in many Nissan and Mitsubishi electric vehicles.

Tesla Connector: Tesla has its proprietary connector, designed for exclusive use with Tesla vehicles. Tesla Superchargers use this connector, which can provide high-power DC charging up to 250 kW.

Tesla Destination Charger Connector: While Tesla vehicles use their proprietary connector for fast charging, Tesla also offers destination chargers with connectors compatible with their vehicles. These chargers are typically located at hotels, restaurants, and other destinations for slower charging during longer stops.

CVR Journal of Science and Technology, Volume 26, June 2024
DOI: 10.32377/cvrjst2611

Renewable Integration:

Challenge: Integrating renewable energy sources (solar, wind) into fast charging networks introduces variability due to weather conditions, potentially leading to mismatches between energy supply and charging demand[13].

Solution: Implementing energy management systems that combine real-time renewable energy generation forecasts with charging demand predictions to optimize energy usage. Energy storage systems can store excess renewable energy and release it during peak charging times.

Smart Charging Algorithms:

Challenge: Developing intelligent charging algorithms that factor in grid conditions, energy prices, and user preferences to optimize charging while maintaining grid stability.

Solution: Utilizing machine learning and artificial intelligence to create adaptive charging algorithms that continuously learn and adjust based on real-time data. These algorithms can also consider factors such as user schedules and available renewable energy.

Cybersecurity and Data Management:

Challenge: As fast charging systems become more interconnected and reliant on digital communication, safeguarding charging infrastructure from cyber threats and managing data privacy become paramount [14].

Solution: Implementing robust cybersecurity measures, including encryption and authentication protocols, to protect charging networks and user data. Establishing data management standards to ensure the secure collection, storage, and sharing of charging-related data.

Navigating these future challenges requires a collaborative effort from various stakeholders, including governments, utilities, automakers, technology providers, and consumers. By addressing these challenges head-on, the transition to a sustainable and grid-friendly fast charging ecosystem can be achieved, facilitating the broader adoption of electric vehicles, and contributing to a cleaner and more resilient energy future.

IV. Impact on Grid Power Quality

4.1 Load Profiles and Peaks

High Power Demand Spikes: Describing how fast charging stations can lead to localized power demand spikes during peak usage times, potentially overloading local grids. Fast charging stations for Electric Vehicles (EVs) can lead to localized power demand spikes during peak usage times because they draw a high amount of electricity in a short time[15]. When multiple EVs charge simultaneously at these stations, it strains the local capacity of grids, potentially causing voltage fluctuations and overloads, as the grid may not be designed to handle such sudden and substantial increases in power demand. This can lead to grid instability and higher costs, necessitating grid upgrades and load management solutions to mitigate the issue.

4.2 Voltage Regulation

Exploring how rapid and intermittent power draws from multiple fast charging stations can lead to voltage fluctuations that challenge grid stability. Rapid voltage changes can damage electrical equipment, such as transformers, switches, and capacitors, leading to increased maintenance costs and potential outages. Voltage fluctuations can result in poor power quality, affecting the efficiency and reliability of electrical devices and appliances connected to the grid. Rapid voltage changes can cause lights to flicker, which is not only annoying but can also indicate power instability. Sustained voltage fluctuations can shorten the lifespan of sensitive electronic equipment and appliances. Frequent voltage fluctuations may destabilize the local grid, potentially causing blackouts or other disruptions. Discussing the potential consequences of voltage deviations on appliances, equipment, and the overall power quality.

To mitigate these issues, grid operators and charging station owners often employ voltage control measures and invest in grid upgrades to ensure power quality and stability during fast charging activities.

4.3 Frequency Stability

Exploring the impact of rapid power demand changes on grid frequency stability and its significance in maintaining a reliable power supply. Fast charging stations draw a significant amount of power in a short time, creating sudden and large power demand spikes. These abrupt changes in power consumption can lead to imbalances in the grid's supply and demand, affecting its frequency stability[16]. Grid frequency is typically maintained at a stable level (e.g., 50 Hz or 60 Hz), and deviations from this standard can indicate grid instability. Fast charging's power surges can lead to frequency deviations, potentially causing power quality issues. Grid operators must invest in frequency regulation mechanisms, such as energy storage and advanced control systems, to counteract the effects of fast charging and maintain grid stability.

The fast charging can impact grid frequency stability by introducing rapid and significant changes in power demand. To address this, grid operators implement measures to regulate frequency deviations and ensure the reliability of the electrical supply.

4.4 Harmonic Distortion

Detailing how fast charging can introduce harmonic distortion into the grid, potentially affecting sensitive electronics and equipment. Fast charging stations often employ power electronics and non-linear devices like rectifiers and inverters to convert and manage electricity for efficient charging. These non-linear loads can introduce harmonics into the grid. Harmonics created by fast charging equipment can cause voltage distortions, which affect the purity and quality of the electrical supply[17]. This can lead to voltage fluctuations and other issues of power quality. Harmonic distortions can interfere with the normal operation of electrical devices and equipment connected to the grid. This can lead to reduced performance and potential damage to sensitive electronics. High harmonic distortions can result in non-compliance with grid quality standards and regulations, which may require grid operators to take corrective actions.

CVR Journal of Science and Technology, Volume 26, June 2024
DOI: 10.32377/cvrjst2611

V. Future Challenges and Solutions

5.1 Grid Integration Strategies

Load Management: Discussing the implementation of advanced load management systems to distribute charging demand evenly and prevent localized power spikes.

Demand Response Programs: Examining the possibilities of demand response initiatives that encourage electric vehicle (EV) owners to charge during off-peak hours, thereby alleviating pressure on the grid [18].

Strategies for integrating fast charging of electric vehicles (EVs) into the grid encompass planning and technological solutions aimed at establishing efficient and dependable charging infrastructure while mitigating impact on the electric grid. Here is a brief outline of these strategies.

Location Planning: Identifying suitable locations for fast-charging stations is crucial. Stations are typically placed along highways, in urban areas, and near high-demand locations like shopping centers. This strategic placement ensures convenience for EV users and efficient use of resources.

Load Management: Grid operators and charging station operators use load management techniques to distribute and schedule fast-charging sessions to avoid overloading the grid during peak demand. This can include demand response programs, dynamic pricing, and real-time monitoring of grid conditions.

High-Voltage Direct Current (HVDC) Charging: HVDC fast chargers are increasingly used to reduce energy losses and provide high-power charging. These chargers convert AC power from the grid into DC power for faster and more efficient charging.

Battery Energy Storage: Incorporating energy storage systems into fast-charging stations can alleviate electricity demand surges and lessen the burden on the grid. Batteries have the capability to store electricity during periods of low demand and discharge it during periods of high demand.

Smart Charging Infrastructure: Deploying intelligent charging technology enables flexible alterations in charging rates depending on grid conditions and the accessibility of renewable energy. This guarantees that aligns of better EV charging with grid demands and promotes environmental sustainability.

Renewable Energy Integration: Co-locating fast-charging stations with renewable energy sources, such as solar panels or wind turbines, helps in reducing the carbon footprint of EV charging and supports grid integration by using clean energy.

Grid Upgrades: In some cases, grid infrastructure may need to be upgraded to accommodate fast-charging stations. This can involve increasing capacity, reinforcing distribution lines, and installing transformers to meet the demand.

Grid Connectivity: Ensuring that fast-charging stations are equipped with reliable and high-speed connectivity to the grid is essential for real-time communication and control, allowing for efficient load management and billing.

Standardization: Standardized connectors, communication protocols, and power levels for fast-charging stations help streamline the deployment of charging infrastructure and improve interoperability between different EV models.

Monitoring and Data Analytics: Continuous monitoring and data analytics enable operators to track charging patterns, usage, and grid impact, helping optimize charging infrastructure and grid integration strategies over time.

These grid integration strategies for fast charging of EVs are vital for meeting the growing demand for electric vehicles while ensuring grid reliability and sustainability. They aim to balance the needs of EV users with the capabilities of the electric grid to ensure a smooth transition to cleaner transportation.

5.2 Energy Storage Integration:

Generally, the problem of Integrating energy storage solutions into fast charging stations requires addressing technical, economic, and regulatory challenges to ensure optimal system performance and cost-effectiveness.

It can be resolved by Researching and developing energy storage technologies that can handle the high-power demands of fast charging, as well as evaluating the potential for repurposing used EV batteries for stationary energy storage[19]. Regulatory frameworks should incentivize the deployment of energy storage at charging sites. It is shown in fig. 4.

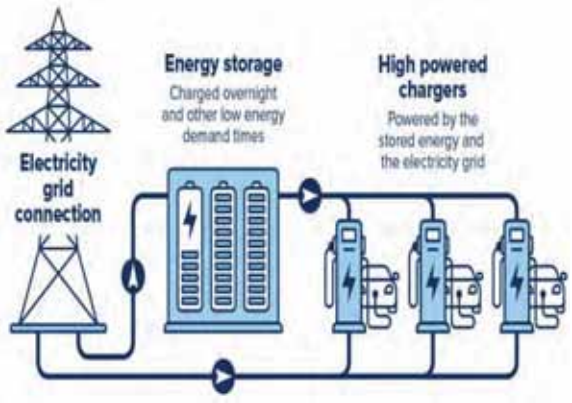

Fig 4. Energy Storage Integration

Battery Energy Storage[20]: Analyzing the role of energy storage systems at charging stations to store excess energy during low demand and release it during peak times, enhancing grid stability.

5.3 Smart Charging Algorithms

AI and Machine Learning: Exploring the utilization of artificial intelligence and machine learning in crafting intelligent charging algorithms that optimize charging schedules [21], considering grid conditions and user preferences.

5.4 Vehicle-to-Grid (V2G) Technology

Grid Support: Describing how V2G technology enables electric vehicles (EVs) to feed power back into the grid during peak demand periods, aiding grid stability and creating potential revenue opportunities. Vehicle-to-Grid (V2G) technology facilitates EVs not only in drawing power from the grid for charging but also in supplying surplus electricity back to the grid when required [22]. This

CVR Journal of Science and Technology, Volume 26, June 2024
DOI: 10.32377/cvrjst2611

bidirectional energy flow is enabled by specialized inverters and communication systems incorporated into both the EV and the electric grid infrastructure. V2G technology offers numerous advantages and applications.

1. Grid Support: Electric vehicles (EVs) have the potential to function as distributed energy resources, aiding in grid stabilization by providing electricity during peak demand periods or emergency scenarios.
2. Peak Shaving: V2G[23] can reduce the strain on the grid during periods of high electricity demand by using the energy stored in EV batteries to power homes and businesses.
3. Renewable Integration[24]: V2G can store excess renewable energy when generation is high and supply it back to the grid when renewable sources are less productive, enhancing grid reliability.
4. Cost Savings: EV owners can earn revenue by selling surplus energy back to the grid or benefit from reduced charging costs during off-peak hours.
5. Environmental Benefits: By utilizing EV batteries for grid support, V2G can help reduce the need for fossil fuel power plants and decrease greenhouse gas emissions[25].

However, there are challenges to widespread V2G adoption, including the need for standardized protocols, grid infrastructure upgrades, and battery durability concerns. Nonetheless, V2G technology holds great promise in enabling more sustainable and resilient energy systems.

5.5 Grid Modernization

Upgrades and Advances: Discussing the necessity of grid modernization efforts to accommodate the increased demand for fast charging, including the integration of advanced monitoring and control technologies. Grid modernization, particularly for accommodating the fast charging of electric vehicles (EVs), presents several challenges and solutions as we move toward a cleaner and more electrically dependent transportation system. Grid modernization efforts may focus on enhancing the resilience and redundancy of grid infrastructure to withstand potential disruptions, ensuring that fast-charging stations remain operational during emergencies. Grid modernization for fast EV charging is crucial for supporting the transition to electric transportation and achieving energy sustainability goals while maintaining grid reliability and efficiency. These measures aim to balance the demands of EV users with the capabilities of the electric grid.

VI. Conclusion

This paper highlights the pivotal role of EV fast charging in shaping the future of sustainable transportation. It stresses the importance of a comprehensive approach that goes beyond technological advancements, emphasizing collaboration among stakeholders—from governments and utilities to automakers and consumers. While the challenges ahead are significant, so too are the opportunities for innovation and positive change. By addressing the complexities of EV fast impact on charging on grid power quality, society can embark on a path toward cleaner, more efficient, and resilient mobility.

While fast charging is crucial for EV adoption and emissions reduction, its implications for grid power quality are multifaceted and require careful consideration. Balancing the accessibility of fast charging with grid stability presents a significant challenge that demands cooperation among governments, utilities, and the private sector.

The fast charging of EVs presents immediate challenges and long-term considerations for the quality of grid power and reliability. Current issues revolve around grid capacity constraints, load fluctuations, and the need for infrastructure upgrades to meet fast-charging demand. As EV adoption grows, these challenges will become more pronounced. Balancing this growth with the quality of grid power is complex but necessary.

Grid modernization, smart grid technologies, and advanced load management strategies will be essential in addressing these challenges and ensuring that fast charging of EVs becomes a sustainable component of the modern energy landscape.

References

[1] D. Lopez-Behar, M. Tran, T. Froese, J. R. Mayaud, O. E. Herrera, and W. Merida, ‘Charging infrastructure for electric vehicles in Multi-Unit Residential Buildings: Mapping feedback and policy recommendations’, Energy Policy, vol. 126, pp. 444–451, Mar. 2019, doi: 10.1016/j.enpol.2018.10.030.

[2] H. Roy et al., ‘Global Advancements and Current Challenges of Electric Vehicle Batteries and Their Prospects: A Comprehensive Review’, Sustainability, vol. 14, no. 24, Art. no. 24, Jan. 2022, doi: 10.3390/su142416684.

[3] T. Gnann, S. Funke, N. Jakobsson, P. Plötz, F. Sprei, and A. Bennehag, ‘Fast charging infrastructure for electric vehicles: Today’s situation and future needs’, Transp. Res. Part Transp. Environ., vol. 62, pp. 314–329, Jul. 2018, doi: 10.1016/j.trd.2018.03.004.

[4] F. Alanazi, ‘Electric Vehicles: Benefits, Challenges, and Potential Solutions for Widespread Adaptation’, Appl. Sci., vol. 13, no. 10, Art. no. 10, Jan. 2023, doi: 10.3390/app13106016.

[5] G. J. Carlton and S. Sultana, ‘Electric vehicle charging station accessibility and land use clustering: A case study of the Chicago region’, J. Urban Mobil., vol. 2, p. 100019, Dec. 2022, doi: 10.1016/j.urbmob.2022.100019.

[6] Z. Gao, H. Xie, X. Yang, W. Niu, S. Li, and S. Chen, ‘The Dilemma of C-Rate and Cycle Life for Lithium-Ion Batteries under Low Temperature Fast Charging’, Batteries, vol. 8, no. 11, Art. no. 11, Nov. 2022, doi: 10.3390/batteries8110234.

[7] A. Shrivastava, J. Ranga, V. N. S. L. Narayana, Chiranjivi, and Y. D. Borole, ‘Green Energy Powered Charging Infrastructure for Hybrid EVs’, in 2021 9th International Conference on Cyber and IT Service Management (CITSM), Sep. 2021, pp. 1–7. doi: 10.1109/CITSM52892.2021.9589027.

[8] N. M. Manousakis, P. S. Karagiannopoulos, G. J. Tsekouras, and F. D. Kanellos, 'Integration of Renewable Energy and Electric Vehicles in Power Systems: A Review', Processes, vol. 11, no. 5, Art. no. 5, May 2023, doi: 10.3390/pr11051544.
[9] M. R. H. Mojumder, F. Ahmed Antara, M. Hasanuzzaman, B. Alamri, and M. Alsharef, 'Electric Vehicle-to-Grid (V2G) Technologies: Impact on the Power Grid and Battery', Sustainability, vol. 14, no. 21, Art. no. 21, Jan. 2022, doi: 10.3390/su142113856.
[10] M. S. Mastoi et al., 'An in-depth analysis of electric vehicle charging station infrastructure, policy implications, and future trends', Energy Rep., vol. 8, pp. 11504–11529, Nov. 2022, doi: 10.1016/j.egyr.2022.09.011.
[11] S. Mateen, M. Amir, A. Haque, and F. I. Bakhsh, 'Ultra-fast charging of electric vehicles: A review of power electronics converter, grid stability and optimal battery consideration in multi-energy systems', Sustain. Energy Grids Netw., vol. 35, p. 101112, Sep. 2023, doi: 10.1016/j.segan.2023.101112.
[12] G. F. Savari et al., 'Assessment of charging technologies, infrastructure and charging station recommendation schemes of electric vehicles: A review', Ain Shams Eng. J., vol. 14, no. 4, p. 101938, Apr. 2023, doi: 10.1016/j.asej.2022.101938.
[13] P. Das, P. Mathuria, R. Bhakar, J. Mathur, A. Kanudia, and A. Singh, 'Flexibility requirement for large-scale renewable energy integration in Indian power system: Technology, policy and modeling options', Energy Strategy Rev., vol. 29, p. 100482, May 2020, doi: 10.1016/j.esr.2020.100482.
[14] S. Hamdare et al., 'Cybersecurity Risk Analysis of Electric Vehicles Charging Stations', Sensors, vol. 23, no. 15, Art. no. 15, Jan. 2023, doi: 10.3390/s23156716.
[15] S. M. Alshareef, 'Analyzing and Mitigating the Impacts of Integrating Fast-Charging Stations on the Power Quality in Electric Power Distribution Systems', Sustainability, vol. 14, no. 9, Art. no. 9, Jan. 2022, doi: 10.3390/su14095595.
[16] S. Alqahtani, A. Shaher, A. Garada, and L. Cipcigan, 'Impact of the High Penetration of Renewable Energy Sources on the Frequency Stability of the Saudi Grid', Electronics, vol. 12, no. 6, Art. no. 6, Jan. 2023, doi: 10.3390/electronics12061470.
[17] A. Lucas, F. Bonavitacola, E. Kotsakis, and G. Fulli, 'Grid harmonic impact of multiple electric vehicle fast charging', Electr. Power Syst. Res., vol. 127, pp. 13–21, Oct. 2015, doi: 10.1016/j.epsr.2015.05.012.
[18] I. Zunnurain, M. N. I. Maruf, M. M. Rahman, and G. M. Shafiullah, 'Implementation of Advanced Demand Side Management for Microgrid Incorporating Demand Response and Home Energy Management System', Infrastructures, vol. 3, no. 4, Art. no. 4, Dec. 2018, doi: 10.3390/infrastructures3040050.
[19] Y. Amry, E. Elbouchikhi, F. Le Gall, M. Ghogho, and S. El Hani, 'Optimal sizing and energy management strategy for EV workplace charging station considering PV and flywheel energy storage system', J. Energy Storage, vol. 62, p. 106937, Jun. 2023, doi: 10.1016/j.est.2023.106937.
[20] P. Barman et al., 'Renewable energy integration with electric vehicle technology: A review of the existing smart charging approaches', Renew. Sustain. Energy Rev., vol. 183, p. 113518, Sep. 2023, doi: 10.1016/j.rser.2023.113518.
[21] Q. Chen and K. A. Folly, 'Application of Artificial Intelligence for EV Charging and Discharging Scheduling and Dynamic Pricing: A Review', Energies, vol. 16, no. 1, Art. no. 1, Jan. 2023, doi: 10.3390/en16010146.
[22] M. S. Mastoi et al., 'A study of charging-dispatch strategies and vehicle-to-grid technologies for electric vehicles in distribution networks', Energy Rep., vol. 9, pp. 1777–1806, Dec. 2023, doi: 10.1016/j.egyr.2022.12.139.
[23] D. Aguilar-Dominguez, A. Dunbar, and S. Brown, 'The electricity demand of an EV providing power via vehicle-to-home and its potential impact on the grid with different electricity price tariffs', Energy Rep., vol. 6, pp. 132–141, May 2020, doi: 10.1016/j.egyr.2020.03.007.
[24] P. Sarsia, A. Munshi, F. Sheikh, K. Yadav, and P. Shukla, 'Driving the Energy Transition: Large-Scale Electric Vehicle Use for Renewable Power Integration', Eng. Proc., vol. 59, no. 1, Art. no. 1, 2023, doi: 10.3390/engproc2023059106.
[25] G. Zhao and J. Baker, 'Effects on environmental impacts of introducing electric vehicle batteries as storage - A case study of the United Kingdom', Energy Strategy Rev., vol. 40, p. 100819, Mar. 2022, doi: 10.1016/j.esr.2022.100819.

E-ISSN 2581 – 7957
P-ISSN 2277 – 3916

CVR Journal of Science and Technology, Volume 26, June 2024
DOI: 10.32377/cvrjst2612

EcoCharge: Wireless Power Hub for Electric Vehicles

Varikuppala Manohar[1], Dhasharatha G[2], Khatravath Santhosh[3], Marigidda Nithin[4], Mylapuram Rashmi Teja[5] and Mukiri Akshay[6]

[1,4,5,6]UG Student, Teegala Krishna Reddy Engineering College/ EEE Department, Hyderabad, India
[1]Email: manoharvarikuppala143@gmail.com
[4]Email: nithinmarigidda@gmail.com
[5]Email: rashmitejamylapuram047@gmail.com
[6]Email: akshaymukiri123@gmail.com

[2,3]Assistant Professor, Teegala Krishna Reddy Engineering College/ EEE Department, Hyderabad, India
[2]Email: g.dhasharatha@gmail.com
[3]Email: Santhosh.btech245@gmail.com

Abstract: **This research paper presents the creation of the "EcoCharge," a cutting-edge wireless charging station designed exclusively for electric cars (EVs). By offering a smooth and eco-friendly charging experience, the system seeks to transform the infrastructure for EV charging. The suggested approach, which makes use of state-of-the-art technology, allows for simple charging in the absence of bulky cables or physical connectors. EcoCharge incorporates cutting-edge wireless power transfer techniques, such resonant or inductive coupling, to guarantee effective energy transmission with a minimum of losses. It also has smart features that optimize charging processes and guarantee compatibility with different EV models and battery sizes. By using dynamic charging algorithms, power management may be made more effective, increasing charging efficiency and cutting down on charging times. The system also places a high priority on sustainability, reducing its negative effects on the environment by using eco-friendly materials and energy-efficient components.**

Index Terms: **Wireless charging station, Electric vehicles (EVs), EcoCharge, Inductive coupling, Charging efficiency.**

I. Introduction

In keeping with the worldwide trend towards sustainability, electric vehicles (EVs) provide a viable way to lessen the environmental effect of traditional internal combustion engine automobiles. Although a large increase in EV adoption is anticipated, a major obstacle is the restricted availability and accessibility of charging infrastructure [1-3]. Traditional EV charging techniques, which depend on physical connections and wires, frequently cause consumers' problems and confusion. The idea of wireless charging for electric cars has attracted a lot of interest lately as a solution to these problems. Wireless charging offers several benefits over conventional cable alternatives, including increased efficiency, convenience, and overall user experience. Wireless charging stations provide an easy and smooth EV owner charging experience by eliminating the need for physical connections [4-7].

The evolution of wireless charging technology for electric vehicles has been significantly propelled by advancements in wireless power transfer mechanisms, notably inductive and resonant coupling [8-12]. These cutting-edge technologies facilitate the efficient transfer of electrical energy from the charging station to the vehicle's battery, obviating the need for direct physical contact. Consequently, EV owners can effortlessly initiate the charging process by parking their vehicles over a designated charging pad or area. A primary driver behind the adoption of wireless charging for electric vehicles lies in its potential to revolutionize the EV charging infrastructure. Unlike conventional charging stations, which necessitate manual plugging-in of vehicles, wireless charging stations offer a user-friendly and convenient alternative. This capability holds the promise of significantly enhancing the overall EV ownership experience, thereby incentivizing more individuals to transition towards electric vehicles [13-17].

Furthermore, wireless charging stations boast versatility in integration across various environments, encompassing residences, workplaces, parking facilities, and public spaces. This widespread integration of charging infrastructure holds the promise of mitigating range anxiety among EV owners, facilitating longer-distance travel without apprehension of battery depletion. Beyond convenience, wireless charging also extends environmental benefits. By minimizing reliance on physical connectors and cables, wireless charging stations contribute to a reduction in the environmental footprint associated with the manufacturing, maintenance, and disposal of charging infrastructure components. Moreover, the integration of renewable energy sources to power wireless charging stations further amplifies their environmental sustainability [18-22]. However, despite the myriad advantages of wireless charging for electric vehicles, several challenges persist. These include the standardization of charging protocols, interoperability among disparate charging systems, and optimization of charging efficiency. Nevertheless, ongoing research and development endeavors are dedicated to surmounting these challenges, thus propelling the adoption of wireless charging technology for electric vehicles. In summary, wireless charging stands poised to revolutionize the paradigm of electric vehicle charging, offering a more convenient, efficient, and environmentally conscious alternative to traditional wired

Received on 07-03-2024, Revised on 06-04-2024, Accepted on 06-05-2024.

CVR Journal of Science and Technology, Volume 26, June 2024
DOI: 10.32377/cvrjst2612

solutions [23-25]. As the demand for electric vehicles continues to soar, the evolution and proliferation of wireless charging infrastructure are poised to play an indispensable role in fostering widespread adoption and realizing a sustainable transportation future.

II. Literature Review

The literature pertaining to wireless charging technology for electric vehicles (EVs) offers a thorough comprehension of its evolution, implementation, and implications. Numerous studies delve into the progression of wireless charging mechanisms, highlighting advancements in inductive and resonant coupling technologies. These mechanisms enable the transfer of electrical energy from charging stations to EV batteries without necessitating direct physical contact, presenting considerable advantages over traditional wired charging systems. Several research endeavors have explored the efficiency and efficacy of wireless charging systems in practical applications. These investigations assess factors such as charging speed, energy transfer efficiency, and reliability, yielding valuable insights into the performance attributes of wireless charging technology for EVs. Additionally, comparisons between wireless and wired charging methodologies have been undertaken to evaluate their respective merits and demerits. Furthermore, the literature investigates the integration of wireless charging infrastructure across various settings, including residential areas, workplaces, public parking facilities, and urban environments. These studies scrutinize the feasibility, cost-effectiveness, and user acceptance of deploying wireless charging stations in diverse contexts, offering pertinent considerations for policymakers, urban planners, and infrastructure developers. Moreover, research in this domain examines the influence of wireless charging technology on EV adoption rates and consumer behavior. Studies delve into factors shaping consumer perceptions, preferences, and willingness to embrace wireless charging-enabled EVs, providing insights into potential market dynamics and adoption trends.

Additionally, the literature reviews regulatory frameworks, standards, and certifications governing wireless charging technology for EVs. These regulatory considerations encompass safety mandates, interoperability standards, electromagnetic compatibility, and grid integration protocols, ensuring the seamless and reliable operation of wireless charging systems within the broader energy ecosystem. Furthermore, research explores the economic ramifications of deploying wireless charging infrastructure for EVs, encompassing investment costs, operational expenditures, and prospective revenue streams. Analyses of cost-benefit and financial models furnish insights into the financial feasibility and long-term viability of wireless charging initiatives, informing strategic planning and investment decisions. Moreover, the literature delves into technological innovations and prospective research directions in wireless charging for EVs. Emerging trends such as bidirectional charging capabilities, dynamic power management algorithms, and integration with smart grid systems are scrutinized, paving the way for improved functionality, efficiency, and scalability of wireless charging infrastructure. In summary, the literature review amalgamates existing knowledge, perspectives, and insights on wireless charging technology for electric vehicles, furnishing a comprehensive overview of its current status, challenges, opportunities, and future trajectories. Through critical evaluation of research findings and synthesis of key insights, the literature review informs and guides further advancements in this rapidly evolving field.

III. Block Diagram of Wireless Charging of an Electric Vehicle

This section delves into the wireless charging station for electric vehicles, detailing its components as depicted in the diagram. The diagram includes the grid, Cycloconverter, compensation network, inductive coils, rectifier, BMS, and battery. The AC supply from the grid is connected to the Cycloconverter to elevate the frequency, facilitating power transfer between the inductive coils. The high frequency output is then directed to the primary compensation network to rectify any power distortion, with the network subsequently linked to the transmitter coil positioned within the charging station. In EcoCharge's design, the transmitter coil is housed in the charging station, while the receiver coil is integrated into the electric vehicle. Utilizing electromagnetic induction, EcoCharge facilitates energy transmission from the transmitter coil to the receiver coil via a magnetic field. When the vehicle aligns with the charging station, an alternating current energizes the transmitter coil, generating a magnetic field that induces a current in the receiver coil. This induced current is then converted back into electrical energy to charge the vehicle's battery. By employing inductive power transfer technology, EcoCharge eliminates the need for physical cables, offering a convenient and efficient charging solution for electric vehicles. The process is grounded in Faraday's law of electromagnetic induction, where placing the two coils together induces an electromotive force (emf) between them, enabling power transfer through the receiver coil.

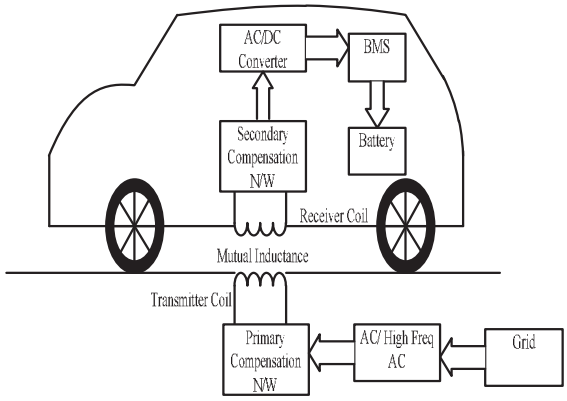

Figure 1. Wireless charging of an electric vehicle

The fundamental principle states that when two coils with varying magnetic fields are brought together, electromotive force (emf) is induced. The receiver coil is linked to the

CVR Journal of Science and Technology, Volume 26, June 2024
DOI: 10.32377/cvrjst2612

compensation network to counterbalance the power distortion. To store the power in the battery, conversion from AC to DC is necessary. Within the Wireless Power Hub for Electric Vehicles, the AC/DC converter assumes a pivotal role in the charging process by transforming alternating current (AC) obtained from the electrical grid into direct current (DC) compatible with the electric vehicle's battery. This conversion is crucial since most electric vehicle batteries operate on DC power. Furthermore, the AC/DC converter regulates voltage and current to ensure safe and efficient charging. By executing these tasks, the AC/DC converter facilitates seamless and dependable wireless charging of electric vehicles through EcoCharge, enhancing the convenience and accessibility of sustainable transportation solutions. The DC supply is linked to the Battery Management System (BMS). In the Wireless Power Hub for Electric Vehicles, the battery management system (BMS) plays a pivotal role in bolstering the performance and durability of the EV's battery pack. Responsible for monitoring critical battery parameters such as voltage, current, temperature, and charge status, the BMS ensures safe battery operation by averting risks of overcharging, over-discharging, and overheating. Additionally, it streamlines charging and discharging processes, thereby optimizing energy usage and extending the EV's driving range. Through the integration of intelligent algorithms, the BMS enables advanced functionalities such as regenerative braking and battery balancing, further enhancing energy efficiency and overall system performance. Ultimately, within EcoCharge, the BMS functions as a critical component, safeguarding battery health, ensuring safety, and maximizing the efficiency and longevity of the electric vehicle's battery pack.

IV. HARDWARE DESCRIPTION

In this section, we discuss about the wireless charging station for an electric vehicle. The components consist in the diagram are LCD, Arduino, Buzzer, Ultrasonic Sensor, Primary Inductive Coil, Secondary Inductive Coil, Regulated Power Supply (RPS), Within the charging station, an Electric Vehicle utilizes two charging slots, referred to as Slot 1 and Slot 2. The coil and RPS takes the supply are 12V. And the remaining parts just require a 5V supply, except the coil. Because of its rating, we can use the RPS to convert 12V to 5V for the remaining components. Transistors allow us to lower the voltage. The station's LCD Display is employed to indicate whether each slot is currently in use or available. As depicted in the accompanying diagram, Slot 2 is currently occupied by a vehicle undergoing charging, while Slot 1 remains unoccupied. This information is accurately reflected on the LCD display, offering users a clear visual depiction of slot availability. Such informative displays streamline the process of identifying available slots, thereby enhancing the efficiency of the charging station and ensuring a seamless charging experience for electric vehicle owners. The role of an Arduino varies depending on its specific application and the instructions it receives through programming. Generally, an Arduino serves as a microcontroller-based platform utilized for constructing digital devices and interactive objects. Its primary function involves interpreting and executing code written in the Arduino programming language, which is a simplified variant of C/C++. Arduino boards are capable of interfacing with a diverse range of sensors, actuators, and other electronic components to carry out various tasks. These tasks may include collecting data from sensors, processing it based on programmed instructions, and controlling actuators accordingly. Typical functions of an Arduino include reading inputs from sensors (such as temperature sensors, motion sensors, or light sensors), processing data (conducting calculations, making decisions based on sensor readings), and controlling outputs (such as activating LEDs, motors, or relays).Arduinos find widespread use in projects related to home automation, robotics, Internet of Things (IoT), data logging, prototyping, and numerous other fields where control and automation are required. Their versatility and user-friendly nature make them popular among hobbyists, students, and professionals alike. The ultrasonic sensor functions by emitting high-frequency sound waves and measuring their reflection off objects in the environment. Consisting of a transmitter and a receiver, it emits ultrasonic waves that bounce off nearby objects and return to the receiver. Through analyzing the time taken for the waves to return, the sensor calculates the distance to the object and detects its presence or absence. Ultrasonic sensors find widespread use in applications such as parking assistance systems, object detection in robotics, and proximity sensing in automated machinery. The buzzer within the Wireless Power Hub for Electric Vehicles serves as an audible alert system, indicating various states or events during the charging process. It alerts users when charging begins or ends, providing immediate feedback on the battery's replenishment status. Additionally, it sounds an alarm if abnormalities like overvoltage, overcurrent, or overheating are detected, signaling potential issues needing attention. Furthermore, the buzzer may indicate specific charging modes or conditions, enhancing user awareness and interaction with the system. Overall, it plays a crucial role in providing audible cues to users and ensuring a safe and efficient charging experience for electric vehicles. The Regulated Power Supply functions to deliver a steady and uniform output voltage or current, irrespective of fluctuations in input voltage, load resistance, or temperature. This ensures that electronic devices receive precise power levels necessary for reliable and efficient operation. By controlling the output voltage or current, the power supply safeguards sensitive components against damage from overvoltage or current surges. Additionally, it reduces signal distortion and noise within electronic circuits, thereby improving overall performance and dependability. Ultimately, the Regulated Power Supply serves as a critical component in powering various electronic devices, ranging from small consumer electronics to intricate industrial machinery, by providing consistent and dependable power delivery.

Wireless inductive charging marks a transformative leap in the realm of electric vehicle (EV) power supply, presenting a convenient and effective departure from traditional plug-in charging modalities. At its heart lies electromagnetic

induction, facilitating energy transfer between two coils: an emitter coil housed within the charging station and a receiver coil integrated into the vehicle. When the vehicle aligns over the charging station, the coils synchronize, initiating the flow of alternating current (AC) through the emitter coil, generating a magnetic field. This field induces a current within the receiver coil, subsequently converted into direct current (DC) to replenish the vehicle's battery. This wireless charging process obviates the necessity for physical cables and connectors, simplifying the charging procedure for EV operators.

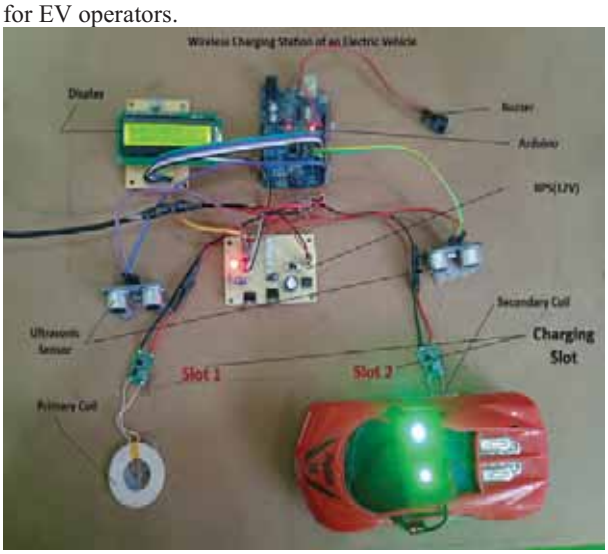

Figure 2. EcoCharge: Wireless Power Hub for Electric Vehicles

A primary advantage of wireless inductive charging lies in its convenience. Drivers can effortlessly park their vehicles atop a charging pad or station, eliminating the need for manual cable connection—an especially appealing feature in urban environments where parking space is often scarce. Moreover, the embedded or integrated nature of the charging infrastructure allows seamless integration into parking lots, garages, and public spaces, ensuring widespread charging accessibility for EV users. Furthermore, wireless inductive charging holds the potential to enhance safety and durability. With no exposed electrical connections, these systems are inherently less susceptible to wear and tear compared to conventional plug-in chargers. Additionally, the absence of cables minimizes the risk of accidents or damage to the charging equipment, bolstering both user experience and infrastructure longevity. Moreover, wireless inductive charging promotes energy efficiency and sustainability. Encouraging more frequent charging sessions by enabling automatic charging whenever the vehicle is parked over the station can optimize battery health and prolong its lifespan. Additionally, utilizing renewable energy sources to power these stations can further diminish the carbon footprint associated with EV charging, fostering a cleaner and greener transportation ecosystem.

V. Conclusions

The EcoCharge Wireless Power Hub for Electric Vehicles is recognized for its potential to revolutionize the landscape of EV charging infrastructure. By eliminating the need for physical cables, EcoCharge ensures unmatched convenience and accessibility for EV owners while facilitating seamless charging experiences. Its environmentally friendly approach aligns with the global shift towards sustainable transportation, contributing to the reduction of carbon emissions and the mitigation of environmental impact. Looking ahead, EcoCharge holds significant promise for further innovation and integration within smart city frameworks. Advancements in efficiency, scalability, and interoperability with emerging EV technologies have the potential to drive widespread adoption, thus fostering a cleaner and more sustainable urban mobility landscape. Continued research and development efforts will be essential in unlocking EcoCharge's full potential and addressing evolving needs within the EV ecosystem.

References

[1] Varma, N. R., Reddy, K. C., Dhasharatha, G., Manohar, V., Kumar, K. K., & Kumar, V. P. (2024). Hybrid Electrical Vehicle Design by Using Solar and Battery Sources. In E3S Web of Conferences (Vol. 472, p. 01006). EDP Sciences.

[2] E. ElGhanam, H. Sharf, Y. Odeh, M. S. Hassan and A. H. Osman, "On the Coordination of Charging Demand of Electric Vehicles in a Network of Dynamic Wireless Charging Systems," in IEEE Access, vol. 10, pp. 62879-62892, 2022, doi: 10.1109/ACCESS.2022.3182700.

[3] A. Fathollahi, S. Y. Derakhshandeh, A. Ghiasian and M. A. S. Masoum, "Optimal Siting and Sizing of Wireless EV Charging Infrastructures Considering Traffic Network and Power Distribution System," in IEEE Access, vol. 10, pp. 117105-117117, 2022, doi: 10.1109/ACCESS.2022.3219055.

[4] S. A. Q. Mohammed and J. -W. Jung, "A Comprehensive State-of-the-Art Review of Wired/Wireless Charging Technologies for Battery Electric Vehicles: Classification/Common Topologies/Future Research Issues," in IEEE Access, vol. 9, pp. 19572-19585, 2021, doi: 10.1109/ACCESS.2021.3055027.

[5] A. Mahesh, B. Chokkalingam and L. Mihet-Popa, "Inductive Wireless Power Transfer Charging for Electric Vehicles–A Review," in IEEE Access, vol. 9, pp. 137667-137713, 2021, doi: 10.1109/ACCESS.2021.3116678.

[6] D. Kosmanos et al., "Route Optimization of Electric Vehicles Based on Dynamic Wireless Charging," in IEEE Access, vol. 6, pp. 42551-42565, 2018, doi: 10.1109/ACCESS.2018.2847765.

[7] M. Adil, J. Ali, Q. T. H. Ta, M. Attique and T. -S. Chung, "A Reliable Sensor Network Infrastructure for Electric Vehicles to Enable Dynamic Wireless Charging Based on Machine Learning Technique," in IEEE Access, vol. 8, pp. 187933-187947, 2020, doi: 10.1109/ACCESS.2020.3031182.

[8] X. Mou, D. T. Gladwin, R. Zhao, H. Sun and Z. Yang, "Coil Design for Wireless Vehicle-to-Vehicle Charging Systems," in IEEE Access, vol. 8, pp. 172723-172733, 2020, doi: 10.1109/ACCESS.2020.3025787.

[9] E. Elghanam, M. Ndiaye, M. S. Hassan and A. H. Osman, "Location Selection for Wireless Electric Vehicle Charging Lanes Using an Integrated TOPSIS and Binary Goal Programming Method: A UAE Case Study," in IEEE Access, vol. 11, pp. 94521-94535, 2023, doi: 10.1109/ACCESS.2023.3308524.

[10] Y. Shanmugam et al., "A Systematic Review of Dynamic Wireless Charging System for Electric Transportation," in IEEE Access, vol. 10, pp. 133617-133642, 2022, doi: 10.1109/ACCESS.2022.3227217.

[11] G. H. Reddy, S. R. Depuru, S. Gope, B. V. Narayana and M. N. Bhukya, "Simultaneous Placement of Multiple Rooftop Solar PV Integrated Electric Vehicle Charging Stations for

Reliability Benefits," in IEEE Access, vol. 11, pp. 130788-130801, 2023, doi: 10.1109/ACCESS.2023.3335093.
[12] D. Ji, M. Lv, J. Yang and W. Yi, "Optimizing the Locations and Sizes of Solar Assisted Electric Vehicle Charging Stations in an Urban Area," in IEEE Access, vol. 8, pp. 112772-112782, 2020, doi: 10.1109/ACCESS.2020.3003071.
[13] T. A. Ocran, J. Cao, B. Cao and X. Sun, "Artificial neural network maximum power point tracker for solar electric vehicle," in Tsinghua Science and Technology, vol. 10, no. 2, pp. 204-208, April 2005, doi: 10.1016/S1007-0214(05)70055-9.
[14] P. H. Kydd, C. A. Martin, K. J. Komara, P. Delgoshaei and D. Riley, "Vehicle-Solar-Grid Integration II: Results in Simulated School Bus Operation," in IEEE Power and Energy Technology Systems Journal, vol. 3, no. 4, pp. 198-206, Dec. 2016, doi: 10.1109/JPETS.2016.2618123.
[15] G. Mathesh and R. Saravanakumar, "A Novel Intelligent Controller-Based Power Management System With Instantaneous Reference Current in Hybrid Energy-Fed Electric Vehicle," in IEEE Access, vol. 11, pp. 137849-137865, 2023, doi: 10.1109/ACCESS.2023.3339249.
[16] C. Oosthuizen, B. Van Wyk, Y. Hamam, D. Desai, Y. Alayli and R. Lot, "Solar Electric Vehicle Energy Optimization for the Sasol Solar Challenge 2018," in IEEE Access, vol. 7, pp. 175143-175158, 2019, doi: 10.1109/ACCESS.2019.2957056.
[17] A. Palomino and M. Parvania, "Data-Driven Risk Analysis of Joint Electric Vehicle and Solar Operation in Distribution Networks," in IEEE Open Access Journal of Power and Energy, vol. 7, pp. 141-150, 2020, doi: 10.1109/OAJPE.2020.2984696.
[18] B. Al-Hanahi, I. Ahmad, D. Habibi and M. A. S. Masoum, "Charging Infrastructure for Commercial Electric Vehicles: Challenges and Future Works," in IEEE Access, vol. 9, pp. 121476-121492, 2021, doi: 10.1109/ACCESS.2021.3108817.
[19] T. Chen et al., "A Review on Electric Vehicle Charging Infrastructure Development in the UK," in Journal of Modern Power Systems and Clean Energy, vol. 8, no. 2, pp. 193-205, March 2020, doi: 10.35833/MPCE.2018.000374.
[20] M. R. Khalid, I. A. Khan, S. Hameed, M. S. J. Asghar and J. -S. Ro, "A Comprehensive Review on Structural Topologies, Power Levels, Energy Storage Systems, and Standards for Electric Vehicle Charging Stations and Their Impacts on Grid," in IEEE Access, vol. 9, pp. 128069-128094, 2021, doi: 10.1109/ACCESS.2021.3112189.
[21] I. Jokinen and M. Lehtonen, "Modeling of Electric Vehicle Charging Demand and Coincidence of Large-Scale Charging Loads in Different Charging Locations," in IEEE Access, vol. 11, pp. 114291-114315, 2023, doi: 10.1109/ACCESS.2023.3322278.
[22] S. Chavhan et al., "Next-Generation Smart Electric Vehicles Cyber Physical System for Charging Slots Booking in Charging Stations," in IEEE Access, vol. 8, pp. 160145-160157, 2020, doi: 10.1109/ACCESS.2020.3020115.
[23] H. M. Abdullah, A. Gastli, L. Ben-Brahim and S. O. Mohammed, "Planning and Optimizing Electric-Vehicle Charging Infrastructure Through System Dynamics," in IEEE Access, vol. 10, pp. 17495-17514, 2022, doi: 10.1109/ACCESS.2022.3149944.
[24] R. Bayani, S. D. Manshadi, G. Liu, Y. Wang and R. Dai, "Autonomous Charging of Electric Vehicle Fleets to Enhance Renewable Generation Dispatchability," in CSEE Journal of Power and Energy Systems, vol. 8, no. 3, pp. 669-681, May 2022, doi: 10.17775/CSEEJPES.2020.04000.
[25] P. Tiwari and D. Ronanki, "Design and Control of Solar Photovoltaic-fed Standalone Wireless Charging of Electric Vehicles," 2022 IEEE Industry Applications Society Annual Meeting (IAS), Detroit, MI, USA, 2022, pp. 1-6, doi: 10.1109/IAS54023.2022.9939808.

E-ISSN 2581 –7957
P-ISSN 2277 – 3916

CVR Journal of Science and Technology, Volume 26, June 2024
DOI: 10.32377/cvrjst2613

An IoT based Low-cost Artificial Mechanical Ventilator for Patients

V. Sreelatha Reddy[1] and Dr. Gopisetty Ramesh[2]
[1,2]Sr. Assistant Professor, CVR College of Engineering/EIE Department, Hyderabad, India
Email: v.sreelatha@cvr.ac.in[1], ramesh.g@cvr.ac.in[2]

Abstract: **This paper presents the construction of a low-cost, open-source mechanicalventilator. The motto behind making this type of ventilator comes from the global shortage of ventilators to treat patients suffering with Covid-19. This paper presents a digital method to monitor the lung status of patients. This is achieved by determining pressure measurements from the inspiratory arm and alerts clinicians if the patient is in a healthy or unhealthy condition. The common symptoms of Covid-19 that can be easily identified are body temperature, blood oxygen level and heart rate that we must check to identify the virus. Hence this system can help in case a patient is unable to meet the doctor or requires frequent monitoring. These are going to develop a system which can monitor, and all the monitored data is stored in the cloud. When people suffer from breathing problems, this can be used for emergencies. The ventilator will be able to monitor the patient's blood oxygen levels and exhaled lung pressure while avoiding high pressure. Designed using Arduino, the ventilator meets all these requirements, creating an affordable ventilator to help during a pandemic. A motor mechanism is used to push the air bag. When the oxygen level counts are low, this mechanism is utilized. LCD screens are used to display oxygen levels. Whenever a patient faces a dangerous position, a buzzer sounds to notify a nearby caretaker. The entire system is driven by an Arduino microcontroller and a buzzer is fitted to detectany low levels of oxygen count.**

Index Terms**: Oxygen, Covid-19, Ventilator, Lung pressure, Air bag.**

I. Introduction

Corona virus, a dangerous disease caused by a virus which got spread two years back, made our lives upside down. Many people died because of this virus due to lack of medicinal facilities. It infects our respiratory system causing difficulty in breathing. Incase if a patient suffers from respiratory failure mechanical ventilators are needed. A ventilator is a medical device used for the breathing process.

Ventilators are needed to treat influenza and corona virus and people in Intensive Care Units (ICU). Before Covid times, people used them only in ICU, but after the heavy spread of Corona, demand for ventilators increased. Ventilator helps in pumping air into the lungs. People infected with Coronavirus need a ventilator because they have difficulty in breathing, or they do not have sufficient oxygen levels. Whereas due to the heavy spread of Corona there is a shortage of ventilators. There is a lack of ventilators for many medical units. Then came the necessity for the invention of artificial mechanical ventilators. After designing them, these models are distributed and, on the web, so that others can also use it and design their own ventilator, even at the small scale.

In recent months, the demand for ventilators to treat Covid-19 patients hassurged and there is currently a global shortage of ventilators. The outcomesof this flaw are devastating, especially in underprivileged areas. Even a well-resourced hospital has developed a protocol for two patients to share the same ventilator. This is a questionable practice since it not only spreadsthe load of bacteria and viruses among patients, but it also puts patients at risk of damage. Researchers have initiated an endeavor to manufacture cost effective open-source ventilators to combat the global shortage of ventilators.

A. Objective

A ventilator is a machine that provides mechanical ventilation by moving breathable air into and out of the lungs, to deliver breath to a patient who is physically unable to breathe or breathing insufficiently. With the current times, we need a safe and inexpensive alternative to handle a respiratory emergency.

The main objective of our system is to design a simple and inexpensive ventilator. It is an alternative to a hand-operated plastic pouch called a bag- valve resuscitator, or AMBU bag. Every hospital has in its inventory in large quantities. It is a hand-on device that means to be operated by hand, by a medical professional or emergency technician. It is to provide continuous breaths to a patient in situations like cardiac arrest until an intervention such as a ventilator becomes available.

The pumping of air into the lung is done by squeezing and releasing the flexible pouch. This is the task of a skilled person, trained in how to evaluatethe patient, and adjust the timing and pressure of the pumping accordingly. Since this is not something that a person could be expected to do for an extended period. However, it is crucial for such a system not to damage the bag and to be controllable so that the amount of air and pressure being delivered can be tailored to the patient.

In this paper, we will design and develop an IoT-based ventilator system. Itdelivers air to breathe by compressing a conventional AMBU bag with the help of a fixed arm connected to a servo motor. Tidal volume and number of breaths per minute are set via user-friendly input modes. It regulates the temperature, and the input pressure can be customized according to the real- time requirements of the patient. The safety mode initiates the backup mechanism without any delay. A built-in alerts system warns during an emergency. This system will improve the quality of life by saving time and resources.

Received on 16-10-2023, Revised on 15-11-2023, Accepted on 15-12-2023.

CVR Journal of Science and Technology, Volume 26, June 2024
DOI: 10.32377/cvrjst2613

B. Motivation

IoT based ventilator provides a continuous breathing process to the patient whose lung capacity has decreased to a point where inhalation and exhalationis not possible on their own. In normal situations, a ventilator is considered asa last alternative for saving a person's life but when the covid-19 hit the globe,the demand for ventilators increased drastically as the virus decreased the lungcapacity of an infected person.

With the integration of IoT, the ventilator will be able to send real-time data of the vital levels of the patient to the doctor. Covid-19 pandemic made us realize that ventilators are far more important than we think. Most of the patients who lost their lives during the pandemic were due to the unavailability of a ventilator. So, this situation has motivated us in developing a system where we need a budget-friendly, portable, and easy to make system.

Because Covid-19 attacks the respiratory system and causes breathing difficulties that ultimately result in mortality, we have chosen this specific system to help combat this global catastrophe. Mechanical ventilation systems are considered as basic systems of life. By enabling remote ventilator control, this technology attempts to create a physical barrier between medical personnel and patients, thereby limiting the spread of this illness.

The history of mechanical ventilation begins with various versions of what was eventually called the iron lung, a form of non-invasive negative-pressure ventilator widely used during the polio epidemics of the twentieth century after the introduction of the "Drinker respirator" in 1928. Most recently, Covid-19 saw a widespread that it has been categorized as a pandemic, and India is the second most affected county in the world. The Covid-19pandemic has cast a spotlight on ventilators but is in acute shortage mainly due to the cost of it. Not everyone can afford it. So, this motivated us to develop the artificial mechanical ventilator.

II. Literature Review

[1] proposed a system in August 2020 which can be monitored anytime and all the data can be stored at a cloud. Also, this system can be used at the entrance of various shops, marts, clinics to monitor customers' health conditions and store their records. The result shows that the proposed system can be more efficient than the normal manualsystem.

[3] proposed a numerical method for monitoring the patient's pulmonary condition. The method considers pressure measurements from the inspiratory limb and alerts physicians in real-time whether the patient is in a healthy or unhealthy situation. Experiments are carried out in the laboratory that have emulated healthy and unhealthy patients to determine the benefits of the mechanical ventilator.

[5] this paper displays the research where it shows the development of a low-cost, open- source mechanical ventilator. Constructing a low-cost, open-source mechanical ventilator aims to mitigate the consequences of this shortage on those regions.

[7] discussed about the Covid-19 global health emergency to accept suggestions for using robots to boost ventilator productivity. Based on what was summarized from the analysis of the academic literature to arrive at the fundamental designs for the manufacture of ventilators that were already investigated, and the practical specifics required, they discussed ventilators at the beginning of this literature review.

III. Implementation

In this system, we are developing an automatic system to monitor patient's body temperature, and blood oxygen levels. Further we extend the existing system to Predict if the patient is suffering from any chronic disorder or Disease using the various health parameter and various other Symptoms that are obtained by the system. A general ventilator just controls oxygen, we monitor oxygen, heart beats, temperature, humidity etc. Then they can be all sent to cloud and then doctor will monitor patient remotely.

In our system we are measuring patient's parameters (temperature, oxygen level concentration in blood) using different available sensors. These sensors collected data i.e., biometric information is given to Arduino and then it is transferred to server. The data stored in a database and can be displayed in a website that can be accessed only by authorized person. The doctors, RMOs, patient or his family members can be given authorization. The system even facilitates the doctor to view the patient's previous history from the data in memory.

A. Block Diagram

The block diagram of the system is shown in figure 1. It consists of an Arduino microcontroller connected with a power supply. The main component of the ventilator is the DC motor. The DC motor is connected to a mechanical arm which will inflate and deflate the AMBU bag. It is used to pump air in and out to a patient who has lost the capacity to breathe on their own. The Arduino is connected to 2 sensors, namely DHT11 temperature sensor, MAX30100 SpO2 sensor. These sensorscollect the readings from the finger of the human body and these values are processed by the Arduino board which further displays them on the LCD module. If the oxygen saturation level falls below 95% and the temperature level falls below 36.5°C, then the microcontroller first activates the buzzer alarm to indicate caution and instructs the dual motor driver to rotate which further rotates the arm fixed to it making the AMBU bag expand & contract so that the oxygen is sent to the mouthpiece of the human being. Apart from this, Arduino is also connected to ESP8266 Wi-Fi module which is used to send the data received from the sensors to the ThingSpeak website.

CVR Journal of Science and Technology, Volume 26, June 2024
DOI: 10.32377/cvrjst2613

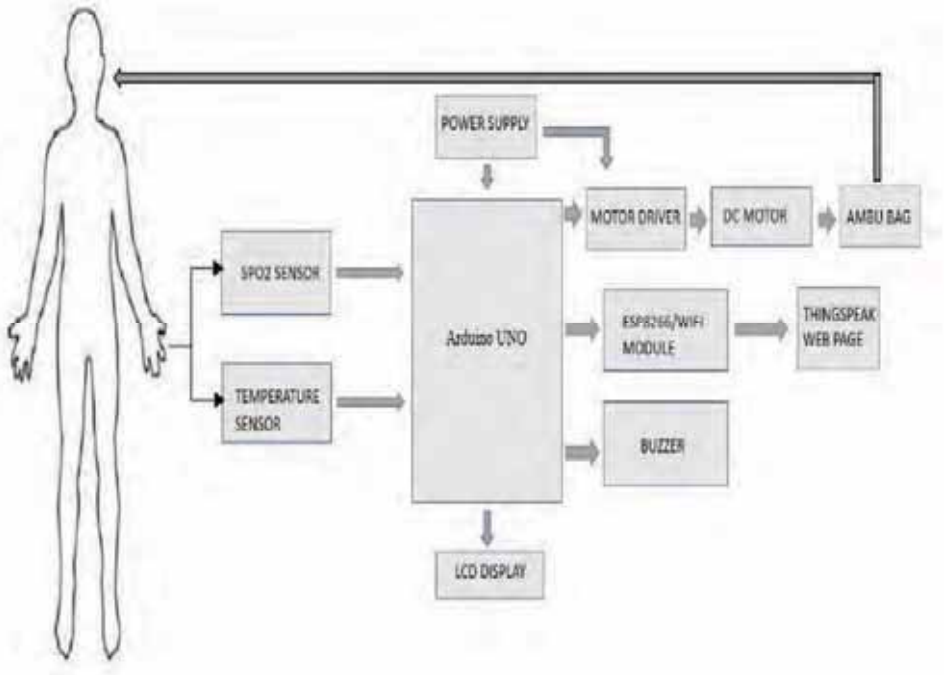

Figure 1. Block diagram of the System

B. Schematic Diagram

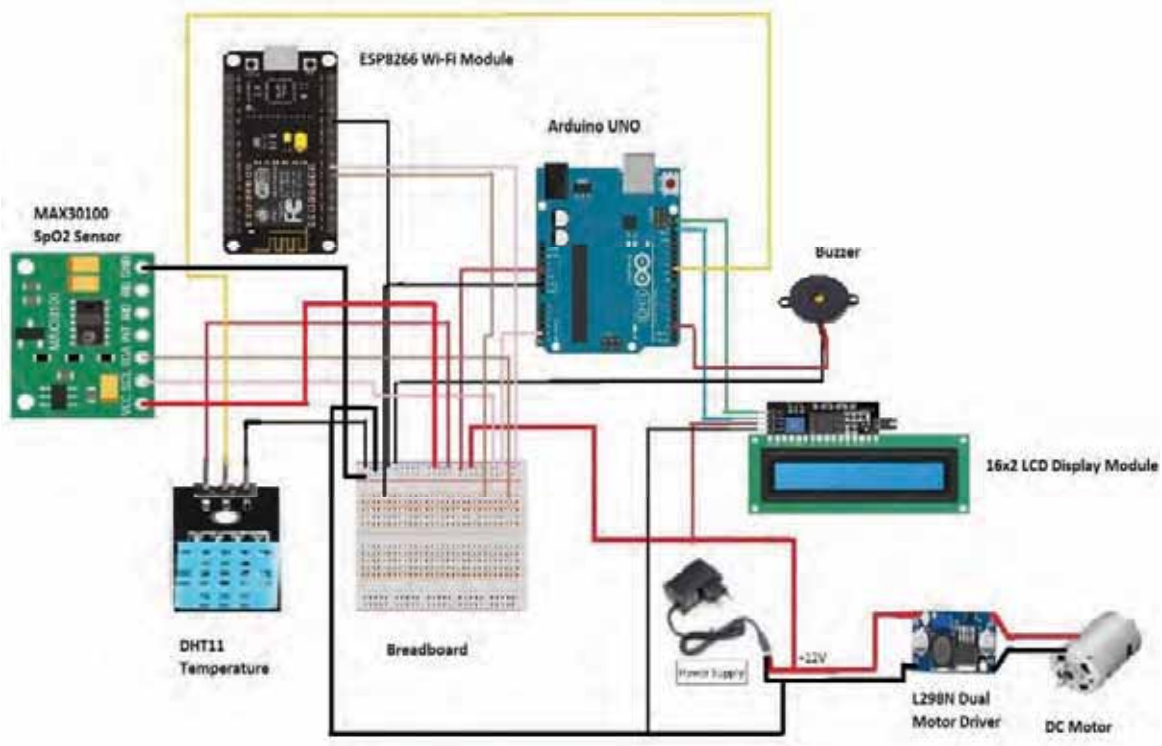

Figure 2. Schematic diagram of the System

The schematic diagram of the system is shown in figure 2. The first and foremost thing is the power supply. Power supply is given tothe kit through a 2A adapter i.e., usually 12 volts. The adapter is plugged into the socket, and the pin is fitted into Arduino board so that it receives power supply. The same 12V power supply is divided to L298N

CVR Journal of Science and Technology, Volume 26, June 2024
DOI: 10.32377/cvrjst2613

dual motor driver through printed circuit board. 5V and GND connections are taken from Arduino through jumper wires, and they are fixed on the breadboard for all other sensors & components to be provided with a reference. MAX30100 Sensor, Serial clock, serial data pins are connected to A4, A5 pins of Arduino respectively and 5V, GND pins are connected to Arduino through bread board. DHT11 Sensor, VCC, GND, 5V are connected to the Arduino consisting of the same pins through the bread board. ESP8266 Wi-Fi Module, GPIO02, GPIO03, GND pins are connected to A2, A3, GND pins of the Arduino respectively.

The power supply for LCD is taken from the 5V, GND pins of Arduino through breadboard and LCD is interfaced to Arduino with I2C serial adapter by connecting the SDA, SCL pins to A0, A1 pins of the Arduino respectively. The 5V and GND pins of DC motor are connected to the output pins of motor driver. The 5V, GND pins of buzzer are connected to the same 5V, GND pins of Arduino respectively through the bread board.

C. Flow Chart

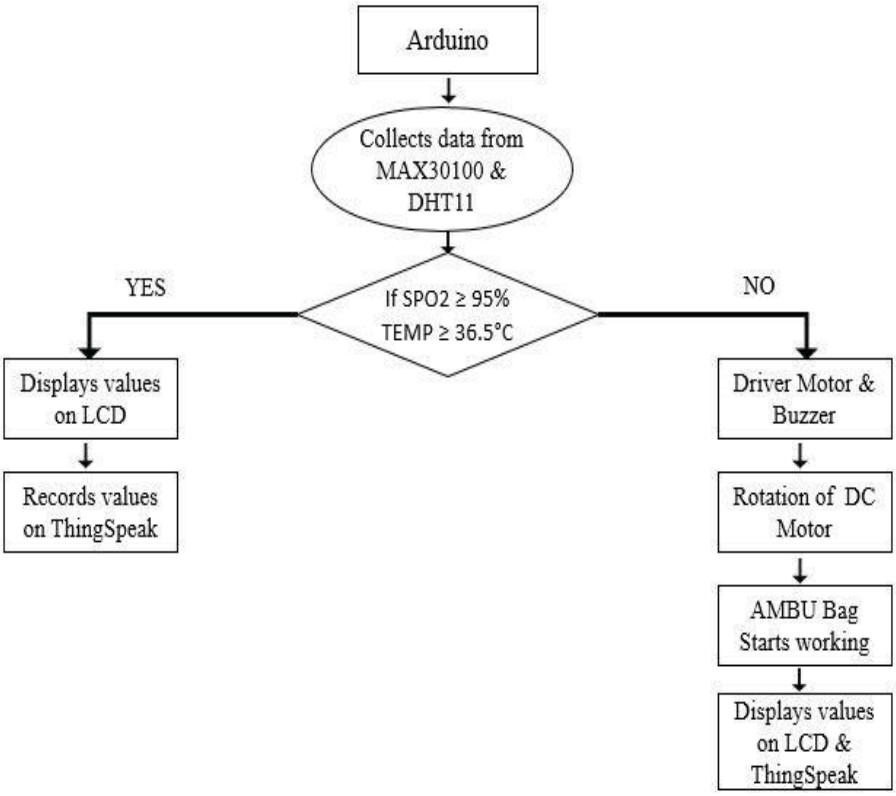

Figure 3. Flow chart of the system

IV. RESULTS

The hardware setup of the system is shown in figure 4. The AMBU bag connected to the ventilator is the most important part of the ventilator. Air from the AMBU bag will be inhaled and exhaled by the patient.A mechanical arm controlled by high-speed DC Motor will inflate and deflatethe AMBU bag with its force. This DC motor will be controlled by the ArduinoUno board. The respected values will be displayed on the 16x2 LCD display.AMBU bag will consist of a mask that will fit the patient's nasal part for inhalation and exhalation.

Our system will be an easy to use, efficient and cost-friendly alternative to theones in use. This can be used separately or with the ventilator depending uponthe need and emergency.

Finally, the important aspect of this system is the integration of data obtained from the hardware with the software part. Connectivity between the ESP 8266 Wi-Fi module and cloud server using authentication tokens and libraries. As a result, the doctor will receive notifications about the health of the patient, be it a ventilator or health monitoring system on his/her PC/phone via the website.The website will have separate logins for patients and doctors and will be connected in the backend by a database. The AMBU bag along with motor and arm, the complete set of the ventilator is shown in figure 5 and 6 respectively.

E-ISSN 2581 –7957
P-ISSN 2277 – 3916

DOI: 10.32377/cvrjst2613

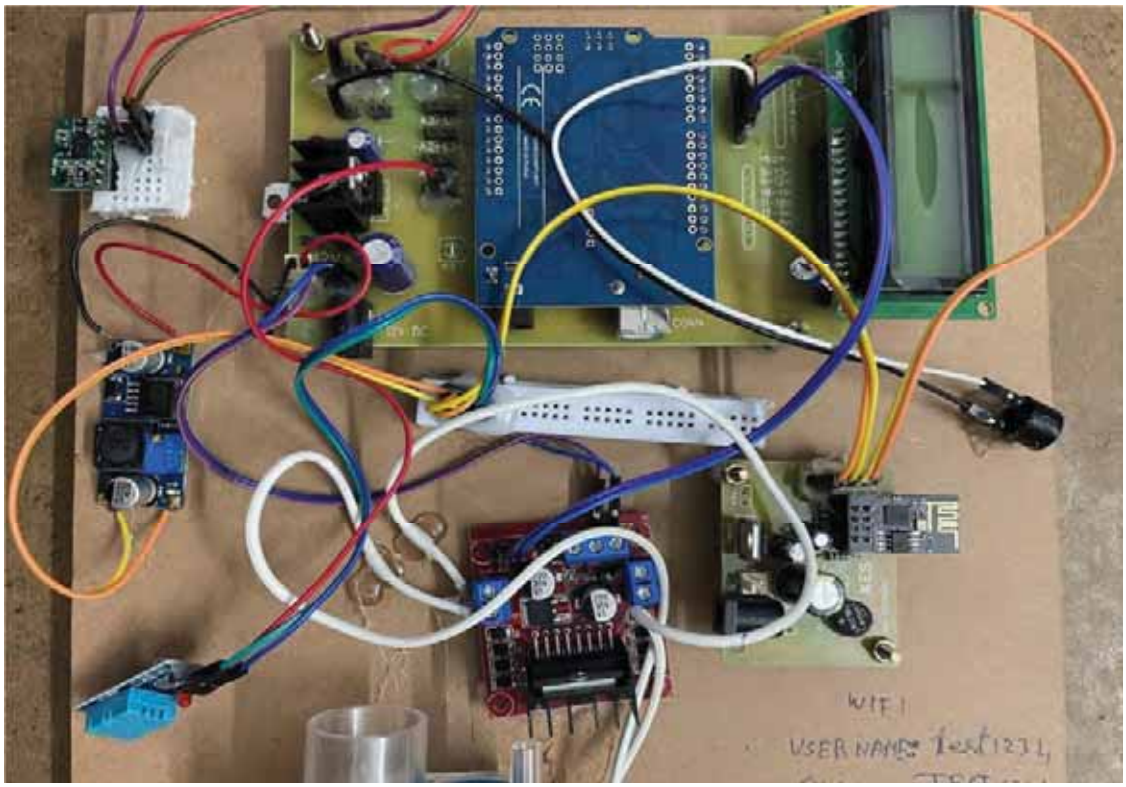

Figure 4. Hardware Setup of the system

Figure 5. AMBU Bag along with motor and arm

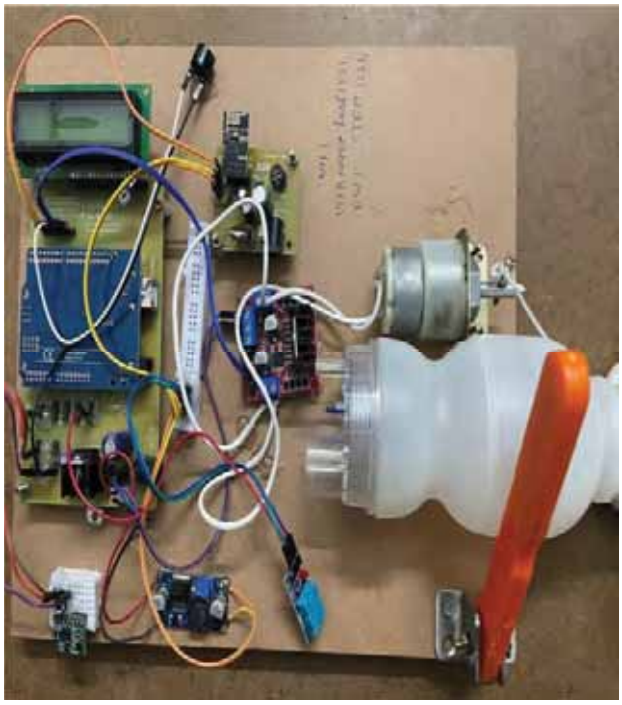

Figure 6. Complete Set-up of Ventilator

V. Conclusions

In this proposed system, a prototype device to assist patients who can partiallybreathe on their own is developed. The motivation comes from the world-wide shortage of mechanical ventilators in the treatment of covid-19 patients. This device is provided with a very basic design and reliable structure that is easilyaccepted by the patient. The focus in this model is to minimize the components and increase its efficiency, so that while using this device to the patient, they should feel as comfortable as the normal ventilator. The biggest advantage ofour system is that it includes a health monitoring system where it measures body temperature, heart rate, oxygen level in blood. Through IoT it ensures the patient is under control and adequate action can be taken. Thus, during pandemics doctors can monitor patients via online in real time.

The future enhancement of the proposed system is, the IoT based ventilator can be embedded with PWM controlling system with the main control chip using ESP32. The use of ESP32 chip aims to control IoTbased ventilator with Bluetooth communication so that distance can be maintained. In addition to the IoT based monitoring and controlling functions.The ventilator can also be adjusted with several control buttons provided nearthe system. An alternator power source can be embedded so that when powergoes down the back up battery automatically kicks in.

References

[1] Md. Rifat Rahman Akash, Yousuf, Kaushik Shikder, “IOT Based Real Time Health Monitoring System”, 2020 Research, Innovation, Knowledge Management and Technology Application for Business Sustainability (INBUSH),

[2] World Health Organization: Critical preparedness, readiness, and response actions for COVID-19: interim guidance, 7 March 2020, WHO/COVID19/Community Actions/2020 World Health Organization.

[3] Alamurugan, C. R, Kasthuri, A, Malathi, E, Dharanidharan, S, Hariharan, D., Kishore, B. V., & Venkadesh, T. (2021). “Design of VentilatorUsing Arduino for Covid Pandemic” Annals of the Romanian Society for Cell Biology, 14530-14533.

[4] Sam Mansfield, Eric Vin, Katia Obraczka "An IoT-Based System for Autonomous, Continuous, Real-Time Patient Monitoring and Its Application to Pressure Injury Management", 17th International Conference on Distributed Computing in Sensor Systems (DCOSS) 2017.

[5] Al-Mutairi A. W, Al-Aubidy K. M. (2020), “Design and construction of a low-cost portable cardiopulmonary resuscitation and ventilator device”, 17th IEEE Intr. Multi-Conf. on Systems, Signals, Devices (SSD2020), Tunisia..

[6] Petsiuk, A, Tanikella, N. G, Dertinger, S, Pringle, A, Oberloier, S., & Pearce, J. M. (2020), “Partially Reparable automated open-source bag valve mask-based ventilator”. HardwareX, 8, e001301.

[7] K. Iyengar, S. Bahl, V. Raju and A. Vaish, "Challenges and solutions in meeting up the urgent requirement of ventilators for COVID-19 patients", Diabetes Metab. Syndr. Clin. Res, 2020.

[8] M. Pons-Odena, A. Valls, J. Grifols, R. Farre, F.J. Cambra Lasosa and B.K.Rubin, "COVID-19 and respiratory support devices", Paediatr. Respir. Rev, 2020.

[9] M.L Ranney, V Griffeth and A.K. Jha, "Critical Supply Shortages-The Need for Ventilators and Personal Protective Equipment during the Covid- 19 Pandemic", N.Engl. J.Med, 2020.

[10] Yin Y, Zeng Y, Chen X, and Fan Y. (2019), “The internet of things in healthcare: an overview”. Journal of Industrial Information Integration, Vol.1,March, pp.3-13.

E-ISSN 2581 –7957
P-ISSN 2277 – 3916

CVR Journal of Science and Technology, Volume 26, June 2024
DOI: 10.32377/cvrjst2614

An Analysis on Recent Approaches for Image Captioning

Qazi Anwar[1], Ch V S Satyamurty[2]
[1]PG Scholar, CVR College of Engineering/IT Department, Hyderabad, India
Email: 20B81DB002@cvr.ac.in
[2]Associate Professor, CVR College of Engineering/IT Department, Hyderabad, India
Email: satatyamurty@cvr.ac.in

Abstract: **Image captioning is an interdisciplinary area that uses techniques from computer vision and natural language processing to provide a textual description of a picture. The Image captioning task is the process of understanding the scene present in the image by identifying objects and associated actions present to create a meaningful human-like caption which can be used for wide range of applications, including image retrieval, video indexing, assistive technology for the visually impaired, content-based image search, biomedicine, and autonomous cars. Formerly, Machine Learning was utilized for this purpose which will be extensive use of hand-crafted features such as Scale-Invariant Feature Transform (SIFT), Local Binary Patterns (LBP), the Histogram of Oriented Gradients (HOG), and combinations of these features. Extracting handmade characteristics from huge datasets is not straightforward or viable. Many deep learning-based techniques were later proposed. Deep Learning retrieval and template-based approaches were presented; however, both had drawbacks such as losing crucial objects. Recent breakthroughs in deep learning and natural language processing have resulted in considerable increases in image captioning system performance which involves adopting attention mechanisms, transformer-based architectures, multi modal connections, Object-Detection based encoder-decoder and many others. In this survey will explore some of the most recent techniques for image captioning, the datasets and evaluation measures that have been employed in deep learning-based automatic image captioning. The ultimate intention of this study is to act as a guide for researchers by emphasizing future directions for research work.**

Index Terms: **image captioning, computer vision, deep learning, Textual description, natural language processing.**

I. Introduction

In recent years, computer vision in image processing has achieved major advances, such as Image categorization [1] and object identification [2]. As a result, it is now feasible to automatically produce one or more phrases to comprehend the visual information of an image, a challenge known as Image Captioning. To develop natural language descriptions of images in image captioning in a way that a person can understand. Because the

images will be translate into words, image captioning is further challenging work than other computer vision tasks. Deep learning algorithms automatically learn characteristics from training data and can handle a large and diverse range of photographs and videos.

Deep learning systems used CNN for image processing. CNN harvests feature without the need for human involvement by automatically training and updating network parameters, while a classifier such as Softmax is used for classification. The previous image description approach employed CNN and RNN such as LSTM as encoder and decoder, respectively. The automatic generation of entire natural picture descriptions has a wide range of possible applications, including titles linked to news photographs, and information related from medical images, text-based image retrieval, information accessed by blind users, and human-robot interaction. After training a CNN on ImageNet [3] Vinyals et al. [4] used an LSTM kind of RNN to decode and output the caption. However, it is recommended to use a range of characteristics from different portions of the image since this strategy misses key regions of the image. The typical LSTM approach focuses on the relatively close vocabulary while ignoring the distant one. Recent improvements in image captioning paved the way for implementing attention methods, transformer-based architectures, multimodal connections, and object-detection based encoder-decoders, among other things may be credited in significant part to vision-language pre-training (the current dominant training paradigm for vision-language (VL) research.

II. Recent Approaches

Ren et al. introduced reinforcement learning for photo captioning in 2017 [5]. This technique's architecture comprises of two networks that work in tandem at each time stamp to find the most suitable phrases. The "policy network" gives regional direction and word projection on the current scenario. The "value network" provides global direction; it considers the reward offered by the reinforcement strategy and analyses the reward value for all prospective improvements to the existing situation. It uses an Actor-Critical Reinforcement learning technique to train this entire system [6].

In [7], researchers employed the YOLO object identification algorithm as the encoder component and the LSTM as the language decoder part to caption for the MSVD dataset, identify relevant frames from the clip that may be used to train the model KATNA, and delete redundant frames.

Following the extraction of relevant frames YOLO is utilized to detect objects, and the found items are recorded in a text file along with their classes and confidences. Then, by scanning three words at a time, LSTM creates a phrase demonstrating the relationship between the discovered items.

In [8], they suggested the Reflective Decoding Network (RDN) for picture captioning, which improves the long sequential modeling capability of classic caption decoders.

Received on 15-11-2023, Revised on 15-12-2023, Accepted on 14-01-2024.

The RDN centers on the target interpreting side and implementation consideration instruments in both the visual and literary spaces, in difference to prior approaches that upgraded captioning execution by improving the visual consideration instrument or by upgrading the encoder to supply a more significant middle of the road representation for the decoder. Upon accepting an input picture, the show begins with using Speedier R-CNN as an encoder to get visual information from the picture. The visual elements are subsequently sent to RDN for caption generation. It is made up of three parts: (1) Attention-based Repetitive Module, which goes to the Encoder's visual highlights (2) Reflective Consideration Module, which provides printed consideration to show the compatibility between current and past interpreting covered up states, permitting it to capture more authentic and comprehensive data for word choice (3) The Reflective Position Module, which gives relative position data for each word within the delivered caption and helps the show in seeing sentence syntactic structure. RDN can beat the long-term certainty issue in caption interpreting.

Transformer-based systems are cutting-edge in sequence modeling applications such as machine translation and language interpretation. However, its relevance to multi-modal situations such as picture captioning remains mainly unexplored. In [9] introduce a Meshed Transformer with Memory for Image Captioning. The architecture improves the language generation stage as well as the image encoding stage: the architecture learns a multidimensional representation of the relationship between the image regions by embedding learned a posteriori, and in the decoding stage it leverages mesh-like connections to leverage low-level as well as high-level functions. The two key features of this architecture (i) picture portions and their connections are encoded on several levels, with low-level and high-level relationships considered. Using permanent memory vectors, the model can learn and encode priori information when modeling these interactions. (ii) Using a multi-layer architecture, the sentence creation harnesses both low- and high-level visual associations rather than relying on a single input from the visual sensory system. This is undertaken using recognized gating mechanism that weights multi-level contributions at each stage. This results in a mesh connection schema between the encoder and decoder layers.

CLIP is employed in [10] to extract visual data from photos, and a mapping network is then used to generate a large number of context tokens. The mapping network employed is a Multi-Layer Perceptron or Transformer, which translates CLIP embeddings to language model space. To generate the image description, the language model will be trained using these context tokens. They choose a language model (GPT-2) [11] to create the next word of a caption from a collection of initial context tokens in less time than heavier architectures, and just the image encoder of CLIP (Contrastive Language-Image Pre-training) is used, with text encoder ignored.

For vision-language issues, large-scale pre-training approaches for learning cross-modal representations on image-text pairings are becoming unmistakable. In [12] Oscar which uses question labels recognized in pictures as grapple focuses to essentially ease arrangement learning was presented. The revelation that the conspicuous things in a picture may be dependably recognized and are regularly tended to within the going with content empowered our procedure. They train an Oscar demonstrate employing a open corpus of 6.5 million text-image pairings some time recently fine-tuning it on downstream assignments, coming about in unused state-of-the-arts on six well-established vision-language understanding and era errands.

[13] This research includes a deep investigation into enhancing visual representations for vision language (VL) problems, as well as the development of an enhanced object identification model to give image-centric representations. Compared to the most popular top-down and bottom-up models, the new model is larger, better suited for VL processes, and has been trained on significantly larger pre-trained corpora that contain several publicly available annotated sets of item identification data. This suggests that a far wider range of pictures and ideas may be represented by the new approach when it comes to building representations. The approach show that visual components are significant in VL processes, in contrast to prior VL research that neglected the original object detection model in favor of improving the vision and language fusion model. The new object identification model's visual characteristics were entered into OSCAR, a transformer based VL fusion model, throughout the tests, and the model was pre-trained and refined on a variety of downstream VL model tasks using an upgraded technique, OSCAR+.

The test results have seen a considerable improvement in the performance of the picture captioning challenge based on vision language pre-training (VLP) in recent years. However, most of the previous research has primarily focused on pre-training transformers of moderate sizes such as 12 or 24 layers on around 4 million photos.

In [14] LEMON, LargE-scale iMage captiONer, driven the primary observational analysis on the scaling behavior of VLP for picture captioning in this work. They utilize the cutting-edge Vinyl demonstration as a reference, which encompasses a picture highlight extractor and a transformer demonstration, and to scale the transformer up and down, with demonstration sizes extending from 13 to 675 million parameter.

[15] The unused show is greater, and superior outlined for VL assignments. It is additionally pre-trained on much bigger preparing corpora containing different straightforwardly explained Object-Identification datasets than most broadly utilized bottom-up or top-down models, permitting it to build representations of a huge set of visual objects/concepts. Though past VL inquire about centered on this work presented mPLUG, the modern vision-language establishment worldview for cross-modal comprehension /generation assignments. The long visual grouping in cross modular arrangement leads to moo computational effectiveness & data lopsidedness in most pre prepared models. To address this, mPLUG offers a progressive cross modular skip-connecting engineering that produces inter-layer alternate routes which bypass the set number of layers, permitting for time devouring full self-attention on vision side. mPLUG is pre-trained conclusion to conclusion on huge scale image-text sets with segregating and generative destinations. It produces cutting edge comes about on a wide extend of downstream VL

CVR Journal of Science and Technology, Volume 26, June 2024
DOI: 10.32377/cvrjst2614

errands, such as picture captioning / image-text recovery / visual establishing / visual address replying. When connected to distinctive video-language assignments, mPLUG moreover shows zero-shot transferability.

[16] They suggest employing CLIP, a multimodal encoder trained on massive image-text pairings from the web, to calculate multimodal similarity and utilize it as a reward function to generate more informative and differentiated captions. They too recommend a basic fine-tuning strategy for the CLIP content encoder that does not require extra content observes to make advances in linguistic use. To survey graphic captions comprehensively, they moreover presented Fine Cap Eval, a novel dataset for caption assessment with fine-grained criteria. The proposed CLIP guided show produces more interesting captions than the CIDEr-optimized show. They too appear that the unsupervised linguistic use fine-tuning of the CLIP content encoder lightens the naive CLIP reward's degeneration issue. At last, they give human examination in which annotators exceedingly favor the CLIP remunerate over the CIDEr and MLE targets based on various parameters.

III. DATASETS

A. Mscoco (Microsoft Common Objects in Context)

It is a significant dataset for segmentation, captioning, and object recognition [17]. 328K images make up the collection. The initial release of this dataset took place in 2014. It comprises three sets of 164K photos: 83K for training, 41K for validation, and 41K for testing. An extra test set of 81K photos was made available in 2015; this set contained 40K new photos in addition to all previous test images. In the year 2017, the split between training and test was changed from 83K/41K to 118K/5K. The updated split makes use of the same images and annotations. The 41K pictures in the 2015 test set are not included in the 2017 test set. An additional new, unannotated dataset of 123K images is included in the 2017 edition.

B. Flickr

A benchmark [18] collection of 8,000 photos comprised with five distinct captions that convey concise explanations of the main things and happenings. The photos were taken from six diverse Flickr bunches and don't as a rule incorporate well-known people or places but were hand-picked to demonstrate a differing quality of scenarios and circumstances. A follow-up to the prior Flickr 8k Dataset, a dataset Flickr 30k was introduced. It is a picture caption corpus comprising 158,915 crowd-sourced captions depicting 31,783 photographs depicting people locked in in standard exercises and occasions.

C. Conceptual Captions

Google's Conceptual collection [19] contains over three million photos accompanied by natural language narratives. The Conceptual Captions images and raw explanations are taken from the web and so reflect a broader range of styles. The raw descriptions are derived from the Alt-text HTML element of online photographs. The splits comprise of 3.3 million training images, 15k validation images and 12k for testing purposes.

D. Coco

COCO Captions [20] offers approximately 0.5 million captions that describe over 330,000 photos. Each picture within the preparing and approval sets will incorporate five distinct human-generated captions. The entire number of captions collected is 413,915 for 82,783 photographs in the organization of 202,520 for 40,504 images in approval, and 379,249 for 40,775 pictures in testing. There's an additional caption for each testing picture to compute human execution evaluations for comparing machine created caption scores. The whole number of captions accumulated is 1,026,459.

D. Hateful Memes

The Hateful Memes collection [21] includes over 10,000 new multimodal instances generated by Facebook AI to assist researchers in developing new algorithms to detect multimodal hate speech. This information includes several modalities, such as text and graphics, making machine comprehension challenging. The photos were licensed from Getty photos so that scholars may utilize the dataset in their studies.

E. No Caps

166,100 human-generated captions portraying 15,100 photographs from the Open photographs training and test sets contain this benchmark [22]. COCO image-caption pairings, as well as Open Pictures image-level names and question bounding boxes, make up the related preparing information. Since Public photographs has distant more classes than COCO, over 400 thing classes found in test photographs have no or few preparing captions.

F. Viz Wiz

It is a visual question answering (VQA) dataset [23] which evolved from a natural visual question answering scenario in which unsighted persons individually took a picture and recorded a spoken inquiry about it, along with ten crowd sourced replies per visual question. For this dataset there are two tasks: (1) imagining the reply to a visual address and (2) determining in case a visual address cannot be replied. There are 20,523 training image/question pairings, 205,230 pairs of training answer/answer confidence, 4,319 image/question validation pairings, 43,190 validation confidence answer/answer pairings, 8,000 image/question pairings for testing.

G. Rsicd

The Remote Sensing Image Captioning Dataset [24] is a dataset used to caption remote sensing images. The dataset includes almost 10 thousand remote sensing photos gathered from Baidu Map, Google Earth, Tianditu. MapABC, and the photos are restrained to 224X224 pixels in a diversity of dimensions. There are 10921 remote sensing photos in all, with five phrase explanations for each image.

H. Image Captioning For Visually Impaired People

This data [25] collection comprises 1600 distinct images organized into 21 major categories. The images remained chosen to represent the various scenarios or obstacles that visually impaired people will encounter in a real-world setting to assist them in a variety of ways, such as

CVR Journal of Science and Technology, Volume 26, June 2024
DOI: 10.32377/cvrjst2614

crosswalks, construction activity to sign boards, food outlets, stairs, elevators, bus terminals, wet surfaces, push buttons, money recognition, and so on.

IV. Evaluation Metrics

A. BLEU

To evaluate the quality of interpreted expressions in machine interpretation, the Bilingual Evaluation Understudy (BLEU) approach [26] is utilized. It investigates person interpretation fragment to a pool of reference interpretations of incredible interpretation quality, gauges each section score, and after that assesses the full interpretation quality. Within the domain of picture portrayal, BLEU uses a coordinating run the show as a similitude measuring approach. Utilizing the co-occurrence frequency of N-gram in both the label and the predicted caption, one may evaluate the BLEU assessment metric. To be computed are four bleu scores. The depiction express and name are separated into words by BLEU-1, which checks the occurrences of each word within the depiction sentence within the name one at a time and logs the smallest number of times a tuple shows up within the depiction sentence and name. To avoid the bias issue of the resulting description sentence being too short, compute the ratio using the description sentence and multiply the result by a penalty factor. For statistical and computational purposes, BLEU-2 separates the descriptive phrase and label into two-word 2-tuples. Typically, a maximum of four tuples are computed.

B. ROUGE

The ROUGE (recall-oriented understudy for gisting evaluation) approach [27] investigations abstracts based on the co-occurrence data of the N-tuples within the assessment abstracts. It is an evaluation method used to gauge the machine's translation fluency that is based on the recall rate of N-tuples. In order to verify the lengthiest common subsequence between the label and the captionl, ROUGE uses dynamic programming in the evaluation process. Based on the computed common subsequence, they next compute their recall to determine how similar the caption and label are. Like BLEU, the higher the ROUGE indicator's value, the higher the quality; however, it does not account for semantic depth of description or grammatical precision., ROUGE is able to capture the phrase's structure.

C. METEOR

METEOR (Metric for Evaluation of Translation with Explicit Ordering) [28] is another machine translation evaluation index. The METEOR before performing a harmonic average for a query image caption estimates recall and precision. The longer the ceaseless length of the longest common subsequence coordinated, we normally accept, the way better. Be that as it may, since the assessment metric assesses a single word, a punishment figure is utilized, where the calculate shows the number of chunks, which means the bordering requested square. METEOR fathoms the issue that BLEU does not dependably coordinate words and does not survey review. METEOR measures exact word-to-word coordinating but BLEU does in an indirect way.

D. CIDER

Consensus-based Image Description Evaluation [29] treats each phrase as an archive and calculates the cosine point of the word frequency-inverse record recurrence vector to decide the closeness between the depiction sentence and the name. At last, the result is calculated by averaging the likeness of tuples of changing lengths. Since tuples that show up more frequently within the corpus by and large carry less data, this method permits different tuples to have shifting weights. As a result, CIDER may assess graphic expressions for rightness etymologically and really.

E.SPICE

Anderson et al. [30] developed Semantic Propositional Image Caption Evaluation (SPICE) to employ graph-based semantic illustration to encode the objects, properties, and connections in the description sentence and to assess the description sentence at the semantic level. SPICE uses a dependency parser to convert the candidate and reference captions into syntactic dependencies trees. The era of the dependency tree, a rule-based method is utilized to interpret the reliance tree into a scene chart. The syntactic Reliance Tree is built particularly by three post-processing stages that streamline quantitative modifiers, investigate pronouns, and handle different things. The tree structure is at that point prepared utilizing nine fundamental dialect rules to recover the scene graph's things, connections, and properties. While Flavor can way better evaluate semantic data, it overlooks linguistic confinements and thus cannot judge sentence stream.

In Table-1 summarizes the most pertinent survey techniques.and their primary features regarding visual encoding, language modelling, and training methodologies along with their performance on the COCO Karpathy test set in terms of BLEU-4, CIDEr,, and METEOR. The strategies are sorted within the table concurring to the evaluations they learned. Strategies that take advantage of pre-training in dialect and visual perception are enhanced and acclaimed by others. In a matter of a long time, picture captioning models have accomplished exceptional results, 25.1 from a normal BLEU-4 of for the strategies utilizing worldwide CNN highlights to the normal BLEU-4 of 35.3 and 40.0 for consideration and self-attention instruments, with the latter peaking at 42.6 within the case of pre-training of vision-and-language. The way better the execution, when measured in terms of the CIDEr score, is when total and organized data approximately semantic visual concepts and their connections is included. With respect to the dialect show, the execution of LSTM-based methods with vigorous visual encoders is individually competitive with that of afterward completely mindful methods.

TABLE 1.
SUMMARY OF DL BASED IMAGE CAPTIONING MODELS

Visual Encoding					Language Model				Training Strategies				Main Results		
Model	Global	Regions	Grid	Graph	Self-Attention	RNN/ LSTM	Transformer	BERT	MLM	XE	Reinforce	VL Pre training	BLEU-4	METEOR	CIDEr
Unified VLP		✓			✓			✓		✓	✓	✓	39.5	29.3	129.3
RDN		✓				✓				✓			36.8	27.2	115.3
M^2 Transformer		✓			✓		✓			✓	✓		39.1	29.2	131.2
Universal Cap			✓		✓		✓			✓	✓	✓	40.8	30.4	143.4
CPTR					✓		✓			✓	✓		40	29.1	129.4
Oscar		✓			✓			✓	✓		✓	✓	41.7	30.6	140
LEMON		✓			✓				✓		✓	✓	42.6	31.4	145.5
Embedding Reward	✓					✓				✓	✓		30.4	25.1	93.7

V. CONCLUSIONS

The study examined the model frameworks proposed in recent years in computer vision for image captioning tasks, specifically the object detection-based approach, Reinforcement Learning, multi-modal connections, and the Vision Language Pre-training approaches and also reviewed different datasets and evaluation metrics associated with the image captioning task. Even though the interpretation of the reinforcement learning, attention methods, and object detection-based techniques are good, it is concluded that employing Vision Language Pre-training approaches for downstream tasks such as picture captioning can outperform conventional designs.

REFERENCES

[1] Philip Kinghorn, Li Zang, “a region based image caption generator with refined descriptions” , Elsiver B V, 6 july 2017, Ling Shao University Northumbria New castle NE1,United Kingdom.

[2] Priyanka Raut, Rushali A Deshmukh, “An Advanced Image Captioning using combination of CNN and LSTM”, Turkish Journal of Computer and Mathematics Education, 05 April 2021, Savitribai Phule Pune Univresity, faculty, Maharhatra/India.

[3] J. Deng, W. Dong, R. Socher, L.-J. Li, K. Li, and L. Fei-Fei, “Imagenet: A large-scale hierarchical image database,” in Proceedings of the IEEE conference on computer vision and pattern recognition, pp. 248–255, 2009.

[4] O. Vinyals, A. Toshev, S. Bengio, and D. Erhan, “Show and tell: A neural image caption generator,” in Proceedings of the IEEE conference on computer vision and pattern recognition, 2015.

[5] Zhou Ren, Xiaoyu Wang, Ning Zhang, Xutao Lv, and Li-Jia Li. 2017. Deep Reinforcement Learning-based Image Captioning with Embedding Reward. In Proceedings of the IEEE conference on computer vision and pattern recognition (CVPR). 1151–1159

[6] L. Zhang, F. Sung, F. Liu, T. Xiang, S. Gong, Y. Yang, and T. M. Hospedales, “Actor-Critic Sequence Training for Image Captioning,” in NeurIPS, 2017

[7] Hanan Nasser Alkalouti, Dr. Mayada Ahmed, “Encoder-Decoder Model for Automatic Video Captioning Using Yolo Algorithm”, IEEE International IOT, Electronics and Mechatronics Conference (IEMTRONICS), 21-24 April 2021.

[8] Ke, L., Pei, W., Li, R., Shen, X., & Tai, Y. W. (2019, October). Reflective Decoding Network for Image Captioning. 2019 IEEE/CVF International Conference on Computer Vision. https://doi.org/10.1109/iccv.2019.00898

[9] Cornia, M., Stefanini, M., Baraldi, L., & Cucchiara, R. (2019). M2: Meshed-Memory Transformer for Image Captioning. ArXiv, abs/1912.08226

[10] R. Mokady, A. Hertz, and A. H. Bermano, “Clipcap: CLIP prefix for image captioning,” Computing research repository, vol. abs/2111.09734, 2021.

[11] Alec Radford, J. Wu, R. Child, D. Luan, D. Amodei, and I. Sutskever, “Language models are unsupervised multitask learners,” OpenAI blog, vol. 1, 2019.

[12] Xiujun Li, Xi Yin, Chunyuan Li, Pengchuan Zhang, Xiaowei Hu, Lei Zhang, Lijuan Wang, Houdong Hu, Li Dong, Furu Wei, Yejin Choi, & Jianfeng Gao. (2020). Oscar: Object-Semantics Aligned Pre-training for Vision-Language Tasks.

[13] Zhang, Pengchuan & Li, Xiujun & Hu, Xiaowei & Yang, Jianwei & Zhang, Lei & Wang, Lijuan & Yejin, Choi & Gao, Jianfeng(2021).VinVL: Revisiting Visual Representations in Vision-Language Models. 5575-5584.

[14] Hu, X., Gan, Z., Wang, J., Yang, Z., Liu, Z., Lu, Y., & Wang, L. (2022, June). Scaling Up Vision-Language Pretraining for Image Captioning. 2022 IEEE/CVF Conference on Computer Vision and Pattern Recognition (CVPR). https://doi.org/10.1109/cvpr52688.2022.01745

[15] Chenliang Li, Haiyang Xu, Junfeng Tian, Wei Wang, Ming Yan, Bin Bi, Jiabo Ye, He Chen, Guohai Xu, Zheng Cao, Ji Zhang, Songfang Huang, Fei Huang, Jingren Zhou, and Luo Si. 2022. mPLUG: Effective and Efficient Vision-Language Learning by Cross-modal Skip-connections. In Proceedings of the 2022 Conference on Empirical Methods in Natural Language Processing, pages 7241–7259, Abu Dhabi, United Arab Emirates. Association for Computational Linguistics.

[16] Cho, J., Yoon, S., Kale, A., Dernoncourt, F., Bui, T., & Bansal, M. (2022). Fine-grained Image Captioning with CLIP Reward. Findings of the Association for Computational Linguistics: NAACL 2022.

[17] Lin, T. Y., Maire, M., Belongie, S., Hays, J., Perona, P., Ramanan, D., Dollár, P., & Zitnick, C. L. (2014). Microsoft COCO: Common Objects in Context. Computer Vision – ECCV 2014, 740–755. https://doi.org/10.1007/978-3-319-10602-1_48

[18] https://www.kaggle.com/datasets/hsankesara/flickr-image-dataset

[19] Piyush Sharma, Nan Ding, Sebastian Goodman, and Radu Soricut. 2018. Conceptual Captions: A Cleaned, Hypernymed, Image Alt-text Dataset For Automatic Image Captioning. In Proceedings of the 56th Annual Meeting of the Association for Computational Linguistics (Volume 1: Long Papers), pages 2556–2565, Melbourne, Australia. Association for Computational Linguistics.

[20] Chen, Xinlei & Fang, Hao & Lin, Tsung-Yi & Vedantam, Ramakrishna & Gupta, Saurabh & Dollar, Piotr & Zitnick, C.. (2015). Microsoft COCO Captions: Data Collection and Evaluation Server.

[21] Douwe Kiela, Hamed Firooz, Aravind Mohan, Vedanuj Goswami, Amanpreet Singh, Pratik Ringshia, and Davide Testuggine. 2020. The hateful memes challenge: detecting hate speech in multimodal memes. In Proceedings of the 34th International Conference on Neural Information Processing Systems (NIPS'20). Curran Associates Inc., Red Hook, NY, USA, Article 220, 2611–2624.

[22] Agrawal, Harsh & Desai, Karan & Chen, Xinlei & Jain, Rishabh & Batra, Dhruv & Parikh, Devi & Lee, Stefan & Anderson, Peter. (2018). Nocaps: novel object captioning at scale.

[23] Gurari, D., Li, Q., Stangl, A. J., Guo, A., Lin, C., Grauman, K., Luo, J., & Bigham, J. P. (2018, June). VizWiz Grand Challenge: Answering Visual Questions from Blind People. 2018 IEEE/CVF Conference on Computer Vision and Pattern Recognition. https://doi.org/10.1109/cvpr.2018.00380

[24] Lu, Xiaoqiang & Wang, Binqiang & Zheng, Xiangtao & Liu, Wei. (2017). Exploring Models and Data for Remote Sensing Image Caption Generation. IEEE Transactions on Geoscience and Remote Sensing.

[25] https://www.kaggle.com/datasets/aishrules25/automatic-image-captioning-for-visually-impaired.

[26] Papineni, K., Roukos S., Ward T., Zhu W.J.: Bleu: A method for automatic evaluation of machine translation. In: Proceedings of the 40th annual meeting of the Association for Computational Linguistics, pp. 311– 318 (2002)

[27] C.-Y. Lin, “Rouge: A package for automatic evaluation of summaries,” in ACL Workshop, 2004.

[28] M. Denkowski and A. Lavie, “Meteor universal: Language specific translation evaluation for any target language,” in EACL Workshop on Statistical Machine Translation, 2014.

[29] R. Vedantam, C. L. Zitnick, and D. Parikh, “Cider: Consensus-based image description evaluation,” arXiv preprint arXiv:1411.5726, 2014.

[30] Anderson, P., Fernando B., Johnson M., Gould S.: Spice: Semantic propositional image caption evaluation. In: Proceedings of the European Conference on Computer Vision, pp. 382– 398 (2016).

E-ISSN 2581 –7957
P-ISSN 2277 – 3916

CVR Journal of Science and Technology, Volume 26, June 2024
DOI: 10.32377/cvrjst2615

Detection and Classification of Brain Tumor in MRI Images using EPCMA+ML-ELM

Dr. M. Deva Priya
Assoc. Professor, Sri Eshwar College of Engineering/CSE Department, Coimbatore, Tamilnadu, India
Email: devapriya.m@sece.ac.in

Abstract: **Substantial clinical statistics along with analytical features can be extracted from brain tumor images. The identified quantitative measures of exact tumor regions aid physicians and radiologists in effective treatment. Magnetic Resonance Imaging (MRI) images of the brain are considered. Handling these images is challenging mainly owing to variance in addition to complexity in detecting tumors. In this paper, images are segmented using Enhanced Possibilistic C-Means Algorithm (EPCMA) and classified using Multi-Layered Extreme Learning Machine (ML-ELM). System performance is observed based on classification accuracy, sensitivity and specificity.**

Index Terms: **Brain Tumor, Possibilistic C-Means Algorithm, Extreme Learning Machine, MRI,**

I. Introduction

Early identification of brain tumors would aid the Physicians to treat them in their initial stage. Tumors can be identified using Magnetic Resonance Imaging (MRI) scan, biopsy, nerve tests, etc., Though physicians get a clear picture of tumors from brain MRI, quantified details are also essential. Brain tumor classification involves the following steps: image pre-processing, feature extraction, training and testing [1 - 3].

In medical imaging, there are chances for images to be noisy, leading to image misclassification and degradation of classifier's performance [4]. Hence, images are pre-processed by filtering to enhance image quality. Feature extraction deals with quantitative measurement of images, wherein image data is converted to statistical numeric values [5, 6]. The features include contrast, homogeneity, correlation, energy, entropy etc.,

The classifiers analyze extracted features and perform classification [7]. There are various learning classifiers like Artificial Neural Network (ANN), Probabilistic Neural Network (PNN), Extreme Learning Machine (ELM), Hidden Markov Model (HMM) and Support Vector Machine (SVM) [8, 9]. Each classifier has its own merits and demerits.

Initially, images are preprocessed to eliminate noise and enhance image quality by using Median Filter (MF). Once the quality of image is enhanced, it is segmented [10]. Image segmentation deals with splitting an image into homogeneous, distinct and significant clusters based on properties including color, texture, gray level, depth, reflectivity etc., In this work, images are segmented and classified using EPCMA+ML-ELM. The network is trained using ELM.

II. Related Work

Bahadure et al (2017) [11] have focused on enhancing performance and reducing the complexity involved in image segmentation. Berkeley Wavelet Transformation (BWT) is used for segmenting brain tumor images. To enhance accuracy of Support Vector Machine (SVM)-based classifiers, appropriate features are extracted from every segment. Performance is analyzed in terms of accuracy, specificity, Dice Similarity Index (DSI) co-efficient and sensitivity. The proposed scheme offers improved overlap between automatically and manually extracted tumor regions.

Amin et al (2018) [12] have used three convolutional, three ReLU along with one softmax layer. MR image is split into numerous patches and center pixel value of each patch is given to DNN which assigns labels based on these pixels and performs segmentation. Experiments are performed using several datasets. Results are assessed based on Accuracy, Jaccard Similarity Index (JSI), specificity, sensitivity, DSI Coefficient, precision, False Positive Rate (FPR) and True PR (TPR).

Amin et al (2020) [13] have proposed an automated scheme to facilitate easy differentiation of cancerous as well as non-cancerous brain MRI. Diverse techniques are applied for segmenting candidate lesions. Feature set is selected for each applicant lesion based on shape, intensity as well as texture. SVM involving diverse cross validations on features is applied to determine precision for varying datasets including Harvard, RIDER as well as Local. The performance of the proposed scheme is analyzed in terms of accuracy, Area Under Curve (AUC), sensitivity and specificity. It involves less processing time in contrast to present approaches.

Gull & Akbar (2021) [14] have focused on extracting vital features and identifying diverse segmentation and classification schemes which can be used for multimodal MRIs for identifying brain tumors. Several ML and DL-based classification methods are applied on tumor MRI images of different datasets.

Rammurthy & Mahesh (2022) [15] have used Whale Harris Hawks Optimization (WHHO) for identifying brain tumors from MRI images. Cellular Automata (CA) and Rough Set (RS) theory are used for segmentation. Further, features are extracted from segments that comprise of tumor size, mean, variance, Kurtosis and Local Optical Oriented Pattern (LOOP). Further, Deep Convolutional Neural Network (DeepCNN) is used, where WHHO is involved in training. A hybrid system is designed which includes Whale Optimization Algorithm (WOA) as well as Harris Hawks Optimization (HHO) algorithm. The performance of the propounded scheme is analyzed in terms of accuracy, specificity and sensitivity.

Mahmud et al (2023) [16] have suggested CNN-based architecture for efficient detection of brain tumors from MRI

Received on 15-12-2023, Revised on 14-01-2024, Accepted on 13-02-2024.

CVR Journal of Science and Technology, Volume 26, June 2024
DOI: 10.32377/cvrjst2615

images. It details diverse models including ResNet-50, VGG16 as well as Inception V3 and performs a comparison between proposed framework and existing models. The performance is analyzed based on diverse metrics including accuracy, recall, loss and AUC. It is seen that the proposed scheme performs better in contrast to standard schemes. The proposed model aids in prompt identification of different kinds of brain tumors.

III. Proposed Model

The proposed scheme focuses on segmentation, feature extraction, training and classification. Tumors are segmented using Enhanced Possibilistic C Means Algorithm (EPCMA) and classified using Multi-Layered Extreme Learning Machine (ML-ELM). Deep Learning (DL) classifier is also propounded in the work.

Segmentation

In the segmentation module, MRI images are pre-processed as well as segmented to eliminate noise using EPCMA. Noise is removed using Median Filtering (MF) and features are extracted from each segment depending on shape, intensity and texture. Once features are extracted, prominent features are chosen by using RP for classification.

Feature Extraction

Most predominant features are chosen. Dimensionality of the dataset has a greater impact on accuracy. It is essential to consider aspects which lessen the system complexity.

Training

ELM-based classifiers are trained based on features of training data.

Classification

In this phase, features obtained from segmented images are sent to trained ELM classifiers to identify whether a region is affected or not.

Enhanced Possibilistic C-Means Algorithm (EPCMA)

Clustering focusses on partitioning a given set of data into significant sub-classes called clusters. It involves grouping of objects based on features, and grouping them based on similarities existing among them. The objects in a group are 'similar' to each other within a cluster, but are 'dissimilar' when compared to objects of other clusters.

In EPCMA, every cluster is independent of another. The objective function of cluster 'i' is expressed as,

$$J(\beta_i, U_i, X) = \sum_{j=1}^{n}(U_{ij})^m\, d^2(x_j, \beta_i) + \eta_i \sum_{j=1}^{n} (1 - U_{ij})^m \quad (1)$$

where,
j - Cluster
m - Fuzzifier
β_i - Prototype related to 'i'
U - Membership associated with cluster 'i'
η_i - Scale parameter

The parameter 'η_i' can be determined from distance statistics of dataset 'X' which is initialized to '1'. Membership update in Possibilistic C-Means (PCM) is given by,

$$U_{ij} = \frac{1}{1+\left(\frac{d^2(x_j,\beta_i)}{\eta_i}\right)^{\frac{1}{m-1}}} \quad (2)$$

By solving for '$d^2(x_j, \beta_i)$' in terms of 'U_{ij}',

$$d^2(x_j, \beta_i) = \eta_i \left(\frac{1-U_{ij}}{U_{ij}}\right)^{\frac{1}{m-1}} \quad (3)$$

From the objective function in Eq. (1), '$d^2(x_j, \beta_i)$' can be eliminated using Eq. (3).

$$J_i(\beta_i, U_i, X) = \eta_i \sum_{j=1}^{n}(1 - U_{ij})^{m-1} \quad (4)$$

For a given value of 'η_i', minimizing '$J_i(\beta_i, U_i, X)$' is equivalent to maximizing '$J_I(\beta_i, U_i, X)$'.

$$J_I(\beta_i, U_i, X) = \eta_i \sum_{j=1}^{n}(1 - (1 - U_{ij})^{m-1} = \eta_i \sum_{j=1}^{n}(\acute{U}_{ij}) \quad (5)$$

Where

$$\acute{U}_{ij} = [1 - (1 - U_{ij})]^{m-1} \quad (6)$$

$\acute{U}_{ij}$- Modified membership

Further, for m = 2, Eq. (5) reduces to

$$J_I(\beta_i, U_i, X) = \eta_i \sum_{j=1}^{n} U_{ij} \quad (7)$$

From Eq. (5) and Eq. (6), for a particular value of 'η_i', every C-sub objective function is improved by selecting suitable prototype locations. It is necessary to ensure that total modified membership is improved. Prototype should be positioned in a dense area as membership is a monotonically declining function that is based on distance.

For C-dense regions in feature space, each prototype converges to a dense region if proper initialization is done.

Even if 'η_i's are equal or all sub-objective functions are identical, each has 'C' unique minima conforming to C-dense regions. The right choice of fuzzifier value (m) is around 1.5.

The algorithm is a variation of the possibilistic method. In case fuzzifier 'm' is eliminated, an alternate formulation is obtained as follows:

For instance,

$$J_I(\beta_i, U_i, X) = \sum_{j=1}^{n}(U_{ij}) d^2(x_j, \beta_i) + \eta_i \sum_{j=1}^{n}(U_{ij}.log\, U_{ij} - U_{ij}) \quad (8)$$

'U_{ij}' is updated as shown below.

$$U_{ij} = exp\ exp\left\{-\frac{d^2(x_j,\beta_i)}{\eta_i}\right\} \quad (9)$$

Prototype update equations are unchanged. Exponential function rapidly deteriorates for high values of '$d^2(x_j, \beta_i)$'. This seems to be suitable when clusters are close to one another.

It is seen that, similar to '$(1 - U_{ij})^m$', '$U_{ij}.log\, U_{ij} - U_{ij}$' is a monotonically declining function in range [0,1]. If Mahalanobis distance is used for '$d^2(x_j, \beta_i)$', then 'η_i' can also be eliminated (set η_i = 1).

Multi-Layer Extreme Layer Machine (ML-ELM)

In the proposed methodology, tumor images are classified using ML-ELM [17]. Auto Encoders (AE) are used as building blocks in every layer for learning. Activation

CVR Journal of Science and Technology, Volume 26, June 2024
DOI: 10.32377/cvrjst2615

functions may be linear or non-linear. ELM-AE reproduces input signals. Input is mapped to ELM feature space of L-dimensions and output is given by,

$$f_l = \sum b_i \quad (10)$$

$$\underline{h}_i(x) = \underline{h}(x).b \quad (11)$$

Output weight matrix amid hidden and output nodes is computed as shown below.

$$b = [b_1, \ldots . b_L]^T \quad (12)$$

For input 'x', output of hidden node is represented as,

$$\underline{h}(x) = [g_1(x), \ldots ., g_L(x)] \quad (13)$$

Where,

$g_i(x)$ - Output of hidden node 'i'

For 'n' training samples $\{(x_i, t_i)\}_{i=1}$, ELM is proficient in solving the learning problem.

$$\underline{h}b = T \quad (14)$$

Target labels are given by,

$$T = [t_1, \ldots, t_N]^T \quad (15)$$

$$\underline{h} = [\underline{h}^T(x_1), \ldots ., \underline{h}^T(x_N)]^T \quad (16)$$

Output weights (b) are computed as shown below.

$$b = \underline{h} \dagger T \quad (17)$$

Where,

$\underline{h}\dagger$ - Moore-Penrose inverse of '$\underline{h}$'

Regularization is done to increase performance of ELM.

$$B = \left(\frac{I}{C} + \underline{h}^T\underline{h}\right)^{-1} \underline{h}^T.\underline{h} \quad (18)$$

Weights as well as biases are orthogonally selected so as to increase the performance of ELM-AE [18]. In ELM-AE, input may be projected to varying or similar dimension space as in Johnson- Lindenstrauss lemma.

$$\underline{h} = g(a.x + m) \quad (19)$$

Where,

$$a^T.a = I \quad (20)$$

$$m^T m = 1 \quad (21)$$

Orthogonal random weights are given by,

$$a = [a_1, \ldots . a_L] \quad (22)$$

Orthogonal random biases amid input as well as hidden nodes are given by,

$$m = [m_1, \ldots . m_L] \quad (23)$$

For sparse as well as compressed ELM-AE illustrations, output weight 'B' is computed as:

$$B = \left(\frac{I}{C}.H^T H\right)^{-1} H^T X \quad (24)$$

Hidden layer outputs are given by,

$$h = [h_1, \ldots, h_N] \quad (25)$$

IV. RESULTS AND DISCUSSION

MRI images from the Kaggle dataset are taken. The proposed technique for identifying brain tumors is applied and performance is analyzed. The proposed scheme offers improved accuracy, sensitivity as well as specificity in contrast to other methods for real-time as well as benchmark datasets.

Experimental setup and assessment metrics

The proposed scheme is implemented using MATLAB. True and False Positive (TP & FP), and True and False Negative (TN & FN) are determined depending on which sensitivity, accuracy and specificity are calculated.

Figure 1 shows some sample input MRI images. Figure 2 shows the images after applying EPCMA+ML-ELM.

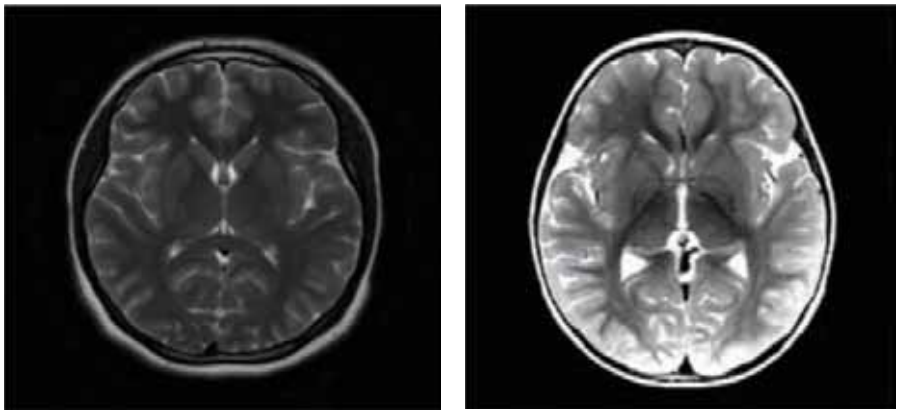

(a) (b)

Figure 1: Input MRI Images

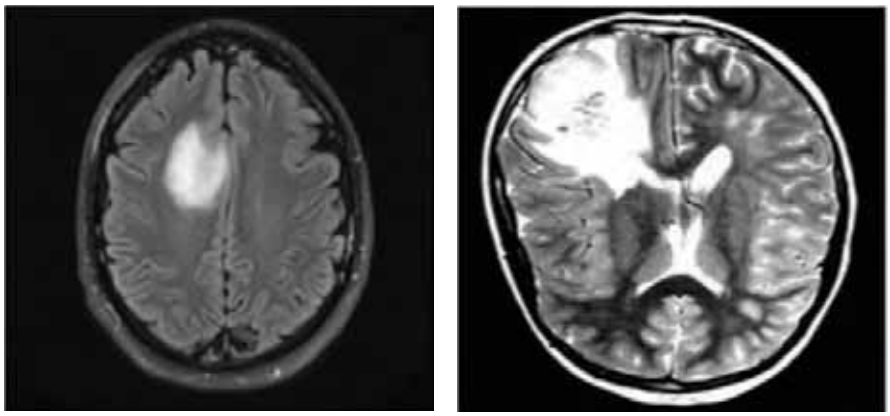

(a) (b)

Figure 2: MRI Image after implementing EPCMA+ML-ELM

Sensitivity is the ratio of TPs which are properly determined using diagnostic tests. It shows the efficiency of a test in identifying a disease.

$$Sensitivity = \frac{TP}{TP + FN} \quad (26)$$

Specificity is a ratio of TNs suitably identified by a test. It shows how an efficient test detects normal conditions.

$$Specificity = \frac{TN}{TN + FP} \quad (27)$$

Accuracy shows the amount of true outcomes, either TP or TN. It denotes the veracity level of a test.

$$\text{Accuracy} = \frac{\text{TN} + \text{TP}}{\text{TN} + \text{TP} + \text{FN} + \text{FP}} * 100 \quad (28)$$

Performance analysis

The performance of propounded scheme is analyzed in terms of sensitivity, specificity as well as accuracy for varying number of hidden neurons in the range of 50 to 200 in step of 25.

Figure 3 shows sensitivity. EPCMA+ML-ELM offers 13% and 5% better sensitivity when compared to ELM and ML-ELM respectively.

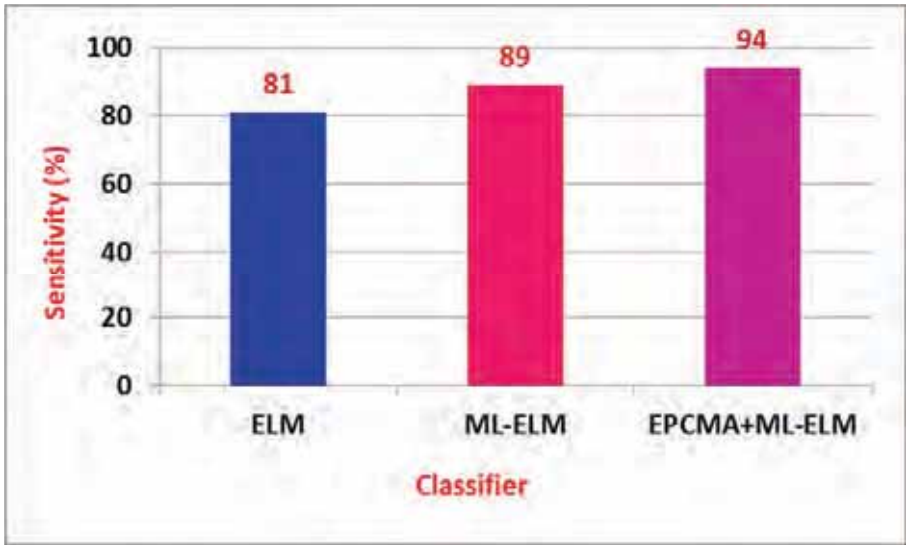

Figure 3: Sensitivity

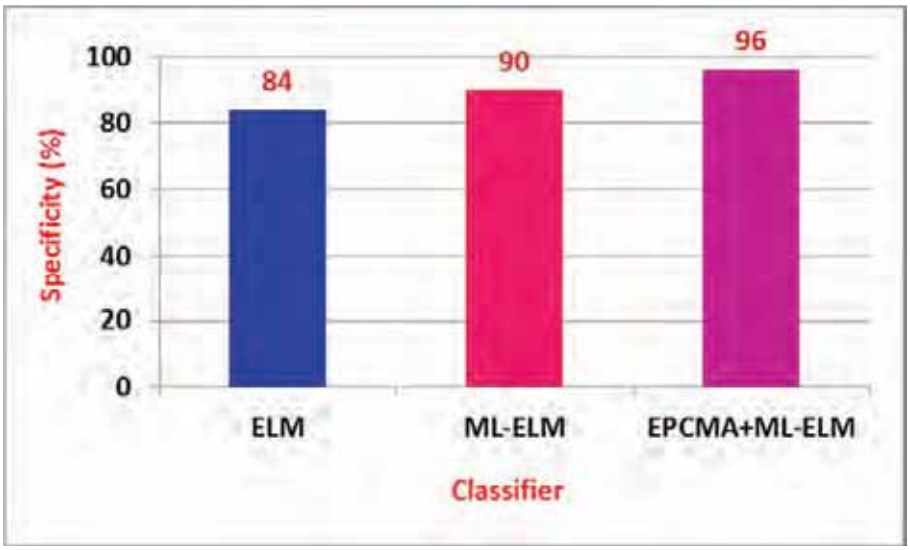

Figure 4: Specificity

Figure 4 shows the specificity. EPCMA+ML-ELM offers 12% and 6% improved specificity in contrast to ELM and ML-ELM respectively.

Figure 5 shows the classification accuracy. EPCMA+ML-ELM offers 13% and 7% better classification accuracy when compared to ELM and ML-ELM respectively.

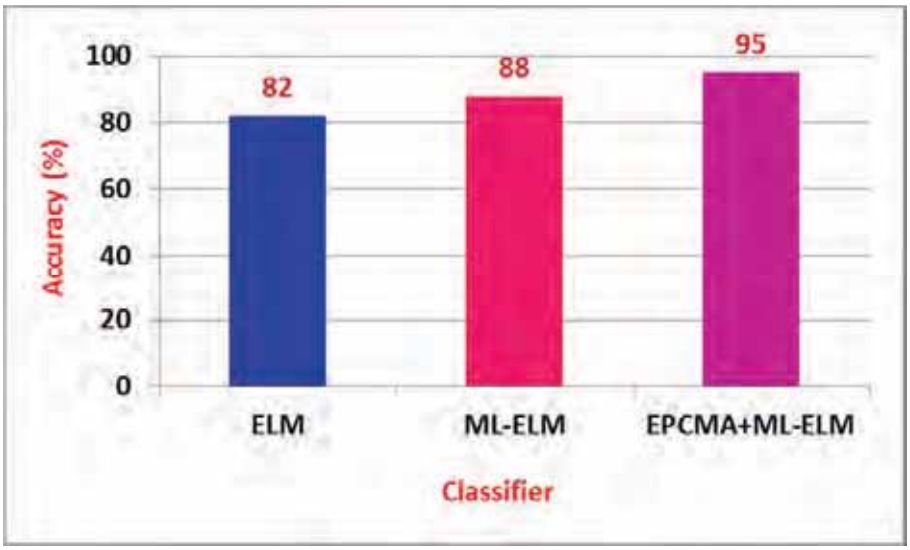

Figure 5: Classification Accuracy

Figure 6 shows the training accuracy. EPCMA+ML-ELM offers 9% and 5% better training accuracy in contrast to ELM and ML-ELM respectively.

Figure 7 shows the testing accuracy. EPCMA+ML-ELM offers 13% and 6% better testing accuracy when compared to ELM and ML-ELM respectively.

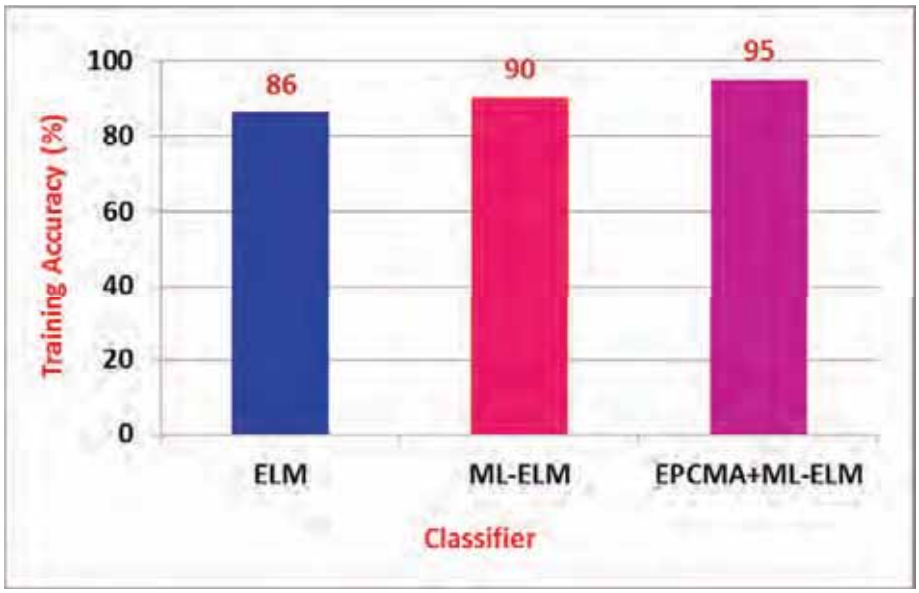

Figure 6: Training Accuracy

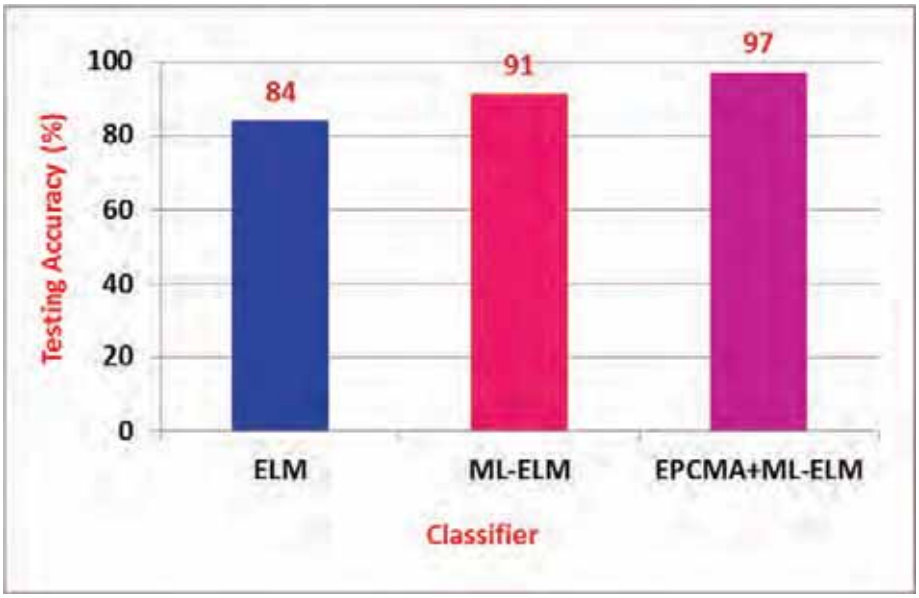

Figure 7: Testing Accuracy

V. Conclusion

In this paper, MRI images of tumors are segmented using EPFCM and classified using ML-ELM. The performance of the proposed mechanism is assessed in terms of sensitivity, specificity and classification accuracy, training as well as testing accuracies. It is seen that EPCMA+ML-ELM yields better results in contrast to DL classifiers and ELM.

References

1. Kadam, D. B. (2012). Neural network based brain tumor detection using MR images.
2. Dong, H., Yang, G., Liu, F., Mo, Y., & Guo, Y. (2017). Automatic brain tumor detection and segmentation using U-Net based fully convolutional networks. In Medical Image Understanding and Analysis: 21st Annual Conference, MIUA 2017, Edinburgh, UK, July 11–13, 2017, Proceedings 21 (pp. 506-517). Springer International Publishing.
3. Madhuri, G. S., Mahesh, T. R., & Vivek, V. (2022). A Novel Approach for Automatic Brain Tumor Detection Using Machine Learning Algorithms. In Big data management in Sensing (pp. 87-101). River Publishers.
4. Pereira, S., Pinto, A., Alves, V., & Silva, C. A. (2016). Brain tumor segmentation using convolutional neural networks in MRI images. IEEE transactions on medical imaging, 35(5), 1240-1251.
5. Mohsen, H., El-Dahshan, E. S. A., El-Horbaty, E. S. M., & Salem, A. B. M. (2018). Classification using deep learning neural networks for brain tumors. Future Computing and Informatics Journal, 3(1), 68-71.

6. Swati, Z. N. K., Zhao, Q., Kabir, M., Ali, F., Ali, Z., Ahmed, S., & Lu, J. (2019). Brain tumor classification for MR images using transfer learning and fine-tuning. Computerized Medical Imaging and Graphics, 75, 34-46.
7. Polly, F. P., Shil, S. K., Hossain, M. A., Ayman, A., & Jang, Y. M. (2018, January). Detection and classification of HGG and LGG brain tumor using machine learning. In 2018 International Conference on Information Networking (ICOIN) (pp. 813-817). IEEE.
8. Abdel-Maksoud, E., Elmogy, M., & Al-Awadi, R. (2015). Brain tumor segmentation based on a hybrid clustering technique. Egyptian Informatics Journal, 16(1), 71-81.
9. Deepak, S., & Ameer, P. M. (2019). Brain tumor classification using deep CNN features via transfer learning. Computers in biology and medicine, 111, 103345.
10. Kircher, M. F., De La Zerda, A., Jokerst, J. V., Zavaleta, C. L., Kempen, P. J., Mittra, E., ... & Gambhir, S. S. (2012). A brain tumor molecular imaging strategy using a new triple-modality MRI-photoacoustic-Raman nanoparticle. Nature medicine, 18(5), 829-834.
11. Bahadure, N. B., Ray, A. K., & Thethi, H. P. (2017). Image analysis for MRI based brain tumor detection and feature extraction using biologically inspired BWT and SVM. International journal of biomedical imaging, 2017.
12. Amin, J., Sharif, M., Yasmin, M., & Fernandes, S. L. (2018). Big data analysis for brain tumor detection: Deep convolutional neural networks. Future Generation Computer Systems, 87, 290-297.
13. Amin, J., Sharif, M., Yasmin, M., & Fernandes, S. L. (2020). A distinctive approach in brain tumor detection and classification using MRI. Pattern Recognition Letters, 139, 118-127.
14. Gull, S., & Akbar, S. (2021). Artificial intelligence in brain tumor detection through MRI scans: advancements and challenges. Artificial Intelligence and Internet of Things, 241-276.
15. Rammurthy, D., & Mahesh, P. K. (2022). Whale Harris hawks optimization based deep learning classifier for brain tumor detection using MRI images. Journal of King Saud University-Computer and Information Sciences, 34(6), 3259-3272.
16. Mahmud, M. I., Mamun, M., & Abdelgawad, A. (2023). A deep analysis of brain tumor detection from mr images using deep learning networks. Algorithms, 16(4), 176.
17. Kasun, L. L. C., Zhou, H., Huang, G. B., & Vong, C. M. (2013). Representational learning with extreme learning machine for big data.
18. Kasun, L. L. C., Yang, Y., Huang, G. B., & Zhang, Z. (2016). Dimension reduction with extreme learning machine. IEEE transactions on Image Processing, 25(8), 3906-3918.

E-ISSN 2581 –7957
P-ISSN 2277 – 3916

CVR Journal of Science and Technology, Volume 26, June 2024
DOI: 10.32377/cvrjst2616

Enhanced Call Admission Control based on History in BWA Networks

Dr. A. Christy Jeba Malar[1] and Dr. M. Deva Priya[2]
[1] Assoc. Professor, Sri Krishna College of Technology/IT Department, Coimbatore, Tamil Nadu, India
Email: a.christyjebamalar@skct.edu.in
[2] Assoc. Professor, Sri Eshwar College of Engineering/CSE Department, Coimbatore, Tamil Nadu, India
Email: devapriya.m@sece.ac.in

Abstract: WiMAX is a wireless technology that supports many blooming applications. To efficiently assign resources to traffic flows, bandwidth allocation and Connection Admission Control (CAC) modules are included in MAC layer and Burst Allocation (BA) module is added to PHY layer. It is essential to lessen delay and effectively schedule requests for BA. In this paper, CAC-based on History (CACH) and scheduler based on Delay Tolerance (SDT) for BA are proposed for WiMAX networks. CACH accepts/ rejects connections based on values in Contention Window (CW) in former Time Frame (TF). SDT and a Bucket-based BA (BBA) assign resources to flows with least amount of DT. Performance is analyzed based on throughput, Packet Loss Ratio (PLR) and delay.

Index Terms: WiMAX, Contention Window, Contention Delay, Delay Tolerance, Traffic Priority, Connection Admission Control, Burst Allocation

I. Introduction

Worldwide Interoperability for Microwave Access (WiMAX) facilitates ubiquitous distribution of wireless broadband service for fixed or mobile users [1, 2]. The forum supports IEEE 802.16 standards for offering Broadband Wireless Access (BWA). IEEE 802.16 standard offers Line of Sight (LoS) communication at 10 - 66 GHz frequency bands [3]. IEEE 802.16a supports non-LoS (NLoS) mode in the frequency range 2 - 11 GHz [4].

WiMAX grants resources in 2 ways. Bandwidth may be allocated using one of the modes namely: Grant Per Connection (GPC) and GP Subscriber Station (GPSS) [5, 6].

- **GPSS:** BS assigns a share of resources to a Mobile Station (MS) with several connections. The MS is responsible for assigning resources to distinct connections, satisfying QoS demands as well as priority agreements. The scheduler takes control of order in which services are offered to connections. It is suitable for real-time applications which are delay-sensitive.
- **GPC:** In this mode, BS individually offers bandwidth to every connection. It is appropriate for a MS involving reduced amount of connections. Requests are piggybacked to data which is forwarded and is appropriate for Point-to-Multipoint (PMP) as well as mesh modes. Extra bandwidth is consumed to deal with Radio Link Control (RLC) demands of MS.

GPSS is better in contrast to GPC mode [7].

In this paper, CAC-based on History (CACH) and Scheduler based on Delay Tolerance (SDT) and Bucket-based Burst Allocator (BBA) are proposed. The CACH module focuses on call acceptance or rejection based on Contention Delay (CD). SDT takes DT of traffic into consideration and BBA assigns resources by prioritizing flows with minimum DT. They are closely coupled and are inseparable. Burst profiles are negotiated with BS.

II. Related Work

In this section, works related to CAC and BA in WiMAX networks are detailed.

Mamman et al (2017) [8] have propounded Adaptive CAC along with bandwidth reservation for downlink LTE networks. It focuses on offering efficient use of resources to evade starvation of BE traffic. The proposed mechanism includes dynamic threshold that regulates network resources under dense traffic. Reservation as well as degradation method to accept users with restricted amount of bandwidth is also achieved. It uses Call Blocking Probability (CBP) as well as Call Dropping Probability (CDP) with dynamic threshold for regulating network status. Finally, it uses analytical model using Markov chain for measuring performance of propounded mechanism. The scheme admits calls effectively and guarantees QoS to all kinds of traffic.

Al-Maitah et al (2018) [9] have proposed Dynamic Weighted Round Robin-CAC (DWRR-CAC) mechanism that focuses on reducing blocking rates of connections. But it wastes resources owing to fixed reservation as well as employed degradation schemes. The proposed algorithm deals with resource wastage by including pre-check, adaptive degradation and weight computation scheme. It accepts connections depending on Maximum Sustained Traffic Rate (MSTR) in case resources are under-utilized. It admits queued connections based on WRR weight. When resources are not adequate to accept new connections, it uses a pre-check scheme to find whether non-UGS connections which degrade offer necessary bandwidth for admitting connections. It admits connections depending on WRR weight. The proposed scheme offers improved call blocking rate and mean throughput.

Gupta et al (2020) [10] have proposed Fuzzy Game based Channel Allocation (FGCA), a hybrid multi-channel assignment formulated using Game Theory (GT) scheme. Fuzzy-based systems may be used for eliminating approaches that are unrealistic. The proposed optimization mechanism focuses on channel allocation using Fuzzy GT (FGT). FGCA diminishes channel interference and improves complete performance of WiMAX system based on factors

Received on 26-02-2024, Revised on 27-03-2024, Accepted on 26-04-2024.

CVR Journal of Science and Technology, Volume 26, June 2024
DOI: 10.32377/cvrjst2616

like channel acquisition delay, utilization and mean throughput.

Ababneh (2021) [11] have proposed Joint Routing and Rate Assignment Protocol (JRRA) for offering better utilization as well as throughput. The proposed routing scheme involving fully distributed ST is bandwidth-aware. The protocol offers maximum remaining capacity routes and guarantees improved data rates thus offering better throughput, capacity as well as fairness. The problem is expressed as Mixed Integer Linear Program (MILP) which improves system efficacy by offering improved QoS. It allocates resources to nodes fairly based on needs as well as priorities.

Taranum (2022) [12] focuses on mobility in an environment with multiple cells where an MS moves from a Base Station (BS) to another based on signal quality. The main aim is to sustain connectivity in heterogeneous network for which thresholds based on Receiver Signal Strength (RSS) are determined. Performance is analyzed in terms of throughput determined using RSS for diverse data rates, mean jitter and delay.

Bandwidth allocation in WiMAX networks dismisses association amid self-centered Service Providers (SPs). Maher et al (2022) [13] have offered Semi-Dynamic Bandwidth Allocation (S-DBA) scheme which determines interest points during the process of integration. In auction-based scheme, optical line terminal implements auction allocate most eminent bidders depending on available bandwidth. The proposed approach uses Stackelberg and coalition game based on throughput as well as delay. Auction on bandwidth need not be repeated in successive short duration, particularly user demands do not vary rapidly.

It is not essential to link a user to a neighboring Relay Station (RS). Banna (2022) [14] has considered standards to improve network efficiency in terms of throughput, network delay and interference while assigning link between MS and RS. The algorithm forms a tree which directs communication amid MS and BS through RS in a multi-hop network. An algorithm that focuses on balancing load amid RSs is proposed along with directing radiations of MSs based on path of minimum interference. The proposed scheme offers improved throughput and reduced delay.

Zou et al (2023) [15] have dealt with optimization of resource organization for supporting adapted service slicing and placing functions produced by varied devices into existing resources. The combinatorial optimization problem is handled by designing Particle Swarm Optimization (PSO)-based scheduling approach based on improved inertia weight, particle disparity as well as non-linear learning factor, thus balancing local as well as global solutions and increasing speed of convergence to global near-ideal solutions. It includes Random Walk (RW)-based model developed with adjustable step size, non-linear learning factor and inertia weight for improving particle survivability, variability and adaptation. The proposed scheme involves better convergence speed as well as efficient use of resources in contrast to variations of PSO.

III. Call Admission Control (CAC)

Decision to make call admissions depending on traffic descriptor specifies traffic features and QoS demands. CAC module focuses on rejecting calls when incoming as well as outgoing traffic exceeds pre-specified thresholds. It offers assured signal quality, Call Dropping Probability (P_D), prioritization to various categories of traffic, maximum revenue, fair resource sharing, rate of transmission as well as packet-based QoS.

BS defines contention period during which MS forwards bandwidth requests. When more than one MS contends for medium and sends requests simultaneously, collision occurs. Contention Window (CW) includes slots for packets which wait for getting into medium. It holds packets until the medium is free. The amount of contention slots represents chances given to MS for sending requests. The MS waits for pre-set amount of slots for receiving Uplink (UL) maps and gets to back-off process. Contentions are resolved depending on Truncated Binary Exponential Backoff (TBEB). CD refers to interval amid packet arrival time at Head of Queue (HoQ) and time at which it is sent on PHYsical medium. It depends on contention features of channel existing between adjoining nodes.

CACH considers former CW (CW_{PRE}) values, determines present values and accepts MSs with improved (CW_{CUR}) values.

IV. CAC Based on History (CACH)

A call is accepted only when it does not lead to deterioration of QoS of calls prevailing in network. Once bandwidth is assigned to every flow, scheduled calls in every flow are admitted based on the fact that accepting it does not lead to increased CD. CAC depends on available bandwidth. Checking availability of remaining bandwidth is not adequate for accepting calls. Channel should be verified for collision as CD increases when medium is fully occupied.

CACH framework admits requests for establishing connection from every service flow, verifies CW and decides whether to accept or reject calls. CACH accepts calls based on demand of resources, traffic behavior, availability, network conditions as well as CD.

CACH Policy

CW comprises of values of CD. Requests from MSs involving less CD are included in the medium. Requests from MSs with '$CD < CD_{TH}$' are only accepted. CD differs based on kinds of request made by MS. Time for servicing a request differs based on flow type. Figure 1 shows complete flow of CACH module.

CVR Journal of Science and Technology, Volume 26, June 2024
DOI: 10.32377/cvrjst2616

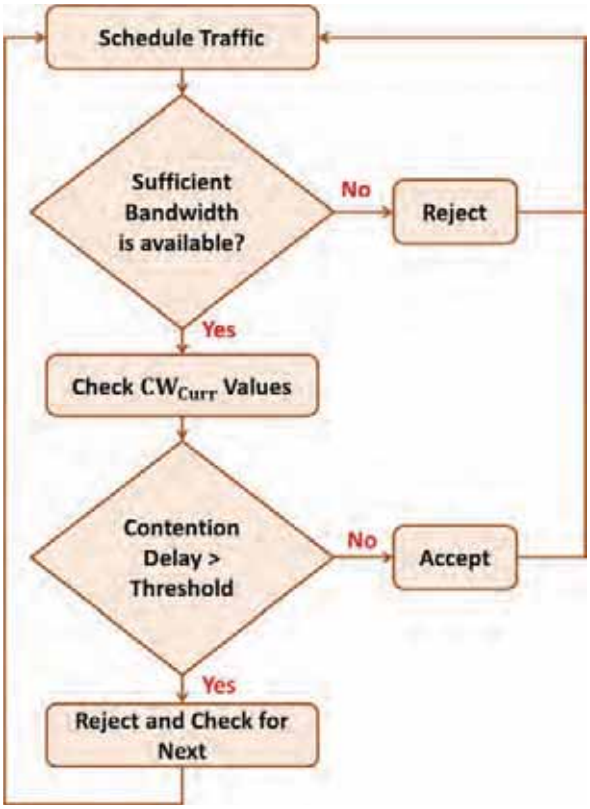

Figure 1. CACH Policy

MAC agent copies Variance of CD (CD_{VAR}) from fragment to packets. During fragmentation, the MAC agent selects contention sample from last fragment and copies from packet. Deviation of 'CD' can be found at a MS. Timestamp is involved in process of fragmentation to maintain 'CD' of fragment in contemporary MS. 'CD_{VAR}' is stored in fragment and 'n^{th}' or 'n^{th}_{CURR}' MS copies mean value into 'ACK' from segment. As value of 'CD_{Var}' increases, the probability of contention also increases. 'CD' increases with MAC contention and Retransmission Time Out (RTO) is triggered with packet losses.

Let 'n_{Max}' represent maximum quantity of MSs and 'n_{Curr}' represents quantity of MSs presently serviced by BS. There are chances for 'n_{Curr}' to be more than 'n_{Max}'. This happens when MSs enter range of BS and maximum quantity of MSs is surpassed. When number of users increase, network will not be capable of including MSs. This increases quantity of requests competing for medium, thus raising the value of 'CD'.

'VCD' is computed from past values.

$$E_{Curr} = \frac{(n_{Curr}-1).E_{Prev} + CD_{Curr}}{n_{Curr}} \quad (1)$$

if $n_{Curr} < n_{Max}$

$$VCD_{Curr} = \frac{(n_{Curr}-1)(V_{Prev} + E^2_{Prev}) + CD^2_{Curr}}{n_{Curr}} - E^2_{Curr} \quad (2)$$

$$E_{Curr} = E_{Prev} + \frac{CD_{Curr} - CD_{Prev}}{n_{Max}} \quad (3)$$

if $n_{Curr} \geq n_{Max}$,

$$VCD_{Curr} = \frac{n_{Max}\,(V_{Prev} + E^2_{Prev}) + CD^2_{Curr} - CD^2_{Old}}{n_{Max}} - E^2_{Curr} \quad (4)$$

'CD_{Th}' is initialized. Based on former values, when threshold of 'CD_{Var}' (CD^{Th}_{Var}) is exceeded, $CD_{Var} > CD^{Th}_{Var}$, then request from incoming MS will not be accepted as contention degree is high. Every MS updates 'CD_{Var}' for present transmission before comparing with 'CD_{Th}'.

V. SDT For Burst Allocation

DT of 'k^{th}' packet of priority class 'j' represents the time consumed by a packet to get into UL channel.

$$DT^j_k = W^j_k + \sigma^j_k + P^j_k + F_L \quad (5)$$

Where,

W^j_k - Waiting time of packet

σ^j_k - Time taken for transmitting 'k^{th}' packet of class 'j'

F_L - Mean latency

P^j_k - Propagation delay

Scheduling is performed depending on priority of incoming traffic. With each type of traffic, a combination of factors is included depending on which MSs are sorted. SDT schedules MS depending on following factors.

- Current Rate of Transmission (TR^i_{CUR})
- Allowable Data Rate (ADR_i)
- Quantity of Pending Data (PD_i)
- Serviced Data (SD_i)
- DT (DT_i)

Permitted delay for every flow is taken into consideration for scheduling requests. UGS as well as rtPS flows do not tolerate delays, whereas nrtPS as well as BE flows can withstand delays. Although UGS and rtPS flows are serviced first, DT is a significant factor that must be taken into account. If UGS flows are serviced before rtPS, then rtPS flows will suffer delay. In case there is no pending UGS traffic, rtPS flow is serviced.

'TR^i_{Curr}' is forwarded to scheduler and BA. The scheduler has details of updated 'PD_i' lined up in every flow. 'ADR_i' is dynamically fed to scheduler. The quantity of Data Serviced (SD_i) is considered by the scheduler to find Factor representing Contentment ($\acute{C}_i$) for delay-independent traffic. Resources are assigned based on Assignments (AS) given by scheduler.

CVR Journal of Science and Technology, Volume 26, June 2024
DOI: 10.32377/cvrjst2616

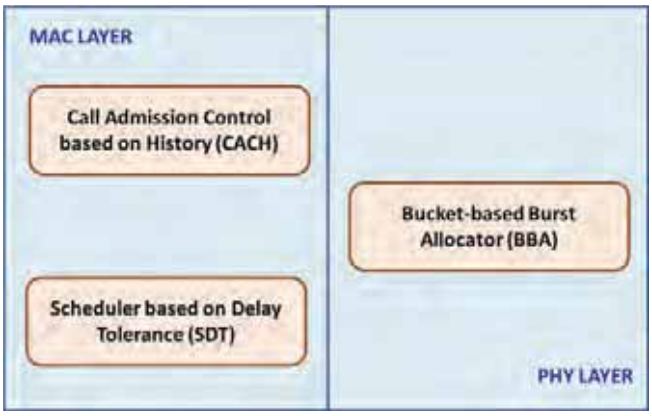

Figure 2. CACH and SDT coupled with BBA

A 2-tier framework, in which scheduler allocates priorities to MS' traffic and assigns resources to traffic depending on priority is designed. In initial tier, traffic is categorized by kind as well as priority is allotted in the following order: UGS, rtPS and nrtPS flows.

Excessive UGS traffic is circumvented in ensuing frame and nrtPS flow does not starve. In second tier, traffic of same priority in 1st tier is allocated varying priorities based on ensuing factors - present and mean transmission rates, accepted data rates as well as length of queues.

As shown in Figure 2, admitted traffic is given to SDT. SDT schedules flows depending on quantity of delay tolerated by each type of traffic. In a round, BBA finds available free space and allowable bucket size (Δbkt). SDT focuses on mapping traffic to buckets and forwarding them to BBA. BBA organizes IEs as well as bursts to every MS. Information regarding burst assigned traffic for each MS is forwarded to SDT. Both UGS as well as rtPS flows are scheduled based on DT value.

In case of UGS flows, MS with least DT and increased data rate is given priority.

$$\rho_i = \frac{1}{DT} \quad (6)$$

$$P_i^{UGS} = TR_{Curr}^i * \rho_i \quad (7)$$

- In case DT is less, then specific request must be serviced before the rest. So a least DT yields a larger 'ρ_i'.
- For rtPS, 'TR_{Curr}^i' is considered along with 'PD_i' and 'ADR_i'. Like UGS, DT determines priority of traffic.

$$P_i^{rtPS} = TR_{Curr}^i * \frac{PD_i}{ADR_i} * \rho_i \quad (8)$$

- For nrtPS, '$\acute{C}_i$' is considered. It depends on ratio of quantity of SD in former Time Frames (TFs) to mean 'TR_{Curr}^i'. 'T' represents current TF.

$$P_i^{nrtPS} = TR_{Curr}^i * \frac{1}{\beta_i} \quad (9)$$

where

$$\beta_i = \frac{\sum_{i=0}^{T-1} SD}{T * \frac{\sum_{i=1}^{N} TR_{Curr}^i}{n}} \quad (10)$$

Algorithm: SDT Algorithm
UGS: Sort MSs in descending order of Priority
do
  if (MS 'i' with $DT_i^{rtPS} > DT_i^{UGS}$ is present)
    Service MS that has rtPS traffic
  else
    Service MS that has UGS traffic
  end
  if (Free Space is present)
    Assign resources
  else
    Adjust resources
  end
while (MS that has UGS traffic is present)
  Service MSs in rtPS flow

rtPS: Sort MS in descending order of Priority
do
  Service MS that has UGS traffic
  if (Free Space is present)
    Assign resources
  else
    Adjust resources
  end
while (MS that has rtPS traffic is present)
  Service MSs in nrtPS flow

nrtPS: Sort MSs in descending order of Priority
do
  Service MS that has UGS traffic
  if (Free Space is present)
    Assign resources
  else
    Adjust resources
  end
while (MS that has nrtPS traffic is available)
  Adjust resources

CVR Journal of Science and Technology, Volume 26, June 2024
DOI: 10.32377/cvrjst2616

Flows are organized based on determined priorities. As SDT of requests are taken into consideration, requests at HoQs are the ones with reduced DT. They are scheduled first, thus dropping packet losses and increasing throughput.

BA allocates bursts to traffic depending on priority defined by scheduler. BA forwards information about availability of resource along with assignment to scheduler.

VI. Bucket based Burst Allocator (BBA)

Burst Allocator (BA) splits free space of every DL sub-frame into 'buckets' and organizes bursts in form of buckets. For 'k' requests in a sub-frame, the burst allocation mechanism produces 'k' in addition to a constant quantity of IEs. BA organizes bursts based on priority from scheduler so that BA satisfies traffic demands.

Free space of every Downlink (DL) sub-frame is split horizontally into a number of 'buckets'. Bursts are organized as buckets of size 'Δ_{bkt}'. Assignments made by scheduler for real-time/non-real-time traffic are in multiples of 'Δbkt'. Resources involving less number of bursts and IEs are well-used. Quantity of IEs varies with amount of scheduled MSs as well as split bursts.

With 'k' requests to be filled in sub-frame, BBA produces atmost 'k' bursts with small amount of IEs. Further, BBA organizes bursts based on scheduler's suggestions. BBA involves less computation complexity and is implemented on chips involving less cost.

Based on information from scheduler, BA allocates bursts and IEs. BA is based on DT-based scheduler of MS. The scheduler connects with BA to gain knowledge about 'Δbkt' and existing Unexploited Space (US) in current DL sub-frame. This facilitates scheduler to distribute resources to different flows.

$$US = t \times c - (FCH_{Size}) - (UL\_MAP_{Size}) - (DL\_MAP\_CF_{Size}) \quad (11)$$

Where,

t - Starting time

c - Starting sub-channel

FCH - Frame Control Header

UL_MAP size is pre-determined as UL sub-frame is assigned before. The Control Fields of 'DL_MAP' (DL_MAP_CF) include portions of 'DL_MAP', excluding IEs that are found by BA.

The above-mentioned model offers ensuing advantages.

- As scheduler and BA are joined together, traffic from MSs may be prioritized leading to reduced amount of request dropping.
- Fewer amounts of IEs are used as scheduler knows about burst organization.
- As DT of traffic plays a dominant role, MS with delay-intolerant traffic obtains priority.
- Unnecessary UGS/rtPS traffic is not produced in following TF. The nrtPS traffic need not wait for a long time.

VII. Results And Discussion

The proposed system is simulated using ns2. Simulation parameters are shown in Table 1.

Table 1. Simulation Parameters of HRA

Parameter	Value
MAC	IEEE 802.16e
Routing Protocol	DSDV
Duration of Frame	0.004
VCD Threshold	0.8
Length of Queue	50
Size of Packet	1492 bytes
Number of MSs	50
Start Time	20 Sec
Stop Time	120 Sec

SDT offers 13.12% better throughput in contrast to Priority Scheduler (PS) (Figure 3). SDT offers 2.4 times lesser average delay when compared to PS (Figure 4). Similarly, SDT involves 10.16% lesser PLR in contrast to PS (Figure 5).

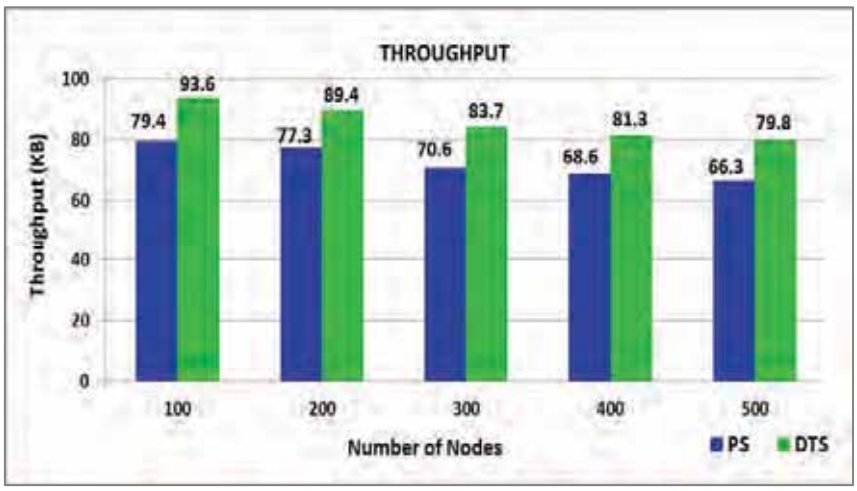

Figure 3: Throughput

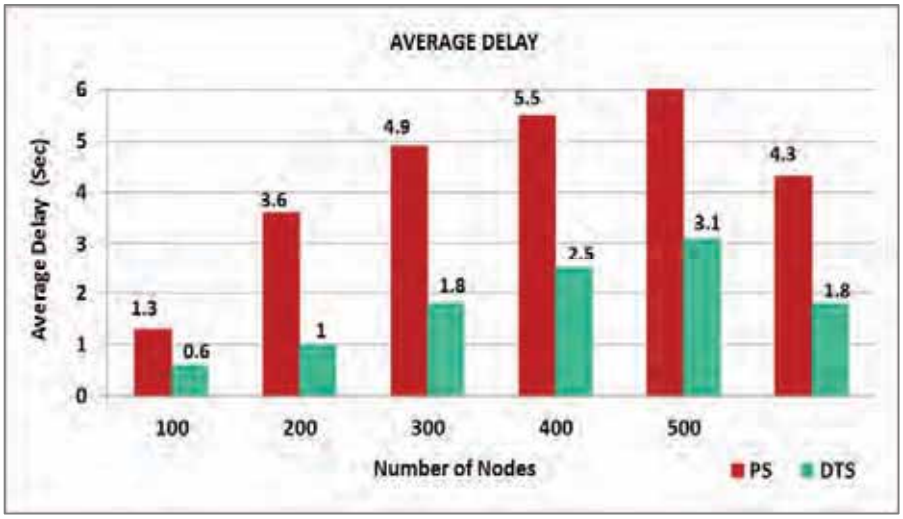

Figure 4: Average Delay

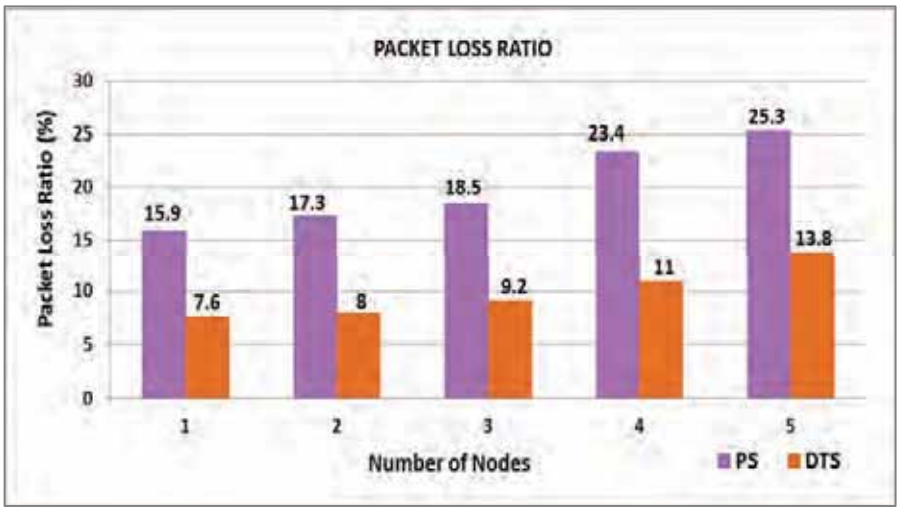

Figure 5: Packet Loss Ratio (PLR)

VIII. Conclusion

The CAC based on History (CACH) schemes accept calls only when an incoming call has no impact on QoS when new calls are accepted. This avoids QoS degradation to a larger extent when compared to present mechanisms. Further DT-based BA considers allowable delay of every flow and assigns bursts depending on priority and DT of every request. It is obvious that proposed cross-layer framework offers better results based on throughput, average delay and PLR.

References

[1] Ahmadi, S. (2009). An overview of next-generation mobile WiMAX technology. IEEE communications Magazine, 47(6), 84-98.

[2] Ahson, S. A., & Ilyas, M. (Eds.). (2018). WiMAX: technologies, performance analysis, and QoS. CRC press.

[3] Niyato, D., & Hossain, E. (2018). Resource allocation and admission control using fuzzy logic for OFDMA-based IEEE 802.16 broadband wireless networks. WiMAX, 235.

[4] Saidu, I., Roko, A., Shinkafi, N. A., & Yese, S. (2019). Congestion Control Call Admission Control (CC-CAC) Algorithm for Mobile Broadband Networks. European Journal of Electrical Engineering and Computer Science, 3(5).

[5] Mamman, M., & Hanapi, Z. M. (2020, December). An Efficient Dynamic Call Admission Control for 4G and 5G Networks. In 9th International Conference on Signal, Image Processing and Pattern Recognition (SPPR 2020) (pp. 55-60).

[6] Raja, S. K. S., & Louis, A. B. V. (2021). A review of call admission control schemes in wireless cellular networks. Wireless Personal Communications, 120(4), 3369-3388.

[7] Mohammed, A., Solomon, Y. O., & Saidu, I. (2019). A QoS guaranteed call admission control (QOG-CAC) algorithm for broadband networks. International Journal of Wireless Networks and Broadband Technologies (IJWNBT), 8(1), 46-63.

[8] Mamman, M., Hanapi, Z. M., Abdullah, A., & Muhammed, A. (2017). An adaptive call admission control with bandwidth reservation for downlink LTE networks. IEEE Access, 5, 10986-10994.
[9] Al-Maitah, M., Semenova, O. O., Semenov, A. O., Kulakov, P. I., & Kucheruk, V. Y. (2018). A hybrid approach to call admission control in 5G networks. Advances in Fuzzy Systems, 2018, 1-7.
[10] Gupta, K. D., Ansari, A. Q., Saxena, P., & Dwivedi, R. (2020). Optimizing channel allocation in WiMAX MIMO model using fuzzy game theory. Journal of Information and Optimization Sciences, 41(7), 1633-1644.
[11] Ababneh, N. (2021). Quality-aware resource allocation protocol for improved WiMAX video surveillance system. International Journal of Computing and Digital Systems, 10(1), 207-216.
[12] Taranum, F. (2022). The Horizontal Handover Mechanism Using IEEE 802.16e Standard. In Emerging IT/ICT and AI Technologies Affecting Society (pp. 309-323). Singapore: Springer Nature Singapore.
[13] Maher, M. A., El-Samie, F. E. A., & Zahran, O. (2022). A hybrid bandwidth allocation algorithm for EPON-WiMAX integrated networks based on auction process. Optical and Quantum Electronics, 54(6), 333.
[14] Banna, H. A. (2022). Improve WiMAX performance using directional antennas and resource management algorithms. Journal of Engineering Sciences & Information Technology, 6(6).
[15] Zou, S., Wu, J., Yu, H., Wang, W., Huang, L., Ni, W., & Liu, Y. (2023). Efficiency-optimized 6G: A virtual network resource orchestration strategy by enhanced particle swarm optimization. Digital Communications and Networks.

E-ISSN 2581 – 7957
P-ISSN 2277 – 3916

CVR Journal of Science and Technology, Volume 26, June 2024
DOI: 10.32377/cvrjst2617

A Study on Handwritten Text Recognition Classification using Diverse Deep Learning Techniques and Computation of CTC Loss

Ratnam Dodda[1], S Balakrishna Reddy[2], Azmera Chandu Naik[3], Venugopal Gaddam[4]
[1]Sr. Assistant Professor, CVR College of Engineering / Dept. of CSE(AI&ML), Hyderabad, India.
Email: ratnam.dodda@gmail.com
[2]Assistant professor, CVR College of Engineering/ Department of CSE(DS), Hyderabad, India.
Email: sama.balakrishnareddy@gmail.com
[3]Sr. Assistant Professor, CVR College of Engineering/ Dept. of CSE(AI&ML), Hyderabad, India.
Email: azmerachandunaik@cvr.ac.in
[4]Associate Professor, KL University/ Dept. of CSE, Guntur, India.
Email: venugopal.gaddam@gmail.com

Abstract: **Handwriting recognition encompasses the conversion of hand-written text images into digital text, where input images yield predicted textual output. Optical Character Recognition (OCR) technology has conventionally fulfilled this role. With surging mobile phone usage, leveraging text detection via mobile cameras gains significance in fields like medical script processing and exam evaluation. To enhance image quality, noise reduction techniques like binarization and thresholding are applied. Image processing entails letter segmentation and extraction. In this paper, we propose a neural network classifier model amalgamating Convolution Neural Networks (CNNs) and Long Short-Term Memory (LSTM) networks. Leveraging an existing feature dataset, the model is trained. Input images are evaluated through the neural network, yielding recognized words in a text document format. Ultimately, the predicted output is derived via Connectionist Temporal Classification (CTC)- based loss computation.**

Keywords: **Handwritten Recognition, Deep Learning Techniques, Optical Character Recognition.**

I. Introduction

Handwriting recognition is a valuable technique used to convert handwritten text, captured as images from mobile phones, into machine-readable text. While Optical Character Recognition (OCR) scanners are typically employed for this purpose, the prevalence of mobile phones has expanded the scope of text detection from mobile cameras [1]. This has led to numerous practical applications, including medical script processing and exam script evaluation. However, mobile camera images tend to be noisier compared to OCR-scanned images. To mitigate this image processing techniques like binarization and thresholding are applied for noise reduction. Subsequently, the handwritten characters are segmented and isolated from the image. Features, such as binary codes, are extracted from these characters [2]. To classify these characters, a neural network classifier, often built on a Long Short-Term Memory (LSTM) network, is trained using a character dataset. This neural network is then utilized to analyze input images and produce a text document containing the recognized words [3]. Given that input sources are image-based, noise levels are typically higher than those found in systems using scanned images. Consequently, noise reduction methods, such as low-intensity pixel removal, are employed to enhance the efficiency of the process [4].

A. Recurrent neural networks (RNN)

Recurrent neural networks (RNNs) belong to a category of artificial neural networks specifically designed for handling sequential data, making them well-suited for tasks that rely on memory and sequential dependencies. They find extensive applications in various domains such as speech recognition, language translation, natural language processing (NLP), and more. RNNs are categorized as supervised learning algorithms [5].

In the architecture of an RNN, a crucial feature is its ability to preserve memory. This is achieved by feeding the output of the current time step back into the network as input for the subsequent time step. This iterative process can be repeated as needed, making it adaptable to problems of varying complexity. Once the output for the final time step is computed, it is compared to the actual target output. Any discrepancies, or errors, between the predicted and actual values are then propagated backward through the network. This back-propagation process is instrumental in training the RNN, enabling it to learn and improve its performance over time [6].

B. Convolutional Neural Networks (CNN)

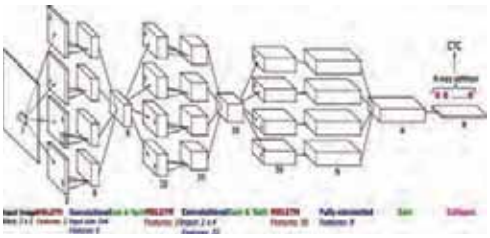

Figure 1. Convolutional Neural Network Framework

The proposed design is as follows, the input image is taken as a 2x2 block at once and given as an input to the first LSTM and convolution layer where the activation functions used are tanh. Finally, before the output is predicted a soft

Received on 03-02-2024, Revised on 04-03-2024, Accepted on 03-04-2024.

CVR Journal of Science and Technology, Volume 26, June 2024
DOI: 10.32377/cvrjst2617

max activation function is applied [7]. Convolutional neural networks are a class of artificial neural networks utilized primarily for pixel processing and image recognition. The architecture consists of three layers, firstly a convolutional layer followed by a pooling layer, and finally a Fully Connected (FC) layer, with increasing complexity [8]. The convolutional layer serves as the fundamental building block within a Convolutional Neural Network (CNN), responsible for the bulk of data processing and calculations. Depending on the complexity of the task at hand, multiple convolutional layers can be stacked on top of one another. In this layer, a pivotal operation known as convolution takes place. Here, a kernel or filter traverses the receptive field of the input image, systematically inspecting for the presence of features. Through multiple iterations, the kernel traverses the entire image, calculating the dot product between the input pixels and the filter during each pass. The cumulative result of these dot products yields a feature map or convolved feature, which encapsulates important spatial information [8]. Importantly, the image is transformed into numerical values within this layer, enabling the CNN to interpret the image and discern relevant patterns. Following the convolutional layers, the pooling layer comes into play, facilitating dimensionality reduction. While this process trims down data, it comes at the cost of some loss of information. The pooling layer can perform two distinct types of pooling, namely max pooling and average pooling [9]. The final piece of the puzzle resides in the Fully Connected (FC) layer, where image classification takes center stage based on the features extracted in the preceding layers. The term ”fully connected” implies that every input or node from one layer is linked to each activation unit or node in the subsequent layer. However, it’s worth noting that not all layers within a CNN are fully connected. This strategic design choice helps prevent the network from becoming unnecessarily dense, reducing potential losses, maintaining output quality, and ensuring computational efficiency [10].

II. Methodology

The handwriting recognition model proposed in this paper takes input in the form of an image and then converts it into digital text. This model consists of a CNN-LSTM architecture. The loss used in the end is the CTC (Connectionist Temporal Classification) loss [11].

Importing Data and Dependencies We import the data using the Pandas Data frame. The data needed is only the images of the words and the word.txt file. We then place the downloaded files inside the data directory [12].

Data Pre-processing and preparing the images for training the input images are initially loaded in grayscale format and then undergo a series of transformations. First, they are reshaped to adhere to a standardized size with a width of 128

pixels and a height of 32 pixels. If the original image dimensions exceed these specifications (i.e., the width is greater than 128 or the height is greater than 32), cropping is applied to adjust the image to the required size while retaining the most significant content. On the other hand, iftheoriginalimagedimensionsaresmallerthan128pixelsinwidthor32pixels in height, the image is padded with white pixels to reach the prescribed dimensions. Following these adjustments, the image is rotated in a clockwise direction to achieve the desired shape, typically specified as (x, y). Lastly, to facilitate consistent processing, the image is normalized, scaling its pixel values to fall within the range of [0, 1]. This normalization simplifies subsequent computations and ensures uniformity across all input images [13].

A.Label Encoding for CTC Loss

The primary objective function employed for minimizing the loss is the Connectionist Temporal Categorical loss function, commonly referred to as CTC. In contrast to other loss functions that optimize a single objective, the CTC loss uniquely addresses a dual optimization task. It is specifically designed to optimize not only the accurate prediction of class labels within a sequence but also the optimal alignment and length of the predicted sequence. This dual optimization is particularly advantageous when dealing with input images of varying nature [14]. To facilitate the training process, the image labels in the data set need to be converted into numerical representations that correspond to each character found in the training set. The character set, often referred to as the ”Alphabet,” encompasses the letters A to Z and includes three special characters: hyphen (’-’), apostrophe (’), and space. This transformation is essential for enabling the network to learn and make predictions effectively during training and inference [15].

B.Model Building

In our architectural design, tailored for input images with dimensions of 32 pixels, 32 pixels in height, and 128 pixels in width, we’ve in incorporated a sequence of seven convolutional layers. Among these, six employ a kernel size of (3,3), while the final one employs a kernel size of (2,2). We progressively increase the number of filters in a layer-by-layer fashion, ranging from 64 to 512 filters. To capture and distill relevant features, we intersperse max-pooling layers with a size of (2,2). Additionally, we introduce two max-pooling layers with a size of (2,1) to focus on extracting features with larger widths, which is particularly advantageous for accurately predicting long text sequences [16]. To expedite the training process and enhance stability, we incorporate batch normalization layers after the completion of the fifth and sixth convolutional layers. To ensure seamless compatibility with the subsequent LSTM layer, we employ a lambda function to preprocess the output from the convolutional layers. Following this, our network utilizes two Bidirectional LSTM layers, each comprising 128 units. These RNN layers yield an output with dimensions (batch size,31,79), where 79 represents the total number of output classes, encompassing both characters and blank spaces [17].

CVR Journal of Science and Technology, Volume 26, June 2024
DOI: 10.32377/cvrjst2617

TABLE1.
MODEL DESCRIPTION

Layer(type)	Output shape	Param
input1(Input Layer)	(None,32,128,1)	0
conv2d(Conv2D)	(None,32,128,64)	640
maxpooling2d	(None,16,64,64)	0
conv2d1(Conv2D)	(None,16,64,128)	73856
Max pooling 2d1(MaxPooling2D)	(None,8,32,128)	0
conv2d2(Conv2D)	(None,8,32,256)	295168
conv2d3(Conv2D	(None,8,32,256)	590080
Max pooling 2d2(MaxPooling2D)	(None,4,32,256)	0
conv2d4(Conv2D)	(None,4,32,512)	1180160
batch normalization	(None,4,32,512)	2048
conv2d5(Conv2D)	(None,4,32,512)	2359808
batch normalization1	(None,4,32,512)	2048
Max pooling 2d3(MaxPooling2D)	(None,2,32,512)	0
conv2d6(Conv2D)	(None,1,31,512)	1049088
Lambda (Lambda)	(None,31,512)	0
Bidirectional (Bidirectional)	(None,31,512)	1574912
bidirectional1(Bidirectional)	(None,31,512)	1574912
Dense (Dense)	(None,31,79)	40527

Defining Loss Function

$$L(\theta) = \frac{1}{N}\sum_{i=1}^{N} L(f(x_i;\theta), y_i)$$

- $L(\theta)$ represents the loss function.
- N represents the total number of samples.
- $f(x_i;\theta)$ represents the model prediction for the ith sample with parameters θ.
- y_i represents the true label for the i th sample.
- L represents the loss function applied to the predicted value and the true label.

In this step we use the Connectionist Temporal Categorical CTC Loss function which calculates the loss between a continuous series and a target sequence. Here we use the CTC loss function over other loss functions as the CTC loss can optimize the length of the sequence that is predicted as well as the classes of the predicted sequence [18].

C. Training Model

Here we use batch size 5 and run 25 epochs. We use the Stochastic Gradient Descent (SGD) optimizer which iteratively optimizes an objective function with appropriate smoothness properties. We use the SGD optimizer as it reduces excessive computational burden thereby achieving faster iterations for a lower convergence rate.

D. Decoding Outputs from Prediction

Performance evaluation is conducted using the Levante in distance metric. To assess the quality of recognition, we employ the Jaro-Winkler algorithm, which gauges the similarity between the text captured by our system and the ground truth or actual text. This algorithm is instrumental in quantifying the accuracy of our text recognition process. This is also allowing us to get a quantitative understanding of how good our model is.

E. Architecture

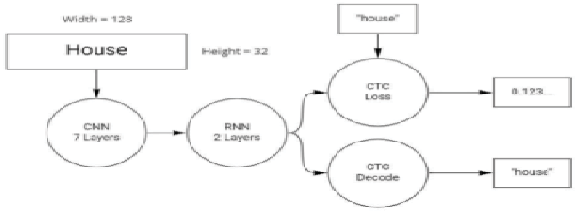

Figure 2. System Architecture

The system architecture represents the underlying architecture of the neural network used to represent images. First, the image (after preprocessing into 128x32) is passed into the 7 CNN layers where the feature extraction and transformation take place. After this step the 2 RNN or LSTM layers are used to predict the text from the images. The CTC decode is the method used to predict the text whereas the CTC Loss is the method used to calculate the loss of the predicted text. The technology used for the construction of this project is a combination of neural networks. First, we encounter convolutional neural networks (7 layers) which are used to process the input image. They change the dimensionality of the image while retaining the data to be able to pass this input to the next layer. Next, we use two bi-directional LSTM networks where the text on the image is recognized. Finally, the transcription layer translates the per-frame predictions into the final label sequence. For calculating the loss, we are using the CT Closes function which is very apt for handwriting recognition as it calculates the loss based on character scores [8].

III. RESULTS

The final model can identify English words with an accuracy of up to 63.1

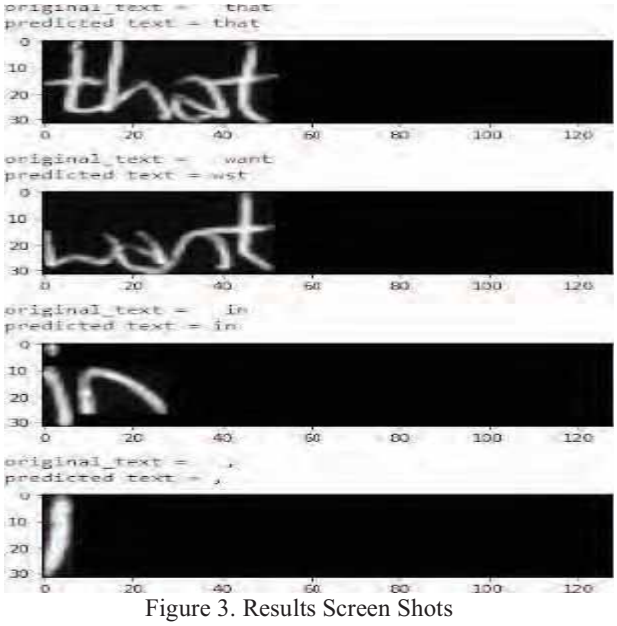

Figure 3. Results Screen Shots

CVR Journal of Science and Technology, Volume 26, June 2024
DOI: 10.32377/cvrjst2617

As shown in the screenshot, our model can predict words and symbols. The word “that” is predicted as that, and “want” is predicted as wst - this inaccuracy can be attributed to the fact that “a” and “n” in the image are very closely written and the model is unable to distinguish the letter as it is not provided with any context, “in” is predicted a sin, and the “,” symbol is predicted as, Learning curves plot the loss of training and validation of a sample of training examples by adding new training examples incrementally. Learning curves help us determine whether adding more training examples would improve the validation score (score on unseen data). If the model is overfitting, adding more training examples can improve the model’s performance on unseen data. Similarly, if the model is undersized, adding training examples will not help. The first learning curve is the loss graph that is plotted along each epoch or cycle for both the training and validation data. It is observed that as the epoch increases, over time the loss decreases. This Cond. learning curve is the accuracy graph that is plotted along each epoch or cycle for both the training and validation data. It is observed that as the epoch increases, over time the accuracy increases and eventually flattens out. So, in our model with each epoch, the loss decreases and accuracy increases.

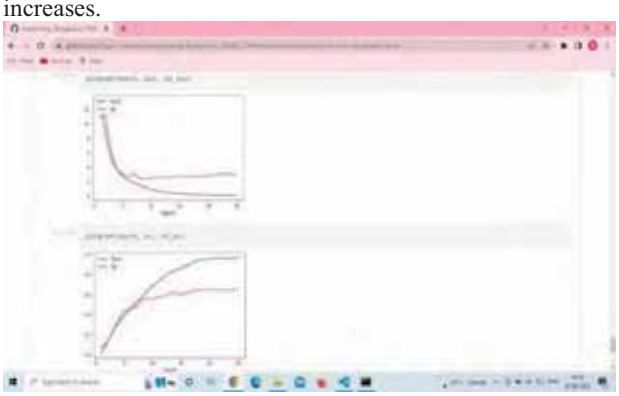

Figure 4. Loss and Accuracy Graphs

IV. Conclusion

The current model demonstrates proficient prediction capabilities for words, numbers, and symbols. However, the potential for enhancing its capabilities lies in the incorporation of line segmentation. By integrating line segmentation, the model can be expanded to encompass complete paragraph text recognition. This advancement opens doors to achieving efficient recognition of handwriting across various languages, transcending the confines of English. Modifying and extending the existing CRNN+LSTM+CTC architecture serves as the foundation for creating a versatile system capable of both segmenting and recognizing handwritten text, thereby facilitating its widespread applicability.

References

[1] B. Balci, D. Saadati, and D. Shiferaw, “Handwritten text recognition using deep learning,” CS231n: Convolutional Neural Networks for Visual Recognition, Stan- ford University, Course Project Report, Spring, pp. 752–759, 2017.

[2] C. C. Tappert, C. Y. Suen, and T. Wakahara, “The state of the art in online handwriting recognition,” IEEE Transactions on pattern analysis and machine intelligence,vol.12,no.8,pp.787–808,1990.

[3] J.Brownlee,“Sequence classification with lstm recurrent neural networks in python with keras,” Deep Learning for Natural Language Processing, Machine Learning Mastery, 2016.

[4] L. Malinski, K. Radlak, and B. Smolka, “Is large improvement in the efficiency of impulsive noise removal in color images till possible?,”Plosone,vol. 16,no.6, p.e0253117,2021.

[5] R. DiPietro and G. D. Hager, “Deep learning: Rnns and lstm,” in Handbook of medical image computing and computer assisted Intervention, pp. 503–519, Elsevier, 2020. Sutskever, Training recurrent neural networks. University of Toronto Toronto, ON, Canada, 2013.

[6] S.Iqbal,A.N.Qureshi,J.Li,andT.Mahmood, “On the analyses of medical images using traditional machine learning techniques and convolutional neural networks,” Archives of Computational Methods in Engineering,vol.30,no.5,pp.3173–3233, 2023.

[7] R. Yamashita, M. Nishio, R. K. G. Do, and K. Togashi, “Convolutional neural networks:an overview and application in radiology,”Insights into imaging, vol. 9, pp.611–629,2018.

[8] J.Brownlee,“Agentleintroductiontopoolinglayersforconvolutionalneuralnet- works,”Machine Learning Mastery,vol.22,2019.

[9] S. Patel and A. Patel, “Object detection with convolutional neural networks,” Machine Learning for Predictive Analysis: Proceedings of ICTIS 2020, pp. 529– 539, 2021.

[10] Abdallah, M. Hamada, and D. Nurseitov, “Attention-based fully gated cnn-bru for Russian handwritten text,” Journal of Imaging, vol. 6, no. 12, p. 141, 2020.

[11] S. Khalid, S. Wu, A. Alam, and I. Ullah, “Real-time feedback query expansion technique for supporting scholarly search using citation network analysis,” Journal of Information Science, vol. 47, no. 1, pp. 3–15, 2021.

[12] V. V. Mainkar, J. A. Katkar, A. B. Upade, and P. R. Pednekar, “Handwritten character recognition Conference on Electronics and Sustainable Communication Systems (ICESC), pp. 599–602, IEEE, 2020.

[13] Kim, S., Hori, T., & Watanabe, S. (2017). “Joint CTC-attention based end-to-end speech recognition using multi-task learning”. In 2017 IEEE International Conference on Acoustics, Speech and Signal Processing (ICASSP) (pp. 4835-4839).

[14] N.H.Feldman, T.L. Griffiths, S . Goldwater, and J.L.Morgan,“ Role for the developing lexicon in phonetic category acquisition., ”Psychological Review, vol. 120, no. 4, p. 751, 2013.

CVR Journal of Science and Technology, Volume 26, June 2024
DOI: 10.32377/cvrjst2617

[15] R. Ramya, A. Anandh, K. Muthulakshmi, and S. Venkatesh, "Gender recognition from facial images using multi-channel deep learning framework," in Machine Learning for Biometrics, pp. 105–128, Elsevier, 2022.
[16] Xie, S., Girshick, R., Dollár, P., Tu, Z., & He, K. (2017). "Aggregated Residual Transformations for Deep Neural Networks". In Proceedings of the IEEE Conference on Computer Vision and Pattern Recognition (CVPR)
[17] W. W. Cohen, P. Ravikumar, S. E. Fienberg, et al., "A comparison of string distance metrics for name-matching tasks.," in IIWeb, vol. 3, pp. 73–78, 2003.
[18] M. Soh, "Learning cnn- lstm architectures for image caption generation," Dept. Comput. Sci., Stanford Univ., Stanford, CA, USA, Tech.Rep, vol.1,2016.

E-ISSN 2581 – 7957
P-ISSN 2277 – 3916

CVR Journal of Science and Technology, Volume 26, June 2024
DOI: 10.32377/cvrjst2618

Predictive Modeling of Diabetes Mellitus Utilizing Machine Learning Techniques

N Nagarjuna[1] and Dr. Lakshmi HN[2]
[1]Senior Assistant Professor, CVR College of Engineering/ CSIT Dept., Hyderabad, India
Email: n.nagarjuna@cvr.ac.in
[2]Professor&Head, CVR College of Engineering/ Emerging Technologies Dept., Hyderabad, India
Email: hn.lakshmi@cvr.ac.in

Abstract: **Diabetes mellitus represents a persistent metabolic condition distinguished by elevated levels of blood sugar, which results from the inadequacy of the body to secrete and respond to insulin, leading to health risks and frequent hospitalizations. Accurate predictive models are vital for targeted interventions to reduce readmissions and improve healthcare quality and cost. Early prediction can mitigate its impact, aid in control, and potentially save lives. Machine learning algorithms show promise in medical applications, including diabetes prediction and diagnosis. Limited data quality hinders accurate diabetes prediction due to missing values and inconsistencies. This paper investigates machine learning's potential for predicting and diagnosing diabetes, aiming to enhance accuracy and efficiency in disease management. Feature engineering techniques are applied to preprocess the data and extract relevant features for model development. To address class imbalance, SMOTE (Synthetic Minority Oversampling Technique) is employed. Various machine learning algorithms, including logistic regression, Naïve Bayes, random forests, support vector machines (SVM), K-Nearest Neighbors (KNN), and eXtreme Gradient Boosting (XGBoost), are utilized to build predictive models. The performance evaluation employs standard metrics such as accuracy, recall, precision, and F1-Score. Notably, Random Forest achieves an accuracy of 82% followed by XGBoost(80%) , surpassing other ML algorithms utilized.**

Index Terms: **Diabetes mellitus, Machine learning, Prediction, SVM, logistic regression, Accuracy.**

I. Introduction

Diabetes is a long-term health condition caused by either inadequate production of insulin or the body's ineffective use of insulin. Insulin, a hormone crucial for regulating blood sugar levels, plays a key role in this mechanism. Common symptoms comprise increased thirst, frequent urination, blurred vision, fatigue, and unintentional weight loss. Prolonged diabetes can harm the heart, eyes, kidneys, and nerves, increasing the risk of heart attack, stroke, kidney failure, and vision loss, along with potential foot ulcers and amputation [1].

Currently, 537 million adults worldwide have diabetes, and by 2030, an estimated 643 million people will be living with diabetes, rising to a staggering 783 million by 2045. Over three-quarters reside in low- to middle-income nations. In 2021, diabetes claimed 6.7 million lives, with a health expenditure toll of at least USD 966 billion—a 316% surge over 15 years. Additionally, 541 million adults face Impaired Glucose Tolerance (IGT), heightening their risk of developing type 2 diabetes [2].

There are three major forms of diabetes: type-1, type-2, and gestational diabetes. Type-1, affecting 5-10% of cases, is an autoimmune condition where the body mistakenly attacks insulin-producing cells. This necessitates lifelong insulin therapy to manage blood sugar levels. Type 2, comprising 90-95% of cases, occurs when insulin is ineffective in regulating blood sugar, often diagnosed in adults but increasingly in younger individuals. Regular blood sugar testing is crucial due to subtle symptoms, and prevention through lifestyle changes is feasible. Gestational diabetes affects pregnant women, raising health risks for both mother and baby, with implications for future health conditions. [3].

While a cure for diabetes remains elusive, early, and accurate prediction offers promising avenues for control and prevention. However, predicting diabetes poses a challenge due to the non-linear nature of data. Recent research, employing machine learning's ability to learn without explicit programming, has shown promising results in forecasting diabetes risk. While machine learning holds promise in medicine, ensuring consistent accuracy across different algorithms remains a challenge. Identifying the algorithm with the highest performance is crucial for building better classifiers. The pervasive reach of machine learning across industries extends to medicine, where its potential to revolutionize healthcare is significant [4]. Machine learning and statistics are used in predictive modeling to find patterns in data and estimate the likelihood that certain events will occur [5]. This work aims to create a model predicting diabetes in patients. Afterward, different methods are investigated to increase the model's accuracy.

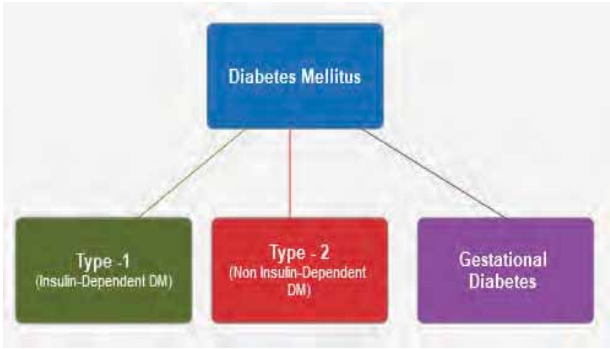

Figure1. Diabetes Mellitus types

Received on 09-03-2024, Revised on 08-04-2024, Accepted on 08-05-2024.

CVR Journal of Science and Technology, Volume 26, June 2024
DOI: 10.32377/cvrjst2618

II. Related Work

In a study by Iyer A. [6], a diabetic dataset was analyzed to identify hidden patterns using classification algorithms. Naive Bayes and Decision Trees were compared, demonstrating the effectiveness of both methods.

In a study by Mercaldo et al. [7], researchers investigated machine learning algorithms for diagnosing diabetes. They compared six algorithms, including J48, multilayer perceptron, JRip, Hoeffding Tree, Bayes Net, and random forest, using the WEKA software and the PIDD dataset. Notably, the Hoeffding Tree algorithm showed promising results for diabetes prediction.

Sisodia et al. [8] compared three classifiers (Naïve Bayes, SVM, Decision Trees) for diabetes prediction using the Pima Indian Diabetes Database. Naïve Bayes achieved the highest accuracy (76.30%) among F-Score, Precision, Recall, and Accuracy metrics.

Maniruzzaman et al. [9] conducted in-depth research on filling in missing variables and rejecting outliers to improve the performance of the machine learning model.

Sneha et al. [10] used feature selection to identify the most informative attributes from the PIMA diabetes dataset for their prediction model. They evaluated several machine learning algorithms, including Support Vector Machine, k-Nearest Neighbors, Naive Bayes, Decision Tree, and Random Forest. Naive Bayes achieved the best accuracy of 82.2%.

Lukmanto et al. [11] utilized feature selection on PIMA Indian dataset using Fuzzy SVM for their prediction with a promising accuracy of 89.02%.

In a study by Ahuja et al. [12], researchers evaluated 15 classification algorithms, including Multilayer Perceptron, using Python. They addressed missing data by imputing missing values with the median and replacing outliers. The performance of the algorithms was assessed using five different dataset selection methods and 2, 4, 5, and 10-fold cross-validation. Their findings revealed that Multilayer Perceptron achieved the highest accuracy (78.7%) when combined with feature selection using Linear Discriminant Analysis.

Morgan-Benita et al. proposed Hard Voting Ensemble Approach (HVEA) for diabetes prediction [13]. Compared to individual models like Logistic Regression (88.01%), Support Vector Machine (89.82%), and Artificial Neural Network (88.46%), HVEA achieved significantly higher accuracy (90.05%) using non-glucose data from Mexico and 10-fold cross-validation.

III. Methodology

The key elements of the methodology for predicting diabetes are visualized in figure 2. The input data is preprocessed by handling missing values and outliers. Feature extraction and selection are performed to reduce complexity and focus on relevant information. Data is split into training and testing sets. The model is trained on the training data and evaluated on the test data. Results are presented as confusion matrices. Using the trained model and selected features, predictions for new diabetic patients are made.

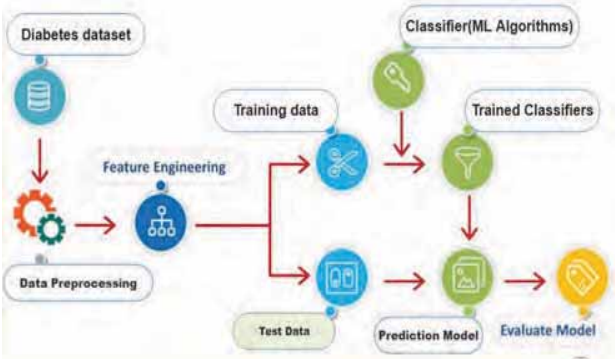

Figure 2. Proposed methodology

A. Dataset

This study utilized the PIDD (Pima Indians Diabetes Database), available from the UCI (University of California), Irvine repository. The dataset contains information on 768 females aged 21 or older. PIDD offers ample recorded instances and requires minimal pre-processing for integration into various learning models. As a result, it is widely used in machine learning and deep learning models for detecting diabetes.

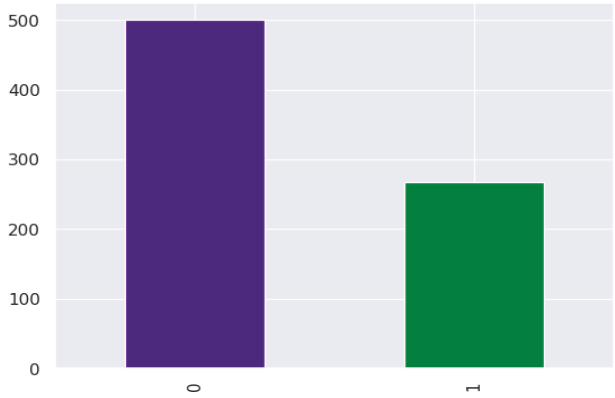

Figure 3. number of individuals with and without diabetes

In Figure 3, a bar chart illustrates the distribution of patients with and without diabetes. X-axis displays the outcome and y-axis displays the count. Of these, 268 have been diagnosed with diabetes (designated as 1), and 500 do not have diabetes (designated as 0). Figure 3 reveals a significant class imbalance in the dataset (268 diabetes vs. 500 non-diabetic). This imbalance can hinder machine learning model performance. To address this, SMOTE (Synthetic Minority Oversampling Technique) is employed. SMOTE generates synthetic samples for the minority class, balancing the class distribution.

Table 1 provides description of dataset. It contains nine feature columns, including the month of pregnancy, glucose, plasma, blood pressure, triceps, insulin, BMI, age, and Diabetes Pedigree Function (DPF). The dataset's missing

CVR Journal of Science and Technology, Volume 26, June 2024
DOI: 10.32377/cvrjst2618

values, which were at first thought to be complete, were eventually determined to be zeros. Zero values, however, were thought to be physiologically impractical for some characteristics, such as age or blood pressure. In a similar vein, readings for plasma glucose, 2-hour serum insulin, and body mass index were implausible, with almost 50% showing zero. Crucially, every attribute present in the database is either a real number or an integer.

TABLE I.
DATA SET DESCRIPTION

Attribute	Description	Data type	Range
Pregnancy	Number of pregnancies	Number	0 –17
Plasma glucose	Blood sugar level	Number	0 –199
Triceps	Subcutaneous fat thickness(mm)	Number	0–99
Blood pressure	blood pressure, expressed in mm Hg	Number	0–122
BMI	Body mass index, kg/m²	float	0 – 67.1
Serum insulin	Two hour serum insulin (μU/mL)	Number	0 – 846
Age	Age in Years	Number	21 – 81
DPF	diabetes risk based on family history	float	0.078 – 2.42
Outcome	Value indicating diabetes diagnosis (Positive/Negative)	Boolean	0,1

B. *Pre-processing*

Machine learning algorithms rely heavily on data for effective model training. Initially, datasets collected from various sources are often in a raw format, prone to inconsistencies that models may struggle with. Pre-processing is crucial to clean the data, involving tasks such as handling missing values, creating new features, and splitting the data into train-test sets. To address the issue of certain features with zero values, such as blood pressure, skin thickness, BMI, mean, and median imputations are employed to replace missing or zero values. Consequently, missing values for select attributes, including Blood Pressure, Glucose level, BMI, Skin Thickness, and Age, were imputed, given that these attributes cannot logically hold zero values. Following the imputation process, the dataset was scaled to normalize all values.

A carefully chosen data set is characterized by features that exhibit substantial correlations with the target class along with substantial discordances with one another. A filter-based feature selection is used for selecting features to identify the uncorrelated features. Figure 4 illustrates the relationship between all features. The darker colors represent less association, while lighter colors indicate greater correlation.

Feature importance identifies the most influential features in a machine learning model, aiding in understanding data relationships, feature selection, model interpretation, and debugging. Figure 5 demonstrates that the Glucose feature has the most significant influence on predicting diabetes.

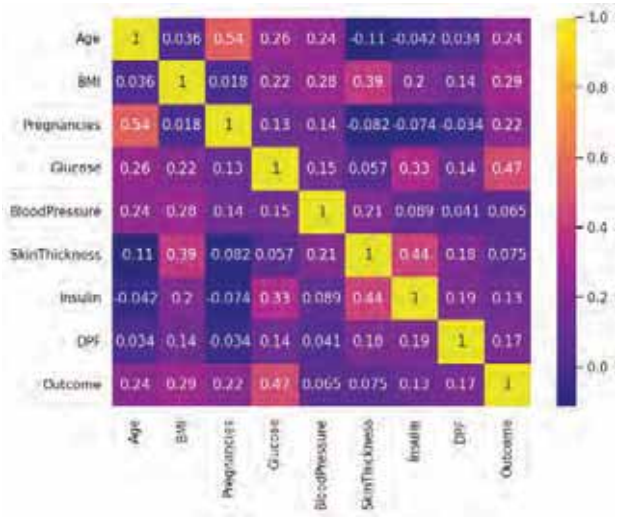

Figure 4. Heatmap showing Correlation between features.

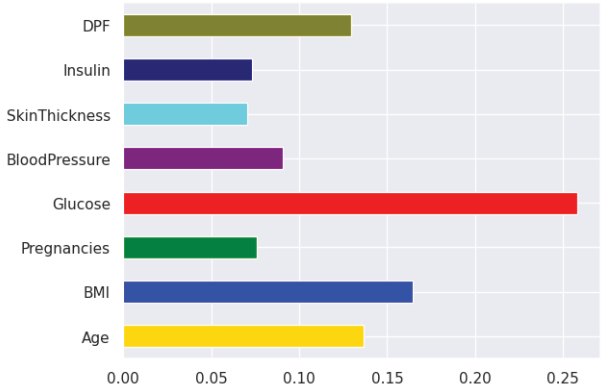

Figure 5. Feature importance of diabetes data set

A. *Algorithms used:*

i. Logistic Regression

For binary classification, logistic regression estimates outcome probabilities from predictor variables. It is widely used in binary classification tasks. Logistic regression estimates the probabilities using the logistic function, which maps any real-valued input into the range 0 and 1 [14].

ii. Support Vector Machines

SVM stands out as an algorithm adept at both classification and regression tasks. It achieves this by identifying, within a high-dimensional space, the hyperplane that best segregates classes. This is accomplished by maximizing the margin, or distance, between these classes. Even in high-dimensional spaces, SVMs remain effective due to their versatility in handling non-linear data through kernel functions [15].

iii. K-Nearest Neighbors (KNN)

For classification tasks, the KNN (K-Nearest Neighbors) algorithm identifies the k closest data points in the feature space and assigns the majority class label. It is simple yet effective for both classification and regression tasks. However, it can be computationally expensive for large datasets [16].

CVR Journal of Science and Technology, Volume 26, June 2024
DOI: 10.32377/cvrjst2618

iv. Naïve Bayes:

The Naive Bayes algorithm is a probabilistic classification method that calculates the probability of each class for a given set of input features. It leverages Bayes' theorem and assumes independence between features to make these classifications. Naïve Bayes is particularly popular in text classification tasks due to its simplicity and efficiency [17].

v. Random Forest

Random Forest, a powerful machine learning algorithm for classification and regression, achieves its strength by combining a multitude of diverse decision trees. Each tree, built on random data subsets and features, casts a vote (classification) or contributes to an average (regression). This democratic approach improves accuracy, handles diverse data, and reduces overfitting, making it powerful and versatile. It shines in various domains but might not always outperform complex algorithms on specific tasks.

vi. Decision Tree

Decision trees, resembling upside-down trees, excel at both classification and regression, splitting data based on features for clear predictions. These models shine in interpretability, handling diverse data, and revealing feature importance. However, they can overfit the data, are sensitive to noise, and favor features with many categories. Despite these limitations, decision trees remain valuable for tasks where understanding the "why" behind predictions is essential[19].

vii. XGBoost

XGBoost, or eXtreme Gradient Boosting, is a highly optimized implementation of the gradient boosting algorithm, widely recognized for its efficiency and scalability. XGBoost boasts built-in features like automated missing value handling, tree pruning, and hyperparameter tuning, streamlining the process. Additionally, it unlocks insights into important features through feature importance scores, enhancing interpretability and model understanding [20].

B. Training and Testing

The PIDD dataset is used to train and evaluate machine learning models in Python. For this, the data is split 70/30 for training and testing.

IV. RESULTS

The final step of evaluating a prediction model involves assessing its performance using various metrics like accuracy, confusion matrix, precision, recall, and F1-score. These metrics rely on ground truth labels, also known as classification labels.

A. Confusion Matrix:

In classification tasks like diabetes prediction, a confusion matrix clearly shows how the model performed.

TABLE II.
CONFUSION MATRIX FOR DIABETES PREDICTION

Predicted	Actual Positive (Diabetes)	Actual Negative (No Diabetes)
Positive (Predicted Diabetic)	True Positives (TPD)	False Positives (FPD)
Negative (Predicted Non-Diabetic)	False Negatives (FND)	True Negatives (TND)

Table 2 depicts the confusion matrix for diabetes prediction. True Positives are the cases where the SVM model correctly predicted patients who actually have diabetes. False Positives are the cases where the model incorrectly classified patients as diabetic when they actually don't have diabetes (Type I Error). False Negatives are the cases where the model incorrectly classified patients as non-diabetic when they actually have diabetes (Type II Error). True Negatives are the cases where the model correctly predicted patients who do not have diabetes.

TABLE III.
PERFORMANCE COMPARISON OF ML ALGORITHMS FOR DIABETES PREDICTION

Algorithms	Accuracy	Precision	Recall	F1-Score
SVM	0.74	0.74	0.74	0.74
Logistic Regression	0.74	0.71	0.80	0.75
Naïve Bayes	0.77	0.78	0.75	0.77
KNN	0.72	0.71	0.75	0.73
Random Forest	0.82	0.83	0.82	0.82
Decision Tree	0.75	0.74	0.78	0.76
XGBoost	0.80	0.81	0.81	0.80

B. Accuracy:

This metric measures how well the classifier can identify cases of diabetes. Overall, the performance of the algorithms on this metric is good, with all models achieving an accuracy of over 0.72. .Random Forest and XGBoost achieve the highest accuracy (0.82,,0.80), indicating good ability to distinguish diabetic and non-diabetic individuals.

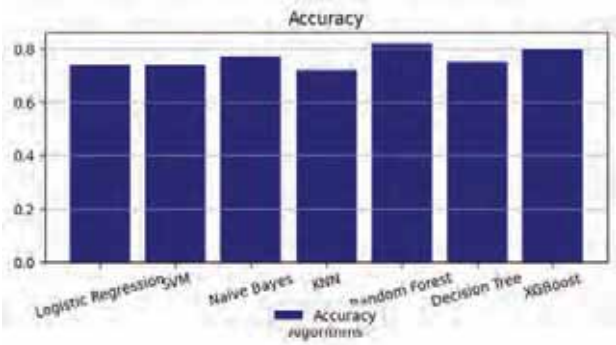

Figure 6. Accuracy of classifiers for diabetes prediction

CVR Journal of Science and Technology, Volume 26, June 2024
DOI: 10.32377/cvrjst2618

C. Precision:

$$Precision = (TPD) / (TPD + (FPD). \quad (1)$$

It indicates the proportion of patients predicted to have diabetes who do have it. A high precision signifies the model's effectiveness in identifying individuals with diabetes and minimizing false positives. Here, again Random Forest(0.83) and XGBoost (0.81) outperform other models.

Figure 7. Precision of classifiers for diabetes prediction

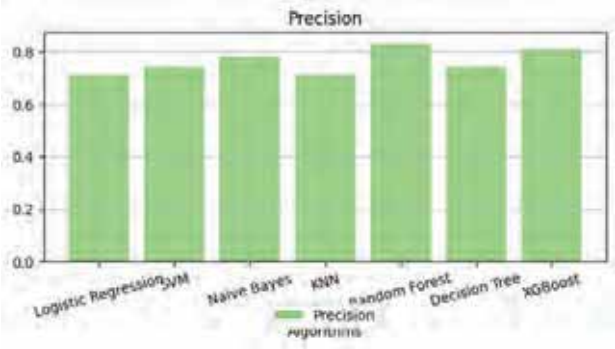

D. Recall (Sensitivity):

$$Recall = TPD / (TPD + FND) \quad (2)$$

Recall indicates the proportion of actual diabetic cases that the model correctly identifies. A high recall means that the model is good at identifying all cases of diabetes and avoiding false negatives. Random Forest, followed by XGBoost, performs the best in terms of recall.

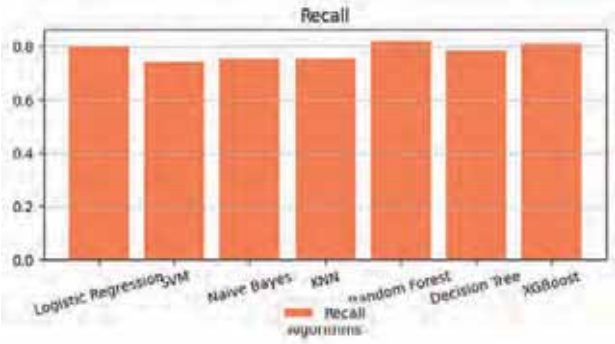

Figure 8. Recall of classifiers for diabetes prediction

E. F1-Score:

$$f1 - Score = 2 * \frac{(precision * Recall)}{(Precision + Recall)} \quad (3)$$

This metric balances the importance of precision and recall in a single score, and it takes both these factors into account. It is a good overall measure of a model's performance. Random Forest (0.82) and XGBoost have the best F1-score among all the models, which indicates that it achieves a good balance between precision and recall.

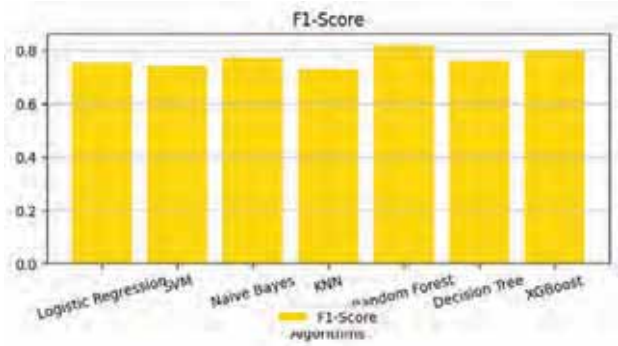

Figure 9. Precision of classifiers for diabetes prediction

Figure 10. Performance metrics of ML classifiers in Line graph

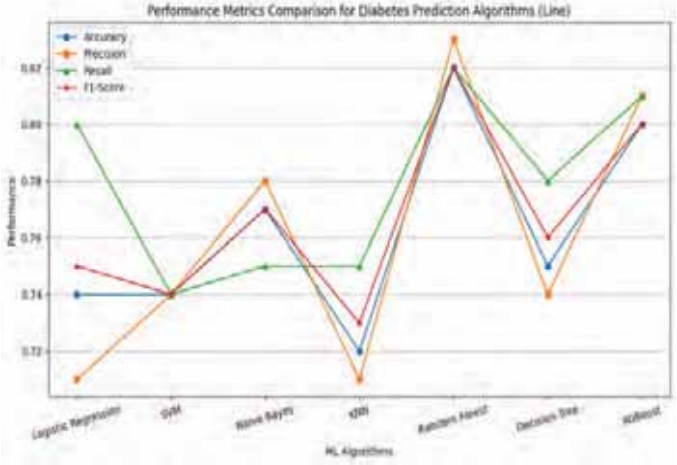

Figure 10 presents a line graph comparing evaluation metrics for various machine learning algorithms.

V. Conclusions

Early detection of diabetes is crucial for many who remain unaware. This paper explores machine learning techniques for high-accuracy diabetes risk prediction. Random Forest and XGBoost algorithms show promise, but success hinges on data preprocessing (cleaning, normalization, feature selection). A key challenge in diabetes prediction is class imbalance. SMOTE, applied during preprocessing, mitigates this issue by generating synthetic data for the underrepresented class, improving model performance. The choice between precision and recall depends on the cost of errors. For minimizing unnecessary tests, prioritize high-precision models like Random Forest. Conversely, for identifying all diabetic cases, focus on high-recall models like XGBoost. Our study achieved 82.5% accuracy using a Random Forest classifier, demonstrating a good balance between identifying healthy individuals and catching diabetic cases. This system's adaptability to other diseases paves the way for broader advancements in automated disease analysis and user-friendly web apps for risk prediction.

REFERENCES

[1] Diabetes. (2023, April 5). World Health Organization (WHO).
[2] IDF diabetes atlas 2021. (n.d.). IDF Diabetes Atlas | Tenth Edition.
[3] What is Diabetes? (2023, September 5). Centers for Disease Control and Prevention.
[4] Wagai, G., Firdous, S., & Sharma, K. (2022). A survey on diabetes risk prediction using machine learning approaches. Journal of Family Medicine and Primary Care, 11(11), 6929.
[5] Rajendra, P., & Latifi, S. (2021). Prediction of diabetes using logistic regression and ensemble techniques. Computer Methods and Programs in Biomedicine Update, 1, 100032.
[6] Iyer, A., S, J., & Sumbaly, R. (2015). Diagnosis of diabetes using classification mining techniques. International Journal of Data Mining & Knowledge Management Process, 5(1), 01-14.
[7] Mercaldo, F., Nardone, V., & Santone, A. (2017). Diabetes mellitus affected patients classification and diagnosis through machine learning techniques. Procedia Computer Science, 112, 2519-2528.
[8] Sisodia, D., & Sisodia, D. S. (2018). Prediction of diabetes using classification algorithms. Procedia Computer Science, 132, 1578-1585.
[9] Maniruzzaman, M., Rahman, M. J., Al-MehediHasan, M., Suri, H. S., Abedin, M. M., El-Baz, A., & Suri, J. S. (2018). Accurate diabetes risk stratification using machine learning: Role of missing value and outliers. Journal of Medical Systems, 42(5).
[10] Sneha, N., & Gangil, T. (2019). Analysis of diabetes mellitus for early prediction using optimal features selection. Journal of Big Data, 6(1).
[11] Lukmanto, R. B., Suharjito, Nugroho, A., & Akbar, H. (2019). Early detection of diabetes mellitus using feature selection and fuzzy support vector machine. Procedia Computer Science, 157, 46-54.
[12] Ahuja, R., Dixit, P., Banga, A., & Sharma, S. C. (2021). Classification algorithms for predicting diabetes mellitus: A comparative analysis. Pervasive Healthcare, 233-253.
[13] Morgan-Benita, J. A., Galván-Tejada, C. E., Cruz, M., Galván-Tejada, J. I., Gamboa-Rosales, H., Arceo-Olague, J. G., Luna-García, H., & Celaya-Padilla, J. M. (2022). Hard voting ensemble approach for the detection of type 2 diabetes in Mexican population with non-glucose related features. Healthcare, 10(8), 1362.
[14] David W. Hosmer, J., & Lemeshow, S. (2004). Applied logistic regression. John Wiley & Sons.
[15] Cortes, C., & Vapnik, V. (1995). Support-vector networks. Machine Learning, 20(3), 273-297.
[16] Cover, T., & Hart, P. (1967). Nearest neighbor pattern classification. IEEE Transactions on Information Theory, 13(1), 21-27.
[17] Rish, I. (2001). An empirical study of the naive Bayes classifier. IJCAI 2001 workshop on empirical methods in artificial intelligence (p./pp. 41--46).
[18] Ensembles: Gradient boosting, random forests, bagging, voting, stacking. (n.d.). scikit-learn. Retrieved February 22, 2024, from
[19] James, G., Witten, D., Hastie, T., & Tibshirani, R. (2013). An introduction to statistical learning: With applications in R. Springer Science & Business Media.
[20] XGBoost documentation — xgboost 2.1.0-dev documentation. (2022). XGBoost Documentation — xgboost 2.0.0 documentation.
[21] Pima Indians Diabetes Database. (2023, July 29). Kaggle.

E-ISSN 2581 – 7957
P-ISSN 2277 – 3916

CVR Journal of Science and Technology, Volume 26, June 2024
DOI: 10.32377/cvrjst2619

Design and Analysis of Plastic Injection Mold for Hexagon Socket Head Cap Screw

Neeraj Kumar Jha
Assoc. Professor, CVR College of Engineering/ Mechanical Engg. Department, Hyderabad, India
Email: neerajjha.me@gmail.com

Abstract: **Plastic is a majorly used material for making customer goods. It is appealing to customers as well as manufacturers. Properties like durability, light weight and moldability make it a suitable choice for consumer goods which are made by mass production. Plastic materials are soft, but they possess adequate strength to be utilized for different engineering applications. After the development of various grades of plastic, it has replaced metals from different engineering applications in the recent past. This article aims at analyzing the suitability of making Hexagon Socket Head Cap Screws (HSHCS) out of a plastic material by injection molding processes. These screws are widely used as threaded fasteners at different places. They are preferably made of ferrous metals and possess semi complex design. They are mass produced by following a series of manufacturing operations. This article will observe the manufacturability of HSHCS by injection molding process. Based on the observation a model mold will be prepared to make HSHCS. The software used for modeling the parts is Autodesk Fusion 360 and that for the simulation of process parameters is Autodesk Moldflow Adviser 2023.**

Index Terms: **Hexagon Socket Head Cap Screws, plastic mold, manufacturability, threaded fasteners, injection molding, simulation.**

I. Introduction

Rapid growth in materials and manufacturing technology is making all engineering challenges achievable. Design innovations are contributing to ease the manufacturing. New materials are allowing engineers to think beyond conventional. After the invention of polymers, they are being conveniently used to meet specific technical needs. Various plastic processing techniques are developed for processing tailored polymers to different shapes [1]. Injection molding is one such process. This process utilizes facilities to convert plastic material to semisolid phase and pressurizes it to a shaped cavity. The cavity possesses the shape of the required product. It is made of a metallic mold, often called plastic mold, or die. This mold is designed by following a standard set of procedures. Getting a defect free product from this process depends on controlled process parameters and effective design of die. The design of this mold can be simple, or complex based on complexity possessed by the component. A component with more undercuts and pockets may need inserts in the die. Sometimes for complex part multidaylight molds are needed. The decision about number of cavities, gate location, runner diameter, ejector pin location etc. is also part of the design process. Controlling the process parameters means controlling injection temperature, cooling time, injection pressure and cycle time. The injection molding process is the most suitable for mass production of plastic parts irrespective of size and shape of the part. Current trend in manufacturing justifies 3D printing for making various plastic parts. But it is evident that the parts made by 3D printing have large lead time [1]. Thus, the parts which are very complex and nearly impossible to make by injection molding are only made by 3D printing. Threaded parts are usually considered under the category of complex parts. Usually, threaded parts are obtained by machining process. But it is unique advantage of injection molding process that a part obtained by injection molding can have threaded profile on it [1, 2].

HSHCS are threaded parts. They are a type of screw, which are designed and made with internal hexagonal drive formed into the head while the outer edge of screw head remains round. They are actuated with a hex key often called Allen key for tightening or loosening purposes. They differ from conventional screws and bolts in many ways. They do not need a nut to be positioned for locking. They utilized internal thread of to be joined parts like a screw does. HSHCS possess many advantages over their conventional counterparts. The hexagonal socket enables the screw to resist cam-out better than other similar drives. This is also evident that HSHCS of the same size enable us to gain higher torque and clamping force. When applied, the whole head of HSHCS sinks into the workpiece, thus the surface of workpiece remains projection free and appears good aesthetically. They are not very easy to disassemble, as they need a special type of tooling for actuation. They have a wide range of applications, especially in tooling and manufacturing industries. Usually, to join multiple plates and parts together HSHCS is used. They can be observed beneath the surface of external plates of various tools viz. forming tools, jigs and fixtures, plastic molds, die casting dies and machine tools. They are made of metal, preferably alloy steel following a sequence of manufacturing processes. A rolled bar is first cut to a calculated length which goes through heading operation to form head of the HSHCS. At the same time the hexagonal recess in the head is also formed. Further threading is done on its body either by thread cutting operation or by the thread rolling process. Additionally, the side face of the head is knurled for better grip during casual actuations. There is a possibility of another combination of operation also to manufacture SHCS but the one discussed has the smallest lead time.

This article made an attempt to make HSHCS out of a suitable plastic material by injection molding process. The purpose of developing HSHCS out of plastic was to gain benefit of single station manufacturing there by reduced manufacturing cost and implementing them for joining metal parts in low load conditions. Further this article

Received on 27-01-2024, Revised on 26-02-2024, Accepted on 27-03-2024.

CVR Journal of Science and Technology, Volume 26, June 2024
DOI: 10.32377/cvrjst2619

explains the product design phase in Section II. Section III deals with design calculations. The discussion about process parameters and simulation of the process is in Section IV. Section V is about the trial of the manufactured die. Finally in Section VI the conclusion of this work is demarcated.

II. Product Design

Product design is the most important element of mold design [2]. An effective product design ensures simple mold design and overall profitability of process [3]. Smooth process flow and defect free products are outcomes of product design [3, 4]. The 2D drawing and solid model of M8 X 1.25 HSHCS considered for this work as well as its solid model is shown in Fig. 1. HSHCS dimensions include height and diameter of the head, shaft diameter, length of threaded shaft. The dimensions are influenced by BIS 2269: 2006, ISO4762: 2004.

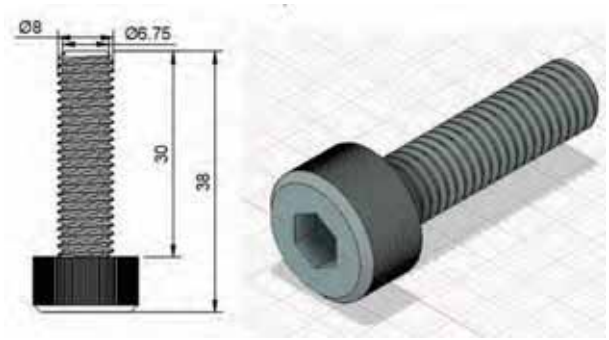

Figure 1. 2D Drawing of HSCHS and Solid Model
(All dimensions are in mm)

The part was modeled by considering metallic part. It has hexagonal recess on head and the side face of the head has straight knurling. The part was keenly observed for its effective shaping by injection molding process. Its draft analysis was done to plan its profiles in the halves of the mold. The draft analysis is shown in Fig. 2. According to vertical axis (Z Axis, mold opening direction), top half profiles are shown in green color, bottom half profiles are shown in blue color and straight faces are shown by red color.

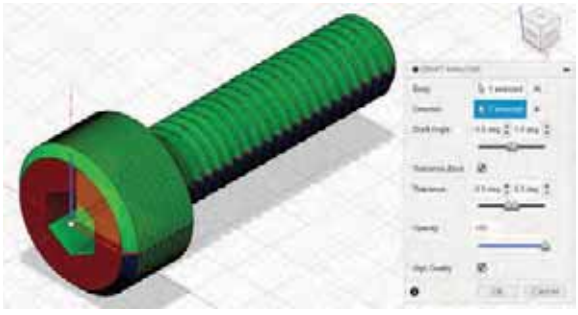

Figure 2. Draft Analysis

Availability of one color in other half indicates possibility of undercut. This indicates trouble in achieving such profiles while opening of mold. It can be observed that there are undercuts in hexagonal recess region and in the knurling. For ease of die manufacturing, it was decided that the hexagonal recess will be obtained with a side insert and the knurling will be avoided from side face of the head. Further observations predicted that entire head can be taken as insert while the threaded shaft will come in the two halves of the mold. The final model of HSHCS with representation of parting planes is shown in Fig. 3. Blue color plane shows splitting of insert to make socket head with body. By this way straight knurling on the side face if the head is possible. But considering the cost of mold making, knurling is avoided from the side face of head. The same can be observed in Fig. 3. The plane in orange color shows splitting of two halves of mold to split threaded shaft.

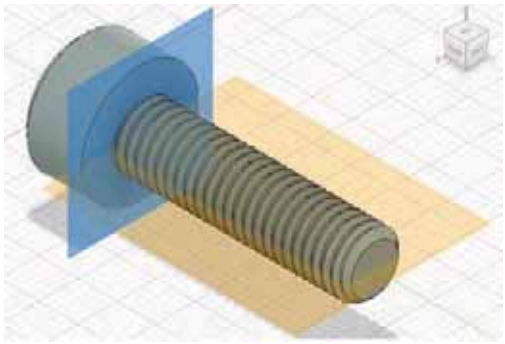

Figure 3. Parting Planes

Material selection can also be considered as part of the product design [5, 6]. This research considered polypropylene (PP) for plastic molding of HSHCS due to its own advantages. A few of the important properties of PP is mentioned in Table I. Finally, 1.5% shrinkage allowance is added to the model as per ISO 294-4 for thermoplastics, considering polypropylene material.

TABLE I.
Material Specification (PP)

Material Properties	PP
Density	946 kg/m³
Softening Point	150 °C
Formula	$(C_3H_6)_n$
Shrinkage	1-2.5%
Tensile Strength	21-37 N/mm²
Injection Temperature	260 °C
Heat Deflection Temperature	120 °C
Mold Temperature	60°C

III. Design Calculations

Before proceeding for simulation, it is necessary to know about some important aspects of a mold viz. number of cavities, shot volume, clamping capacity. These parameters directly influence the process simulation. In Table II common specifications of an injection molding machine is indicated. These parameters will be considered as references for design calculation as well as for the simulation. This is a vertical injection horizontal clamping injection molding machine.

CVR Journal of Science and Technology, Volume 26, June 2024
DOI: 10.32377/cvrjst2619

TABLE II.
MACHINE SPECIFICATION
(TEXPLASST 1HD, MP LAB, CVRCE, HYDERABAD)

Shot Capacity	2 – 45 gms / shot
Plunger Diameter	25 mm
Stroke Length	450 mm
Clamping Capacity	6.0 Tons
Injection Pressure	80 kg/cm^2
Heating Capacity	1.5 kw
Total Installed Power	3.7 kw
Total Shut Height	100 – 450 mm

A. Number of cavities

Decision about the number of cavities in a mold is prime step for the mold design. It is directly influenced by the number of parts to be produced. A lower number of cavities refers to longer lead time and at the same time a greater number of cavities can give defective product if the design is not aligned with the process parameters. The number of cavities is also planned as per space available in the machine between tie bars as it affects the size of the mold.

There are different methods to calculate the number of cavities for a mold [7]. Number of cavities based on shot capacity can be obtained as shown in (1).

$$Ns = \frac{0.85\ Ms - Rw}{Cw} \quad (1)$$

Where,

Ns = No. of cavity based on shot capacity
(Based on 85% of rated shot capacity)
Ms = Rated shot capacity of machine (gm/shot)
Rw = Weight of all sprues and runners (gm)
Cw = Component weight per cavity (gm)

$$Ns = \frac{0.85X18 - 2.15}{4.75} = 2.77$$

The rated shot capacity is considered from the usual shot capacity on which the considered machine works. As per need it can be increased further. Other values are taken from the solid model. The number of cavities is coming out to be approximately three. But considering proper filling of the cavities this research has considered two cavities.

B. Shot Volume

Shot volume is volume of material sufficient to fill all the cavities of the die for one shot. Equation (2) represents all the necessary elements considered for the calculation of shot volume [7].

$$Sv = Vs + Vr + Vg + Vc \quad (2)$$

Where,

Sv= Shot volume (mm^3)
Vs = Volume of sprue (mm^3)
Vr = Volume of runner (mm^3)
Vg = Volume of gate (mm^3)
Vc = Volume of mold cavity (mm^3)

$$Sv = 44 + 1285 + 24 + 9500$$
$$= 10853 \text{ mm}^3$$

All these values were conveniently taken from the modeled part. Considering the two cavities and the runner system accordingly, the shot volume is coming as 10.85 gm (10853 mm^3). The actual needed material is going to be slightly more than this because shrinkage is also to be considered. It is observable that the required shot volume is well within the shot capacity of the machine.

C. Calculation of Clamping Capacity

Adequate clamping force is needed to hold the split mold so that they will not open due to injection pressure. Equation (3) represents all the necessary elements considered for the calculation of shot volume [7].

$$Cf = PPA \ X \ \frac{1}{3}(IP) \quad (3)$$

Where,

Cf = Clamping capacity (kg)
PPA = Plan projected area of mold (cm^2)
IP = Injection pressure(kg/cm^2)

$$Cf = 6.72\ X\ \frac{1}{3}\ (80)$$
$$= 179.2 \text{ kg}$$

The required clamping force is also within the clamping capacity of the machine. Utilizing outcomes of calculations and product design, planned flow path is shown in Fig. 4. The same outcomes are utilized in process simulation.

IV. PROCESS SIMULATION

The process simulation provides the necessary information to prepare the mold as per process parameters for smooth flow of process to get defect free products. It additionally helps in finding proper gate location for material injection, positions of vents, fill time, flow behavior and possibility of defects.

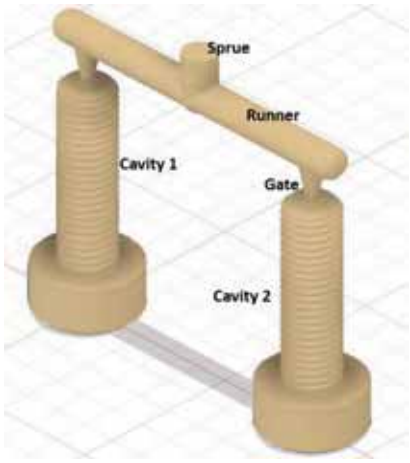

Figure 4. Model of Mold Cavity for Flow Analysis

Considering design standards and values obtained by design calculations from the previous section, a doble cavity mold with flow path was modeled and the same is represented in Fig. 4. The elements of flow paths are labeled. The circular cross section of flow path elements ensures proper flow of melt through the mold [8]. Though

CVR Journal of Science and Technology, Volume 26, June 2024
DOI: 10.32377/cvrjst2619

other cross sections are also used for convenience in machining. The gate is usually maintained with least cross section among all the elements of the flow path. It prevents back flow of melt after injection stops. The injection location in HSHCS cavity is planned by considering multiple aspects. Part symmetry plays a major role in this decision. Natural draft available in the part profile, selected parting plane and mold opening directions are other factors affecting selection of the injection location. For mold flow analysis the proper boundary conditions viz. mold temperature (60°C), injection temperature (260°C), injection pressure (4MPa) etc. corresponding to PP were provided as per discussion in previous sections. Mold flow analysis was performed on the model shown in Fig. 4 and the obtained results from Autodesk Mold Flow Adviser 2023 are discussed further.

A. Temperature at Flow Front

In the process of mold filling, flow front temperature should not change beyond 2°C to 5°C [9]. Larger difference represents long injection time. Thus, there might occur solidification of flow front before complete filling of mold. The obtained result is represented in Fig. 5. The difference of maximum and minimum temperature is within the acceptable range.

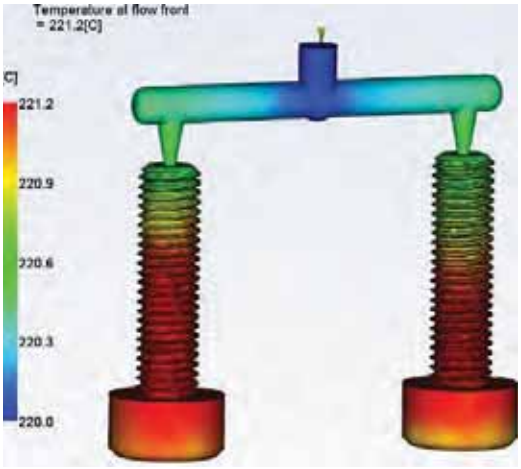

Figure 5. Temperature at Flow Front

B. Weld Lines

The weld lines in injection molding indicate the region where two flow front meet. They are very critical to be examined as they are potential regions of defects [9, 10]. Especially for the parts like HSHCS, weld lines must be avoided for the durability viewpoint. The obtained weld line result is represented in Fig. 6. There were negligible weld lines observed. Longer weld lines around any cross section can be the spots of crack initiation and propagation. Correct gate location can be a reason behind positive weld line result. They can also be avoided by maintaining adequate injection pressure and temperature at the time of mold filling.

Figure 6. Weld Lines

C. Air Traps

An air trap occurs when the melt accumulates and compresses a bubble of air or gas in the flow fronts or between the flow front and the wall of mold cavity [7, 10]. Their quantity and location are very important to be estimated. They also leave week spots in the product cross section like weld lined does. Additionally, this analysis helps to identify the possible locations of air vents to be provided in the mold cavity. The air trap result is shown in Fig. 7.

Figure 7. Air Traps

The result shows no air trapped in the cavity. The main reason behind this result can be the existence of parting line along length of mold cavity. This result eliminates the need of providing air vent in the mold. Still, as a standard practice it was decided to provide air vent for the cavities in the direction opposite to the injection location.

D. Frozen Layer Percentage at the Time of Ejection

The Frozen layer percentage at the time of ejection represents the percentage of thickness solidified at the end-of ejection process. The values of this result range from 0% to 100%. A greater value represents a thicker solidified layer and a lesser value represents thinner layer of frozen polymer [11]. It can be seen from Fig. 8 that majority of the cavity is solidified at the time of ejection. A minute portion near the junction of head and body is still solidifying. This is due to

CVR Journal of Science and Technology, Volume 26, June 2024
DOI: 10.32377/cvrjst2619

high material as well as heat accumulation in that region. There is no design solution possible for this. This issue can be handled by providing cooling channel in that region or by taking some time before opening the mold.

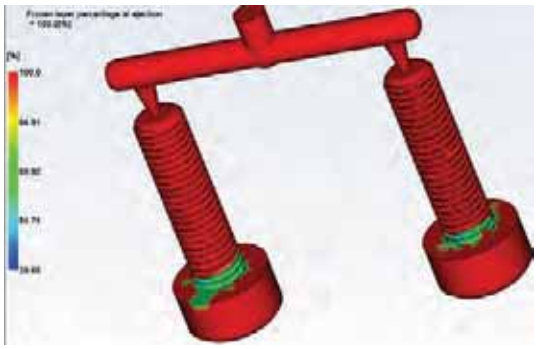

Figure 8. Frozen Layer Percentage at the Time of Ejection

Figure 9. Warpage Indicator

E. Warpage indicator

The warpage indicator shows the area of the part where the deflections may appear [12, 13]. Based on this result corrective actions can be taken to protect the correct profile of injection molded part. As can be seen from Fig. 9, that entire area is showing least possibility of warpage. Thus, there is no need to take any corrective measure into consideration.

F. Confidence of Fill

The confidence of fill result indicates the ease of filling the mold cavity i.e. the area of the mold may be difficult to fill with plastic [14]. The obtained result which is indicated in Fig. 10 is not very convincing as the entire threaded region is showing low confidence of getting filled. This issue can be tackled by increasing injection temperature and injection pressure at the time of mold filling. The process utilized 260°C injection temperature and 4 MPa injection pressure. It is not advisable to inject PP beyond 260°C for injection. Overheating can make plastic week and durability of plastic accumulated in threaded region will decrease drastically. Thus, it was decided to use higher injection pressure to ensure proper filling of the mold.

With the indications obtained from mold flow analysis, this work proceeded with manufacturing of model mold. Further the trial on the mold was taken which is discussed in next section.

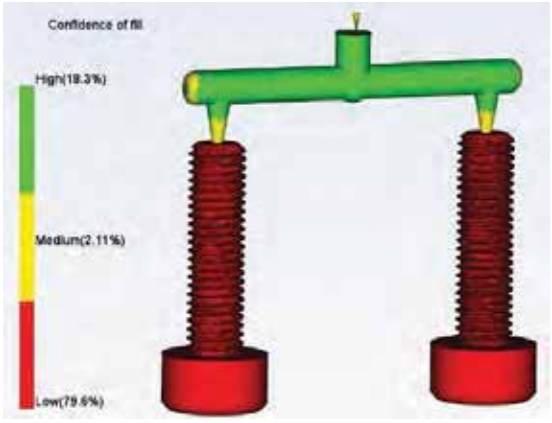

Figure 10. Confidence of fill

V. Die Trial

A die was prepared for trial purpose. This is unlike the actual injection molding die which is manufactured for industrial production. In Fig. 11 the manufactured die is shown. It is aligned with the nozzle of injection molding machine mentioned in Section III. The die was manufactured in three parts, according to split of parting line shown in Fig. 3. For better visibility of internal cavities one portion of the die is removed and shown in Fig. 11.

Figure 11. Mold for Trial

The machine was adjusted for values as per previous discussion. Injection pressure was considered 6 MPa which was beyond simulation value and less than the maximum capacity of machine. It was done to ensure proper filling as discussed in Section IV. The shot was taken to obtain the required impression, which is shown in Fig. 12. Multiple shots were taken to ensure the results obtained in the simulation. All the impressions obtained from HSHCS were observed against shrinkage, deflection, unfilled section etc. the obtained quality was found as per the results obtained in

the simulation. In none of the shot unfilled section or any other defect was seen.

Figure 12. Obtained Impression (L) and Molded Plastic HSHCS (R)

VI. Conclusions

The choice of manufacturing processes is of strategic importance in new product development [1]. It has a significant impact on cost of production. The recent materials and manufacturing technology is making it possible to process any material by any manufacturing process. It is the responsibility of engineers to utilize technology for economic benefits. Scope this work is limited to evaluating feasibility of making HSHCS by injection molding process using plastic material. The content provided in this article can be utilized to design an injection molding die as well as to perform and analyze the mold flow analysis for plastic components. Modifying the die for industrial production, molding HSHCS by a type of polymer with comparable properties of a metal, testing these HSHCS in different loading conditions can be further scope of research work. This research attempted to provide researchers with an insight that there is always scope for betterment.

References

[1] David Kazmer, Amy M. Peterson, Davide Masato, Austin R. Colon, Joshua Krantz, "Strategic cost and sustainability analyses of injection molding and material extrusion additive manufacturing", Volume63, Issue3, March 2023, Pages 943-958, https://doi.org/10.1002/pen.26256

[2] Neeraj Kumar Jha, Bhavya Sri Tadiparthi, "*Design and Analysis of the Sleeve Ejection System in Injection Molding Die for Trolley Wheel*", CVRJST, Vol. - 17, pp. 132-137, 2019.

[3] E.Farotti, M.Natalini, "Injection molding. Influence of process parameters on mechanical properties of polypropylene polymer. A first study", Procedia Structural Integrity, Vol.- 8, 2018, pp. 256-264.

[4] R.Sánchez, A.Martinez, D.Mercado, A.CarbonelJ.Aisa, "*Rapid heating injection moulding: An experimental surface temperature study*", Polymer Testing, Volume 93, 2021, 106928

[5] Simion Haragas, Ovidiu Buiga, Ovidiu Buiga, Claudiu Popa, Florina Maria, ŞerdeanFlorina, Maria Şerdean," *Demolding Moment Calculation for Injected Parts with Internal Saw Thread*", MATERIALE PLASTICE, 2016, 53(3):378-381

[6] Giovanni Lucchetta, Davide Masato, Marco Sorgato, "Optimization of mold thermal control for minimum energy *consumption in injection molding of polypropylene parts*", Journal of Cleaner Production, Vol.- 182, 2018, pp. 217-226.

[7] Neeraj Kumar Jha, P V Ramana, "*Design Methodology and Analysis of Double Cavity Metal-Plastic-Insert Injection Molding Die for Push Board Pin*". CVRJST, Vol. - 14, pp. 91-96, 2018.

[8] N. Sateesh, S. Devakar Reddy, G. Praveen Kumar, Ram Subbiah," *Optimization of injection moulding process in manufacturing the flip cover of water meter*", Materials Today: Proceedings 26, 2020, pp. 240-246.

[9] Babur Ozcelik , Alper Ozbay, Erhan Demirbas, "*Influence of injection parameters and mold materials on mechanical properties of ABS in plastic injection molding*", International Communications in Heat and Mass Transfer, Vol.- 37, Issue 9, 2010, pp. 1359-1365.

[10] Abdulmecit Güldaş, Onuralp Uluer & Ahmet Özdemir, "*The Numerical Analysis of a Mold Cavity Filling Using the Finite Control Volume Method and Comparison to the Experimental Results*", Polymer-Plastics Technology and Engineering, 48:4, 2009 , pp. 389-396.

[11] Jiseon Hong, Sun Kyoung Kim, Young-Hak Cho, "*Flow and solidification of semi-crystalline polymer during micro-injection molding*", International Journal of Heat and Mass Transfer Vol.- 153, June 2020, 119576.

[12] Marton Huszar, Fawzi Belblidia, Helen M.Davies, Cris Arnold, David Bould, Johann Sien, "*Sustainable injection moulding: The impact of materials selection and gate location on part warpage and injection pressure*", Sustainable Materials and Technologies, Vol.- 5, 2015, pp. 1-8.

[13] Parth Patpatiya, Anshuman Shastri. "*Additive Manufacturing of Thermoplastic M8 Fasteners Using Photopolymer Jetting Technology for Low-Strength Fastening Applications*", 30 July 2021, PREPRINT (Version 1) available at Research Square [https://doi.org/10.21203/rs.3.rs-525671/v1]

[14] Czepiel M, Bańkosz M, Sobczak-Kupiec A. "*Advanced Injection Molding Methods: Review. Materials (Basel)*". 2023 Aug 24;16(17):5802. doi: 10.3390/ma16175802. PMID: 37687494; PMCID: PMC10489002.

E-ISSN 2581 – 7957
P-ISSN 2277 – 3916

CVR Journal of Science and Technology, Volume 26, June 2024
DOI: 10.32377/cvrjst2620

Biomechanical Analysis of a Femur Bone

C. Sai Kiran[1], M. Siva Sai[2] and P. Surya Teja[3]

[1]Asst. Professor, CVR College of Engineering/Mechanical Engg. Department, Hyderabad, India
Email: csaikiran001@gmail.com
[2] UG Scholar, CVR College of Engineering/Mechanical Engg. Department, Hyderabad, India
Email: avisias1971@gmail.com
[3]UG Scholar, CVR College of Engineering/Mechanical Engg. Department, Hyderabad, India
Email: suryateja43623@gmail.com

Abstract: **In this paper, a CAD model of human femur bone was generated and was analysed which is useful for medical industry for implementing the correct size and correct plate that can withstand the stresses developed by the user. The purpose of the work is to find a suitable material which can withstand the maximum stress made by the user. In this paper internal fixation is analysed. The image of femur bone is generated by using the 3D slicer where CT scan data in form of DICOM files is sent to the software to generate 3D model and the Bone plate, screws are modelled by using SolidWorks, the dimensions of the plate and screws are taken according to the generated femur bone. The function of the bone was analyzed for four different materials i.e. Nylon, PMMA, SS316L, TI-6Al-4V by using Ansys software and when the body is physically active. Total deformation and von-misses stress analysis help to choose the material which can withstand the max stress under different activities.**

Index Terms: **Femur, 3D Slicer, SolidWorks, Ansys, Von-mises stress.**

I. Introduction

The femur bone, which is commonly known as the thigh bone is the longest and strongest bone in the human body. Femur plays a crucial role in supporting body weight and facilitating movement of the human body.

S. Kirthana et al. [1]. In this paper, biomechanical analysis is performed for the right femur bone, also known as the thigh bone. Under static structural analysis, the authors conducted equivalent (von-Mises) stress, total deformation and factor of safety analysis were conducted. The boundary conditions applied to the femur bone included considering the bottom of the femur bone as a fixed support, while the other end is free in all directions, with force applied on the circumferential bone. They utilized five different materials for the analysis. From their analysis, they concluded that titanium is the most suitable material among the others. Additionally, they considered the cost factor, suggesting PMMA and PEEK as potential choices for the plate and screw material. *P.S.R. Senthil Maharaj* et al. [2]. In this paper, numerical analysis is performed on fractured femur bone with prosthetic plates. The prosthetic bone plate was modelled using SolidWorks software and the femur bone is modelled using mimics software. Then the prosthetic plate was attached to the femur using SolidWorks software. Equivalent stress and directional deformation are performed for five different materials. From the results, titanium was found to have the lowest stress out of the five materials. *K.C. Nithin Kumar* et al. [3]. In this paper, biomechanical analysis of femur bone using Finite Element technique is conducted. The CAD model of femur bone was modelled from MRI/CT scan data using ITK-snap software and pre-processing & post-processing operations are performed using HYPERWORKS software, whereas the solver is NASTRAN 10.0 software. The analysis is conducted using three materials - natural bone material, AZ31, CP Ti. In this study maximum stress and maximum displacement is done for jumping & walking conditions and compared the AZ31, CP Ti with natural bone. From the results it is found out that AZ31 is best suited material for bone implants because of its low stress & displacement compared to natural bone and CP Ti. *S.G. Aftab* et al. [4]. In this paper, biomechanical analysis of femur bone using FEA method is conducted. The 3D model of femur bone was created by using MRI scanning technique and then the model was converted into IGES format for analysis in ANSYS software. Equivalent stress is applied to natural material of femur bone & other three materials (PMMA, Al2O3, Nylon 66) understanding, walking, jumping, and running conditions. After the analysis, the material with low stress compared to natural femur bone for different conditions is selected and this process is considered for the other conditions. *S. Mathukumar, VA Nagarajan* et al. [5]. In this paper, the researchers used the modelling technique to get the 3D model of femur bone from the CT scan data and with the help of computational method i.e. FEA method. Stress and strain analysis is performed on the femur bone under the loads of 490N, 540N, 588N and 640N and the strain gauges were positioned at designated locations labelled 1, 2, 3 and 4. The bottom of the femur bone is considered as fixed support and the opposite end of the femur bone remained fixed in all degrees of freedom. Higher stress values were observed at the neck inferior, and neck superior positions compared to the shaft lateral and shaft medial positions, additionally analysis highlighted this increased weight led to a greater total displacement, with the neck side of the femur exhibiting the highest strain. The research findings propose that conducting experiments directly on femur bones may become unnecessary, given the higher accuracy and reliability of results obtained through finite element (FE) analysis. This suggests that FE analysis offers a possible alternative that could potentially replace or reduce the need for physical experimentation on real femur bones. *P Kishore* et al. [6]. In this paper the researchers conducted an analysis of the femur bone, focusing on evaluating normal stress and total deformation. The CAD model of femur bone

Received on 10-03-2024, Revised on 09-04-2024, Accepted on 09-05-2024.

CVR Journal of Science and Technology, Volume 26, June 2024
DOI: 10.32377/cvrjst2620

is modelled by using the CT scan data, which comprises DICOM files consisting of thousands of bone images. This are further imported to 3D slicer to get 3D model of the femur bone and this model is saved in the form of .stl format, it is imported into blender where if the model has any unwanted parts here, they are removed and saved and this .stl format is imported to CATIA V5 where it is converted into .stp format for analysis. The analysis is performed under three different loads 270N, 400N and 650N. The results of their analysis indicate varying levels of normal stress and total deformation experienced by the femur bone under these loads. Additionally, they observed that the femur neck exhibited maximum stress under the applied loads, with higher loads potentially leading to femur neck fractures and associated patient discomfort. *Pravat Kumar Satapathy* et al. [7]. In this paper the authors performed an FE analysis on the femur bone. The bone modelled by using the data from the CT scan and the material properties are assigned using Mimics software. The implant plate materials they considered are titanium, FG material is a homogenous material which consist of different types of materials. Results of the analysis revealed the behaviour of the femur bone under various loading conditions. Deformation and stress distribution were evaluated for both the titanium and FG implant materials. It was observed that the FG material exhibited different mechanical responses compared to titanium, suggesting potential advantages in terms of strength and stability. The results states that the plate material with FG demonstrated good performance compared to the other materials. *Albert E. Yousif and Mustafa Y. Aziz* et al. [8]. has performed biomechanical analysis on femur bone while sitting and going upstairs. The femur bone model by using CT scan data is imported to mimics software in the form of DICOM files. The authors applied fixed constraints at both the distal and proximal ends of the femur this constraint aids the calculation of normal stresses during activities such as going upstairs and sitting down. This study highlights the significance of estimated stress profiles in injury prevention, prosthesis development and the design of more durable implants. Moreover, these stress values have implications for sports medicine, fitness-related research and various biomechanical applications. *Yegireddi Shireesha* et al. [9]. In this paper the authors conducted an FEA analysis on femur bone under equivalents stress and total deformation. The femur bone model is generated by using CT scan data. Further, this model is imported to Ansys software for equivalent stress and total deformation to the femur bone. The analysis is conducted under static loading conditions using ANSYS software, evaluated stresses formed in different femur implant materials, including structural steel and Ti-6Al-4V. These analyses are performed under three different loads 550kg, 650kg & 750kg. They Compared the performance of the two implant materials, here the Ti-6Al-4V demonstrated less deformation under static load conditions. This material's low density and excellent biocompatible make this material as an ideal choice for surgical implants. *Raji Nareliya And Veerendra Kumar.* [10]. In this paper FEA analysis is applied on the femur bone. The femur bone model is generated by importing CT scan data into mimics software from there it is imported to workbench in form of .stp file. They considered the bottom of the femur bone in medical field this bottom (medial and lateral condyle) of femur is known as condyle as the fixed support and applied a load of 750N to the head of the femur bone. Results indicated that higher weight led to increased total displacement, with maximum total deformation observed at the femur's head and minimum at the lower end. Maximum principal stress occurred at the middle section of the femur, accompanied by an equivalent (Von Misses) stress and fatigue life was estimated, and a constant factor of safety of 15 was maintained throughout the femur. Ultimately this research contributes valuable insights into the biomechanical behaviour of the femur bone.

From the literature we concluded that researchers generally suggest titanium stands out as the most biocompatible material. However regarding material choices and loading conditions make it challenging for drawing definitive conclusions, while some studies briefly mention cost considerations in material selection, there is a lack of comprehensive analysis regarding the cost effectiveness of different materials, as FEA shows promise in predicting bone behaviour, the lack of uniformity in how models are constructed and boundaries are defined can lead to contradictions in results and hinder the comparability of studies.

From the studies we explored a wide range of materials for femur bone analysis, including titanium, PMMA, SS316l, Nylon 66, and composite materials.

- Titanium emerged as a favourable material due to its low stress levels and favourable mechanical properties.
- More research needed to assess materials for durability, compatibility with cost-effectiveness in clinical use.

II. Methodology

A. Generating CAD Model of Human Femur Bone

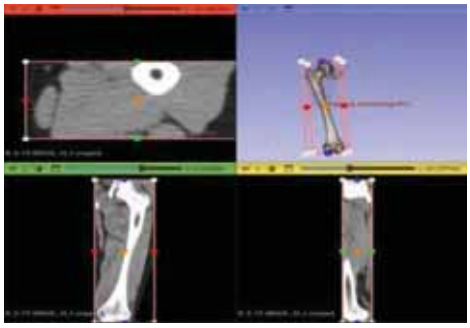

Figure 1. CAD Model Generated Using 3D Slicer Software

The CAD model of bone is generated by importing the DICOM files which are generated from patients CT or MRI scan data and this DICOM files are imported to generate the CAD model of the bone as shown in Fig. 1.

The modelling of plate and screws are done using the SolidWorks software. The dimension of the plate is taken by considering the height of the femur bone and its width. The dimensions of the screw are also taken by considering the CAD model of bone.

CVR Journal of Science and Technology, Volume 26, June 2024
DOI: 10.32377/cvrjst2620

B. Refinement of Femur Bone Model Using Meshmixer

Here, after creating a CAD model we import it to mesh mixer Fig. 2 shows the CAD model of bone after trimming of extra parts and refinement of bone model.

The dimensions of Bone:

Figure 2. CAD Model Generated Using 3D Slicer Software

Height of femur bone = 426.3mm

Width of femur bone (shaft) = 30mm (Approx)

Width of condyle (bottom of bone) = 77.58mm

C. Modelling of Fixation Plate

The dimensions of the fixation plate, determined based on the height width of the bone shaft, were modelled using solid works. The dimensions are as follows:

Length of plate: 5mm

Breadth of plate: 16mm

Height of plate: 140mm

D. Modelling of Screw

The shape of screw or threads can significantly impact the stability of plate, ensuring secure fixation to the bone surface. Therefore, careful consideration should be given to the design of screws, modelled using SolidWorks. In this research paper, the dimensions were selected deliberately rather than randomly.

Shape of drive = Hex

Total screw length = 27.7mm

Shank of screw = 5mm

E. Assemble of Fixation Plate to Femur Bone

The internal fixation is assembled to the femur bone using SolidWorks. Fig. 3 shows the assembled model of femur bone.

F. Materials for The Bone, Plate and Screw

The plate and screw materials must be biocompatible to minimize the risk of harmful reactions or rejection by the body. The plate and screw materials should possess adequate strength and durability to withstand the mechanical forces exerted on them during daily activities. For analysis Nylon, PMMA (polymethyl methacrylate), SS316L (stainless steel alloy with a low carbon) and Ti-6Al-4V has been selected. The material properties are referred from Table I.

Nylon 6/6:

Figure 3. Assembled Model of Femur Bone

- Advantages: High strength-to-weight ratio, corrosion resistance.
- Limitations: Chemical sensitivity, creep resistance and moisture absorption.

PMMA (Polymethyl Methacrylate):

- Advantages: Transparency and biocompatibility.
- Limitations: Brittleness and scratch sensitivity

SS316L (Stainless Steel 316L):

- Advantages: Corrosion resistance, high strength and biocompatibility.
- Limitations: Cost, weight and machinability.

Ti-6Al-4V (Titanium Alloy):

- Advantages: Biocompatibility, corrosion resistance and high strength to weight ratio.
- Limitations: Cost, difficulty in machining and low modulus

TABLE I.
MECHANICAL PROPERTIES OF BIOMATERIALS FOR FEMUR, PLATE AND SCREW

Bone & prosthetic plate materials	Young's modulus (GPa)	Density (gm/cc)	Poisson Ratio (γ)
Femur Bone	1.8	18	0.33
Nylon 6/6	3.72	300	0.21
PMMA	1.18	220	0.2
SS316L	7.75	193	0.31
Ti-6Al-4V	120	4.5	0.32

These materials were chosen based on their properties, biocompatibility and their utility in various medical fields.

G. Load Calculations

These load values are calculated for four activities:

For standing activities:

Total weight of human (m) = 75 kg

CVR Journal of Science and Technology, Volume 26, June 2024
DOI: 10.32377/cvrjst2620

Weight of one leg (assuming equal distribution) = $\frac{75\ kg}{2}$

$= 37.5\ kg$

Using the formula,

$f = m \times g.$ (1)

$where, g = 9.81 \frac{m}{s^2}$

$f = 37.5 \times 9.81$

$= 367.8\ N$

$\approx 370\ N$

For jumping activity:

Step 1: Calculate the new acceleration (a_{jump}) using the formula for vertical displacement:

Jump (h) = 0.1m

Jump duration (t) = 0.1sec

$h = \frac{1}{2} \times a_{\text{jump}} \times t^2$ (2)

Submitting the values:

$0.1 = \frac{1}{2} \times a_{\text{jump}} \times (0.1)^2$

$0.1 = \frac{1}{2} \times a_{\text{jump}} \times 0.01$

$10 = 0.005 \times a_{\text{jump}}$

$a_{\text{jump}} = 20\ \text{m/s}^2$

Step 2: Calculating the force exerted by one leg F :

$F = m \times a_{\text{jump}}$ (3)

$m = 75\ kg$

Submitting the values:

$= 75 \times 20 = 1500\ \text{N}$

$F = \frac{1500}{2}$

$= 750\ N$

Therefore, the force exerted by one leg during the jump is 750 N.

For Walking Activity:

An average person exerts 3 times of their body weight. so,

$= 3 \times 37.5$

$= 1103.62\ N$

$\approx 1100\ N$

For Running Condition:

An average person exerts three and half times of his body weight based on this if a person weighs 75 kg then,

75 x 3.5 x 9.81 = 2571.98N

for one leg = $\frac{2572}{2}$

=1286N

≈ 1300

III. Finite Element Analysis

The 3D CAD model is saved in .stp format for the assembly of the plate and screws with femur bone, as well as for analysis purposes. The assembly process is performed in SolidWorks software as shown in Fig. 2, while the analysis is performed in ANSYS Workbench 2022 R1 software.

A. Meshing

Figure 5. Meshing of a Femur Bone

Meshing is performed to divide the geometry into smaller and simpler elements, allowing for the approximation of complex shapes and the numerical solution of equations governing the behaviour of the system. Fig. 4, Shows the generated mesh for the femur bone.

B. Applying Loads.

Different loads are taken for different activities, such as standing, jumping, walking and running.

Figure 4. Applying loads

E-ISSN 2581 – 7957
P-ISSN 2277 – 3916
CVR Journal of Science and Technology, Volume 26, June 2024
DOI: 10.32377/cvrjst2620

The load values are taken respectively 370 N, 750 N, 1100 N and 1300 N, these loads are applied on the head of the bone as shown in Fig. 5.

As shown in Fig. 6, at the bottom of the femur bone, fixed support is applied to withstand the pressure acting on the femur bone replicating the real-life activity.

Figure 6. Applying Fixed Support

C. Applying Moment

In biomechanical analysis, moment represent rotational forces on structures like the femur bone. During standing, a small non-zero moment, like 0.01 N-mm, simulates stability. Dynamic activities like walking or running require higher moments up to 1000 N-mm to mimic the forces experienced by the femur. Fig. 7. Shows about the moment applied for jumping, walking and running activity and Fig. 8. Shows about moment applied for standing activity.

Figure 7. Moment For Standing Activity

Figure 8. Moment For Jumping, Walking and Running Activity

IV. Results and Discussions

After applying fixed support and pressure on the bone, structural analysis is performed for four different materials (Nylon, PMMA, SS316l and Ti-6Al-4V) in Ansys workbench software to determine the equivalent (von-mises) stress and the total deformation for four activities/conditions (i.e. standing, jumping, walking and running). The following results were observed in the analysis.

A. Total Deformation of Femur Bone

Total deformation is applied for four materials i.e. Nylon, PMMA, SS316l and Ti-6Al-4V under different activities like standing, jumping, walking and running conditions.

1. Total deformation of Nylon material for four activities

Under the standing condition with a pressure of 370 N, the nylon material exhibits a maximum deformation of 1.0489 mm as shown in Fig. 9.

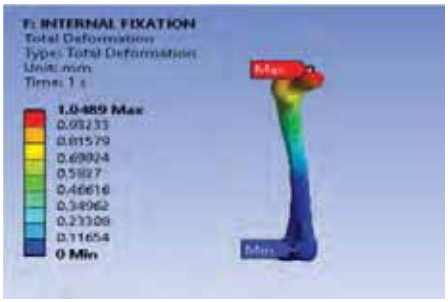

Figure 9. Standing Activity/Condition

As shown in Fig. 9, the total deformation is applied to other activities and the results are given in the below Table II.

TABLE II.
Total Deformation for Nylon Material

Activity/Conditions	Total Deformation [mm]	
	Max	Min
Standing (370N)	1.0489	0
Jumping (750N)	2.1261	0
Walking (1100N)	3.1183	0
Running (1300N)	3.6852	0

2. Total deformation of PMMA material for four activities

Now, the total deformation for the PMMA material for four activities is given in Table III.

TABLE III.
Total Deformation for PMMA Material

Activity/Conditions	Total Deformation [mm]	
	Max	Min
Standing (370N)	1.0827	0
Jumping (750N)	2.1902	0
Walking (1100N)	3.2137	0
Running (1300N)	3.7989	0

3. Total deformation of SS316l material for four activities

Now, the total deformation for the SS316L material for four activities is given in Table IV.

TABLE IV.
TOTAL DEFORMATION FOR SS316L MATERIAL

Activity/Conditions	Total Deformation [mm]	
	Max	Min
Standing (370N)	1.0968	0
Jumping (750N)	2.2187	0
Walking (1100N)	3.2555	0
Running (1300N)	3.8483	0

4. Total deformation of Ti-6Al-4V material for four activities

Now, the total deformation for the Ti-6Al-4V material for four activities is given in Table V.

TABLE V.
TOTAL DEFORMATION FOR TI-6AL-4V MATERIAL

Activity/Conditions	Total Deformation [mm]	
	Max	Min
Standing (370N)	1.4388	0
Jumping (750N)	2.9119	0
Walking (1100N)	4.2729	0
Running (1300N)	5.0506	0

B. Equivalent Stress of Femur Bone

After performing total deformation, the equivalent stress is performed on the femur bone under different activities i.e. standing, jumping, walking and running conditions.

1. Equivalent stress of Nylon material for four activities

Under the standing condition with a pressure of 370 N, the nylon material exhibits a maximum stress of 1538 MPa as shown in Fig. 10.

Figure 10. Standing Activity/Condition

As shown in Fig. 10, Von-mises stress is applied to other activities and the results are given in the below Table VI.

TABLE VI.
EQUIVALENT STRESS FOR NYLON MATERIAL

Activity/Conditions	Equivalent stress [MPa]	
	Max	Min
Standing (370N)	1538	2.39E-05
Jumping (750N)	3117.7	4.843E-05
Walking (1100N)	4572.6	7.103E-05
Running (1300N)	5404	8.42E-05

2. Von-mises stress of PMMA material for four activities

Now, the total deformation for the PMMA material for four activities is given in Table VII.

TABLE VII.
EQUIVALENT STRESS FOR PMMA MATERIAL

Activity/Conditions	Equivalent stress [MPa]	
	Max	Min
Standing (370N)	1188.5	1.53E-05
Jumping (750N)	2411	2.93E-05
Walking (1100N)	3533.5	4.37E-05
Running (1300N)	4175.3	5.19E-05

3. Von-mises stress of SS316l material for four activities

Now, the total deformation for the SS316L material for four activities is given in Table VIII.

TABLE VIII.
EQUIVALENT STRESS FOR SS316L MATERIAL

Activity/Conditions	Equivalent stress [MPa]	
	Max	Min
Standing (370N)	1006.7	1.02E-05
Jumping (750N)	2040	2.68E-05
Walking (1100N)	2990.9	4.04E-05
Running (1300N)	3534.5	4.56E-05

4. Von-mises stress of Ti-6Al-4V material for four activities

Now, the total deformation for the Ti-6Al-4V material for four activities is given in Table IX.

TABLE IX.
EQUIVALENT STRESS FOR TI-6AL-4V MATERIAL

Activity/Conditions	Equivalent stress [MPa]	
	Max	Min
Standing (370N)	9.2911	8.00E-08
Jumping (750N)	18.836	1.59E-07
Walking (1100N)	27.624	2.35E-07
Running (1300N)	32.646	2.78E-07

The graph of total deformation for four different materials is observed in above Fig. 11.

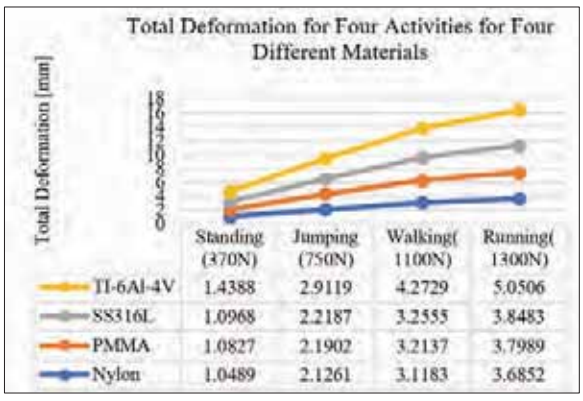

Figure 11. Total Deformation Graph for Different Materials

The graph of Equivalent stress for four different materials is observed in below Fig. 12.

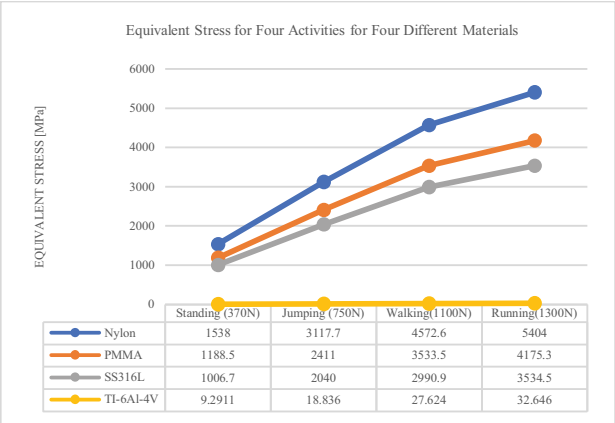

Figure 12. Equivalent stress Graph for Different Materials

V. Conclusion

In this paper, the femur model is generated by importing DICOM files into 3D slicer and the analysis is done by using ANSYS workbench 2022 R1 software. The analysis is made for four different materials under different activities i.e. Standing (370 N), Jumping(750 N), Walking(1100N), Running (1300N).

From the results it is observed that the Ti-6Al-4V material demonstrates the lowest equivalent stress values, ranging from 9.2911 MPa for standing to 32.646 MPa for running, indicating its effectiveness in withstanding various loading conditions. After the Ti-6Al-4V, SS316L has the better results compared to PMMA and Nylon. While all four materials are biocompatible the choice of material may vary depending upon specific requirements and if we're considering cost factor into account, TI-6Al-4V is priced approximately Rs 1600 to 2500 per kg, while PMMA price around Rs 135 per kg.

References

[1] S. Kirthana, M. Bindhu Supraja , A.S.N Vishwa, Mahalakshmi, "Static structural analysis on femur bone using different plate material," *Materials Today: Proceedings*, Volume 22, Part 4, pp. 2324-2333, 2020.

[2] P.S.R. Senthil Maharaj, R. Maheswaran, A. Vasanthanathan, "Numerical analysis of fractured femur bone with prosthetic bone plates," *Procedia Engineering*, Volume 64, pp. 1242-1251, 2013.

[3] K.C. Nithin Kumar, Narendra Griya, Amir Shaikh, Vaishali Chaudhry, Subhash Chavadaki, "Structural analysis of femur bone to predict the suitable alternative material," *Procedia Manufacturing*, Volume 26, Part 2, pp. 364-368, 2020.

[4] S.G. Aftab, Ahmed Faisal, Hamid Hussain, B. Sreedhara, N. Ramesh Babu, B.A. Praveen, "Structural analysis of human femur bone to select an alternative composite material," *Procedia Manufacturing*, Volume 48, pp. 82-89, 2020

[5] S. Mathukumar, VA Nagarajan and A. Radhakrishnan, "Analysis and validation of femur bone data using finite element method under static load condition," *Proc IMechE art C: J Mechanical Engineering Science 2019*, Volume 233(16), pp. 5547–5555.

[6] P. Kishore, Anjan Kumar Dash, K Dhilip Kumar, "Modelling and analysis of femur bone from CT scan," *International Conference on Advances in Materials Processing and Characterization",* volume 764-012003 (2020).

[7] Pravat Kumar Satapathy, Bamadev Sahoo, Panda L N and Das S, "Finite element analysis of functionally graded bone plate at femur bone fracture site," *IOP Conference Series: Materials Science and Engineering*, Volume 330 (2018) -012027.

[8] Albert E. Yousif and Mustafa Y. Aziz, "Biomechanical analysis of the human femur bone during going upstairs and sitting down," *IOSR Journal of Engineering,* ISSN: 2250-3021 Volume 2, Issue 8 (August 2012), pp.13-19.

[9] Yegireddi Shireesha, Dr S. V. Ramana and P. Govinda Rao, "Modelling and static analysis of femur bone by using different implant materials," *IOSR Journal of Mechanical and Civil Engineering (IOSR-JMCE)*, e-ISSN: 2278-1684, p-ISSN: 2320-334X, Volume 7, Issue 4 (Jul. - Aug. 2013), pp. 82-91.

[10] Raji Nareliya and Veerendra Kumar, "Biomechanical Analysis of Human Femur Bone," *IOSR Journal of Engineering (IOSRJEN)*, ISSN: 2250-3021 Volume 2, Issue 8 (August 2012), pp. 13-19.

E-ISSN 2581 – 7957
P-ISSN 2277 – 3916

CVR Journal of Science and Technology, Volume 26, June 2024
DOI: 10.32377/cvrjst2621

Modeling and Thermal Analysis of Engine Block

Sk. Mohammad Shareef
Assistant Professor, CVR College of Engineering/Mechanical Engg. Department, Hyderabad, India
Email: shareefshaik4@gmail.com

Abstract: **In the realm of internal combustion engines, the engine block plays a pivotal role, where the combustion of the air-fuel mixture occurs. Due to this combustion process, high heat is released and transferred to the walls of the engine block. If this heat is not dissipated properly to the outside, it will affect the engine's performance. Hence the heat should be removed from the engine block. The heat removal rate from the engine block mainly depends on the material's thermal conductivity. Hence, this study endeavors to conduct thermal analysis on an engine block composed of various materials using ANSYS Workbench software, and modeling was done in Creo Parametric. The findings are meticulously analyzed to identify the material offering superior heat transfer performance.**

Index Terms: **Engine block, modeling, thermal analysis, Creo Parametric, and Ansys Workbench.**

I. Introduction

The performance of vehicles is predominantly reliant on the performance of the engine. The selection and manufacturing of the optimal engine design hinges greatly upon the choice of materials, as the performance of internal combustion engines is directly linked to the thermal behavior of these materials. Thermal analysis, a branch of material science, delves into the properties of materials affected by temperature variations. It is frequently utilized to study heat transfer phenomena in structures such as internal combustion engines, molding blocks, and various other applications where heat transfer occurs through conduction and convection.

This paper endeavors to identify the most suitable material for the engine block. To achieve this, a thermal analysis of the engine block was conducted using different composite materials. The engine block design was modeled using CREO software. Heat transfer simulations were executed using ANSYS workbench software to ascertain the temperature distribution across the various materials of the engine block. The rate of heat transfer is contingent upon factors such as the engine block model, number of fins, wind velocity, and primarily the material of the block. Hence, this paper conducts a thermal analysis of the engine block using different materials.

II. Literature Survey

Shubham Shrivastava et al [1] have conducted a thermal analysis of a Cylinder Block with Fins Perpendicular to the Axis of the Piston Movement using different alloys like AA 1050, Aluminum alloy, gray cast iron, and Magnesium alloy. In the results, it is concluded that Aluminum alloy was chosen for a better heat transfer rate.

Pulkit Sagar et al [2] have done Heat transfer analysis and optimization of engine fins of varying surface roughness. In this paper authors have taken roughness 250 microns, 300 microns, and 400 microns. AUTODESK INVENTOR 2014 is used for modeling and simulation in Nastran 2015. The complete analysis is done by using Aluminum alloy 6061. In the results, it is concluded that by increasing the surface roughness value heat release rate also increased.

Thornhill, D. et al [3] have done experimental work on the surface heat transfer coefficient of finned metal cylinders in a free stream. In this paper, the authors have used eight cast aluminum alloy cylinders with four different pitches and five various fin lengths. The results show that at lower air speeds the exponent related velocity to the fin surface heat transfer coefficient.

Esfahanian et al [4] have analyzed SI engine piston using three combustion boundary condition techniques. It has been concluded that employing a spatial and time-averaged combustion side boundary condition proves more effective compared to utilizing surface and time-averaged boundary conditions in piston thermal analysis. Furthermore, the application of transient boundary conditions is noted to be time-intensive; however, within engineering approximations, it demonstrates minimal influence on the results of piston thermal analysis. Similarly, the utilization of a time-varying piston temperature boundary condition throughout the engine cycle does not markedly impact the outcomes of combustion analysis.

III. Materials and Properties

A. Mechanical Properties of Materials Aluminium Alloy:

TABLE I.
Mechanical Properties Of Materials Aluminum Alloy

S. No	Material Properties	Units	Values
1	Density	Kg/m3	2770
2	Specific heat	J/Kg -ºC	875
3	Coefficient of thermal expansion	1/K	$23x\ 10^{-6}$
4	Compressive yield strength	Pa	$2800x\ 10^{-5}$
5	Young's modulus	GPa	71
6	Bulk modulus	Pa	$6.9608x\ 10^{10}$
7	Shear modulus	Pa	$2.6992x\ 10^{10}$
8	Thermal conductivity	W/m-k	120-160
9	Tensile ultimate strength	Pa	3100
10	Poisson's ratio	-----	0.33

Table. I show the Mechanical properties of aluminum alloy.

Received on 15-03-2024, Revised on 14-04-2024, Accepted on 14-05-2024.

B. Mechanical Properties of Materials Grey cast iron:

TABLE II.
MECHANICAL PROPERTIES OF MATERIALS GREY CAST IRON

S. No	Material Properties	Units	Values
1	Density	Kg/m3	7200
2	Specific heat	J/Kg -ºC	447
3	Coefficient of thermal expansion	1/K	11x 10^{-6}
4	Compressive ultimate strength	Pa	8.2 x 10^{8}
5	Young's modulus	GPa	110
6	Bulk modulus	Pa	8.33x 10^{10}
7	Shear modulus	Pa	4.2969x 10^{10}
8	Thermal conductivity	W/m-k	52
9	Tensile ultimate strength	Pa	2.4x 10^{8}
10	Poisson's ratio	-----	0.28

Table. II shows the Mechanical properties of grey cast iron.

C. Mechanical Properties of Materials Structural steel:

TABLE III.
MECHANICAL PROPERTIES OF MATERIALS STRUCTURAL STEEL

S. No	Material Properties	Units	Values
1	Density	Kg/m3	7850
2	Specific heat	J/Kg -ºC	420
3	Coefficient of thermal expansion	1/K	1.2 × 10−5
4	Compressive ultimate strength	Pa	2.50E+08
5	Young's modulus	Pa	2.079E+11
6	Bulk modulus	Pa	1.725E+11
7	Shear modulus	Pa	7.9615E+10
8	Thermal conductivity	W/m-k	45
9	Tensile ultimate strength	Pa	2.5E+08
10	Poisson's ratio	-----	0.3

Table. III shows the Mechanical properties of structural steel.

IV. FINITE ELEMENT MODELLING

Creo Parametric is used for modeling engine blocks.

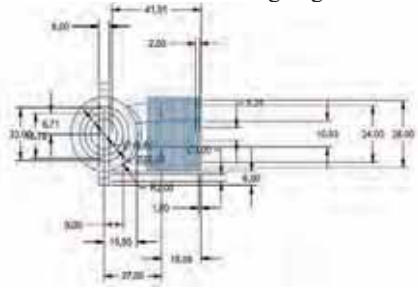

Figure 1. Engine block dimensions.

Fig.1 shows the dimensions of the engine block which is used for modeling in Creo Parametric.

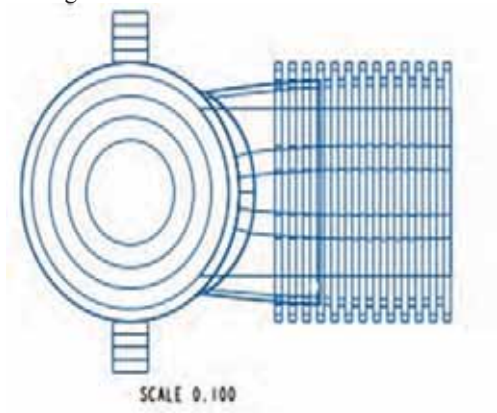

Figure 2. Top view of the Engine block.

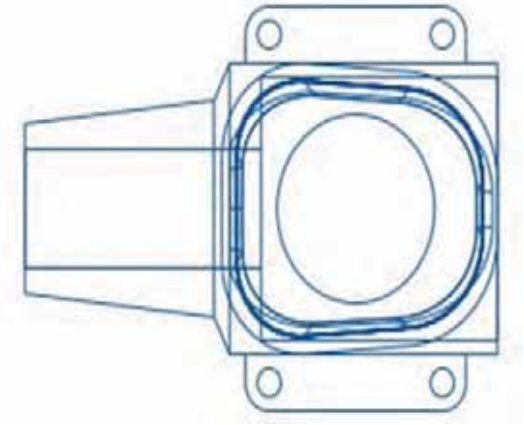

Figure 3. Side view of the Engine block.

Figure 4. 3D-View of the Engine block

Fig.2 shows the Top view, Fig.3 shows the side view and Fig.4 shows the 3D view of the Engine block.

CVR Journal of Science and Technology, Volume 26, June 2024
DOI: 10.32377/cvrjst2621

V. Thermal Analysis

TABLE IV.
MESHING OF ENGINE BLOCK

Nodes	Elements	Elements Size
59371	35317	0.2m

Table. IV shows the nodes, elements, and elemental sizes that are taken into consideration in the engine block for thermal analysis.

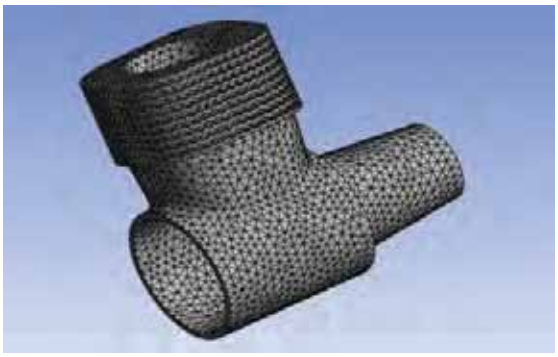

Figure 5. The meshing of the Engine block

Fig.5 shows the meshing of the engine block.

A. Aluminum alloy:

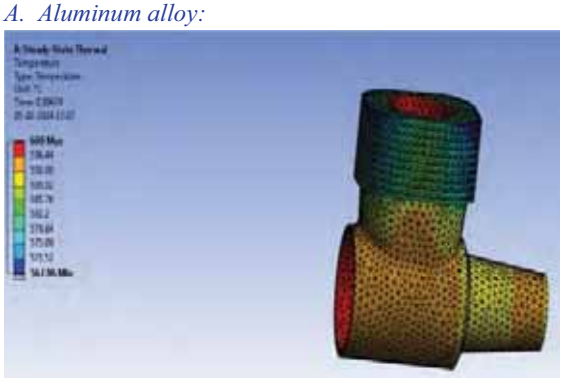

Figure 6. Temperature distribution in the Engine block using aluminum alloy

Fig.6 shows the temperature distribution in the engine block using aluminum alloy as a material and it is observed that the max temperature induced is 600ºC and the minimum temperature is 567.96ºC.

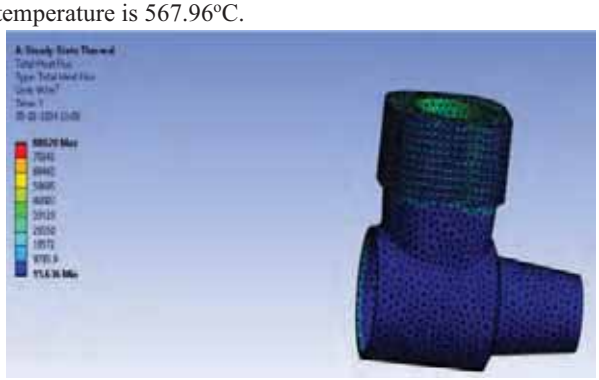

Figure 7. Heat flux distribution in the Engine block using aluminum alloy

Fig.7 shows the Heat flux in the engine block using aluminum alloy as a material and it is observed that the max heat flux is 88020 W/m^2 and the minimum heat flux is 15.636 W/m^2.

B. Grey Cast Iron:

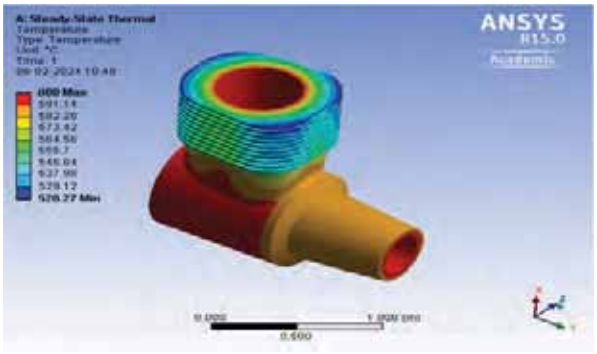

Figure 8. Temperature distribution in the Engine block using grey cast iron

Fig.8 shows the temperature distribution in the engine block using grey cast iron as a material and it is observed that the max temperature induced is 600ºC and the minimum temperature is 520.27ºC.

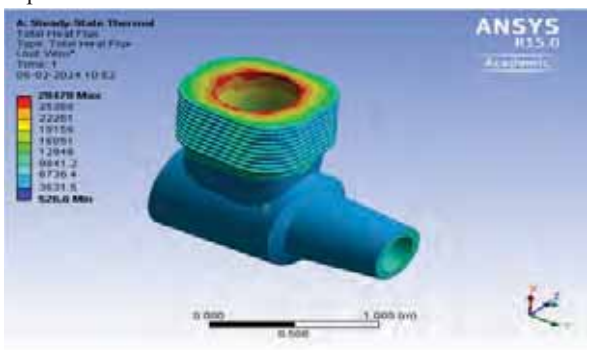

Figure 9. Heat flux distribution in the Engine block using aluminum alloy

Fig.9 shows the Heat flux in the engine block using grey cast iron as a material and it is observed that the max heat flux is 28470 W/m^2 and the minimum heat flux is 526.6 W/m^2.

C. Structural Steel:

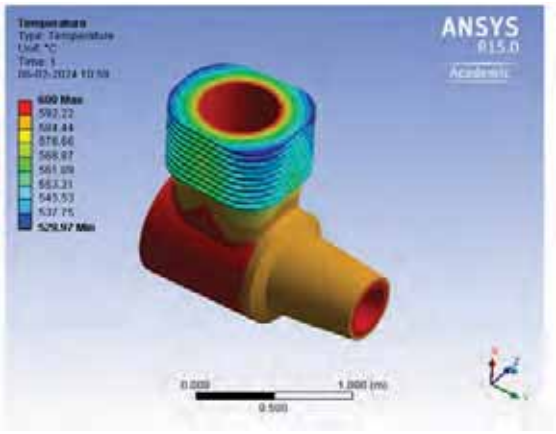

Figure 10. Temperature distribution in the Engine block using structural steel

CVR Journal of Science and Technology, Volume 26, June 2024
DOI: 10.32377/cvrjst2621

Fig.10 shows the temperature distribution in the engine block using structural steel as a material and it is observed that the max temperature induced is 600ºC and the minimum temperature is 529.97ºC.

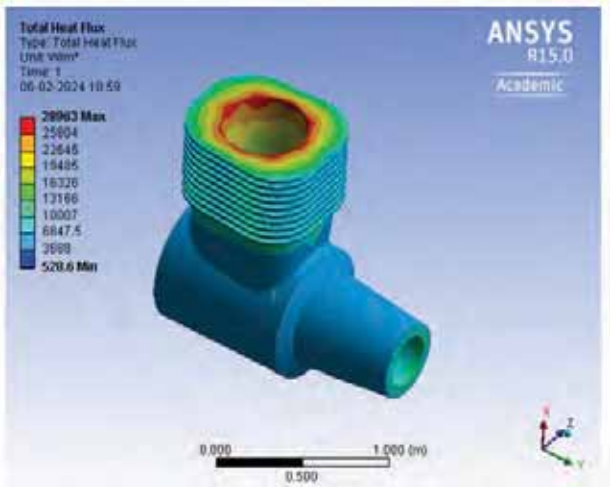

Figure 11. Heat flux distribution in the Engine block using structural steel

Fig.11 shows the Heat flux in the engine block using structural steel as a material and it is observed that the max heat flux is 28963 W/m^2 and the minimum heat flux is 528.6 W/m^2.

VI. Conclusions

TABLE V.
Comparison between different materials

S. No	Material	Temperature(ºC)		Heat flux(W/m^2)	
		Min	Max	Min	Max
1	Aluminum alloy	567.96	600	15.636	88020
2	Grey cast iron	520.25	600	526.6	28470
3	Structural steel	529.97	600	528.6	28963

Table. V shows the comparison between temperature distribution and Heat flux in the engine block using different materials respectively.
It is observed that Heat flux values are higher for Aluminum alloy compared to grey cast iron and structural steel. Higher values of the heat flux are to be higher the heat release rate to the atmosphere.

References

[1] Shubham Shrivastava and Shikar Upadhyay “Thermal Analysis of IC Engine Cylinder Block with Fins Perpendicular to the Axis of Piston Movement”, International Journal of Mechanical and Industrial Technology, Vol. 3, Issue 2, pp: (139-149), Month: October 2015 - March 2016.
[2] Pulkit Sagara, Puneet Teotiab, Akash Deep Sahlotc, and H.C Thakur “Heat transfer analysis and optimization of engine fins of varying surface roughness” International Conference on Advancements in Aeromechanical Materials for Manufacturing (ICAAMM-2016), Materials Today: Proceedings 4 (2017) 8565–8570.
[3] Thornhill, D., A. Graham, G. Cunnigham, P. Troxler, and R. Meyer. “Experimental Investigation into the Free Air-Cooling of Air-Cooled Cylinders.” SAE Transactions 112 (2003): 2046–57. http://www.jstor.org/stable/44741419.
[4] Esfahanian, V., A. Javaheri, and M. Ghaffarpour. "Thermal Analysis of an SI Engine Piston Using Different Combustion Boundary Condition Treatments." Applied Thermal Engineering 26, no. 2-3 (2006): 277-287. Accessed March 15, 2024. https://doi.org/10.1016/j.applthermaleng.2005.05.002.

In the next issue (Vol. 27, December 2024)

1.	*Smart Road Safety and Vehicle Accident Prevention System for Mountain Roads*	*Vangala Praveen Kumar* *Kalagotla Chenchi Reddy* *Varikuppala Manohar*
2.	*An IoT Enabled Real Time Communication and Location Tracking System for Vehicular Emergency*	*S. Harivardhagini*
3.	*Customized Convolutional Neural Network for Detection of Emotions from Facial Expressions*	*D. Shyam Prasad* *Dr. K. Arun Kumar*
4.	*Performance Evaluation of UFMC for Future Wireless communication Systems*	*Malleswari Akurati* *Satish Kumar Pentamsetty* *Satya Prasad Kodati*
5.	*Design and Simulation of Doherty Power Amplifier for 2.4 GHz Frequency Applications*	*Racha Ganesh* *Dr. K. Lal Kishore* *Dr. Yedukondalu Kamatham* *Dr. P. Srinivasa Rao*

E-ISSN 2581 – 7957
P-ISSN 2277 – 3916

CVR Journal of Science and Technology, Volume 27, December 2024
DOI: 10.32377/cvrjstxxxx

Template for the Preparation of Papers for Publication in CVR Journal of Science and Technology

First A. Author[1] and Second B. Author[2]
[1]Designation, Name of Institution/Department, City, Country
Email: first.author@hostname1.org
[2]Designation, Name of Institution/Department, City, Country
Email: second.author@hostname2.org

Abstract: **These instructions give you basic guidelines for preparing camera-ready papers for CVR College journal Publications. Your cooperation in this matter will help in producing a high-quality journal.**

Index Terms: **first term, second term, third term, fourth term, fifth term, sixth term**

I. Introduction

Your goal is to simulate the usual appearance of papers in a Journal Publication of the CVR College. We are requesting that you follow these guidelines as closely as possible. It should be original work. Format must be done as per the template specified. Diagrams with good clarity with relevant reference within the text are to be given. References are to be cited within the body of the paper. Number of pages must not be less than five with minimum number of 4000 words and not exceeding eight pages. The journal is published in colour. Colours used for headings, subheadings and other captions must be strictly as per the template given in colour.

A. Full-Sized Camera-Ready (CR) Copy

Prepare your CR paper in full-size format, on A4 paper (210 x 297 mm or 8.27 x 11.69 in). No header or footer, no page number.

Type sizes and typefaces: Follow the type sizes specified in Table I. As an aid in gauging type size, 1 point is about 0.35 mm. The size of the lowercase letter "j" will give the point size. Times New Roman has to be the font for main text. Paper should be single spaced.

Margins: Top and Bottom = 24.9mm (0.98 in), Left and Right = 16 mm (0.63 in). The column width is 86mm (3.39 in). The space between the two columns is 6mm (0.24 in). Paragraph indentation is 3.7 mm (0.15 in).

Left- and right-justify your columns. Use tables and figures to adjust column length. On the last page of your paper, adjust the lengths of the columns so that they are equal. Use automatic hyphenation and check spelling. Digitize or paste down figures.

For the Title use 24-point Times New Roman font, an initial capital letter for each word. Its paragraph description should be set so that the line spacing is single with 6-point spacing before and 6-point spacing after. Use two additional line spacings of 10 points before the beginning of the double column section, as shown above.

TABLE I.
TYPE SIZES FOR CAMERA-READY PAPERS

Type size (pts.)	Appearance		
	Regular	Bold	Italic
6	Table caption, table superscripts		
8	Tables, table names, f irst letters in table captions, figure captions, footnotes, text subscripts, and superscripts		
9	References, authors' biographies	Abstra ct	
10	Section titles ,Authors' affiliations, main text, equations, first letters in section titles		Subheading
11	Authors' names		
24	Paper title		

Each major section begins with a Heading in 10 point Times New Roman font centered within the column and numbered using Roman numerals (except for REFERENCES), followed by a period, two spaces, and the title using an initial capital letter for each word. The remaining letters are in SMALL CAPITALS (8 point). The paragraph description of the section heading line should be set for 12 points before and 6 points after.

Subheadings should be 10 point, italic, left justified, and numbered with letters (A, B, …), followed by a period, two spaces, and the title using an initial capital letter for each word. The paragraph description of the subheading line should be set for 6 points before and 3 points after.

For main text, paragraph spacing should be single spaced, no space between paragraphs. Paragraph indentation should be 3.7mm/0.21in, but no indentation for abstract & index terms.

II. Helpful Hints

A. Figures And Tables

Position figures and tables at the tops and bottoms of columns. Avoid placing them in the middle of columns. Large figures and tables may span across both columns. Leave sufficient room between the figures/tables and the main text. Figure captions should be centered below the figures; table captions should be centered above. Avoid placing figures and tables before their first mention in the

Received on xx-xx-xxxx, Revised on xx-xx-xxxx, Accepted on xx-xx-xxxx.

CVR Journal of Science and Technology, Volume 27, December 2024
DOI: 10.32377/cvrjstxxxx

text. Use the abbreviation "Fig. 1," even at the beginning of a sentence.

To figure axis labels, use words rather than symbols. Do not label axes only with units. Do not label axes with a ratio

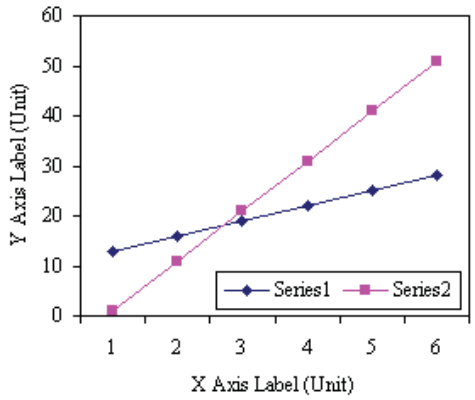

Figure 2. Note how the caption is centered in the column.

of quantities and units. Figure labels should be legible, about 8-point type.

All figures, tables and references must be cited in the text.

Please indicate the broad area/specializations into which the research paper falls, in the covering letter/mail to the Editor, so that reviewers with those specializations may be identified.

B. References

Number citations consecutively in square brackets [1]. Punctuation follows the bracket [2]. Use "Ref. [3]" or "Reference [3]" at the beginning of a sentence:

Give all authors' names; use "et al." if there are six authors or more. Papers that have not been published, even if they have been submitted for publication, should be cited as "unpublished" [4]. Papers that have been accepted for publication should be cited as "in press" [5]. In a paper title, capitalize the first word and all other words except for conjunctions, prepositions less than seven letters, and prepositional phrases. Good number of references must be given.

Latest references in the area must be included and every refence must be cited in the text of the research article.

C. Footnotes

Number footnotes separately in superscripts [1, 2, ⋯]. Place the actual footnote at the bottom of the column in which it was cited, as in this column. See first page footnote as an example.

D. Abbreviations and Acronyms

Define abbreviations and acronyms the first time they are used in the text, even after they have been defined in the abstract. Do not use abbreviations in the title unless they are unavoidable.

E. Equations0

Equations should be left justified in the column. The paragraph description of the line containing the equation should be set for 6 points before and 6 points after. Number equations consecutively with equation numbers in parentheses flush with the right margin, as in (1). Italicize Roman symbols for quantities and variables, but not Greek symbols. Punctuate equations with commas or periods when they are part of a sentence, as in

$$a + b = c \ . \qquad (1)$$

Symbols in your equation should be defined before the equation appears or immediately following. Use "(1)," not "Eq. (1)" or "equation (1)," except at the beginning of a sentence: "Equation (1) is ..."

F. Other Recommendations

Use either SI (MKS) or CGS as primary units. (SI units are encouraged.) If your native language is not English, try to get a native English-speaking colleague to proofread your paper. Do not add page numbers.

III. Conclusions

The authors can conclude on the topic discussed and proposed, future enhancement of research work can also be briefed here.

References

[1] G. Eason, B. Noble, and I. N. Sneddon, "On certain integrals of Lipschitz-Hankel type involving products of Bessel functions," Phil. Trans. Roy. Soc. London, vol. A247, pp. 529–551, April 1955.

[2] J. Clerk Maxwell, *A Treatise on Electricity and Magnetism*, 3rd ed., vol. 2. Oxford: Clarendon, 1892, pp.68–73.

[3] I. S. Jacobs and C. P. Bean, "Fine particles, thin films and exchange anisotropy," in *Magnetism*, vol. III, G. T. Rado and H. Suhl, Eds. New York: Academic, 1963, pp. 271–350.

[4] K. Elissa, "Title of paper if known," unpublished.

[5] R. Nicole, "Title of paper with only first word capitalized", *J. Name Stand. Abbrev.*, in press.

[6] Y. Yorozu, M. Hirano, K. Oka, and Y. Tagawa, "Electron spectroscopy studies on magneto-optical media and plastic substrate interface," *IEEE Transl. J. Magn. Japan*, vol. 2, pp. 740–741, August 1987 [Digests 9th Annual Conf. Magnetics Japan, p. 301, 1982].

[7] M. Young, *The Technical Writer's Handbook*. Mill Valley, CA: University Science, 1989.

[8] T. Ali, B.K. Subhash and R.C. Biradar, "A Miniaturized Decagonal Sierpinski UWB Fractal Antenna", PIERS C, vol. 84, pp. 161-174, 2018.

ABOUT THE COLLEGE

CVR College of Engineering, an autonomous institution under the UGC, was established in the Year 2001, the first college in Telangana to be promoted by NRI technology professionals resident in the USA. The NRI promoters are associated with cutting-edge technologies of the computer and electronics industry. They also have strong associations with other leading NRI professionals working for world-renowned companies like IBM, Intel, Cisco, Facebook, AT & T, Google, and Apple who have agreed to associate with the College with a vision and passion to make the College a state-of-the-art engineering institution.

All B. Tech Programmes which are eligible are accredited three or four times by the NBA since 2007. Two UG Programmes namely ECE & EEE are accredited for Six years by the NBA under Tier-I. As of now, 7 B. Tech Programmes and 2 P.G Programmes are accredited. NAAC reaccredited the college for five years with grade 'A' with effect from 2022. Two M. Tech Programmers of AI and Data Science in 2018-2019 and three B. Tech CSE Programmes (AI & ML, DS & CS) in 2020-2021 and 3 new branches in Emerging Technologies namely B. Tech AI & ML, AI & DS and CSBSs are the Recent Programs in 2023-24.

As formulated by the IQAC, many FDPs and workshops are organized by departments. College has MoUs with organizations such as Virtusa, Mitsubishi, NRSC, COMSAT, CADENCE, IIIT. Under innovation activities faculty have published around 150 patents so far. Projects from NRSC under the RESPOND programme of ISRO, AICTE-RPS, TEQIP-III from JNTU, MODROBS-AICTE worth Rs.71 Lakhs are some of the recent projects funded by central agencies. Total funds received are Rs. 160 lakhs. Newgen IEDC of Government of India (DST) has sanctioned Rs.287 Lakhs for a period of five years in 2018-19, for Innovative Entrepreneurship Development Programmes by students and staff. 10 Projects were completed in 2019-20, 16 in 2020-21, 20 in 2021-22, 21 projects in 2022-23 and 20 projects in 2023-24. An exclusive Innovation Centre of 5000 Sqft. has been created for practical work and counseling.

The college has been creating records year after year. With more than 100 companies visiting CVRCE and 900+ placements for the 2023 - 2024 academic year, it is the highest among the peer group of colleges. This is despite the challenging environment of the job market and our placement percentage is higher than many leading institutions of the country. The highest offer is **44 Lakhs** by 4 students at AMAZON, 33 Lakhs by 2 students at Commvault and 30+ students received offers higher than **Rs. 18 Lakhs**. More than **150 students** received offers of About **Rs. 10 Lakhs**. About **200 offers** are higher than **Rs. 6 Lakhs**. With this, CVRCE becomes one of the leading colleges in the state in terms of offers with highest Average Salary. The placement percentage continues to be 100% since 5 years. The college has made huge progress in a short span of time and is preferred by the students and parents during the EAMCET counselling this year and is among the **top 3 colleges** in the state. College has been consistently in the range of 101-150 by NIRF over last Seven years. Many students have received special cash prizes in competitions like Hackathon, Mitsubishi etc., worth 1 to 2 Lakhs.

CVR is rated amongst the top 100 engineering institutions in the country by Outlook and holds many more recognitions.

CALL FOR PAPERS:

Papers in Engineering, Science and Management disciplines are invited for Publication in our Journal. Authors are requested to mail their contributions to Editor, CVR Journal of Science and Technology (Email Id: journal@cvr.ac.in). Authors can also submit their papers through our online open journal system (OJS) www.ojs.cvr.ac.in or www.cvr.ac.in/ojs. Papers are to be written using a Standard Template, which may be obtained on request from the Editor. It is also available on the college website www.cvr.ac.in

CVR JOURNAL OF SCIENCE AND TECHNOLOGY

CVR COLLEGE OF ENGINEERING

(UGC Autonomous- Affiliated to JNTU Hyderabad)
Mangalpalli (V), Ibrahimpatnam (M),
R.R. District, Telangana - 501510
http://cvr.ac.in